Entanglement in Chiral Topological Systems

Anna Sophie Hackenbroich

Ludwig-Maximilians-Universität München

Max-Planck-Institut für Quantenoptik

München 2020

Entanglement in Chiral Topological Systems

Anna Sophie Hackenbroich

Dissertation
an der Fakultät für Physik
der Ludwig–Maximilians–Universität
München

vorgelegt von
Anna Sophie Hackenbroich
aus München

München, den 14. Dezember 2020

Erstgutachter: Prof. Dr. Jan von Delft
Zweitgutachter: Prof. Dr. Norbert Schuch
Tag der mündlichen Prüfung: 23. Februar 2021

Abstract

Topological phases of matter describe systems beyond the paradigm of spontaneous symmetry breaking, giving rise to unconventional phenomena with possible applications in topological quantum computing. Almost 40 years after their discovery, topological phases remain among the most active research fields of condensed matter physics. As evidenced by the recent discovery of higher order topological insulators (HOTIs), novel physics can emerge even in non-interacting systems. Theoretical investigations of strongly correlated systems are extremely difficult due to the exponential growth of the quantum-mechanical Hilbert space and frequently require the application of approximative methods such as model wave functions. Tensor network states (TNS) are a class of variational wave functions which allow an efficient encoding of relevant quantum many body states and which form the basis for very successful numerical algorithms. Projected entangled pair states (PEPS), a class of TNS in two and higher dimensions, permit the exact representation of many interacting topological phases with time reversal symmetry. However, the description of experimentally relevant chiral topological phases like the integer and fractional quantum Hall effects is much more subtle using the TNS framework.

The first part of this thesis focuses on the description of chiral topological phases using PEPS. Firstly, we study a previously proposed chiral PEPS that was conjectured to possess anyonic excitations. By a careful analysis of its symmetries we are able to align important entanglement observables more closely with the expected universal behavior. This highlights that efficient PEPS can possess characteristic properties of chiral topological phases. Secondly, we focus on the issue that all known chiral PEPS have algebraic bulk correlation functions and therefore cannot be the ground states of gapped local Hamiltonians. Since this problem arises already for non-interacting chiral topological phases, we focus on two examples of such systems and show that their ground states can be represented exactly by efficient PEPS in a hybrid lattice with one momentum-space direction. After an inverse Fourier transform, the PEPS with only real-space coordinates requires an exponentially growing number of parameters for an exact representation. This provides a concrete illustration of the impossibility to encode gapped chiral phases exactly with efficient PEPS.

Finally, we analyze a model wave function for a three-dimensional (3D) HOTI with strong intrinsic correlations using large-scale variational Monte Carlo simulations. This wave function is obtained by projection of two copies of a non-interacting HOTI with chiral hinge states. We characterize the gapless hinge states of the interacting system and show that they are of the same nature as the edge states of the 1/2 Laughlin state. Surprisingly, the gapped surfaces host a two-dimensional (2D) phase whose topological entanglement entropy is half of that of the 1/2 Laughlin state. Such a value cannot be obtained by any of the known 2D topological orders, showing a clear departure not only from the Laughlin 1/2 physics but from conventional 2D topological order. This demonstrates that 3D topological phases can host rich phenomena that are not yet fully understood.

Zusammenfassung

Topologische Phasen der Materie beschreiben Systeme, die über das Paradigma der spontanen Symmetriebrechung hinausgehen und unkonventionelle Phänomene hervorbringen. Mögliche Anwendungen dieser Systeme sind topologische Quantencomputer. Fast 40 Jahre nach ihrer Entdeckung stellen topologische Phasen eines der aktivsten Forschungsfelder in der Physik der kondensierten Materie dar. Die Entdeckung von topologischen Isolatoren höherer Ordnung (HOTIs) hat kürzlich neuartige Physik selbst in nicht wechselwirkenden Systemen aufgedeckt. Theoretische Untersuchungen stark korrelierter Systeme sind aufgrund des exponentiellen Wachstums des quantenmechanischen Hilbertraums extrem anspruchsvoll und erfordern in der Regel die Anwendung approximativer Methoden wie Modell-Wellenfunktionen. Tensor-Netzwerk-Zustände (TNS) sind eine Klasse variationeller Wellenfunktionen, die eine effiziente Encodierung relevanter Quantenvielteilchenzustände erlauben und welche die Grundlage sehr erfolgreicher numerischer Algorithmen darstellen. Sogenannte "Projected entangled pair states" (PEPS), eine Gruppe von TNS in zwei und mehr Dimensionen, gestatten die exakte Darstellung vieler wechselwirkender topologischer Phasen mit Zeitumkehrsymmetrie. Allerdings ist die Beschreibung experimentell relevanter chiraler topologischer Phasen wie der integralen und fraktionalen Quanten-Hall-Effekte durch TNS sehr viel subtiler.

Der erste Teil dieser Arbeit befasst sich mit der Beschreibung chiraler topologischer Phasen durch PEPS. Zunächst wird ein aus der Literatur bekannter chiraler PEPS studiert, der mutmaßlich anyonische Anregungen besitzt. Durch eine sorgfältige Analyse seiner Symmetrien können wichtige Verschränkungs-Observablen genauer mit dem erwarteten universalen Verhalten in Einklang gebracht werden. Dies zeigt, dass effiziente PEPS charakteristische Eigenschaften chiraler topologischer Phasen besitzen können. In einem zweiten Schritt fokussiert sich die Arbeit auf das Problem, dass alle bekannten chiralen PEPS algebraisch abfallende Korrelationsfunktionen in ihrem Inneren besitzen und deswegen nicht die Grundzustände lokaler Hamiltonoperatoren mit einer Energielücke sein können. Da dies bereits für nicht wechselwirkende chirale topologische Phasen der Fall ist, konzentriert sich die Analyse auf zwei Beispiele solcher Systeme. Es wird gezeigt, dass die Grundzustände exakt darstellbar sind durch effiziente PEPS in einem hybriden Gitter mit einer Impulsraumrichtung. Nach einer inversen Fouriertransformation benötigt der PEPS eine exponentiell wachsende Zahl von Parametern, um mit ausschließlich Ortsraumkoordinaten exakt dargestellt zu werden. Dies ist ein konkretes Beispiel für die Unmöglichkeit, chirale Phasen mit einer Energielücke exakt mit effizienten PEPS zu encodieren.

Abschließend wird eine Modell-Wellenfunktion für einen dreidimensionalen (3D) HOTI mit starken intrinsischen Korrelationen durch großangelegte variationelle Monte-Carlo-Simulationen analysiert. Diese Wellenfunktion ist als die Projektion zweier Kopien eines nicht wechselwirkenden HOTI mit chiralen Kantenzuständen konstruiert. Es wird gezeigt, dass die Kantenzustände des wechselwirkenden Systems dieselben Eigenschaf-

ten haben wie die Randzustände eines 1/2-Laughlin-Zustands. Überraschenderweise besitzt die zweidimensionale (2D) Phase der Oberflächen mit einer Energielücke eine topologische Verschränkungsentropie, deren Wert halb so groß ist wie die topologische Verschränkungsentropie des 1/2-Laughlin-Zustands. Dies kann durch keine der bekannten 2D topologischen Ordnungen erklärt werden. Damit zeigt sich eine klare Abkehr nicht nur von der Physik des 1/2-Laughlin-Zustands, sondern von allen bekannten 2D topologischen Ordnungen. Dies legt nahe, dass 3D topologische Phasen eine reiche Phänomenologie zeigen können, die noch nicht vollständig verstanden ist.

List of publications

This thesis is based on the following publications:

1. Anna Hackenbroich, Antoine Sterdyniak, and Norbert Schuch. "Interplay of SU(2), point group, and translational symmetry for projected entangled pair states: Application to a chiral spin liquid". In: *Phys. Rev. B* 98 (8 Aug. 2018), p. 085151

2. Anna Hackenbroich, B. Andrei Bernevig, Norbert Schuch, and Nicolas Regnault. "Fermionic tensor networks for higher-order topological insulators from charge pumping". In: *Phys. Rev. B* 101 (11 Mar. 2020), p. 115134

3. Anna Hackenbroich, Ana Hudomal, Norbert Schuch, B. Andrei Bernevig, and Nicolas Regnault. "Fractional Chiral Hinge Insulator". In: *arXiv e-prints* (Oct. 2020). arXiv: 2010.09728 [cond-mat.str-el] (Submitted to Physical Review Letters)

Acknowledgment

This thesis could not have been completed without the help and support of many people.

I am thankful to my supervisor Norbert Schuch for giving me the opportunity to work at MPQ, for his scientific insight and for the freedom to choose my own projects.

I would like to express my deep gratitude to Nicolas Regnault for designing and leading my last two projects, in which I rediscovered the joy of successful research. His guidance and support during countless hours of video calls, several visits to Paris and even a trip to Princeton have been of invaluable help to me. I will always remember the evenings of good food and company!

I am grateful to Ignacio Cirac for leading the theory group at MPQ, and the support and open ear that he offers to everyone in his division.

I would like to thank Jan von Delft for being my supervisor at the LMU and for his great help and support with the formalities of submitting my thesis.

I am grateful to all members of my PhD commission, especially to Jan von Delft and Norbert Schuch for reviewing my thesis, and to Ilka Brunner for presiding over the commission and organizing everything for the day of the defense.

I sincerely thank my co-authors Hong-Hao Tu, Antoine Sterdyniak, Ana Hudomal, Andrei Bernevig, Valentin Crépel and Benoît Estienne for the productive collaboration and friendship.

A big thank you goes to my office mates and all my friends and colleagues at MPQ for help with countless small things that make life so much easier, many hours of good conversations over tea and coffee, and fond memories from shared workshops and conferences. I am deeply grateful to Andrea for her incredible commitment and energy towards keeping the theory group alive, and her help with so many things! I would like to thank Sonya Gzyl for her investment and determination for improving the situation of doctoral students in the IMPRS.

Finally, I am thankful to my friends in Munich for many good times in the climbing gym, the beer garden or in front of a Woody Allen film. I am especially grateful to the members of our Plätzchen manufacture, Vanessa, Nina and Asli (and Max and Marin?), for true and great friendship! Most of all, I am indebted to Antoine and my family for their unwavering love and support over the past years. Without you, this thesis would not exist!

Contents

Chapter 1

Introduction

The objective of Condensed Matter Physics is to study and to understand the properties of materials in different conditions. To this end, it is of special importance to identify universal properties which are shared by all systems in the same phase. Theoretical physicists can then construct simplified models which reproduce the universal properties of a given phase, and whose analysis often results in a deeper understanding of the latter's nature. The theoretical study of simple models can also lead to experimentally verifiable predictions. For example, it has become possible to engineer complex material heterostructures chosen for their predicted useful properties.

Since the discoveries of the integer and fractional quantum Hall effects (QHE) in 1980 [4] and 1982 [5], topological phases of matter have been the subject of intense research efforts in Condensed Matter Physics. In contrast to conventional phases generated by spontaneous symmetry breaking, topological phases cannot be characterized using a local order parameter. Their defining properties are instead of a topological nature, implying that they are robust towards local perturbations. This can lead to an astounding quantization of observables in macroscopic samples, allowing for instance the measurement of the Hall conductivity e^2/h of the integer QHE to a precision of more than 10 digits.

From a theoretical point of view, topological phases may be broadly separated into two groups. Phases in the first group can be described using simple models that neglect the interactions between electrons. The universal properties of these models can therefore effectively be computed by considering only a single particle, making them very numerically tractable. Examples include the phase of the integer QHE [6] and those of the celebrated topological insulators in two and three dimensions [7], which were theoretically predicted to occur in two-dimensional (2D) and three-dimensional (3D) materials in 2006 [8] and 2007 [9] and experimentally realized in 2007 [10] and 2008 [11, 12], respectively.

On the other hand, topological phases in the second group feature strong electronic interactions, rendering their theoretical description much more complex. As a result of the strong correlations, these phases can also give rise to a host of novel and fascinating phenomena subsumed under the term intrinsic topological order [13]. For instance, 2D phases with intrinsic topological order have point-like anyonic excitations which obey neither fermionic nor bosonic exchange statistics. Such systems have thus been proposed

as platforms for topological quantum computing, which would enjoy an inbuilt protection from local errors due to the topological quantization [14]. Numerous theoretical models displaying different kinds of intrinsic topological order have been constructed. However, to date the only experimentally realized system with this kind of topological ordering is the fractional QHE, where excitations with fractional charge [15, 16] and fractional statistics [17, 18] have been observed in experiments.

After 40 years of research, many universal properties of 2D phases with intrinsic topological order are well understood and classified theoretically. However, several important open problems remain. For example, the generalization of topological order to 3D systems is a subject of current interest with many questions as yet unsettled. It has already become apparent that the phenomenology of interacting topological phases can be even richer in three dimensions, including for instance the recently proposed fractonic systems [19]. Another avenue towards higher-dimensional topological order may be presented by the recently discovered higher order topological phases [20, 21, 22, 23, 24]. They are an entirely new class of topological phases possessing universal boundary properties similar to the characteristic edge physics of lower-dimensional conventional topological phases. There is strong experimental evidence that bismuth realizes a higher order topological phase [25].

Moreover, it is an important task of theoretical Condensed Matter Physics to predict the topological phase of a given interacting microscopic model. In the presence of strong interactions, this is a highly non-trivial undertaking which can usually only be achieved using numerical simulations. Due to the exponential growth of the quantum-mechanical Hilbert space, straightforward numerical methods such as exact diagonalization are limited to systems with very few particles. However, topological properties are emergent effects requiring the presence of many particles, such that numerical methods based on well-chosen approximations are highly important.

Historically, the method of model wave functions has enjoyed great success. Here, the ground state of a quantum system in a given phase is approximated by a many body state which displays the correct universal features and is obtained by an educated guess rather than an exact solution of the problem. The most well-known example is the Laughlin wave function introduced in 1983 as a model state for the fractional QHE [26]. It can correctly predict the quantized Hall conductivity as well as the fractional charge and fractional statistics of the bulk excitations. There are frameworks that allow the systematic construction of model wave functions, for instance using conformal field theory [27, 28] or Gutzwiller projections. The properties of the resulting model wave functions can often be analyzed in numerical computations using for example Monte Carlo simulations.

Topological phases are characterized by unusual patterns of quantum entanglement [29, 30], intrinsic correlations that can be present between different parts of a quantum system. Whereas entanglement is usually not directly experimentally observable, it can be computed in numerical simulations and has become an important theoretical tool to diagnose different kinds of topological phases [31]. Tensor network states (TNS) are a class of model states which intrinsically follow the entanglement patterns characteristic for ground states of gapped Hamiltonians. They can be viewed as natural generalizations of trivial product states and are therefore highly numerically efficient. TNS lie at the heart of extremely

successful variational algorithms [32, 33, 34, 35], and they have also led to analytical understanding of topological phases [36, 37]. TNS can naturally describe ground states of many simple models with intrinsic topological order that are invariant under time reversal symmetry [38, 39]. However, the description of experimentally relevant chiral topological systems, where time reversal symmetry is broken like in the fractional QHE, is much more subtle in the TNS framework and remains one of the open challenges in the field.

The first part of this dissertation focuses on different problems relating to the description of chiral topological phases using projected entangled pair states (PEPS) [40], a class of TNS in two and higher dimensions. Due to the numerical usefulness of TNS, it would be highly desirable to find efficient PEPS encodings of chiral topological phases. Indeed, it is possible to construct PEPS possessing key universal properties of chiral topological phases [41, 42, 43, 44, 45, 46, 47]. However, such TNS have algebraic bulk correlation functions and therefore cannot be the ground states of gapped local Hamiltonians [43, 48].

Firstly, we study a chiral PEPS that has been conjectured to possess intrinsic topological order [45, 46]. By a careful analysis of its symmetries we are able to align key entanglement observables more closely with the expected universal behavior. This highlights that efficient PEPS can possess certain characteristic properties of chiral topological phases. We then consider PEPS for certain non-interacting chiral topological phases. We show that their ground states can be represented exactly by efficient PEPS in a hybrid lattice with one momentum-space direction. After an inverse Fourier transform, the PEPS with only real-space coordinates requires an exponentially growing number of parameters for an exact encoding. This provides a concrete illustration of the impossibility to encode gapped chiral phases exactly with efficient PEPS. Finally, we consider a 3D higher order topological phase with strong intrinsic correlations using a model wave function constructed from Gutzwiller projection. Via large-scale variational Monte Carlo simulations, we are able to characterize the gapless hinge states. We are also able to show that the gapped surfaces host a topological phase beyond the known topological orders in purely 2D systems.

This dissertation is structured as follows. In the first three chapters, we provide an overview of several important concepts underlying our research projects. In Chapter 2, we review topological phases that can be realized in systems of free fermions in the presence of certain symmetries. In Chapter 3, we discuss systems with intrinsic chiral topological order, in particular the Laughlin wave function for the fractional QHE. In Chapter 4, we review the concept of quantum entanglement including the entanglement entropies and the entanglement spectrum, and we discuss TNS as a class of model wave functions based on entanglement. Chapter 5 contains the reprints of my publications. Finally, in Chapter 6 we summarize and provide an outlook on possible directions of future research.

Chapter 2

Symmetry protected topological phases in free fermion systems

In this chapter we take a look at symmetry protected topological (SPT) phases that can be realized in fermionic systems even without strong interactions between the electronic constituents. In the literature, such systems are also frequently referred to as topological insulators (TIs), but we will use the more modern term 'SPT' when referring to the collection of all such phases. We begin in Sec. 2.1 with a historical overview of the discovery of SPT phases, focusing in particular on the integer quantum Hall effect. We then review two examples of systems hosting SPT phases: The one-dimensional (1D) Su-Schrieffer-Heeger (SSH) model in Sec. 2.2 and a two-dimensional (2D) Chern insulator model in Sec. 2.3. In both cases, we discuss the existence of protected gapless edge states and of a topological invariant characteristic for the SPT phase. In Sec. 2.4 we then give a brief overview of how this discussion can be generalized to other SPT phases. Finally, in Sec. 2.5 we discuss two examples of the recently discovered higher order TIs.

2.1 Historical overview: The integer quantum Hall effect

We give a brief historical overview, starting with a discussion of spontaneous symmetry breaking in quantum phases in Sec. 2.1.1. We then describe the experimental discovery of the integer quantum Hall effect in Sec. 2.1.2, and summarize some key properties of SPT phases in Sec. 2.1.3.

2.1.1 Quantum phases and spontaneous symmetry breaking

Until 1980, it was believed that the primary mechanism for phase transitions in condensed matter systems is that of spontaneous symmetry breaking: a system whose equations of motion possess a certain symmetry is in a symmetry-broken phase if the preferred

configuration of its constituents is not invariant under this symmetry. For example, as the temperature is lowered below a critical temperature T_c the 2D Ising model undergoes a thermal phase transition from a paramagnetic phase preserving the spin-flip symmetry to a symmetry-broken ferromagnetic phase, where the system chooses a preferred spin direction.

Quantum systems at zero temperature can also undergo symmetry-breaking quantum phase transitions, if the symmetry of the ground state changes as certain parameters in the Hamiltonian are varied. For instance, the 1D quantum Ising model in a transverse field on a chain with N sites is described by the Hamiltonian

$$H = -\big[\sum_{j=1}^{N-1} \sigma_{z,j}\sigma_{z,j+1} + g\sum_{j=1}^{N} \sigma_{x,j}\big], \tag{2.1}$$

where $\sigma_{x,j} = \left(\begin{smallmatrix} 0 & 1 \\ 1 & 0 \end{smallmatrix}\right)$, $\sigma_{y,j} = \left(\begin{smallmatrix} 0 & -i \\ i & 0 \end{smallmatrix}\right)$ and $\sigma_{z,j} = \left(\begin{smallmatrix} 1 & 0 \\ 0 & -1 \end{smallmatrix}\right)$ are the Pauli matrices for the spin on lattice site $j \in \{1, \ldots, N\}$ [49]. The parameter g describes the strength of the transverse field compared to the nearest-neighbour spin coupling.

For all values of g, the Hamiltonian H commutes with the global $\mathbb{Z}_2$ symmetry

$$U = \prod_{j=1}^{N} \sigma_{x,j} \tag{2.2}$$

representing a global spin flip. Indeed, U acts on the eigenstates $\{|\uparrow\rangle, |\downarrow\rangle\}$ of σ_z with $\sigma_z|\uparrow\rangle = |\uparrow\rangle$ and $\sigma_z|\downarrow\rangle = -|\downarrow\rangle$ as $\sigma_x|\uparrow\rangle = |\downarrow\rangle$. At zero field strength $g = 0$, H has two degenerate ground states $|\psi_1\rangle = |\uparrow \cdots \uparrow\rangle$ and $|\psi_2\rangle = |\downarrow \cdots \downarrow\rangle$ corresponding to all spins pointing upwards and downwards, respectively. The system will spontaneously choose its ground state as a superposition of $|\psi_1\rangle$ and $|\psi_2\rangle$. Since $U|\psi_1\rangle = |\psi_2\rangle$, the ground state is generally *not* invariant under the global spin flip U. However, in the limit $g \to \infty$, H has a unique eigenstate $|\psi_0\rangle = |\rightarrow \cdots \rightarrow\rangle$ with $|\rightarrow\rangle = (|\uparrow\rangle + |\downarrow\rangle)/\sqrt{2}$, such that $\sigma_x|\rightarrow\rangle = |\rightarrow\rangle$ and $U|\psi_0\rangle = |\psi_0\rangle$ is invariant under the global spin flip symmetry. Therefore, for some critical value g_c, the quantum Ising chain undergoes a quantum phase transition from a symmetry-broken phase for $g < g_c$ to a symmetric phase for $g > g_c$. The phase can be diagnosed using the magnetization $m = \sum_{j=1}^{N} \sigma_{z,j}$ as a local order parameter. Since m changes sign under the global spin flip, a non-zero expectation value of the magnetization implies a spontaneous breaking of the symmetry by the ground state.

2.1.2 The integer quantum Hall effect

The discovery of the quantum Hall effect (QHE) [4, 5] demonstrated that there exist phases beyond the paradigm of spontaneous symmetry breaking, which are now referred to as topological phases. The QHE is observed in 2D electron gases at very low temperatures subject to a strong transverse magnetic field B. A typical set-up is sketched in Fig. 2.1(a), with the 2D electron gas in the xy-plane and the transverse magnetic field pointing in the positive z direction. An electrical current in the positive x direction then causes the

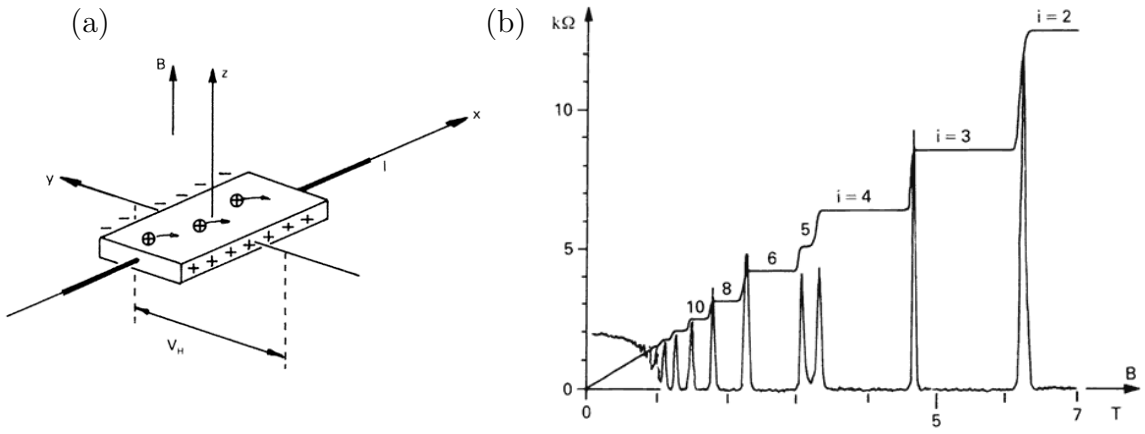

Figure 2.1: (a) Schematic of an experimental setup for observing the quantum Hall effect. (b) Hall resistance and longitudinal resistance as a function of magnetic field B in the integer QHE. The plateaus in the Hall resistance with vanishing longitudinal resistance are clearly visible. From the 1998 Press Release of the Swedish Academy of Sciences.

appearance of a Hall voltage V_H in the y direction between the edges of the sample. Classically, the associated Hall resistance R_H is expected to grow linearly with the magnetic field strength B. However, von Klitzing *et al.* found in 1980 [4] that at very low temperatures and strong magnetic fields, R_H displays plateaus where it remains constant as a function of B and the longitudinal resistance vanishes. This is shown in Fig. 2.1(b). They observed that the value of the Hall conductivity $\sigma_H = 1/R_H$ on these plateaus is given to extremely high precision by

$$\sigma_H = \nu \times \frac{e^2}{h} \tag{2.3}$$

with a positive integer $\nu \in \mathbb{N}_{>0}$. This is referred to as the integer QHE.

Fig. 2.1(b) shows that the longitudinal resistance displays strong peaks when the value of the Hall resistance changes from one plateau to the next. These are signatures of phase transitions that the system undergoes between different quantum Hall plateaus. Notably, these phase transitions are *not* caused by symmetry breaking, since the symmetries of the system are the same on all Hall plateaus (the only difference being the strength of the magnetic field). Therefore, there has to be a mechanism beyond spontaneous symmetry breaking that can cause the appearance of quantum phases and quantum phase transitions.

2.1.3 Symmetry protected topological phases

In modern terminology, the integer QHE constitutes the first experimental observation of a symmetry protected topological (SPT) phase. SPT phases can be realized in electronic systems even without strong interaction effects. Every SPT phase is protected by certain symmetries: it can only occur in systems which possess these symmetries, and it is stable

under all perturbations respecting these symmetries. The integer QHE is a special case of an SPT phase. It occurs in the absence of all symmetries except charge conservation, in particular the absence of time reversal invariance, which is broken due to the magnetic field. The phase of the integer QHE is thus stable to any (non-interacting) perturbations as long as they preserve charge conservation.

For many SPT phases, one of their main signatures is the existence of gapless $(d-1)$-dimensional modes at physical edges of a d-dimensional system, which are topologically protected as long as the symmetries of the SPT phase are preserved. Due to their topological protection, the edge modes provide dissipation-less transport even in the presence of disorder. As we will show in Sec. 2.3.3, in the case of the QHE they lead to the observed quantization of the Hall conductance.

SPT phases cannot be detected by any local order parameter such as the magnetization, but instead by a non-local quantity characterizing the system's *topology*, a topological invariant [6]. For each combination of symmetries that can lead to SPT phases, there is an associated topological invariant which can take a certain set of discrete values. When a system possessing these symmetries is in an SPT phase, the topological invariant evaluates to a non-zero value. However, if the system is in the trivial phase that is adiabatically connected to a trivial insulator, the value of the topological invariant is zero. Any two systems possessing the symmetries in question and for which the topological invariant takes the same value are in the same quantum phase. This means that their Hamiltonians can be deformed into each other while respecting the symmetries and without a closing of the bulk energy gap. Note that the set of values which a topological invariant can take, and hence the number of possible non-trivial SPT phases, varies based on the protecting symmetries. In Sec. 2.3.4 we discuss that for the integer QHE the appropriate topological invariant is the Chern number, whose value is directly proportional to the observed Hall conductance σ_H.

In order to illustrate the existence of gapless edge states and topological invariants, we will now discuss two examples of systems which can host non-trivial SPT phases. We begin with the 1D SSH model, before moving to a 2D Chern insulator (CI) model, which can realize the same SPT phase as the integer QHE.

2.2 The Su-Schrieffer-Heeger model

The SSH model [50] is a simple example of an SPT phase in one dimension. In Sec. 2.2.1 we introduce the model using a tight-binding Hamiltonian, before discussing its gapless protected edge states in Sec. 2.2.2 and the winding number as the appropriate topological invariant in Sec. 2.2.3.

2.2.1 Hamiltonian

The SSH model describes the hopping of spinless fermions on a chain with two sites per unit cell denoted A and B (see Fig. 2.2). On a chain with N unit cells and open boundary

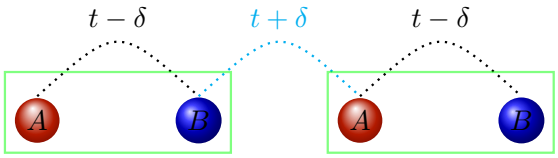

Figure 2.2: Sketch of the SSH Hamiltonian, with the unit cell that consists of an A site (red balls) and a B site (blue balls) marked by a green rectangle.

conditions (OBC), the tight-binding Hamiltonian is given by

$$H_{SSH} = (1-\delta)\sum_{j=0}^{N-1}(c_{A,j}^\dagger c_{B,j} + \text{h.c.}) + (1+\delta)\sum_{j=0}^{N-2}(c_{B,j}^\dagger c_{A,j+1} + \text{h.c.}), \tag{2.4}$$

with the dimerization parameter δ. Here, $c_{A,j}$ and $c_{B,j}$ are the annihilation operators for a fermion on site A and B in unit cell j with $j = 0, \ldots, N-1$, respectively. They obey canonical anti-commutation relations. Sites on the same unit cell are connected by a real hopping of strength $(1-\delta)$, whereas B and A sites on adjacent unit cells are connected by a real hopping of strength $(1+\delta)$. Therefore, δ characterizes how much the hopping strength differs between lattice sites in the same and in different unit cells.

The SSH Hamiltonian of Eq. (2.4) is invariant under the anti-unitary time reversal operation. It is also invariant under spatial inversion acting on the fermionic orbitals as

$$c_{A,j} \mapsto c_{B,N-j+1}, \tag{2.5a}$$
$$c_{B,j} \mapsto c_{A,N-j+1}. \tag{2.5b}$$

In addition, the Hamiltonian anti-commutes with the unitary chiral symmetry C defined by

$$Cc_{A,j}C \mapsto c_{A,j}, \tag{2.6a}$$
$$Cc_{B,j}C \mapsto -c_{B,j}, \tag{2.6b}$$

since all nearest-neighbour hopping terms connect two sites on different sublattices, which pick up a negative sign under the application of C. Therefore, $\{H_{SSH}, C\} = 0$, where the curly brackets denote the anti-commutator. If $|\psi\rangle$ is an eigenstate of the Hamiltonian with energy E, $H_{SSH}|\psi\rangle = E|\psi\rangle$, then the chiral symmetry implies that $C|\psi\rangle$ is an eigenstate with energy $-E$. Indeed, $H_{SSH}C|\psi\rangle = -CH_{SSH}|\psi\rangle = -EC|\psi\rangle$ due to the anti-commutation of the Hamiltonian with the chiral symmetry. Therefore, C implies that the spectrum of the Hamiltonian is symmetric *w.r.t.* the energy zero, since any eigenstate with energy E has an image under the chiral symmetry with energy $-E$.

On a chain with periodic boundary conditions (PBC), we can easily compute the energy spectrum of the SSH Hamiltonian by moving to momentum space. The Fourier transform of the fermionic mode operators for the A sites is given by

$$c_{A,k}^\dagger = \frac{1}{\sqrt{N}}\sum_{j=0}^{N-1} e^{-ijk} c_{A,j}^\dagger, \tag{2.7}$$

and similarly for the B sites. Here, $k = 2\pi n/N$ with an integer $n \in \{0, \ldots, N-1\}$ is the lattice momentum. Applying this Fourier transform to the SSH Hamiltonian, one obtains the Bloch Hamiltonian

$$H_{SSH}(k) = \sigma_x \left[(1-\delta) + \cos(k)(1+\delta)\right] + \sigma_y (1+\delta)\sin(k), \tag{2.8}$$

with energy bands $\pm\epsilon(k)$ and dispersion

$$\epsilon(k) = \sqrt{2} \times \sqrt{(1+\delta^2) + \cos(k)(1-\delta^2)}. \tag{2.9}$$

This dispersion is gapless if $\delta = 0$ with a gap closing at $k = -\pi$, and gapped otherwise. Therefore, the only parameter value where a phase transition may occur is $\delta = 0$. We now want to determine if the phases of the SSH model for $\delta < 0$ and $\delta > 0$ are identical, or if they are distinct phases, in which case the value $\delta = 0$ would mark a phase transition. Notably, the dispersion relation of Eq. (2.9) is symmetric under the transformation $\delta \mapsto -\delta$. The bulk energy spectrum thus offers no distinction between the regions $\delta < 0$ and $\delta > 0$. However, we now show that the energy spectrum of the SSH model on a chain with OBC is very different in these two regions.

2.2.2 Gapless edge states for $\delta > 0$

Since we know that the only bulk gap closing in the SSH model occurs for $\delta = 0$, it is in principle enough to determine the phase of the model for a single value of δ from each of the two regions $\delta < 0$ and $\delta > 0$ of the phase diagram. Therefore, let us first study the value $\delta = -1$ to understand the phase of the SSH model for $\delta < 0$. At this point, the second term in the Hamiltonian of Eq. (2.4) vanishes identically such that there is no hopping between adjacent unit cells. We therefore say that the SSH model at $\delta = -1$ is fully dimerized. In this limit the Hamiltonian with OBC is identical to the Hamiltonian with PBC. The dispersion relation of Eq. (2.9) then implies that the single particle energy spectrum is fully gapped with N levels at $+2$ and N levels at -2.

On the other hand, in order to understand the nature of the phase for $\delta > 0$ we consider the point $\delta = 1$. In this case, the first term in the Hamiltonian of Eq. (2.4), describing the hopping between sites in the same unit cell, is identically zero. Hence, the SSH model is fully dimerized. In the bulk of the SSH chain, two sites in adjacent unit cells form pairs that decouple from the rest of the system. In analogy to the case $\delta = -1$, they lead to $N-1$ levels at $+2$ and $N-1$ levels at -2 in the single particle energy spectrum. However, the mode operators for the fermions at the two ends of the chain, $c^\dagger_{A,0}$ and $c^\dagger_{B,N-1}$, do not appear in the Hamiltonian. Hence, these operators create excitations with zero energy, which are fully localized on the two ends of the chain.

The presence and absence of these mid-gap states is characteristic for the parameter regions $\delta > 0$ and $\delta < 0$, respectively. In Fig. 2.3(a) we show the single particle energy spectrum of the SSH model on an open chain with $N = 20$ unit cells for 20 values of δ ranging between -1 and 1. Whereas the spectrum is fully gapped for all negative values of δ, for all positive values of δ there are two mid-gap states close to zero energy. On a

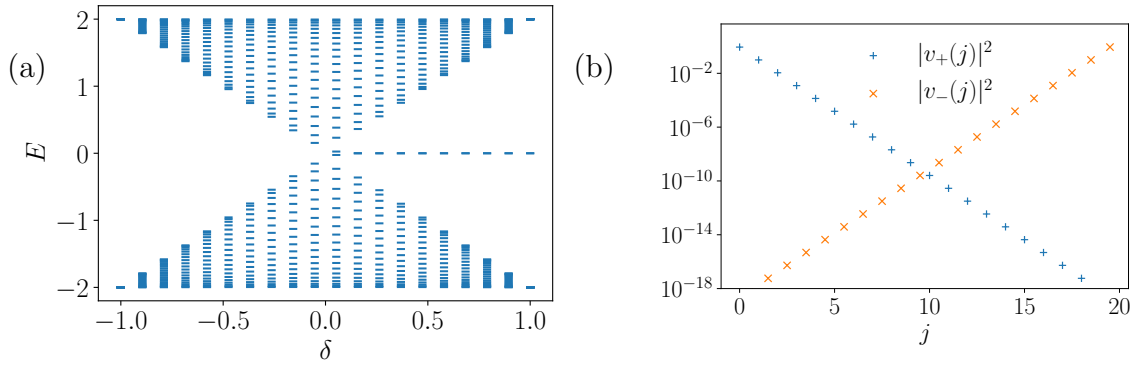

Figure 2.3: (a) Single particle energy spectrum of the SSH model on an open chain with $N = 20$ unit cells and $t = 1$ for different values of the dimerization $-1 \leq \delta \leq 1$. For $\delta > 0$, there are two in-gap states close to zero energy, whereas the spectrum is fully gapped for $\delta < 0$. (b) Density of the two eigenvectors v_+ and v_- of the Hamiltonian matrix of Eq. (2.10) corresponding to the mid-gap states of the SSH model, showing their exponential localization at the edges. As in (a), the chain has $N = 20$ sites, $t = 1$, $\delta = 0.5$ and we have added a small staggered chemical potential $\mu = 0.3$ to break the inversion symmetry of the SSH model. The x-axis shows the unit cell index j, where integer and half-integer values of j correspond to A and B sites, respectively. Density values below 10^{-18} are suppressed.

chain with a finite number of sites and away from the dimerized limit $\delta = 1$, they acquire a small finite energy which decays exponentially with the system size.

The mid-gap states for $\delta > 0$ are exponentially localized at the two ends of the chain. In order to show this, it is convenient to add a small staggered chemical potential to the SSH Hamiltonian, which is μ on A sites and $-\mu$ on B sites. The chemical potential breaks both inversion symmetry and chiral symmetry. A small μ therefore breaks the degeneracy of the edge modes, and determines which of the two modes is occupied at half filling. Indeed, in the dimerized limit for $\delta = 1$, the left edge mode associated with $c^\dagger_{A,0}$ acquires a small positive energy μ, whereas the right mode associated with $c^\dagger_{B,N-1}$ obtains a small negative energy $-\mu$. With respect to the basis of local mode operators for the chain ordered as $c^\dagger_{A,0}, c^\dagger_{B,0}, c^\dagger_{A,1}, \ldots, c^\dagger_{B,N-1}$, the SSH Hamiltonian including the staggered chemical potential can be written as a $2N \times 2N$ matrix of the form

$$\mathcal{H}_N(\mu, t, \delta) = \begin{pmatrix} \mu & t-\delta & 0 & 0 & \ldots & 0 & 0 \\ t-\delta & -\mu & t+\delta & 0 & \ldots & 0 & 0 \\ 0 & t+\delta & \mu & t-\delta & \ldots & 0 & 0 \\ 0 & 0 & t-\delta & -\mu & \ddots & 0 & 0 \\ \vdots & \vdots & \vdots & \ddots & \ddots & \ddots & \vdots \\ 0 & 0 & 0 & \ldots & \ddots & \mu & t-\delta \\ 0 & 0 & 0 & 0 & \ldots & t-\delta & -\mu \end{pmatrix}. \tag{2.10}$$

For the SSH Hamiltonian of Eq. (2.4) we have $\mu = 0$ and $t = 1$. For $\delta > 0$, we denote the two eigenvectors of Eq. (2.10) that lead to the mid-gap states at energies close to $\pm\mu$ by $v_\pm$. In Fig. 2.3(b), we plot the density $|v_+(j)|^2$ and $|v_-(j)|^2$ for an open chain with $\delta = 0.5$, $t = 1$ and a small chemical potential $\mu = 0.1$ as a function of the unit cell index j. The eigenstates are exponentially localized at the left and right edges of the chain, respectively. Moreover, up to exponentially small corrections the left and right edge modes are supported on only A and only B sites, respectively.

It is not difficult to show the exponential localization of the edge modes analytically. Indeed, as long as $t-\delta < t+\delta$, the mid-gap states of $\mathcal{H}_N(\mu, t, \delta)$ are given up to exponentially small corrections by the vectors

$$v_+(t,\delta) = \begin{pmatrix} 1 & 0 & -\frac{t-\delta}{t+\delta} & 0 & \dots & -\left(\frac{t-\delta}{t+\delta}\right)^{N-1} & 0 \end{pmatrix}, \tag{2.11a}$$

$$v_-(t,\delta) = \begin{pmatrix} 0 & -\left(\frac{t-\delta}{t+\delta}\right)^{N-1} & 0 & -\left(\frac{t-\delta}{t+\delta}\right)^{N-2} & \dots & 0 & 1 \end{pmatrix}, \tag{2.11b}$$

where we used the same basis of mode operators as for $\mathcal{H}_N(\mu, t, \delta)$. Indeed, applied to the Hamiltonian matrix of Eq. (2.10), these vectors satisfy the equation

$$\mathcal{H}_N(\mu, t, \delta) v_\pm(t, \delta) = \pm\mu\, v_\pm(t, \delta) + \mathcal{O}\left((t-\delta)\left(\frac{t-\delta}{t+\delta}\right)^{N-1}\right), \tag{2.12}$$

and are therefore eigenvectors with eigenvalues $\pm\mu$ up to a correction which decays exponentially with the system size N (remember that $(t-\delta)/(t+\delta) < 1$). The vector v_+ has support only on the A sites of the chain and is strongly localized at the left end of the chain with an exponentially decaying tail in the bulk. On the other hand, the vector v_- has support only on the B sites of the chain and is localized at the right end of the chain. This is precisely the behavior shown in Fig. 2.3(b).

For $\delta > 0$, the SSH model on an open chain therefore possesses robust mid-gap states which are localized at the two edges of the chain. This hints at a topologically non-trivial nature of the phase for $\delta > 0$. On the other hand, for $\delta < 0$, the open SSH model does not possess any edge states. In the following subsection, we show that the topological nature of the phase for $\delta > 0$ can be confirmed by considering its topological invariant, the winding number.

2.2.3 Winding number

In Sec. 2.2.1 above we showed that the dispersion relation of the SSH model is invariant under the exchange $\delta \mapsto -\delta$, such that the two regions $\delta > 0$ and $\delta < 0$ appear identical in the bulk energy spectrum. However, in Sec. 2.2.2 we showed that the energy spectrum with OBC is very different in the two regions, suggesting the existence of two distinct phases. It is therefore natural to ask how the two phases can be distinguished in the system with PBC. For the SSH model, this can be done by computing the winding number of the Bloch Hamiltonian, the topological invariant for the SSH phase.

Since the SSH model has only two energy bands, its Bloch Hamiltonian from Eq. (2.4) can be written as a linear combination of the Pauli matrices,

$$H_{SSH}(k) = \mathbf{h}(k) \cdot \sigma. \tag{2.13}$$

Here, $\sigma = (\sigma_x \ \sigma_y)^T$ is the 2D vector of Pauli matrices, and $\mathbf{h}(k) = (h_x(k) \ h_y(k))^T$ is a 2D vector of real numbers that depends on the lattice momentum $k \in [0, 2\pi)$. Note that a term proportional to σ_z in Eq. (2.13) is forbidden due to the chiral symmetry C of the SSH model.

Away from $\delta = 0$, the SSH model is gapped such that $\mathbf{h}(k) \neq \mathbf{0}$ for all momenta k. Due to the periodicity of the lattice momentum k in the Brillouin zone, $\mathbf{h}(k)$ therefore describes a loop in the 2D punctured plane $\mathbb{R}^2 \setminus \{\mathbf{0}\}$. The winding number $\mathcal{W}_\delta \in \mathbb{N}$ then measures how often this loop winds around the origin $\mathbf{0}$ counter-clockwise. For the fully dimerized limit of the SSH model in the topological phase at $\delta = 1$, the Bloch Hamiltonian is described by the vector

$$\mathbf{h}(k) = 2 \times \begin{pmatrix} \sin k \\ \cos k \end{pmatrix}. \tag{2.14}$$

Clearly, this function describes one full circle around the origin, such that the associated winding number is $\mathcal{W}_{\delta=1} = 1$. On the other hand, in the trivial phase for $\delta = -1$, the Hamiltonian vector is given by the constant

$$\mathbf{h}(k) = \begin{pmatrix} 2 \\ 0 \end{pmatrix}, \tag{2.15}$$

such that the loop does not enclose the origin and the winding number is $\mathcal{W}_{\delta=-1} = 0$. For general values of δ, the Hamiltonian vector describes a circle with radius $1 + \delta$ around the point $([1 - \delta] \ 0)^T$. This circle encloses the origin if and only if $\delta > 0$.

Therefore, the value of the winding number serves as an unambiguous distinction between the topological and the trivial phases of the SSH model. Moreover, as it can take only discrete integer values, the winding number cannot change under small perturbations respecting the chiral symmetry C. The edge modes of the SSH model can be seen as the necessary gap closing point between a region with $\mathcal{W} \neq 0$ and the vacuum with $\mathcal{W} = 0$. Their presence is therefore topologically protected by the winding number against perturbations respecting the chiral symmetry. This is an instance of the bulk-boundary correspondence in SPT phases, where a non-trivial bulk implies a non-trivial protected edge physics.

2.3 The two-dimensional Chern insulator

As we mentioned in Sec. 2.1 above, the integer QHE is an example of an SPT phase which requires an explicit breaking of time reversal symmetry. This phase is therefore referred to as a *chiral* phase. In the QHE, time reversal is broken by the external magnetic field. However, as first suggested by Haldane in 1988 [51], systems which break time

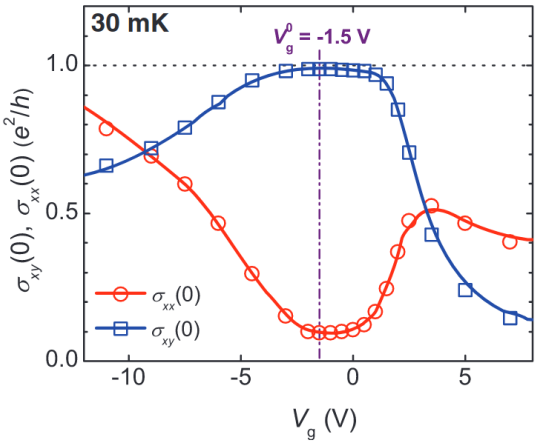

Figure 2.4: Hall conductivity σ_{xy} and longitudinal conductivity σ_{xx} at zero external magnetic field as a function of gate voltage in a magnetic TI. The plateau of σ_{xy} close to the value e^2/h with a simultaneous dip in σ_{xx} demonstrate the quantum anomalous Hall effect. From Cui-Zu Chang et al. "Experimental Observation of the Quantum Anomalous Hall Effect in a Magnetic Topological Insulator". In: *Science* 340.6129 (2013), pp. 167–170. Reprinted with permission from AAAS.

reversal intrinsically can host this phase also without an external magnetic field. This is referred to as the quantum anomalous Hall effect. The quantum anomalous Hall effect has been observed experimentally in magnetic materials with spin-orbit coupling [52], see Fig. 2.1. Moreover, ultracold atoms in optical lattices have allowed the implementation of models with topologically non-trivial band structures [53, 54, 55], including the Haldane model [56]. They therefore constitute a promising platform for the observation of the quantum anomalous Hall effect.

As we will discuss below, the topological invariant appropriate for the characterization of integer and anomalous quantum Hall phases is the Chern number. Lattice systems in this phase are thus referred to as Chern insulators (CIs). We now consider a simple tight-binding model which can host a CI phase. We do not use Haldane's original honeycomb lattice model, but instead make use of a simpler square lattice model [57]. This model is also relevant for our publication of Ref. [3] (see Sec. 5.3). We begin by introducing the Hamiltonian in Sec. 2.3.1, before studying its gapless chiral edge modes in Sec. 2.3.2. In Sec. 2.3.3, we then show how the edge modes lead to a Hall conductivity $\sigma_{xy} = e^2/h$, and we conclude in Sec. 2.3.4 with a discussion of the Chern number.

2.3.1 Hamiltonian

The tight-binding model describes spinless fermions hopping on a square lattice with N_x unit cells in the horizontal direction and N_y unit cells in the vertical direction, where each unit cell consists of two lattice sites labeled A and B. The system is sketched in Fig. 2.5(a),

where the A and B sites are drawn in blue and red, respectively, and the unit cells are marked by green rectangles. With PBC in both directions, the Hamiltonian is given by

$$H_{CI} = \sum_{x=0}^{N_x-1}\sum_{y=0}^{N_y-1}\Big[t\left(c^\dagger_{A,(x,y)}c_{A,(x+1,y)} + c^\dagger_{A,(x,y)}c_{B,(x,y)} + c^\dagger_{A,(x,y)}c_{B,(x,y+1)} - c^\dagger_{B,(x,y)}c_{B,(x+1,y)}\right) \\ + i\Delta\left(c^\dagger_{B,(x+1,y)}c_{A,(x,y)} + c^\dagger_{A,(x+1,y)}c_{B,(x,y)} + c^\dagger_{A,(x,y)}c_{B,(x+1,y+1)} + c^\dagger_{B,(x,y)}c_{A,(x+1,y-1)}\right) + \text{h.c.}\Big]. \tag{2.16}$$

Here, $c^\dagger_{i,(x,y)}$ is the creation and $c_{i,(x,y)}$ the annihilation operator for a fermion on site $i \in \{A, B\}$ in the unit cell at position (x, y) for $x = 0, \ldots, N_x - 1$ and $y = 0, \ldots, N_y - 1$. These operators obey canonical anti-commutation relations

$$\{c^\dagger_{i,(x,y)}, c^\dagger_{j,(x',y')}\} = \{c_{i,(x,y)}, c_{j,(x',y')}\} = 0, \tag{2.17a}$$

$$\{c^\dagger_{i,(x,y)}, c_{j,(x',y')}\} = \delta_{i,j}\delta_{x,x'}\delta_{y,y'}, \tag{2.17b}$$

for $i, j \in \{A, B\}$, $x, x' \in \{0, \ldots, N_x-1\}$ and $y, y' \in \{0, \ldots, N_y-1\}$. The couplings of the CI Hamiltonian of Eq. (2.16) are sketched in Fig. 2.5(a). Each pair of nearest-neighbour sites is connected by a real hopping of strength t marked by black lines. Between two B sites, the nearest-neighbour hopping has a negative sign (marked by dashed black lines) to ensure that there is a flux π through every plaquette. In addition, next-nearest neighbour sites are connected by a purely imaginary hopping $i\Delta$ across the diagonals of the plaquettes, marked in Fig. 2.5(a) by red arrows. In the following, we consider the model at half filling, where the number of particles is equal to the number N_xN_y of unit cells.

The Hamiltonian of Eq. (2.16) breaks time reversal symmetry $\mathcal{T}$ explicitly whenever the purely imaginary next-nearest neighbour hopping is non-vanishing. Indeed, under time reversal, the fermionic real-space creation operators are invariant,

$$\mathcal{T}: \quad c^\dagger_{A,(x,y)} \mapsto c^\dagger_{A,(x,y)}, c^\dagger_{B,(x,y)} \mapsto c^\dagger_{B,(x,y)}. \tag{2.18}$$

Therefore, the nearest-neighbour hopping terms in Hamiltonian (2.16) are unchanged. However, due to the anti-unitarity of $\mathcal{T}$, the imaginary next-nearest neighbour hopping changes sign under time reversal, $i\Delta \mapsto -i\Delta$.

In order to study the bulk properties of the CI model, it is convenient to express the Hamiltonian of Eq. (2.16) in momentum space. The Fourier transform of the real-space creation operators is given by

$$c^\dagger_{\alpha,(k_x,k_y)} = \frac{1}{\sqrt{N_xN_y}}\sum_{x,y} e^{-i(xk_x+yk_y)}c^\dagger_{\alpha,(x,y)}, \tag{2.19}$$

where $\alpha \in \{A, B\}$, $k_x = 2\pi n_{k_x}/N_x$ with an integer $n_{k_x} \in \{0, \ldots, N_x-1\}$ and $k_y = 2\pi n_{k_y}/N_y$ with an integer $n_{k_y} \in \{0, \ldots, N_y - 1\}$ are the lattice momenta in the first Brillouin zone.

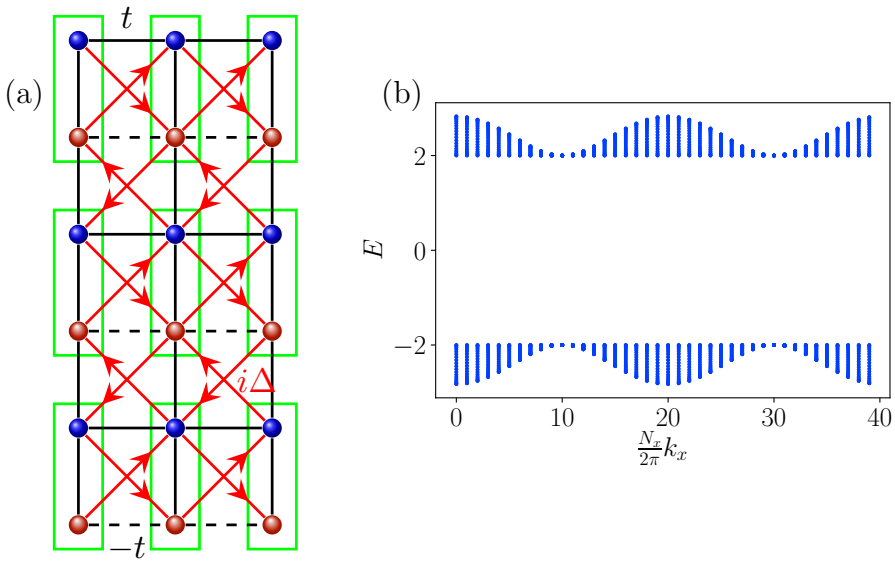

Figure 2.5: (a) Microscopic model for the CI defined on a square lattice with two sublattices, A in blue and B in red. The nearest-neighbour hopping t ($-t$ for dashed lines) drawn in black is real, whereas the next-nearest neighbour hopping $i\Delta$ in the direction of the red arrows is purely imaginary. (b) Single particle energy spectrum of the CI model with parameters $t = 1$ and $\Delta = 1/2$ for a system of 40×40 unit cells and PBC in both directions, as a function of k_x.

Due to the translation invariance of the CI Hamiltonian, it is diagonal in momentum space and can be written as

$$H_{CI} = \sum_{k_x,k_y} \left(c^\dagger_{A,(k_x,k_y)} \, c^\dagger_{A,(k_x,k_y)} \right) H_{CI}\left(k_x, k_y\right) \begin{pmatrix} c_{A,(k_x,k_y)} \\ c_{B,(k_x,k_y)} \end{pmatrix}, \tag{2.20}$$

where $H_{CI}(k_x, k_y)$ is the Bloch Hamiltonian matrix of size 2×2 at the momentum (k_x, k_y). As a function of the momenta, the Bloch Hamiltonian for the model of Eq. (2.16) is given by

$$\begin{aligned} H_{CI}\left(k_x, k_y\right) = &\left[(2\Delta \sin(k_x) + t)\cos(k_y) - 2\Delta \sin(k_x) + t\right]\sigma_x \\ &+ \left[(2\Delta \sin(k_x) + t)\sin(k_y)\right]\sigma_y + 2t\cos(k_x)\sigma_z. \end{aligned} \tag{2.21}$$

The eigenvalues of the Bloch Hamiltonian define the Bloch bands, which have energy $\pm\epsilon\left(k_x, k_y\right)$, with

$$\epsilon\left(k_x, k_y\right) = \sqrt{\left[(2\Delta \sin(k_x) + t)\cos(k_y) - 2\Delta \sin(k_x) + t\right]^2 + \left[(2\Delta \sin(k_x) - t)\sin(k_y)\right]^2 + \left[2t\cos(k_x)\right]^2}. \tag{2.22}$$

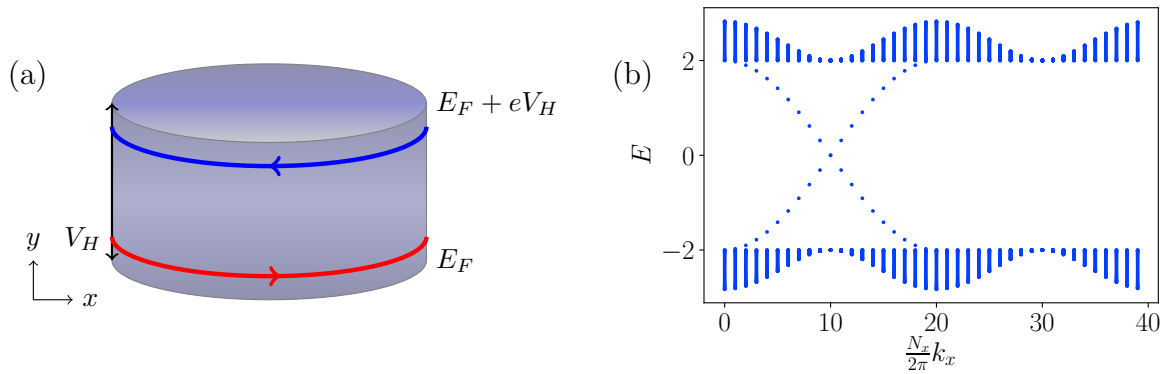

Figure 2.6: (a) Cylinder geometry of the CI with PBC in the x direction and OBC in the y direction. There are chiral modes of opposite chirality at the top and bottom edges. (b) Single particle energy spectrum of the CI model in the cylinder geometry with parameters $t = 1$ and $\Delta = 1/2$ for a system of 40×40 unit cells as a function of k_x. The gapless edge modes are clearly visible.

For a non-zero nearest-neighbour hopping t, the dispersion ϵ is gapped unless $\Delta = 0$. Therefore, the model has two gapped phases for $\Delta/t > 0$ and $\Delta/t < 0$, separated by a gap closing at $\Delta = 0$. Since the sign of Δ changes under time reversal $\mathcal{T}$, the two phases are time reversal conjugates, and we can focus on the phase $\Delta/t > 0$. In Fig. 2.5(b), we show the single particle energy spectrum of the CI model with PBC in both directions for parameters $t = 1$ and $\Delta = 1/2$.

2.3.2 Edge states and relation to SSH model

We now want to show that the CI model hosts gapless edge modes in a geometry with open boundaries. To that end, we consider the model in a cylinder geometry with PBC in the x direction, but OBC in the y direction as sketched in Fig. 2.6(a). After a partial Fourier transformation in the periodic x direction, the Bloch Hamiltonian of the CI model takes the form

$$\begin{aligned} H_{CI}(k_x) = \sum_{y=0}^{N_y-1} \Big[& t'(k_x) \left(c^\dagger_{A,(k_x,y)} c_{A,(k_x,y)} - c^\dagger_{B,(k_x,y)} c_{B,(k_x,y)} \right) \\ & + (t - \Delta'(k_x)) \left(c^\dagger_{B,(k_x,y)} c_{A,(k_x,y)} + c^\dagger_{A,(k_x,y)} c_{B,(k_x,y)} \right) \Big] \\ & + \sum_{y=0}^{N_y-2} \Big[(t + \Delta'(k_x)) \left(c^\dagger_{A,(k_x,y)} c_{B,(k_x,y+1)} + c^\dagger_{B,(k_x,y+1)} c_{A,(k_x,y)} \right) \Big], \end{aligned} \tag{2.23}$$

where we defined the effective k_x-dependent couplings

$$t'(k_x) = 2t\cos(k_x), \tag{2.24a}$$
$$\Delta'(k_x) = 2\Delta\sin(k_x). \tag{2.24b}$$

When comparing the Hamiltonian of Eq. (2.23) to the Hamiltonian of the SSH model of Eq. (2.4), we see that for each value of the lattice momentum k_x, the CI model with OBC in the y direction defines an effective SSH model with dimerization $\delta = \Delta'(k_x)$ and staggered chemical potential $\mu = t'(k_x)$. At the two momenta $k_x = \pi/2$ and $k_x = 3\pi/2$, the effective chemical potential $t' = 2t\cos(k_x)$ vanishes such that the effective SSH model recovers its chiral symmetry. Moreover, at these two momenta the effective dimerization is equal to $\Delta'(\pi/2) = 2\Delta$ and $\Delta'(3\pi/2) = -2\Delta$, such that the SSH model is in its topological and trivial phase, respectively (remember that we are focusing on the case $\Delta/t > 0$). For this reason, the CI can be interpreted as a *charge pumping* interpolation between the trivial and the topological phases of the SSH model, along which the chemical potential μ is varied such that there is some charge transport.

With this knowledge, we can characterize the edge modes of the CI model using the edge states of the SSH model discussed in Sec. 2.2.2 above. Indeed, we showed that the open SSH model with $\delta > 0$ with a finite staggered chemical potential μ has two eigenmodes that lie inside the band gap with energies $\pm\mu$ and which are exponentially localized at the edges. Applied to the CI model, this implies that for any momentum $k_x \in (0, \pi)$ such that $\Delta'(k_x)/t > 0$, there are two mid-gap states with dispersion

$$E_{\text{edge},\pm}(k_x) = \pm 2t\cos(k_x) \tag{2.25}$$

which are exponentially localized at the top edge (in the case of $E_{\text{edge},+}$) and the bottom edge of the cylinder (in the case of $E_{\text{edge},-}$). The single particle energy spectrum of the CI model for parameters $t = 1$ and $\Delta = 1/2$ is shown in Fig. 2.6(b) and the edge modes with dispersion given in Eq. (2.25) are clearly visible. In particular, at $k_x = \pi/2$, the two mid-gap modes have zero energy and cross each other. At this point, the dispersion of the two modes is linear, and we say that they are chiral modes of opposite chirality, corresponding to the opposite signs of the velocity $v_\pm = (1/\hbar)\partial E_{\text{edge},\pm}/\partial k_x$. Note that single chiral modes such as the CI edge modes cannot occur in a purely one-dimensional lattice system, which necessarily features an equal number of chiral and anti-chiral modes.

2.3.3 Relation to Hall conductance

We can understand how the chiral edge modes of the CI model lead to a Hall conductance $\sigma_{xy} = e^2/h$ using the Landau-Büttiker formalism [58] and a simple semi-classical argument. Indeed, let us consider the CI as sketched in Fig. 2.6(a) with PBC in the x direction and OBC in the y direction, such that there is one chiral edge mode at the top edge and one chiral mode of opposite chirality at the bottom edge. We assume that the Fermi energy E_F lies in the band gap, such that only the two edge states are crossed by it. We now

apply a Hall voltage V_H between the top and bottom edges of the CI, and want to infer which current I_x in the horizontal direction is caused by it.

As sketched in Fig. 2.6(a), V_H leads to a shift of the Fermi energy $E_F \to E_F + eV_H$ only at the top edge of the sample, while the Fermi energy at the bottom edge remains unchanged. Therefore, an additional n single particle modes from the chiral mode at the top edge become occupied. If we denote by $\hbar v_+ = \partial E_{\text{edge},+}/\partial k_x$ the slope of the edge mode dispersion close to the Fermi energy, the number of additional occupied orbitals is

$$n = eV_H \times (\hbar v_+)^{-1} \times \left(\frac{2\pi}{N_x}\right)^{-1}, \tag{2.26}$$

where $2\pi/N_x$ is the spacing of the single particle orbitals in the Brillouin zone. Each of these occupied modes causes a current

$$I_{\text{mode}} = v_+ \times \frac{e}{N_x}, \tag{2.27}$$

where we used that v_+ is the group velocity and assumed an equal distribution of the charge e over the whole edge of the cylinder of length N_x. Combining the number of modes n and the current per mode I_{mode}, we find that the horizontal current is given by

$$I_x = I_{\text{mode}} \times n = \frac{e^2}{h} \times V_H, \tag{2.28}$$

leading to a Hall conductance $\sigma_{xy} = I_x/V_H = e^2/h$.

2.3.4 Chern number

In a more rigorous argument, it can be shown that the Hall conductance for a system in a CI or integer quantum Hall phase is given as in Eq. (2.3) by $\sigma_{xy} = (e^2/h)\nu$ where the integer ν is the Chern number [6]. The Chern number is the topological invariant of the integer quantum Hall phase and enjoys an integer quantization. For a translation invariant tight-binding Hamiltonian for free fermions defined on a lattice, the Chern number is given by the first Chern class of the principal bundle over the Brillouin zone defined by the occupied Bloch bands [59]. In practice, it can be computed as the integral of the Berry connection over the Brillouin zone [49].

In order to compute the Chern number of the CI model of Eq. (2.16), we make use of a simpler topological index, the Pontryagin index, which is applicable to models with only two energy bands and can be used to compute the Chern number of the lower band [49]. To that end, similarly to the case of the SSH model, we consider the Bloch Hamiltonian of the model and express it as a linear combination of the Pauli matrices,

$$H_{CI}(k_x, k_y) = \mathbf{h}(k_x, k_y) \cdot \sigma. \tag{2.29}$$

Here, $\sigma = (\sigma_x \;\; \sigma_y \;\; \sigma_z)^T$ is the three-dimensional (3D) vector of Pauli matrices, and the 3D Hamiltonian vector $\mathbf{h}(k_x, k_y) = (h_x(k_x, k_y) \;\; h_y(k_x, k_y) \;\; h_z(k_x, k_y))^T$ depends on the lattice

momentum in the 2D Brillouin zone. Since the CI model is gapped for $\Delta/t > 0$, which is the case we are considering here, the vector $\mathbf{h}(k_x, k_y)$ cannot be equal to $\mathbf{0}$ for any momentum value. The Pontryagin index then measures how often the map $\mathbf{h}$ from the 2D Brillouin zone to $\mathbb{R}^3 \setminus \{\mathbf{0}\}$ covers a closed surface (such as a sphere) around the origin $\mathbf{0}$. For the CI model, the Hamiltonian vector can be directly read off from Eq. (2.21) as

$$\mathbf{h}(k_x, k_y) = \begin{pmatrix} (2\Delta \sin(k_x) + t)\cos(k_y) - 2\Delta \sin(k_x) + t \\ (2\Delta \sin(k_x) + t)\sin(k_y) \\ 2t\cos(k_x) \end{pmatrix}. \tag{2.30}$$

For simplicity, we focus on the parameters $t = 1$ and $\Delta = 1/2$ since we know that the phase is the same for all values of $\Delta/t > 0$. In this case, the map $\mathbf{h}(k_x, k_y)$ reaches the points $(0 \;\; 0 \;\; \pm 2)^T$ corresponding to the north and south poles of a sphere around the origin for $k_x \in \{0, \pi\}$ and $k_y = \pi$, respectively. On the other hand, for $k_x = \pi/2$, the map $\mathbf{h}(k_x, k_y)$ describes a circle around the origin in the xy-plane. In this way, it is easy to see that the map defines a surface that encloses the origin exactly once. As a result, the Chern number of the CI model is equal to unity, $\nu = 1$, as expected based on the relation $\sigma_{xy} = (e^2/h)\nu$.

Due to its integer quantization, the Chern number is robust against perturbations as long as the bulk gap does not close. It can be shown that the boundary between a region with $\nu \neq 0$ and a trivial region must host gapless chiral edge states [49]. This is another example for the bulk-boundary correspondence in SPT phases. Therefore, the presence of the chiral edge modes is topologically protected, explaining the extreme accuracy even in the presence of disorder of the experimentally observed value for the Hall conductivity.

2.4 Extension to other symmetry classes

The SSH model and the CI model are two examples of non-trivial SPT phases protected by a combination of time reversal symmetry and particle-hole symmetry. In total, there are 10 symmetry classes that can be defined by these two anti-unitary symmetries and their product, the chiral symmetry. The non-trivial SPT phases that can occur in these symmetry classes in different spatial dimensions have been classified theoretically in the 10-fold way [60, 61, 62].

An important SPT phase from the 10-fold way is given by the TI in two and three dimensions protected by time reversal symmetry [63, 64]. A minimal model for a 2D TI can be constructed by combining two copies of the Haldane model in a time reversal invariant way [7]. In 2006, a 2D TI was theoretically predicted in 2D HgTe quantum wells [8] and experimentally observed in 2007 [10]. The existence of a 3D TI was predicted for certain materials in 2007 [9] and experimentally observed shortly thereafter [11, 12]. The experiments included the direct observation of an odd number of surface Dirac cones characteristic for the 3D bulk TI via angle-resolved photoemission spectroscopy (see Fig. 2.7). Similar to the 1D chiral edge modes of the CI, the existence of an odd number of Dirac cones is forbidden in a purely 2D system and possible only on the surface of a higher-dimensional system.

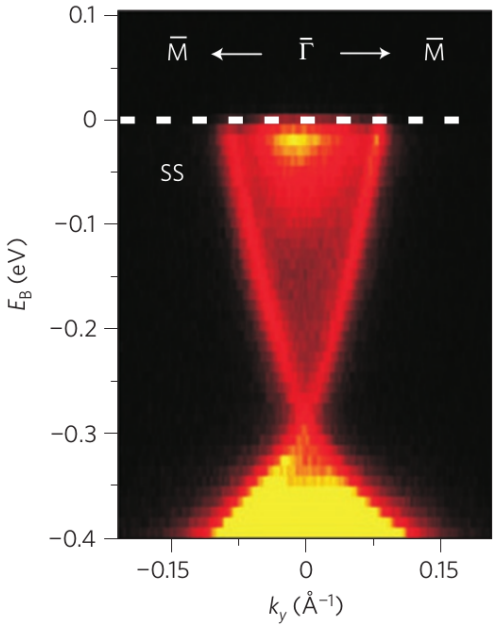

Figure 2.7: Angle-resolved photoemission spectroscopy measurement of a single Dirac cone at the surface of a 3D TI. From Yiman Xia et al. "Observation of a large-gap topological-insulator class with a single Dirac cone on the surface". In: *Nature Physics* 5 (May 2009), pp. 398–402. Reprinted with permission from Nature Publishing Group.

The classification of SPT phases has been extended to crystalline symmetries such as mirror and rotation symmetries. In fermionic systems, they give rise to crystalline TIs which can have protected gapless states at high-symmetry-surfaces [65, 66]. Akin to the TIs from the 10-fold way, crystalline TIs are characterized by bulk topological invariants which take a non-zero value in a topologically non-trivial phase. In the next section, we will discuss a generalized form of crystalline TIs, which have gapped edges and surfaces, but gapless states at corners and hinges in two and three dimensions, respectively.

The topological properties of TIs can be traced back to the non-trivial nature of their band structures, exemplified for instance by a non-zero Chern number. The band structure is a single particle property and thus not inherently quantum mechanical. Indeed, it is possible to construct classical systems with coordinate spaces of non-trivial connectivity, which have band structures akin to those of TIs. These systems have a similar phenomenology including gapless boundary modes. Such classical topological models have been realized in photonic [67, 68], mechanical [69, 70], acoustic [71] and electronic [72, 73] systems. Note that in classical systems, there is usually no topological quantization, and the boundary modes often do not enjoy a topological protection, such that the systems are much weaker to perturbations.

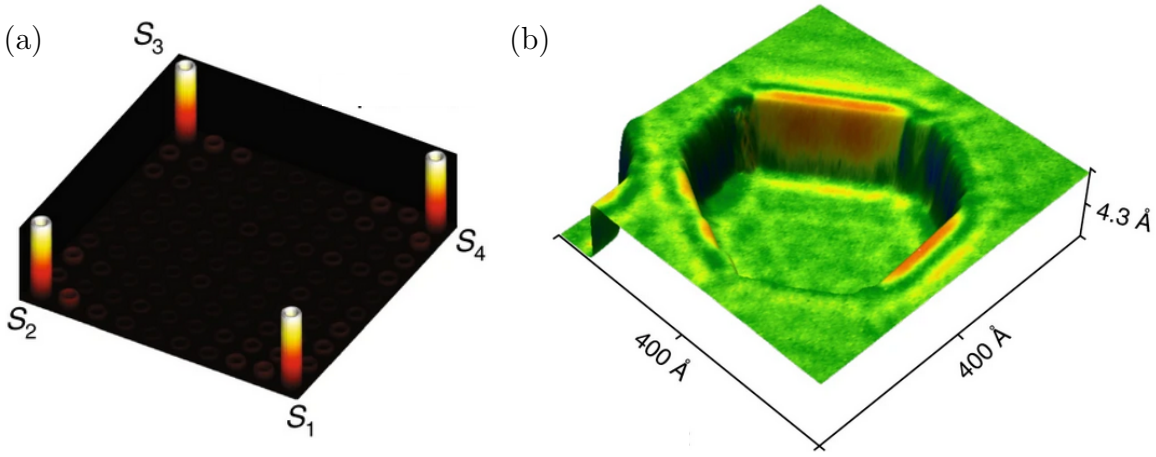

Figure 2.8: (a) Experimentally observed spatial intensity profiles showing localized corner modes in a photonic lattice realization of the topological quadrupole model. From Sunil Mittal et al. "Photonic quadrupole topological phases". In: *Nature Photonics 13, 692-696 (2019)* (Dec. 21, 2018). arXiv: 1812.09304v2 [physics.optics]. Reprinted wit permission. (b) Differential conductance map of a hexagonal pit on a bismuth (111) surface, showing high conductance at every other edge of the hexagonal pit, a pattern characteristic for the hinge modes of a helical 3D HOTI. From Frank Schindler et al. "Higher-order topology in bismuth". In: *Nature Physics* 14.9 (Sept. 2018), pp. 918–924. Reprinted with permission.

2.5 Higher order topological insulators

Recently, an entirely new class of topological phases has been discovered among the crystalline TIs: Higher order topological insulators (HOTIs) [20, 21, 22, 23, 24]. Like conventional crystalline TIs, HOTIs are protected by crystalline symmetries such as mirror and rotation symmetries, possibly augmented by time reversal symmetry. In contrast to a conventional TI in d dimensions, whose protected boundary modes are of dimension $d-1$, a HOTI of order n has $(d-n)$-dimensional protected boundary modes. In this terminology, conventional TIs are therefore of order $n=1$. On the other hand, second order TIs in two dimensions and third order TIs in three dimensions have protected zero-dimensional corner modes. In three dimensions, second order TIs have protected 1D hinge modes. Bosonic models hosting higher order topological phases have also been found [74, 75].

Important examples of second order topological phases include the 2D quadrupole model of Ref. [20] and the 3D chiral and helical hinge insulators of Ref. [21]. The topological phase of the quadrupole model is protected by two anti-commuting mirror symmetries and has been experimentally observed in mechanical [77], acoustic [78, 79], photonic [76, 80, 81] and electrical [82, 83, 84] systems (see Fig. 2.8(a)). There is strong experimental evidence that the 3D helical hinge insulator is realized in Bismuth, where conductance patters indicative of hinge modes have been observed (see Fig. 2.7(b)) [25]. In the following,

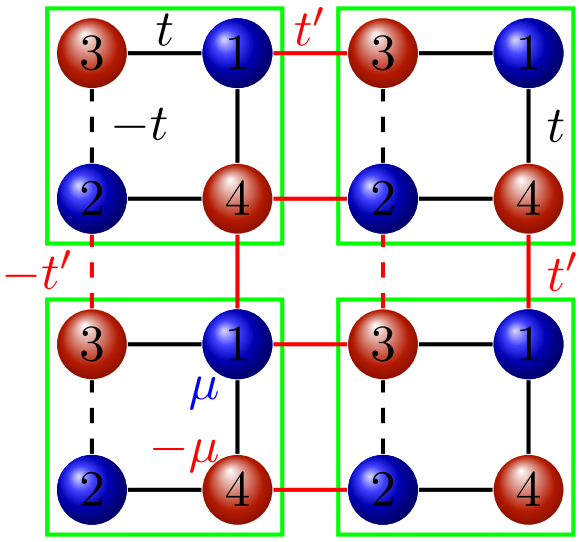

Figure 2.9: Sketch of the quadrupole model from Ref. [20]. A unit cell (marked with a green square) contains four sites. The nearest-neighbour hopping t within unit cells is sketched in black, whereas the nearest-neighbour hopping t' between unit cells is sketched in red. The couplings corresponding to dashed bonds carry a negative sign to ensure a flux π through every plaquette. Lattice sites marked in blue and red have a chemical potential μ and $-\mu$, respectively.

we will illustrate the characteristics of HOTIs using the 2D quadrupole model by discussing its Hamiltonian in Sec. 2.5.1 and key properties of its topological phase in Sec. 2.5.2. We conclude by highlighting some aspects of the 3D chiral hinge insulator in Sec. 2.5.3.

2.5.1 The topological quadrupole model

The topological quadrupole model [20] is described by a tight-binding Hamiltonian of free fermions on the square lattice. Each site hosts one spinless fermionic mode and a unit cell consists of 2×2 sites labeled $1, 2, 3, 4$ as depicted in Fig. 2.9. We consider the system at half-filling where only the lowest two bands are occupied. On a lattice with PBC and N_x and N_y unit cells in the x and y directions, respectively, the Hamiltonian is given by

$$H_{\text{Quad}} = \sum_{x=0}^{N_x-1} \sum_{y=0}^{N_y-1} \Big[t \left(c^\dagger_{1,(x,y)} c_{3,(x,y)} + c^\dagger_{4,(x,y)} c_{2,(x,y)} + c^\dagger_{1,(x,y)} c_{4,(x,y)} - c^\dagger_{3,(x,y)} c_{2,(x,y)} + h.c. \right)$$
$$+ t' \left(c^\dagger_{1,(x,y)} c_{3,(x+1,y)} + c^\dagger_{4,(x,y)} c_{2,(x+1,y)} + c^\dagger_{1,(x,y)} c_{4,(x,y+1)} - c^\dagger_{3,(x,y)} c_{2,(x,y+1)} + h.c. \right) \Big]. \quad (2.31)$$

Here, (x, y) is the position of the unit cell with $0 \leq x \leq N_x - 1$ and $0 \leq y \leq N_y - 1$. For $\tau = 1, \ldots, 4$, $c^\dagger_{\tau,(x,y)}$ denotes the creation operator for a fermion on the site τ in the unit cell at position (x, y). The Hamiltonian of Eq. (2.31) describes hopping between nearest-neighbour sites in the same unit cell with amplitude t, and between nearest-neighbour sites

in adjacent unit cells with amplitude t'. The signs of the hopping amplitudes ensure that there is a flux π through every plaquette of the square lattice. Due to the alternating hoppings t and t' in each row and column of the square lattice, the quadrupole model can be viewed as a 2D generalization of the SSH model of Sec. 2.2. Similarly to the SSH model, we will also consider the Hamiltonian of Eq. (2.31) with an additional staggered chemical potential μ which is μ on sites 1 and 2 of each unit cell, and $-\mu$ on sites 3 and 4 of each unit cell (see Fig. 2.9(a)).

On a square lattice with PBC in both directions, the four-band Bloch Hamiltonian of the quadrupole model including the staggered chemical potential is given by

$$\begin{aligned} H_{\text{Quad}}(k_x, k_y) = &\left(t + t'\cos(k_x)\right)\sigma_1 \otimes \sigma_0 + t'\sin(k_x)\left(-\sigma_2 \otimes \sigma_3\right) \\ &+ \left(t + t'\cos(k_y)\right)\left(-\sigma_2 \otimes \sigma_2\right) + t'\sin(k_y)\left(-\sigma_2 \otimes \sigma_1\right) + \mu\sigma_3 \otimes \sigma_0, \end{aligned} \tag{2.32}$$

where $k_x = 2\pi n_{k_x}/N_x$ with an integer $n_{k_x} \in \{0, \ldots, N_x - 1\}$ and $k_y = 2\pi n_{k_y}/N_y$ with an integer $n_{k_y} \in \{0, \ldots, N_y - 1\}$ are the lattice momenta in the first Brillouin zone.

For zero chemical potential $\mu = 0$, the Hamiltonian of the quadrupole model is invariant under the two mirror symmetries M_x and M_y. On the Bloch Hamiltonian, the mirror symmetries are implemented as

$$\hat{m}_x H_{\text{Quad}}(k_x, k_y)\hat{m}_x^\dagger = H_{\text{Quad}}(-k_x, k_y), \tag{2.33a}$$

$$\hat{m}_y H_{\text{Quad}}(k_x, k_y)\hat{m}_y^\dagger = H_{\text{Quad}}(k_x, -k_y), \tag{2.33b}$$

where

$$\hat{m}_x = \sigma_x \otimes \sigma_z, \tag{2.34a}$$

$$\hat{m}_y = \sigma_x \otimes \sigma_x. \tag{2.34b}$$

Therefore, the mirror symmetries anti-commute $\{\hat{m}_x, \hat{m}_y\} = 0$. They are the symmetries which protect the topological phase of the quadrupole model [20]. In addition to the mirror symmetries, the Hamiltonian of Eq. (2.31) is invariant also under time reversal symmetry, charge conjugation and C_4 rotation symmetry (up to a gauge transformation). However, these symmetries are not necessary for the realization of the higher order topological phase [20].

The four energy bands of the Bloch Hamiltonian of Eq. (2.32) form two degenerate pairs with energy $\pm\epsilon(k_x, k_y)$, where the dispersion is

$$\epsilon(k_x, k_y) = \sqrt{2t^2 + 2(t')^2 + 2tt'\left[\cos(k_x) + \cos(k_y)\right] + \mu^2}. \tag{2.35}$$

This dispersion is gapped unless $\mu = 0$ and $|t'| = |t|$. Therefore, the phase diagram at zero chemical potential splits into two regions $|t/t'| < 1$ and $|t/t'| > 1$. Similarly to the case of the SSH model, the bulk energy spectrum does not allow to distinguish these parameter regions since the dispersion of Eq. (2.35) is invariant under exchange of the two hoppings t and t'. However, we show now that analogously to the SSH model, the energy spectrum with OBC in both directions is very different in the case $|t/t'| < 1$ and the case $|t/t'| > 1$, indicating that they describe different phases.

2.5.2 Topological signatures of the quadrupole model: corner modes and quantized bulk multipole moments

In order to understand the structure of the energy spectrum of the quadrupole model at zero chemical potential $\mu = 0$ with OBC in both directions in the two regions $|t/t'| > 1$ and $|t/t'| < 1$, we first consider the two dimerized cases where $t' = 0$ and $t = 0$, respectively. For $t' = 0$, there is no coupling between different unit cells. Therefore, the Hamiltonian with OBC is identical to the Hamiltonian with PBC. From the dispersion relation of Eq. (2.35) we see that the single particle energy spectrum is fully gapped, with $2N_xN_y$ levels at energy $\sqrt{2}|t|$ and $2N_xN_y$ levels at energy $-\sqrt{2}|t|$.

On the other hand, for $t = 0$, there is no coupling between sites in the same unit cell. The resulting pattern of coupled sites is shown in Fig. 2.10(a). In the bulk, the system splits into plaquettes of four sites from four different unit cells, which are coupled through the hopping t'. Similarly to the case $t' = 0$, these plaquettes lead to $2(N_x - 1)(N_y - 1)$ levels with energy $\sqrt{2}|t'|$ and $2(N_x - 1)(N_y - 1)$ levels with energy $-\sqrt{2}|t'|$. However, the remaining lattice sites at the edges of the system form a very different pattern: At each edge, one obtains one copy of the SSH model in its topological dimerized phase. According to the SSH model dispersion relation of Eq. (2.9) evaluated in the topological dimerized phase at $\delta = 1$ and rescaled by a factor $t'/2$, the bulks of these SSH chains give rise to $2(N_x + N_y - 2)$ levels at energy $|t'|$ and $2(N_x + N_y - 2)$ levels at energy $-|t'|$. In addition, at each corner where two SSH chains meet, there is one mode that decouples entirely from the rest of the system and hence lies at zero energy. Each of these four modes corresponds to a shared edge mode of the two SSH chains that meet at the corner. Therefore, for $t = 0$ the quadrupole model possesses four mid-gap states at zero energy.

Away from the dimerized points at $t = 0$ and $t' = 0$, we can evaluate the single particle energy spectrum of the quadrupole model with OBC in both directions numerically. It is shown in Fig. 2.10(b) for several values of t/t'. For $|t/t'| > 1$ the energy spectrum is fully gapped. On the other hand, for $|t/t'| < 1$, there are four gapless modes close to zero energy, which are localized at the corners. The edges of the system are gapped. This indicates that the quadrupole model in this region is in a topologically nontrivial phase.

Similarly to the SPT phases discussed above, the nature of the phases for $|t/t'| > 1$ and $|t/t'| < 1$ can also be understood through a bulk topological invariant, which vanishes for $|t/t'| > 1$ but has a non-zero value if $|t/t'| < 1$. For the quadrupole model, the bulk topological invariant is the bulk quadrupole moment q_{xy}, which can be computed via nested Wilson loops [20]. Due to the mirror symmetries M_x and M_y, the quadrupole moment is quantized and can only take the values $q_{xy} = 0$ or $q_{xy} = e/2$. In the trivial phase for $|t/t'| > 1$, one finds $q_{xy} = 0$ [20]. However, in the topological phase for $|t/t'| < 1$, the bulk quadrupole moment is $q_{xy} = e/2$, which leads to a non-vanishing edge polarization and fractional corner charge $\pm e/2$. The latter manifests in the single particle energy spectrum through the four zero energy modes we observed in Fig. 2.10(b) [22].

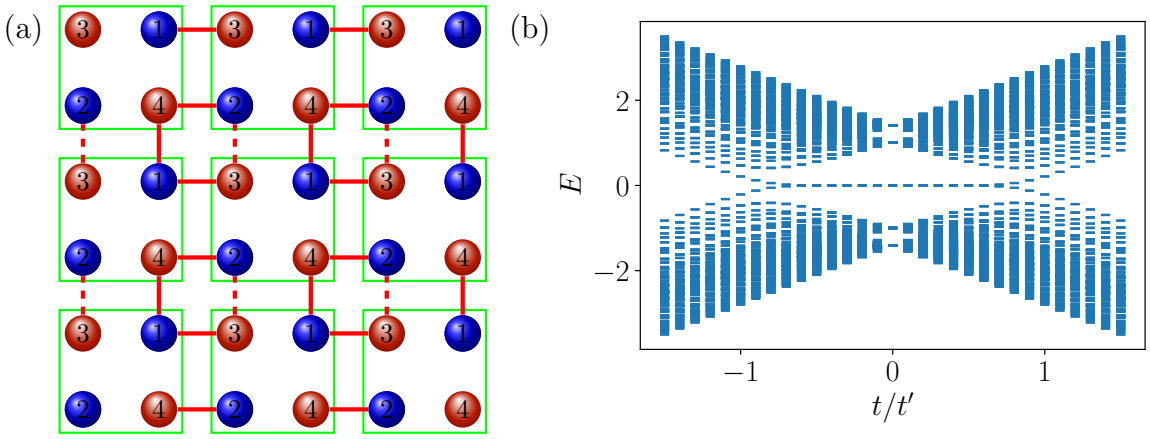

Figure 2.10: (a) Coupling pattern in the dimerized topological phase of the quadrupole model for $t = 0$ on a lattice with OBC in both directions. (b) Single particle energy spectrum of the topological quadrupole model on a square lattice with $N_x = N_y = 10$ unit cells and OBC in both directions for different values of t/t' ranging from $t/t' = -1.5$ to $t/t' = 1.5$, and $t' = 1$. Note that the states around zero energy correspond to the four corner state modes discussed in the text.

2.5.3 The chiral hinge insulator

In Sec. 2.3.2 we mentioned that the 2D CI can be viewed as the result of a charge pumping cycle of the 1D SSH model. Similarly, it is possible to define a 3D second order TI with chiral hinge modes [21] via a dipole pumping cycle of the quadrupole insulator with staggered chemical potential μ [22]. In this picture, the chiral hinge modes emerge as a consequence of the corner modes of the quadrupole model in the same way as the edge modes of the CI are related to the edge states of the SSH model. This connection is explored in the language of tensor network states in our publication of Ref. [2] (see Sec. 5.2).

The 3D chiral hinge insulator is protected by the product $C_{4z}\mathcal{T}$ of four-fold rotation symmetry in the xy-plane and time reversal $\mathcal{T}$ [21]. With OBC in the x and y directions, its vertical surfaces are gapped, but the hinges parallel to the z direction host chiral gapless modes akin to the edge modes of a CI (see the sketch in Fig. 2.11(a)). With OBC in the z direction, the top and bottom surfaces host a single gapless Dirac cone each, analogously to the 3D time reversal invariant TI.

The number of these hinge modes per hinge is not protected, but the parity of their number is, similar to the number of edge modes in a 2D time reversal invariant TI. Indeed, the minimal surface perturbation compatible with the $C_{4z}\mathcal{T}$ symmetry is the addition of 2D CIs with Chern number $\nu = \pm 1$ on the gapped vertical surfaces as sketched in Fig. 2.11(b). Here, the CIs on the surfaces normal to the x direction (marked in blue) have $\nu = 1$, while those on the surfaces normal to the y direction (marked in red) are their time reversal conjugates with $\nu = -1$. Each of the CIs possesses edge modes localized at the vertical hinges of the 3D system. As indicated in Fig. 2.11(b), the CI edge modes combine in such

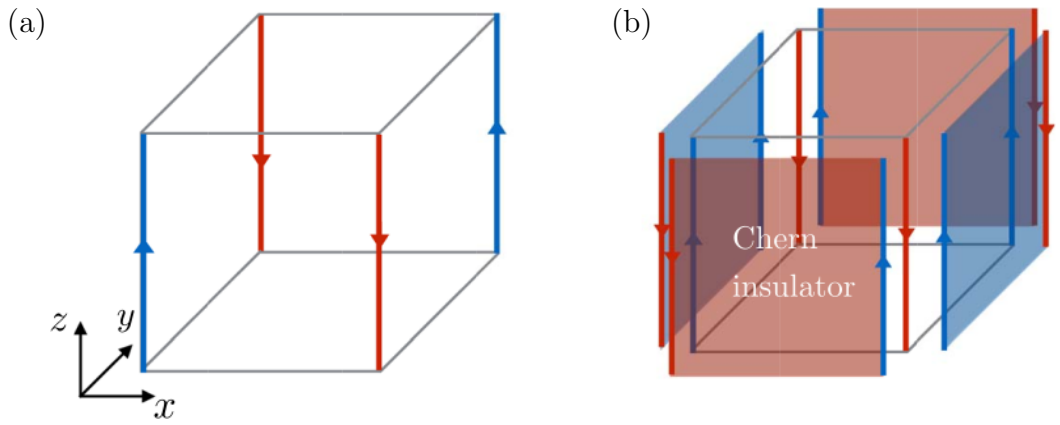

Figure 2.11: (a) Chiral modes at the hinges parallel to the z direction in the chiral hinge insulator with OBC in the x and y directions and PBC in the z direction. (b) Minimal surface perturbation preserving $C_{4z}\mathcal{T}$, which changes the number of hinge modes by two. The 2D CIs on the surfaces normal to the x direction (marked in blue) have $\nu = 1$, while those on the surfaces normal to the y direction (marked in red) are their time reversal conjugates with $\nu = -1$. From Frank Schindler et al. "Higher-order topological insulators". In: *Science advances* 4.6 (2018), eaat0346. Reprinted with permission from AAAS.

a way that the number of chiral hinge modes is changed by 2 on each hinge. Therefore, the number of chiral hinge modes cannot be topologically protected, but their parity is, leading to a $\mathbb{Z}_2$ topological characterization.

Indeed, it can be shown that the bulk topological invariant of the chiral hinge insulator is the magnetoelectric polarizability, the same bulk invariant as for the 3D $\mathbb{Z}_2$ TI [21]. In the case of the chiral hinge insulator, there is a higher order bulk boundary correspondence leading to gapped vertical surfaces and gapless vertical hinges. In our publication of Ref. [3], we study the chiral hinge insulator at fractional band filling and in the presence of strong interactions. The non-interacting HOTI is discussed in greater detail there (see Sec. 5.3).

Chapter 3

Intrinsic topological order and the fractional quantum Hall effect

The integer QHE in 2D electron gases leads to the quantization of the Hall conductivity to values $\sigma_{xy} = (e^2/h)\nu$ with a positive integer ν. As we discussed in Chapter 2, it marks the first example of a topological insulator, a class of phases that can be understood using single particle physics and the theory of topological band structures.

Only two years after the first observation of the integer QHE, the fractional QHE was discovered in very clean experimental samples [5]. In the fractional QHE, the plateaus in the Hall conductivity occur additionally at certain rational values of ν such as $\nu = 1/3$. In contrast to the case of the integer QHE, strong correlations between the electrons are essential for the description of the fractional QHE. Its understanding required the development of an entirely new theory, that of intrinsic topological order [13]. Compared to the SPT phases discussed in the previous chapter, phases with intrinsic topological order give rise to a number of qualitatively new and highly non-trivial phenomena. For example, in two dimensions they can possess elementary excitations with fractional quantum numbers and fractional anyonic exchange statistics that is neither bosonic nor fermionic. The fractional QHE has allowed the direct experimental observation of such excitations with fractional charge [15, 16] and, very recently, fractional exchange statistics [17, 18]. As a result of these properties, systems with intrinsic topological order have been proposed as platforms for topological quantum computation, which would enjoy an inbuilt protection from local errors [14].

Due to the strong interaction effects, the ground states of realistic microscopic models hosting intrinsic topological order are generally very difficult to compute. Instead, one frequently relies on model wave functions which are easier to analyze and capture the essential properties of the phase. Here, we will focus on one specific class of model wave functions, the Laughlin states [26]. They provide very good approximations to the ground state of a fractional quantum Hall system on plateaus with $\nu = 1/q$, where q is an odd integer.

In order to motivate the expression for the Laughlin wave function, we begin with a

brief review of the many body wave function for the integer QHE in Sec. 3.1. This allows us to introduce the Laughlin wave function in Sec. 3.2. We then discuss the characteristic properties of the gapless edge modes at the boundary of Laughlin systems in Sec. 3.3. Next, we briefly review some of the unusual properties in their bulk in Sec. 3.4. Finally, we discuss lattice realizations of fractional quantum Hall physics using fractional Chern insulators in Sec. 3.5.

3.1 The integer quantum Hall effect

We demonstrated in Chapter 2 that the description of CIs and the integer QHE does not require the consideration of interactions between the electrons. Once the single particle energy eigenstates of these systems are known, the many body ground state is obtained by filling the single particle orbitals according to the Pauli principle. In Sec. 2.3, we considered a CI on a periodic lattice, where the single particle orbitals are obtained by a diagonalization of the Bloch Hamiltonian in second quantization. We now repeat this analysis for the integer QHE in the continuum. To that end, we review the single particle wave functions in Sec. 3.1.1 and compute the many body wave function in first quantization in Sec. 3.1.2. This will be useful for understanding the structure of the interacting Laughlin wave function in the next section.

3.1.1 Single particle wave functions

As described in Sec. 2.1.2, the QHE occurs in 2D electron gases in the presence of a strong transversal magnetic field. Let us assume that the electrons with charge $-e$ and mass M are confined to move in the 2D xy-plane, such that the external magnetic field is $\mathbf{B} = (0\,0\,B)^T$. In this section we assume for simplicity that the electrons are spinless (as we will argue below, this is a good approximation for the regime that we are interested in). The motion of a single electron in this setting is governed by the Hamiltonian

$$H = \frac{1}{2M}\left[\left(-i\hbar\partial_x - \frac{e}{c}A_x\right)^2 + \left(-i\hbar\partial_y - \frac{e}{c}A_y\right)^2\right]. \tag{3.1}$$

Here, $\mathbf{A} = (A_x\,A_y\,0)^T$ is the vector potential for the external magnetic field, satisfying $\nabla \times \mathbf{A} = \mathbf{B}$. In the following, we want to focus on a disk geometry which is invariant under rotations around the origin in the xy-plane. It is therefore convenient to work in the symmetric gauge, where the non-vanishing components of the vector potential are $A_x = -y(B/2)$ and $A_y = x(B/2)$.

The energy bands defined by the single particle Hamiltonian of Eq. (3.1), which are referred to as Landau levels, are massively degenerate with energies [49]

$$E_n = \hbar\omega_c\left(n + \frac{1}{2}\right). \tag{3.2}$$

Here, $n \geq 0$ is the Landau level index, and $\omega_c = (eB)/(Mc)$ is the cyclotron frequency, which determines the band gap between different Landau levels. Within each Landau level, the single particle orbitals may be labeled by their angular momentum L_z in the z direction. In the Landau level of index n, the angular momentum takes values $L_z = \hbar m$ with an integer $m \geq -n$ [49]. The angular momentum index m leads to a macroscopic degeneracy of the Landau levels. In a finite system, the number of states in each Landau level is finite and given (in the thermodynamic limit) by the number $N_\Phi = \Phi/\Phi_0$ of flux quanta. Here, Φ is the total flux through the system, and we introduced the flux quantum $\Phi_0 = hc/e$. Denoting by N the total number of filled single particle orbitals, we can define the filling fraction

$$\nu = \frac{N}{N_\Phi}. \tag{3.3}$$

As suggested by our choice of symbol, it is the filling fraction which determines the value of the Hall conductance via $\sigma_{xy} = \nu(e^2/h)$ [49].

From now on we assume that the filling fraction satisfies $\nu \leq 1$, such that only states from the lowest Landau level (LLL) are occupied. For a fixed number of particles N, this can be achieved by increasing the strength of the magnetic field B. In the LLL, the wave function for the single particle orbital with angular momentum m is given by

$$\psi_m(z) = z^m e^{-|z|^2/(4l_0^2)}. \tag{3.4}$$

Here, $l_0 = \sqrt{(c\hbar)/(eB)}$ is the magnetic length and $z = x + iy$ with absolute value $|z|$ denotes a complex position coordinate in the 2D plane. The density $|\psi_m|^2(|z|)$ associated with this wave function is invariant *w.r.t.* rotations around the origin of the xy-plane, and peaks at the radius $|z| = r_m$ with

$$r_m = \sqrt{2m} l_0. \tag{3.5}$$

We now consider a disk with a finite radius $R \gg l_0$, and discard all single particle orbitals of the LLL whose density peaks outside the radius R. Therefore, the number of allowed single particle orbitals with $r_m < R$ is given by

$$\frac{R^2}{2l_0^2} = \pi R^2 B \times \left(\frac{hc}{e}\right)^{-1} = \frac{\Phi}{\Phi_0} \equiv N_\Phi, \tag{3.6}$$

and is therefore equal to the number N_Φ of flux quanta that pierce the system, as we mentioned above.

3.1.2 Many body wave function

Let us consider the integer QHE in the case where the magnetic field B is strong enough that the Fermi energy E_F lies between the LLL and the second lowest Landau level,

$$\frac{1}{2}\hbar\omega_c < E_F < \frac{3}{2}\hbar\omega_c. \tag{3.7}$$

We can also assume that B is sufficiently large that the system is completely spin polarized due to the strong Zeeman splitting between different spin orientations. This is frequently the case in real experiments. The electrons therefore behave like spinless fermions. In this case, the many body ground state of the system is given by filling each of the N_Φ single particle orbitals in the LLL exactly once. Hence, the number of particles is equal to the number of orbitals, $N = N_\Phi$, and the filling fraction is $\nu = 1$.

The corresponding many body wave function is simply the Slater determinant of all admissible single particle wave functions of Eq. (3.4),

$$\Psi_{\nu=1}(z_1, \ldots, z_N) = \left(\prod_{1 \leq i < j \leq N} (z_i - z_j) \right) \times e^{-\frac{1}{4l_0^2} \sum_{i=1}^{N} |z_i|^2}, \tag{3.8}$$

where we have omitted the normalization factor. Here, z_i denotes the 2D position of the particle i for $i = 1, \ldots, N$. As required by the Pauli principle, this wave function is completely anti-symmetric under exchange of particles.

This analysis can be repeated in a toroidal geometry with generalized boundary conditions parametrized by two angles $\theta_1, \theta_2 \in [0, 2\pi)$. The dependence of the single particle wave functions on these angles defines a vector bundle, akin to the vector bundle of the Bloch bands over the 2D Brillouin zone for a CI. It can be shown that the Hall conductivity of the many body wave function of the integer QHE is given by the Chern number of this vector bundle multiplied with e^2/h [6, 85]. In particular, for the LLL the Chern number is unity, such that $\sigma_{xy} = (e^2/h)\nu$ with the filling fraction $\nu = 1$.

3.2 The Laughlin wave function

The Laughlin wave functions are a series of model wave functions which provide very good descriptions for the ground states of fractional quantum Hall systems at filling fractions $1/q$ with q an odd integer [26]. They can be generalized to bosonic systems (with q even in that case), and serve as building blocks for more complicated model wave functions describing other filling fractions [27, 28]. We begin in Sec. 3.2.1 by discussing the fermionic Laughlin wave functions, before considering the bosonic Laughlin wave functions in Sec. 3.2.2. We conclude in Sec. 3.2.3 with a description of the generalized Pauli principle satisfied by the Laughlin wave functions.

3.2.1 Fermionic Laughlin wave functions

The Laughlin wave functions are a series of model wave functions for incompressible quantum fluids, which are labeled by an integer q. The $q = 3$ wave function was proposed in 1983 by Robert Laughlin as a variational many body wave function for the experimentally observed quantum Hall plateau at $\sigma_{xy} = (1/3)(e^2/h)$ [26].

The Laughlin wave functions describe a completely spin-polarized quantum Hall system, where only a fraction of the single particle orbitals of the LLL are occupied. With the same

notations as in Sec. 3.1 above, the many body wave function for N electrons at positions $z_1, \ldots, z_N$ is

$$\Psi_{\nu=1/q}(z_1, \ldots, z_N) = \left(\prod_{1 \leq i < j \leq N} (z_i - z_j)^q \right) \times e^{-\frac{1}{4l_0^2} \sum_{i=1}^N |z_i|^2}. \tag{3.9}$$

Formally, this wave function resembles the ground state wave function of Eq. (3.8) for the integer QHE in the LLL. The crucial difference lies in the power q of the polynomial factor, which is $q = 1$ for the integer QHE, and $q \geq 3$ for the Laughlin wave function of Eq. (3.9).

Let us argue that the Laughlin wave function of Eq. (3.9) describes a system at filling fraction $\nu = 1/q$ in the thermodynamic limit (a rigorous derivation can be made). We assume that the wave function $\Psi_{\nu=1/q}$ describes a system on a finite disk of radius R with a homogeneous electron density. By expanding the first factor in Eq. (3.9), we see that the highest power of any z_i appearing in the polynomial factor is $m_{max}(N) = q(N-1)$. In other words, the single particle orbital with the largest radius that appears in the Laughlin wave function of Eq. (3.9) has radius $r_{m_{max}}(N) = l_0\sqrt{2q(N-1)}$. This implies that the radius R of the disk is given by $R = r_{m_{max}+1}(N)$. According to Eq. (3.6), the number of flux quanta in the system is then $N_\Phi = R^2/(2l_0^2) = q(N-1)+1$. Hence, the filling fraction is $\nu = N/(qN - q + 1)$, which approaches the value $1/q$ in the thermodynamic limit $N \to \infty$.

The Laughlin wave functions are not the exact ground states of realistic Hamiltonians at filling $\nu = 1/q$. However, exact diagonalization studies on numerically accessible systems have shown that the Laughlin states have a very high overlap with the ground states of electrons that interact with the Coulomb interaction in the LLL [86]. Moreover, the Laughlin states are the exact ground states of model Hamiltonians with a finite interaction range. The Laughlin state at filling $\nu = 1/3$ is the unique densest ground state of the shortest-range interaction for fermions. Knowing that realistic interactions usually have a strong short-range repulsion component, this provides some qualitative understanding of why the Laughlin state is a fairly good description of the true ground state.

3.2.2 Bosonic Laughlin wave functions

Until now, we have restricted our discussion to fermionic systems such as 2D electron gases, where the fractional QHE was discovered experimentally. However, the fractional QHE is not a result of the fermionic statistics of the itinerant particles. Instead, it is a consequence of the massively degenerate Landau levels and the resulting importance of interactions. This is a situation which can also occur in bosonic systems with interactions. Indeed, there have been numerous proposals for the realization of fractional quantum Hall physics in bosonic systems.

One possible platform for bosonic fractional quantum Hall physics is given by ultra-cold atoms in rotating harmonic traps [87]. In a certain regime, the single particle levels in this system form Landau level bands, where the angular velocity plays the role of the magnetic

field. In the simplest case, the repulsive interactions between the bosonic atoms can be modeled by a simple δ-function potential

$$V(z_i, z_j) = g\,\delta^{(2)}(z_i - z_j), \tag{3.10}$$

where z_i and z_j are the complex 2D positions of two bosons.

The fermionic Laughlin wave functions of Eq. (3.9) can easily be extended to bosonic systems by choosing an even integer $q \geq 2$ for the power of the Slater determinant, rather than an odd integer as for the fermionic case. Indeed, for even q, the many body wave function of Eq. (3.9) is symmetric under exchange of any two particles, as required by Bose-Einstein statistics. It is clear that the potential energy *w.r.t.* the δ-function potential of Eq. (3.10) vanishes for all bosonic Laughlin states, meaning that they are ground states of the effective Hamiltonian in the LLL. Moreover, it can be shown that the $q = 2$ Laughlin state is the densest such state, *i.e.* the state with the lowest total angular momentum.

A second very promising platform for the observation of the bosonic fractional QHE is given by ultra-cold quantum gases in optical lattices [53, 54, 55, 56]. Due to the periodic potential, such systems are described by periodic Hamiltonians rather than continuum wave functions such as the Laughlin wave function. We will provide more details on these fractional Chern insulators in Sec. 3.5.

3.2.3 Generalized Pauli principle

The Laughlin wave function of Eq. (3.9) defines a many body state in the LLL. Therefore, it can be expressed as a linear combination of Fock states in the occupancy basis of the single particle orbitals in the LLL with index $m \in \{0, \ldots, N_\Phi - 1\}$, whose wave functions are given in Eq. (3.4). In theory, the Fock space representation can be computed by expanding the polynomial factor in Eq. (3.9) into monomials. For example, by picking the first term z_i in every factor $(z_i - z_j)$ with $i < j$, we find that one term in the expansion of the polynomial factor is given by the monomial

$$z_0^{q(N-1)} \times z_1^{q(N-2)} \times \cdots \times z_{N-1}^{q} \times z_N^{0}. \tag{3.11}$$

Since the Laughlin wave function describes fermions for odd q and bosons for even q, we know that this monomial appears with the same coefficient as its images under completely anti-symmetric or symmetric permutations of the particle positions, respectively. The linear combination of these monomials corresponds to the fermionic or bosonic Fock state with one particle in the orbital $m = jq$ for $j = 0, \ldots, N-1$, and no particle in any other orbital. We can refer to this Fock state by its occupation number sequence

$$\lambda = \begin{bmatrix} 1 & 0^{q-1} & 1 & 0^{q-1} & \ldots & 1 & 0^{q-1} \end{bmatrix} \tag{3.12}$$

where a 1 indicates a filled orbital, 0^{q-1} denote $q-1$ successive empty orbitals, and the orbital index m is increasing from left to right. Since the orbital m carries angular momentum $L_z = \hbar m$ as discussed in Sec. 3.1.1, the total angular momentum associated with

the occupation number sequence of Eq. (3.12), and hence that of the Laughlin state, is

$$L_z^{tot} = \hbar \sum_{j=0}^{N-1} jq = \hbar \frac{q}{2}(N-1)(N-2). \tag{3.13}$$

Due to the large number of terms in the polynomial factor of Eq. (3.9), the computation of the Fock space expansion is very difficult and not feasible for big systems. However, it has been shown that the Fock space representation of many fractional quantum Hall wave functions including the Laughlin wave function follows a very specific pattern [88]. Concretely, the polynomial factors are given by Jack polynomials [89], which are determined by a single occupation number sequence like that in Eq. (3.12), referred to as a root partition. The coefficients of other Fock states can be efficiently computed recursively in terms of the root partition.

For the Laughlin wave function on a disk, it can be shown that the root partition is the unique occupation number sequence which minimizes the total angular momentum L_z^{tot} for a given number of particles, and which obeys a generalized Pauli principle [88]. This Pauli principle requires that out of any q adjacent orbitals, only a single one may be occupied. It is easy to see that the root partition for the Laughlin state at filling $1/q$ is given by the occupation number sequence λ of Eq. (3.12).

Crucially, the correspondence between many body wave functions and root partitions satisfying the generalized Pauli principle applies not only to the Laughlin ground state, but also to its elementary excitations in the bulk and at the edges. Therefore, the generalized Pauli principle can be employed to count the number of excitations of the Laughlin wave function and their angular momentum. We will make use of this possibility in the next section describing the edge physics of the Laughlin state.

3.3 Chiral edge mode

In Sec. 2.3.2 above, we showed that the CI in a geometry with OBC possesses chiral edge modes, which are a signature of the topologically non-trivial nature of the bulk phase. Similarly, the integer and fractional quantum Hall systems possess characteristic protected chiral edge modes, which are responsible for the observed quantization of the Hall conductivity. Since the edge modes are a consequence of the topologically non-trivial bulk, a careful analysis of their properties reveals information about the bulk phase. Here, we focus on the edge mode of the Laughlin state at filling $1/q$. We begin in Sec. 3.3.1 by discussing the single particle spectrum on a finite disk in the presence of a confining potential. In Sec. 3.3.2, we then show how the fractional Hall conductivity emerges using the same arguments as in Sec. 2.3.3. We continue by considering the state counting in the many body spectrum of the edge excitations in Sec. 3.3.3. Finally, we briefly discuss the description of the edge mode as a chiral Luttinger liquid in Sec. 3.3.4.

3.3.1 Single particle spectrum with confining potential

We return to the problem of a single electron on a finite 2D disc of radius R in the presence of a transversal magnetic field. In contrast to our earlier discussion from Sec. 3.1.1, we now explicitly include the effects of a radially symmetric confining potential which implements the finite size of the disc. Hence, the potential is zero in the center of the disk for $|z| \ll R$, and very large outside the disk for $|z| \gg R$. Assuming that the potential varies slowly as a function of $|z|$ on the scale of the magnetic length l_0, the single particle orbitals in the LLL of Eq. (3.4) are still energy eigenfunctions. However, their energies are no longer strictly degenerate, but instead follow the confining potential. Hence, the single particle orbitals with small angular momentum localized in the bulk of the disc do not feel the effect of the confining potential and are still quasi-degenerate at energies close to $\hbar\omega_c/2$. On the other hand, the orbitals localized at large radii $r_m \approx R$ close to the edge of the disc bend upwards in energy towards the second lowest Landau level (see Fig. 3.1(a)).

For the remainder of this section, we will assume that the magnetic field is sufficiently strong that only orbitals from the LLL are occupied. The Fermi energy E_F then lies between the LLL and the second lowest Landau level, and therefore crosses the bent-up edge of the LLL at the angular momentum $m = N_\Phi$. Close to this point, the confining potential can be linearized, such that the single particle dispersion close to the Fermi energy is

$$E(m) - E_F = \frac{2\pi v}{\mathcal{L}_{\text{disk}}}(m - N_\Phi). \tag{3.14}$$

Here, $\mathcal{L}_{\text{disk}} = 2\pi R$ is the circumference of the disk, and v is the dispersion velocity at the Fermi energy. This is a chiral dispersion, where the energy above the Fermi energy is proportional to the relative angular momentum $\hbar(m - N_\Phi)$. This single particle dispersion gives rise to a chiral edge mode both for the integer and the fractional QHE.

3.3.2 Hall conductivity

In Sec. 2.3.3, we computed the Hall conductivity σ_{xy} in a cylinder geometry resulting from chiral edge modes in a system of non-interacting fermions using a simple semi-classical argument, finding that $\sigma_{xy} = e^2/h$. Let us now see how this argument can be adapted for the Laughlin states. We use the same geometry and notations as in Sec. 2.3.3.

The number n of additional single particle orbitals that become accessible by a shift in the Fermi energy from E_F to $E_F + eV_H$ at the upper edge of the cylinder is the same in the interacting and non-interacting systems. Therefore, n is still given by Eq. (2.26) for the Laughlin states. However, the current per mode, which is given by Eq. (2.27) for the non-interacting system, needs to be modified for a general Laughlin state. Indeed, as we discussed in Sec. 3.2.3, the Laughlin state at filling $1/q$ is characterized by the root partition of Eq. (3.12), in which only $N = N_\Phi/q$ out of the N_Φ available single particle orbitals for the electrons are filled. Hence, the average charge per single particle orbital is no longer the electronic charge $-e$, but instead a fractional charge $-e^*$ with

$$e^* = \frac{e}{q}. \tag{3.15}$$

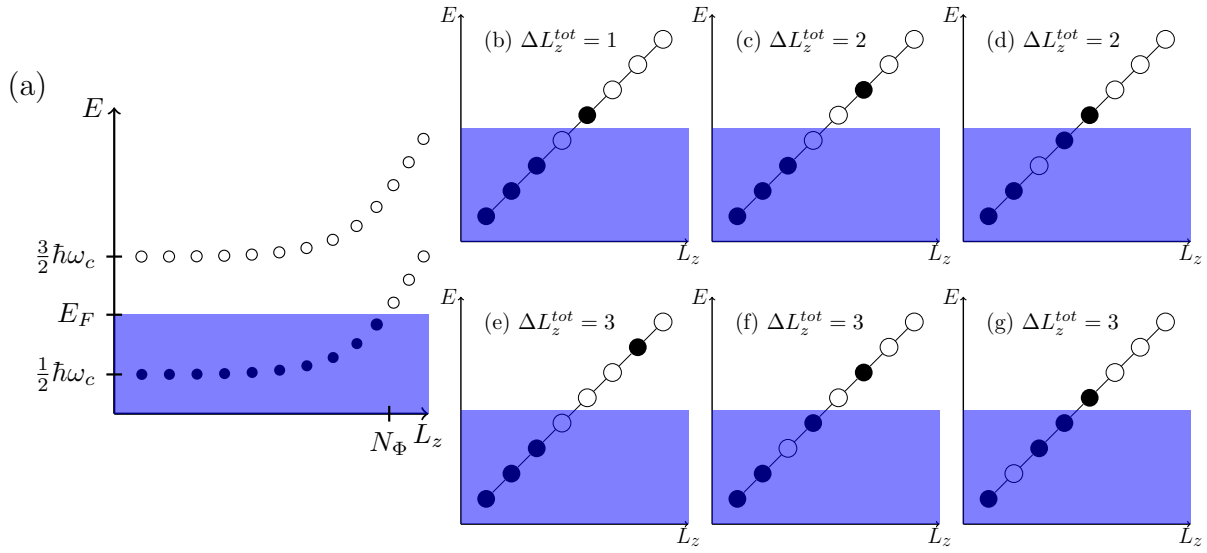

Figure 3.1: (a) Schematic depiction of the ground state in the integer QHE at filling $\nu = 1$ on a open disc with a confining potential. The shaded blue area denotes the orbitals below E_F. (b) - (g) Schematic depictions of the lowest-lying edge excitations. The relative many body angular momentum *w.r.t.* the ground state is in (b) $\Delta L_z^{tot} = 1$, in (c) and (d) $\Delta L_z^{tot} = 2$, and in (e), (f) and (g) $\Delta L_z^{tot} = 3$.

Consequently, the average current per mode is then given by $I_{\text{mode}} = v_+ e^*/N_x$. As a result, the Hall conductivity for the Laughlin state is

$$\sigma_{xy} = \frac{I_x}{V_H} = \frac{I_{\text{mode}} \times n}{V_H} = \frac{1}{q}\frac{e^2}{h}. \tag{3.16}$$

This result confirms the Laughlin state as a model wave function for the Hall plateau at $\nu = 1/q$.

3.3.3 Many body spectrum

Let us now discuss the many body excitation spectra that result from the chiral edge mode for the different Laughlin states on a disk. Due to the dispersion of Eq. (3.14), the many body excitation energy for the edge excitations is directly proportional to their total angular momentum ΔL_z^{tot} measured relative to the ground state. Therefore, we proceed by counting the number of many body states at each value of ΔL_z^{tot}.

We begin with the case of the integer QHE at filling $\nu = 1$, corresponding to the value $q = 1$. The ground state at $\Delta L_z^{tot} = 0$ is given by the filled Fermi sea, where all N_Φ single particle orbitals below E_F are occupied and those above E_F are empty. This is shown schematically in Fig. 3.1(a). Gapless excitations above this ground state are obtained by moving particles from just below the Fermi energy to orbitals just above the

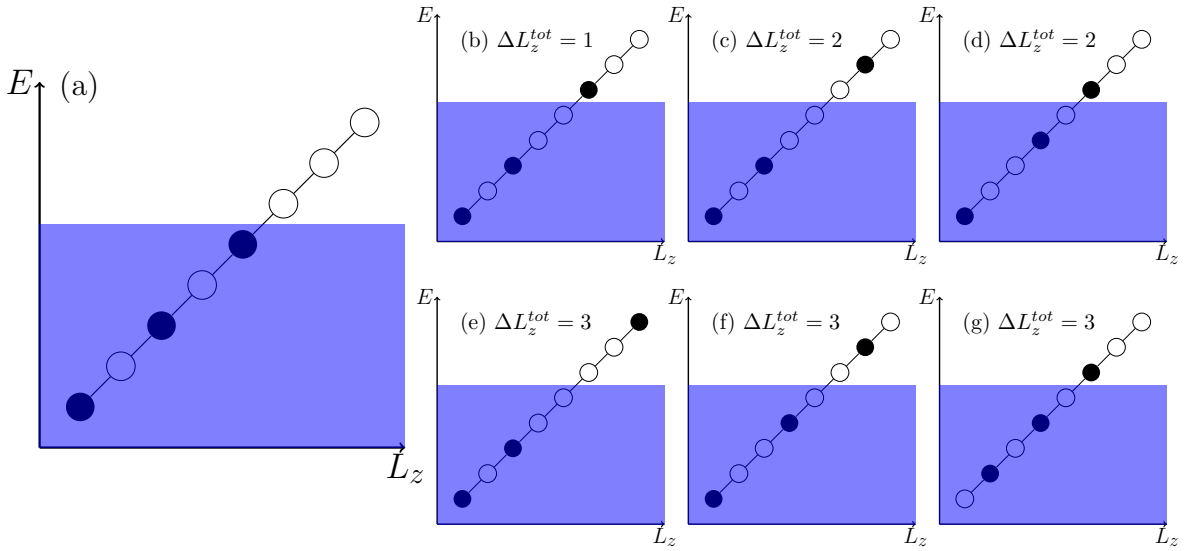

Figure 3.2: (a) Schematic depiction of the root partition of the Laughlin state at filling $\nu = 1/2$ on a open disc with a confining potential. The shaded blue area denotes the orbitals below E_F. (b) - (g) Schematic depictions of the root partitions of the lowest-lying edge excitations. The relative many body angular momentum *w.r.t.* the ground state is in (b) $\Delta L_z^{tot} = 1$, in (c) and (d) $\Delta L_z^{tot} = 2$, and in (e), (f) and (g) $\Delta L_z^{tot} = 3$.

Fermi energy. At $\Delta L_z^{tot} = 1$, there is one state allowed by the fermionic Pauli principle, obtained by moving one particle from the first level beneath E_F to the first level above E_F (see Fig. 3.1(b)). At $\Delta L_z^{tot} = 2$, there are two possible states, with are obtained from the state at $\Delta L_z^{tot} = 1$ by either moving the first particle one level further up, or else by moving the second-lowest particle to the lowest level beneath E_F (see Fig. 3.1(c) and (d)). At $\Delta L_z^{tot} = 3$, there are three possible states, whose occupation number sequences are sketched in Fig. 3.1(e), (f) and (g). In this fashion, one finds that the number of many body excited states for the first few values of $\Delta L_z^{tot} \geq 0$ is given by the sequence

$$1, 1, 2, 3, 5, 7, 11, \ldots \quad . \tag{3.17}$$

Let us now discuss the Laughlin states. As we explained in Sec. 3.2.3, the Laughlin ground state and its many body excited states, as well as their total angular momentum, are determined by root partitions such as in Eq. (3.12). The latter satisfy the generalized Pauli principle requiring that no more than 1 out of any q consecutive single particle orbitals be occupied. In order to determine the number of excited states at a given $\Delta L_z^{tot} \geq 0$, we therefore have to find the number of compatible root partitions. For concreteness, let us focus on the case $q = 2$.

The root partition for the ground state at $\Delta L_z^{tot} = 0$ is sketched in Fig. 3.2(a), with every second single particle orbital occupied as required by the generalized Pauli principle. At $\Delta L_z^{tot} = 1$, there is one root partition allowed by the generalized Pauli principle, obtained

by moving the particle from the second level beneath E_F to the first level beneath E_F (see Fig. 3.2(b)). At $\Delta L_z^{tot} = 2$, there are two possible states, with are obtained from the state at $\Delta L_z^{tot} = 1$ by either moving the first particle one level further up, or else by moving the second-lowest particle (see Fig. 3.2(c) and (d)). At $\Delta L_z^{tot} = 3$, there are three possible states, whose root partitions are sketched in Fig. 3.2(e), (f) and (g). In this fashion, it can be shown that the number of many body excited states of the Laughlin state at $q = 2$ is given by the same sequence of Eq. (3.17) as for the integer QHE. The same holds true for the other Laughlin states at different values of q.

3.3.4 Luttinger liquid with $\mathfrak{u}(1)_{q/2}$ free boson CFT

The low energy physics of interacting fermions in 1D critical systems known as Luttinger liquids can be described in terms of free boson CFTs [90] using a technique called bosonization [91]. The 1D edge of the 2D quantum Hall system can be interpreted as such a Luttinger liquid [92]. As we mentioned in Sec. 2.3.2, the crucial difference to a purely 1D system, which always combines chiral and anti-chiral CFT, lies in the intrinsic chirality of the edge state.

The edge modes of the Laughlin states are Luttinger liquids described by the CFT $\mathfrak{u}(1)_{q/2}$ of a compactified chiral free boson with central charge $c = 1$ and Luttinger parameter $K = 1/q$ [27]. This theory has q primary fields with conformal dimensions

$$h_j = \frac{j^2}{2q} \tag{3.18}$$

and U(1) charge

$$\frac{j}{q} \tag{3.19}$$

for $j = 0, \ldots, q-1$. The Verma modules created by the application of the bosonic mode operators on these highest-weight states have the state counting that we observed for the Laughlin states in Eq. (3.17) [90]. It has been shown that finite-size corrections to this state counting can be used to infer the Luttinger parameter K [93]. Moreover, the central charge and Luttinger parameter can be extracted from the scaling of certain correlation functions at the edge [94, 95]. We make use of this in our publication of Ref. [3] (see Sec. 5.3).

For the first bosonic Laughlin state at $q = 2$, the $\mathfrak{u}(1)_1$ theory has an extended SU(2) symmetry and can be identified with the CFT $\mathfrak{su}(2)_1$. Under this mapping, the U(1) current is identified with the current S^z of SU(2). According to Eq. (3.18), this theory has two primary fields $h_0 = 0$ with spin $S^z = 0$ and $h_1 = 1/4$ with spin $S^z = 1/2$. The states in the two corresponding Verma modules therefore form representations of SU(2) with integer and half-integer spin, respectively [90]. In our publications of Ref. [1] (see Sec. 5.1) and Ref. [3] (see Sec. 5.3), we study chiral topologically ordered systems whose edge states are described by this CFT.

3.4 Bulk properties

The bulk of systems with intrinsic topological order gives rise to a number of unconventional and highly non-trivial phenomena. In two dimensions, these include anyonic excitations with fractional charge and fractional exchange statistics, as well as a ground state degeneracy on surfaces of non-trivial genus. In this section, we briefly discuss some of these properties for the case of the Laughlin states, for which we already encountered elementary excitations with fractional charge $e^* = e/q$ in Sec. 3.3.2. We begin in Sec 3.4.1 by reviewing the bulk boundary correspondence, and proceed by discussing the topological degeneracy of the Laughlin states on a torus in Sec. 3.4.2.

3.4.1 The bulk boundary correspondence

In Chapter 2 we saw using the example of certain fermionic SPT phases that the bulk and edge of topologically non-trivial systems are tightly related. This is referred to as the bulk boundary correspondence. For chiral systems with intrinsic topological order such as fractional quantum Hall systems, this correspondence has been especially well explored [27, 49, 90]. In many cases including the Laughlin states, the gapless chiral edge modes of these systems are described by a chiral CFT which can also be used to characterize the bulk physics. This is a strong form of the bulk boundary correspondence, which has been used to construct fractional quantum Hall wave functions beyond the Laughlin states based on complicated CFTs, such as for the $\nu = 5/2$ state [27].

Concretely, this strong form of the bulk boundary correspondence implies that the chiral edge CFT contains operators which correspond to the electrons and the anyonic excitations in the bulk, as well as certain symmetry currents. For example, the Laughlin state at filling $1/q$ has q types of quasi-holes which are represented by the primary fields of the CFT $\mathfrak{u}(1)_{q/2}$. There is a similar CFT operator which represents a single electron in the bulk. Moreover, the current defining the electric charge is given by the U(1) current of this CFT [27]. The bulk wave functions for the ground state and the states with anyonic excitations can then be evaluated as CFT correlation functions. Moreover, the fractional quantum numbers of the anyonic excitations can be extracted from the properties of their CFT representations. For example, the fractional electric charge of the Laughlin quasi-holes is given by their U(1) charge of Eq. (3.19) (in units of e).

The bulk boundary correspondence is an important aspect of chiral topologically ordered systems, which also has practical relevance. Indeed, the close relation between the edge CFT and bulk properties allows to characterize the topological phase of a given microscopic model by studying its gapless edge physics. The edge properties are often easier to access in numerical computations than the gapped bulk excitations. For example, in our publication of Ref. [3] we study the gapless hinge modes of a 3D interacting model to conclude that the system is in a non-trivial topological phase (see Sec. 5.3). In the next chapter, we will present a method to study the gapless edge spectrum directly from the bulk ground state via the entanglement spectrum (see Sec. 4.2).

3.4.2 Topological degeneracy

Systems with intrinsic topological order have a topological degeneracy: In topologically nontrivial geometries such as a torus, they possess more than one ground state. The number of ground states depends on the topology of the space, and different ground states cannot be distinguished by any local measurement. The existence of a topological degeneracy is a signature of topological order generated by strong interactions. In particular, SPT phases such as the integer QHE do not have a topological degeneracy.

It can be shown that there is a tight relation between topological degeneracy and the number of different elementary bulk excitations with fractional statistics [96]. For example, the Laughlin state at filling $\nu = 1/q$ with q types of quasi-holes has a topological degeneracy of q^g on a 2D surface with genus g [97, 98]. In particular, on a 2D torus with genus $g = 1$, there are q distinct ground states. This can be understood in terms of the root partitions we discussed in Sec. 3.2.3. Indeed, the torus is periodic in both directions, as opposed to the disk, which is periodic only in one direction. Therefore, on the torus, the index m of the single particle orbitals is periodic and we should identify $m = N_\Phi$ with $m = 0$. As the torus has no edge, all single particle orbitals in the LLL are degenerate in energy. Hence, the sequence of Eq. (3.12) describing a Laughlin state on the open disk is not the only admissible root configuration. Instead, there are q different root partitions that satisfy the generalized Pauli principle and which have N out of $N_\Phi = (1/\nu)N$ filled orbitals,

$$\lambda_r = \begin{bmatrix} 0^r & 1 & 0^{q-1} & 1 & 0^{q-1} & \dots & 1 & 0^{q-1-r} \end{bmatrix} \tag{3.20}$$

where $r = 0, \dots, q-1$. These partitions λ_r correspond to the ground states of the Laughlin state on the torus, confirming the topological degeneracy q.

3.5 Fractional Chern insulators

Until now we have focused on describing the fractional QHE in continuous systems such as 2D electron gases. However, the effect can also occur in lattice systems [99]. For example, there are lattice analogs of the Laughlin states, the Kalmeyer-Laughlin states [100], which have the same topological properties as their continuum versions.

In Sec. 2.3 we discussed CIs, which are lattice analogs of the integer QHE without an external magnetic field. They possess bands with a non-zero Chern number, like the Landau levels in the continuum case. The fractional QHE occurs when strong interactions stabilize a ground state at fractional filling of the LLL band. Analogously, strongly correlated topological states can emerge in a band with non-zero Chern number at fractional filling in the presence of interactions: fractional Chern insulators (FCIs) [101, 102, 103, 104].

An FCI can be created using the CI model of Sec. 2.3 [105]. We first include the electronic spin $s = \uparrow, \downarrow$ by considering two uncoupled copies of the Hamiltonian of Eq. (2.16). At half filling, the ground state is given by filling each orbital from the lower band with two electrons of opposite spin. Note that this ground state naturally has an SU(2) symmetry describing the electronic spin. As described above, we need to introduce interactions

to obtain an FCI. The shortest-range interaction is given by an on-site density-density interaction between fermions of different spin,

$$H_{int} = U \sum_{x=0}^{N_x-1} \sum_{y=0}^{N_y-1} \sum_{\alpha=A,B} \left(c^\dagger_{\alpha,\uparrow,(x,y)} c_{\alpha,\uparrow,(x,y)} c^\dagger_{\alpha,\downarrow,(x,y)} c_{\alpha,\downarrow,(x,y)} \right). \tag{3.21}$$

Here, $c^\dagger_{\alpha,s,(x,y)}$ denotes the creation operator of an electron with spin $s \in \{\uparrow,\downarrow\}$ on the site α for $\alpha = A, B$ in the unit cell (x, y) (see Sec. 2.3.1).

If the interaction strength U is sufficiently strong, doubly occupancy of any lattice site is strongly suppressed, and the low-energy physics can be described in terms of the spin degree of freedom. In this case, the ground state forms an FCI described by the CFT $\mathfrak{su}(2)_1$ like the bosonic Laughlin state at filling $\nu = 1/2$. For practical computations, the FCI ground state can be modeled using a Gutzwiller projection [105], which formally corresponds to the limit $U \to \infty$. In our publication of Ref. [3], we use this state as a benchmark for the application of the Gutzwiller projection to a 3D system (see Sec. 5.3).

Chapter 4

Entanglement in quantum many body systems

Over the past years, quantum entanglement has emerged as a crucial numerical and theoretical tool to diagnose and understand quantum many body systems. In the study of topological phases it allows to detect their underlying non-local correlations characteristic for the topological ordering. This can be applied both to the non-interacting SPT phases discussed in Chapter 2 and to the strongly correlated systems with intrinsic topological order discussed in Chapter 3. We begin in Sec. 4.1 with a brief review of the most important measures for quantum entanglement, the entanglement entropies, and their typical scaling laws for different quantum phases. We continue in Sec. 4.2 by discussing a more refined entanglement observable, the entanglement spectrum, and review its application to the SSH model, the CI model and the Laughlin state. Finally, in Sec. 4.3 we consider tensor network states, a class of model states which naturally incorporate the entanglement patterns required to efficiently encode many body quantum states.

4.1 Entanglement entropy

Quantum entanglement denotes the intrinsic correlations that may be present between different parts of a quantum system. For example, a system of two identical spin-1/2 particles which has total spin $S = 0$ is described by the spin-singlet state

$$|S = 0\rangle = \frac{1}{\sqrt{2}} \left[|\uparrow\rangle \otimes |\downarrow\rangle - |\downarrow\rangle \otimes |\uparrow\rangle \right]. \tag{4.1}$$

Here, $|\uparrow\rangle$ and $|\downarrow\rangle$ denote the eigenstates of S_z with $S_z|\uparrow\rangle = (1/2)|\uparrow\rangle$ and $S_z|\downarrow\rangle = (-1/2)|\downarrow\rangle$, and the first and second terms in the tensor product of Eq. (4.1) refer to the first and second spin, respectively. If only the first spin is measured, and found to be in the state $|\uparrow\rangle$, we know that the second spin is in the state $|\downarrow\rangle$, no matter how far the two spins are separated. In the spin-singlet state, the two spins are intrinsically correlated or entangled.

This should be contrasted to the situation if the system has total spin $S = 1$ and $S_z = 1$. In this case, the quantum state is $|S = 1, S_z = 1\rangle = |\uparrow\rangle \otimes |\uparrow\rangle$, which is a simple tensor product of states for the two spins. It is thus a separable quantum state without entanglement.

In this section, we discuss the entanglement entropies (EEs), which allow to systematically distinguish between the two extreme cases of the spin-singlet and the separable state. Applied to quantum ground states, the EEs obey scaling laws showing that different quantum phases possess specific entanglement patterns. We begin with the definition of the different EEs in Sec. 4.1.1, before reviewing their characteristic scaling for different quantum phases in Sec. 4.1.2.

4.1.1 Definition

In a quantum many body system, the amount of entanglement present between two subsystems $\mathcal{A}$ and $\mathcal{B}$ can be quantified using the entanglement entropies (EEs) (see Ref. [106] for a review). The more entanglement is present, the larger the value of the EE. The absence of entanglement is indicated by a vanishing EE. For simplicity, we assume in the following that the total system is in a pure quantum state $|\psi\rangle$ with $\langle\psi|\psi\rangle = 1$, and that $\mathcal{A}$ and $\mathcal{B}$ form a disjoint bi-partition of the system. The key object in the study of the entanglement between $\mathcal{A}$ and $\mathcal{B}$ is the reduced density matrix. The reduced density matrix $\rho_\mathcal{A}$ of the subsystem $\mathcal{A}$,

$$\rho_\mathcal{A} = \mathrm{Tr}_\mathcal{B}\left[\rho\right], \tag{4.2}$$

is obtained as the trace $\mathrm{Tr}_\mathcal{B}$ over the degrees of freedom in $\mathcal{B}$ of the density matrix $\rho = |\psi\rangle\langle\psi|$ of the total system. Similarly, the reduced density matrix $\rho_\mathcal{B}$ of the subsystem $\mathcal{B}$ is $\rho_\mathcal{B} = \mathrm{Tr}_\mathcal{A}\left[\rho\right]$, where we use the notation $\mathrm{Tr}_\mathcal{A}$ for the trace over the degrees of freedom in region $\mathcal{A}$.

Using the reduced density matrix, several EE measures can be defined. The most well-known measure is the von Neumann entropy

$$S_\mathcal{A}^{(vN)} = -\,\mathrm{Tr}_\mathcal{A}\left[\rho_\mathcal{A} \ln\left(\rho_\mathcal{A}\right)\right]. \tag{4.3}$$

Less well-known measures which are easier to evaluate numerically are given by the Renyi entropies of order n defined as

$$S_\mathcal{A}^{(n)} = \frac{1}{1-n} \ln\left(\mathrm{Tr}_\mathcal{A}\left[\rho_\mathcal{A}^n\right]\right). \tag{4.4}$$

In the limit $n \to 1$, $S^{(n)}$ corresponds to the von Neumann entropy. For the characterization of topological phases, the von Neumann and Renyi entropies are equally suited [107].

In practice, the EEs can be evaluated from the Schmidt decomposition of the pure state $|\psi\rangle$,

$$|\psi\rangle = \sum_i^D e^{-\xi_i/2} |v_i^\mathcal{A}\rangle \otimes |v_i^\mathcal{B}\rangle. \tag{4.5}$$

Here, $\{|v_i^{\mathcal{A}}\rangle\}_i$ and $\{|v_i^{\mathcal{B}}\rangle\}_i$ are orthonormal sets in the Hilbert spaces describing the degrees of freedom in $\mathcal{A}$ and $\mathcal{B}$, respectively. Therefore, the smallest of the dimensions of these two Hilbert spaces forms an upper bound on the number D of terms in the Schmidt decomposition. The non-negative numbers $e^{-\xi_i/2}$ are the Schmidt weights of the state $|\psi\rangle$. Since the norm of the state $|\psi\rangle$ is equal to unity, the Schmidt weights satisfy $\sum_{i=1}^{D} e^{-\xi_i} = 1$. As we will discuss below, the set of Schmidt weights of a quantum ground state often gives important information about its structure. Moreover, they determine the EEs of the state $|\psi\rangle$. Indeed, due to the orthonormality of the set $\{|v_i^{\mathcal{B}}\rangle\}_i$, the reduced density matrix $\rho_{\mathcal{A}}$ can be straightforwardly computed from Eq. (4.5) as

$$\rho_{\mathcal{A}} = \sum_{i=1}^{D} e^{-\xi_i} |v_i^{\mathcal{A}}\rangle\langle v_i^{\mathcal{A}}|. \tag{4.6}$$

The reduced density matrix $\rho_{\mathcal{B}}$ for the subsystem $\mathcal{B}$ is given by an analogous expression *w.r.t.* the basis $\{|v_i^{\mathcal{B}}\rangle\}_i$. Therefore, the spectra of both $\rho_{\mathcal{A}}$ and $\rho_{\mathcal{B}}$ are given by the set of the squared Schmidt weights $\{e^{-\xi_i}\}_i$. In terms of these eigenvalues, the von Neumann entropy is

$$S_{\mathcal{A}}^{(vN)} = \sum_{i=1}^{D} \xi_i e^{-\xi_i}, \tag{4.7}$$

and the Renyi entropies are given as

$$S_{\mathcal{A}}^{(n)} = \frac{1}{1-n} \ln \left(\sum_{i=1}^{D} e^{-n\xi_i} \right). \tag{4.8}$$

In particular, the EEs computed *w.r.t.* the subsystems $\mathcal{A}$ and $\mathcal{B}$ are identical.

Let us now illustrate these concepts using the example of the spin-singlet state of Eq. (4.1), where the subsystem $\mathcal{A}$ consists of only the first spin. The spin-singlet is already in Schmidt form, with Schmidt weights $e^{-\xi_i/2} = 1/\sqrt{2}$ for $i = 1, 2$ and orthonormal sets $|v_1^{\mathcal{A}}\rangle = |\uparrow\rangle$, $|v_2^{\mathcal{A}}\rangle = |\downarrow\rangle$, $|v_1^{\mathcal{B}}\rangle = |\downarrow\rangle$ and $|v_2^{\mathcal{B}}\rangle = -|\uparrow\rangle$. Hence, the reduced density matrix $\rho_{\mathcal{A}}$ is given by

$$\rho_{\mathcal{A}} = \frac{1}{2} \left[|\uparrow\rangle \otimes \langle\uparrow| + |\downarrow\rangle \otimes |\downarrow\rangle \right]. \tag{4.9}$$

Therefore, the associated von Neumann entropy is $S_{\mathcal{A}}^{(vN)} = \ln(2)$. It can be shown that the maximal value of the von Neumann entropy for a density matrix ρ with rank r is $S^{(vN)}(\rho) = \ln(r)$. As the Hilbert space of one spin has dimension 2, $S_{\mathcal{A}}^{(vN)} = \ln(2)$ is the maximal possible value for the EE between the two spins. The spin singlet is therefore also referred to as a maximally entangled state. On the other hand, for the separable state $|S = 1, S_z = 1\rangle = |\uparrow\rangle \otimes |\uparrow\rangle$, the reduced density matrix $\rho_{\mathcal{A}} = |\uparrow\rangle \otimes \langle\uparrow|$ has only a single eigenvalue 1, such that the EEs vanish. The EE therefore gives a systematic way to distinguish between the strongly entangled spin-singlet state, for which the EE takes the maximal possible value, and the separable state without entanglement, for which the EE is zero.

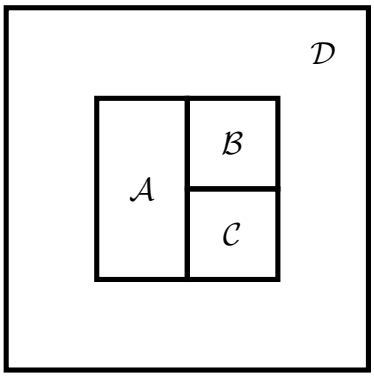

Figure 4.1: Sketch of the partition of a 2D square system into subsystems $\mathcal{A}$, $\mathcal{B}$, $\mathcal{C}$ and their complement $\mathcal{D}$ in a Kitaev-Preskill scheme. The TEE can be computed according to Eq. (4.12).

4.1.2 Area law for gapped quantum ground states

The ground states of gapped quantum many body systems follow an area law for the EE [108, 109]. For 1D systems, this has been proven [110], and it is conjectured for higher-dimensional systems [109]. The area law implies that the EE of a subsystem $\mathcal{A}$ scales with the size $|\partial\mathcal{A}|$ of its boundary rather than its volume $|\mathcal{A}|$ (which is the expected extensive scaling for a thermal system). Concretely, the EE is of the form

$$S_{\mathcal{A}} = \alpha \times |\partial\mathcal{A}| + o(|\partial\mathcal{A}|), \tag{4.10}$$

where α is a constant independent of the system size, but which can depend on the microscopic details of the system and thus does not carry any universal information on the quantum phase. Moreover, α may be different for the different EE measures. The second term in Eq. (4.10) stands for sub-leading corrections to the linear term, which can carry topological information [29, 30].

For example, strongly correlated systems with intrinsic topological order like the fractional quantum Hall systems discussed in Chapter 3 give rise to a constant correction $-\gamma$ to the area law with γ the topological entanglement entropy (TEE) [29, 30]. For 2D systems,

$$\gamma = \ln(\mathcal{D}), \tag{4.11}$$

where $\mathcal{D}$ is the total quantum dimension, which contains information about the anyonic excitations. The TEE provides an important, although non-unique, characterization of the topological order of a given system. For the Laughlin state at filling $\nu = 1/q$ discussed in Chapter 3, $\mathcal{D} = \sqrt{q}$ with q the total number of different elementary anyons. The total quantum dimension of a system with non-trivial topological order satisfies $\mathcal{D} \geq \sqrt{2}$. In numerical simulations on systems of finite size, the TEE can be evaluated using a Kitaev-Preskill or Levin-Wen subtraction scheme [29, 30]. To that end, the system is divided into

four regions $\mathcal{A}$, $\mathcal{B}$, $\mathcal{C}$ and $\mathcal{D}$ as sketched in Fig. 4.1. The EE of these regions and their unions can be collected into the linear combination

$$-\gamma = S^{(2)}_{\mathcal{ABC}} - S^{(2)}_{\mathcal{AB}} - S^{(2)}_{\mathcal{BC}} - S^{(2)}_{\mathcal{AC}} + S^{(2)}_{\mathcal{A}} + S^{(2)}_{\mathcal{B}} + S^{(2)}_{\mathcal{C}} \tag{4.12}$$

which cancels all area law terms and contributions from potential corners of the subsystems. We are employing such a scheme in our publication of Ref. [3] (see Sec. 5.3).

On the other hand, gapped systems of non-interacting fermions follow the area law with a vanishing TEE $\gamma = 0$ for subsystems with a smooth boundary, both in topologically trivial phases and in the SPT phases that we discussed in Chapter 2. Therefore, in this case the area law does not possess any corrections informing about the nature of their topological phase.

Gapless quantum systems with a divergent correlation length do not generally satisfy the area law. For instance, 1D critical systems like Luttinger liquids possess a logarithmic scaling of their EE [111, 94]. It can be shown that the EE of a single interval of length ℓ in a total system of length L satisfies

$$S_{\text{crit}}(\ell; L) = p \times c \times \ln\left[\frac{L}{\pi}\sin\left(\frac{\pi\ell}{L}\right)\right] + const. \tag{4.13}$$

Here, the constant correction is independent of ℓ and L. Moreover, p is a known numerical prefactor which depends on the boundary conditions of the system and the EE measure that is being used [111, 94]. For the von Neumann entropy and a system with PBC, $p = 1/3$. On the other hand, c denotes the central charge of the CFT describing the 1D critical system. The logarithmic scaling of the EE can therefore be used to measure the central charge for a given system in numerical computations. This is used in our publication of Ref. [3] (see Sec. 5.3).

4.2 Entanglement spectrum

In the previous section, we discussed the EEs, which provide information on how strongly two subsystems are entangled in a given quantum state. However, the EEs have limitations. For instance, the EE scaling in the bulk of non-interacting SPT phases contains no signature of their non-trivial phase. However, it is still possible to characterize these phases via quantum entanglement by making use of the entanglement spectrum (ES), which we discuss in this section. We begin in Sec. 4.2.1 with the definition of the ES. In Sec. 4.2.2 we review the single particle ES for non-interacting fermionic systems. To conclude, we discuss the ES for three systems we considered above, namely for the SSH model in Sec. 4.2.3, for the CI in Sec. 4.2.4 and for the Laughlin state on a disk in Sec. 4.2.5.

4.2.1 Definition

The ES applied to topological phases was first introduced in the context of the fractional QHE [31]. In contrast to the EE, which is a single number, the ES aims to take a more

detailed look at a system's entanglement structure by studying the full spectrum of the reduced density matrix $\rho_{\mathcal{A}}$. Since $\rho_{\mathcal{A}}$ is a positive matrix satisfying $\mathrm{Tr}_{\mathcal{A}}[\rho_{\mathcal{A}}] = 1$, we can write it in analogy to a thermal state as

$$\rho_{\mathcal{A}} = e^{-H_{\mathrm{ent}}}, \tag{4.14}$$

with the matrix H_{ent} denoted the entanglement Hamiltonian of $\rho_{\mathcal{A}}$. The ES is defined as the spectrum of the entanglement Hamiltonian. From the expression of Eq. (4.6) for the reduced density matrix $\rho_{\mathcal{A}}$, we see that the ES is given by the collection of real numbers $\{\xi_i\}_i$ and can therefore be directly read off from the Schmidt weights.

Since its introduction, the ES has been applied to a wide variety of quantum systems, including spin chains, strongly correlated topological phases and SPT phases, and has emerged as a crucial numerical tool for the study of these quantum phases (see Ref. [112] for a review). It was found that in many systems, the ES can reveal the structure of low-energy excitations. Depending on the nature of the bi-partition into subsystems, the ES informs about different kinds of excitations. For example, the subsystem $\mathcal{A}$ can be defined as a region in real space or in momentum space. The boundary $\partial\mathcal{A}$ is often referred to as a virtual cut of the total system, as opposed to a physical cut which leads to a system with OBC. If the virtual cut is a real-space cut, the ES reflects the low-energy edge excitations that would occur if the virtual cut were a physical edge of the subsystem. In the context of the fractional QHE it was shown that other kinds of virtual cuts can also inform about the fractional bulk excitations [113].

It should be stressed that the ES provides this information about the excitations from just the ground state wave function with PBC. No computation of higher-lying energy eigenstates or introduction of a physical boundary is required. This is especially useful in strongly interacting systems, where the diagonalization of the Hamiltonian is extremely difficult, or where the ground state is given in terms of a model wave function like the Laughlin state. All in all, the rich information contained in the ES combined with its numerical accessibility make it an extremely useful tool in the study of topological phases.

In many cases, the ES possesses well-defined quantum numbers which allow the separation of the full spectrum into different sectors corresponding to different values of the quantum numbers. Indeed, if the ground state of the total system is an eigenstate of a Hermitian operator $\mathcal{O}$, the density matrix ρ commutes with $\mathcal{O}$ such that $[\rho, \mathcal{O}] = 0$. We now consider the case where the symmetry can be written as a sum $\mathcal{O} = \mathcal{O}_{\mathcal{A}} + \mathcal{O}_{\mathcal{B}}$ of two terms $\mathcal{O}_{\mathcal{A}}$ and $\mathcal{O}_{\mathcal{B}}$ acting only on the subsystems $\mathcal{A}$ and $\mathcal{B}$, respectively. Then,

$$0 = \mathrm{Tr}_{\mathcal{B}}\left([\rho, \mathcal{O}_{\mathcal{A}}]\right) + \mathrm{Tr}_{\mathcal{B}}\left([\rho, \mathcal{O}_{\mathcal{B}}]\right) = [\rho_{\mathcal{A}}, \mathcal{O}_{\mathcal{A}}], \tag{4.15}$$

since the second term vanishes identically. This implies that the spectrum of H_{ent} can be labeled using the eigenvalues of $\mathcal{O}_{\mathcal{A}}$.

4.2.2 Single particle entanglement spectrum

We recall that in systems of free fermions (or more generally Gaussian systems), the many body Hamiltonian H is quadratic in the mode operators. It can therefore be expressed as

$$H = \sum_{i,j} h_{ij} c_i^\dagger c_j \tag{4.16}$$

with a matrix h whose spectrum is the single particle energy spectrum. In such systems, the entanglement Hamiltonian is also quadratic in the mode operators [114] and can be expressed in a completely analogous fashion as

$$H_{\text{ent}} = \sum_{i,j\in\mathcal{A}} h_{ij}^{\text{ent}} c_i^\dagger c_j \tag{4.17}$$

with a matrix h^{ent}. Here, the notation $i, j \in \mathcal{A}$ implies that the summation runs only over the degrees of freedom in the subsystem $\mathcal{A}$. The matrix h^{ent} is directly related to the correlation matrix

$$C_{ij}^{\mathcal{A}} = \langle\psi| c_i^\dagger c_j |\psi\rangle \tag{4.18}$$

of the degrees of freedom in $\mathcal{A}$. As before, $|\psi\rangle$ is the total quantum state of the system. Indeed, it can be shown that [114]

$$\left(C^{\mathcal{A}}\right)^T = \frac{1}{1 + e^{h^{\text{ent}}}}. \tag{4.19}$$

Therefore, the spectrum $\{\lambda_i\}_i$ of $C^{\mathcal{A}}$ is referred to as the single particle ES, where the eigenvalues lie in the range $0 \leq \lambda_i \leq 1$ [114].

Since the single particle ES determines the eigenvalues of the reduced density matrix $\rho_{\mathcal{A}}$, it also determines the EE. Concretely, for the von Neumann entropy one finds

$$S_{\mathcal{A}}^{(vN)} = -\sum_i \left[\lambda_i \log(\lambda_i) + (1-\lambda_i)\log(1-\lambda_i)\right]. \tag{4.20}$$

Eigenvalues $\lambda_i = 0$ or $\lambda_i = 1$ do not contribute to the sum in Eq. (4.20), since the function $x\log(x)$ vanishes at $x = 0, 1$. The single particle modes corresponding to these eigenvalues therefore have no entanglement *w.r.t.* the virtual cut and are fully supported in either the subsystem $\mathcal{A}$ or the subsystem $\mathcal{B}$. On the other hand, eigenvalues $\lambda = 1/2$ contribute the largest possible amount $\log(2)$ to the sum in Eq. (4.20), and therefore correspond to single particle modes which are maximally entangled *w.r.t.* the virtual cut.

For TIs, and more generally systems of free fermions, the single particle ES *w.r.t.* a virtual cut in real space reflects the single particle energy spectrum that would occur if the virtual cut were a physical boundary of the system [115]. In particular, gapless edge modes of SPT phases also occur in the single particle ES. We will now illustrate this correspondence using the two SPT phases discussed in Chapter 2, the SSH model and the CI model.

4.2.3 Single particle entanglement spectrum of the SSH model

Let us consider the SSH model from Sec. 2.2 on a chain with PBC and N unit cells. As sketched in Fig. 4.2(a), we partition the chain into a subsystem $\mathcal{A}$ consisting of the first L unit cells and its complement $\mathcal{B}$ consisting of the remaining $N - L$ unit cells. We want to compute the single particle ES of the SSH ground state *w.r.t.* to $\mathcal{A}$ in the two phases of the SSH model.

In the dimerized limits in the trivial and the topological phases obtained for $\delta = -1$ and $\delta = 1$, respectively, we can compute the single particle ES analytically. Indeed, in these limits the chain spits into N pairs of strongly coupled nearest-neighbour fermions, where each pair decouples from the rest of the chain. As a consequence, we can consider each pair independently from the rest of the chain. Let us denote by $c_1^\dagger$ and $c_2^\dagger$ the creation operators for the left and right fermion in one such pair. In the trivial dimerized phase, $c_1^\dagger = c_{A,j}^\dagger$ and $c_2^\dagger = c_{B,j}^\dagger$ for some unit cell $j \in \{0, \dots, N-1\}$, whereas in the topological dimerized phase, $c_1^\dagger = c_{B,j}^\dagger$ and $c_2^\dagger = c_{A,j+1}^\dagger$ (see Fig. 4.2(a)). The strongly coupled pair is described by the Hamiltonian

$$H_{\text{pair}} = c_1^\dagger c_2 + c_2^\dagger c_1. \tag{4.21}$$

The normalized ground state of the pair Hamiltonian H_{pair} is given by the state

$$|\psi_{\text{pair}}\rangle = \frac{1}{\sqrt{2}} \left[c_1^\dagger - c_2^\dagger\right] |0\rangle, \tag{4.22}$$

where $|0\rangle$ denotes the vacuum state.

As a preparation for computing the single particle ES, let us now derive the correlation matrix C of the ground state of the total system in the dimerized limits. The correlation matrix $C^{\mathcal{A}}$ for the subsystem from Eq. (4.18) is obtained by restricting C to the degrees of freedom in $\mathcal{A}$. Due to the dimerization of the SSH chain, the only non-vanishing elements of C are given by blocks of size 2×2 on the diagonal, which describe one decoupled pair of sites each. Every mode is part of exactly one such pair. The block C_{pair} of C describing the strongly coupled pair we considered above is

$$C_{\text{pair}} = \left(\langle\psi_{\text{pair}}|c_i^\dagger c_j|\psi_{\text{pair}}\rangle\right)_{i,j=1,2} = \frac{1}{2}\begin{pmatrix} 1 & -1 \\ -1 & 1 \end{pmatrix}, \tag{4.23}$$

with eigenvalues $\lambda = 0$ and $\lambda = 1$.

In order to obtain the contribution of the modes $c_1^\dagger$ and $c_2^\dagger$ to the single particle ES of the SSH model, we need to distinguish two cases. In the first case, both modes lie in the subsystem $\mathcal{A}$. Then, the correlation matrix C_{pair} of Eq. (4.23) forms a sub-block of the subsystem correlation matrix $C^{\mathcal{A}}$. As we discussed above, the two modes $c_1^\dagger$ and $c_2^\dagger$ decouple from the rest of the system, such that C_{pair} contains the only non-zero elements of $C^{\mathcal{A}}$ that involve the two modes. It therefore gives rise to two eigenvalues $\lambda = 0$ and $\lambda = 1$ in the single particle ES. As discussed below Eq. (4.20), these eigenvalues do not contribute any EE, which is expected since both modes are fully localised in the subsystem $\mathcal{A}$.

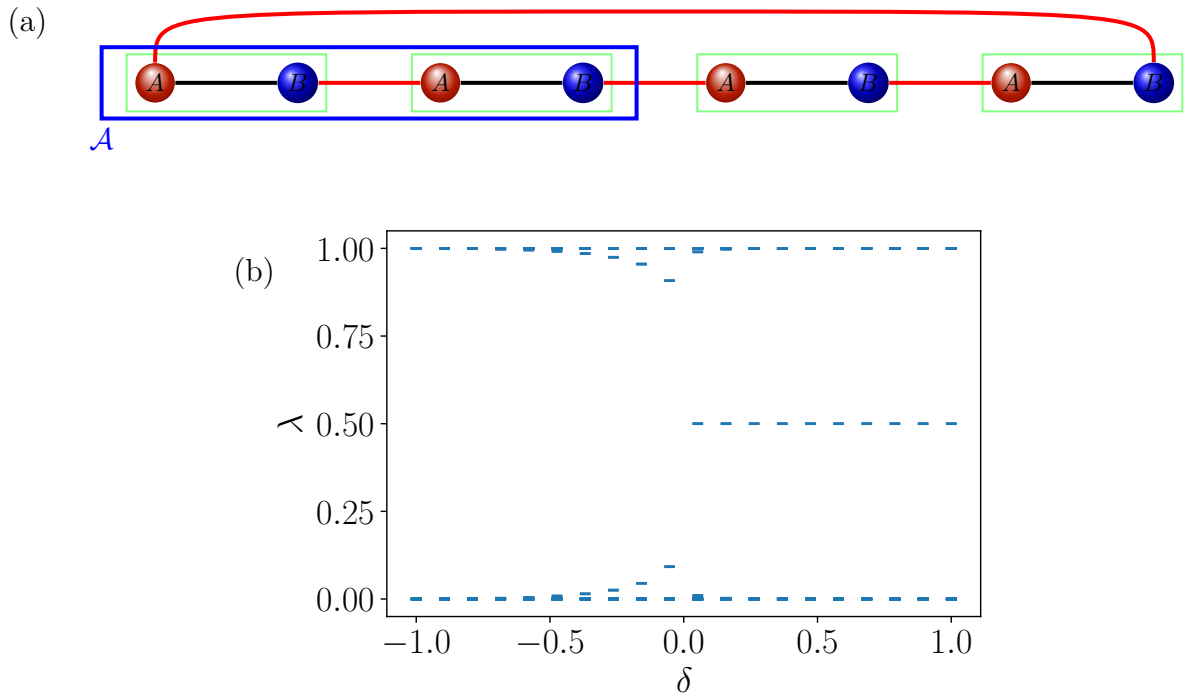

Figure 4.2: (a) Partition of an SSH chain with PBC and $N = 4$ unit cells into a subsystem $\mathcal{A}$ of the first $L = 2$ unit cells (marked in blue) and its complement. The virtual cut lies between the unit cells marked by green rectangles. Sketched in black and red are the non-zero couplings in the dimerized trivial phase at $\delta = -1$ and the dimerized topological phase at $\delta = 1$, respectively. In the dimerized topological phase, the virtual cut crosses two non-zero couplings, whereas this is not the case in the dimerized trivial phase. (b) Single particle ES of the SSH model on a chain with $N = 40$ unit cells and PBC *w.r.t.* the subsystem $\mathcal{A}$ of the first 20 unit cells, for several values of the dimerization δ ranging from $\delta = -1$ to $\delta = 1$. The two mid-gap levels for $\delta > 0$ are signatures of topological edge modes at the virtual edges of $\mathcal{A}$.

In the second case, only one of the two modes, denoted $c_i^\dagger$ for either $i = 0$ or $i = 1$, lies in the subsystem $\mathcal{A}$, whereas the second lies in the subsystem $\mathcal{B}$. This can occur only in the topological dimerized phase at the edges of $\mathcal{A}$. Then, the block $(C_{\text{pair}})_{ii}$ is the only part of $C^{\mathcal{A}}$ involving the mode i and therefore contributes an eigenvalue $\lambda = (C_{\text{pair}})_{ii} = 1/2$ to the single particle ES. In this case, the pair contributes strongly to the EE of $\mathcal{A}$, as expected since the virtual cut crosses the strong bond between the two modes.

At the fully dimerized point $\delta = -1$ in the trivial phase of the SSH model, there is no coupling between sites on different unit cells (see Fig. 4.2(a)). Therefore, no pair of coupled sites is separated by the virtual cut (which lies between unit cells) and only the first of the two cases above occurs. Hence, the single particle ES consists of L eigenvalues $\lambda = 0, 1$ and is fully gapped like the single particle energy spectrum for $\delta = -1$. On the

other hand, at the fully dimerized point $\delta = 1$ in the topological phase of the SSH model, the pairs of coupled sites are formed from sites of two adjacent unit cells (see Fig. 4.2(a)). Therefore, the virtual cut crosses the two bonds between sites $N-1$ and 0 and between sites $L-1$ and L. Each crossed bond corresponds to the second case discussed above, and contributes a level $\lambda = 1/2$ to the single particle ES. The other bonds inside the subsystem are not crossed by the virtual cut and contribute $L-1$ levels $\lambda = 0, 1$ as discussed above. Therefore, the single particle ES contains two mid-gap levels coming from the edges of $\mathcal{A}$, akin to the single particle energy spectrum of an *open* SSH chain defined on $\mathcal{A}$.

For other values of δ ranging from $\delta = -1$ to $\delta = 1$, the single particle ES of the SSH chain is shown in Fig. 4.2(b). For negative values of δ, the spectrum is fully gapped. On the other hand, for positive values of δ there are two to mid-gap levels close to the value $\lambda = 1/2$. Therefore, throughout the full parameter range the single particle ES computed from the ground state with PBC resembles the single particle energy spectrum for an SSH chain with OBC. This is an instance of the bulk boundary correspondence for topological phases, where the bulk ground state with PBC reflects the boundary spectrum in its ES.

Correspondingly, the single particle ES *w.r.t.* the subsystem $\mathcal{A}$ in the topological dimerized phase of a chain with OBC contains a single mid-gap state from the virtual cut in the bulk. In this case, the single particle ES does not depend on the Fermi energy level as long as it lies in the bulk gap. In particular, the ES is the same no matter if the physical boundary modes are empty or occupied.

4.2.4 Single particle entanglement spectrum of the Chern insulator

Let us now compute the ES for the CI model discussed in Sec. 2.3. We consider the cylinder geometry sketched in Fig. 4.3(a) with PBC in the x direction and OBC in the y direction. As subsystem $\mathcal{A}$ we choose the lower half of the cylinder, *i.e.* all sites with $0 \leq y \leq N_y/2 - 1$, such that $\mathcal{A}$ preserves translation invariance in the x direction. This subsystem possesses one virtual edge in the physical bulk, which is parallel to the physical edges. Based on the discussion of the single particle ES of the SSH model with OBC, we expect this virtual edge to cause one chiral edge mode in the ES.

The single particle ES in the topological phase of the CI model is shown in Fig. 4.3(b) as a function of the conserved momentum k_x. As expected, there is a single chiral edge mode associated with the virtual edge. The appearance of the chiral mode in the ES does not depend on the Fermi level, as long as it lies in the bulk energy band gap.

The CI model can be driven into a topologically trivial phase by the addition of a sufficiently strong staggered chemical potential μ which is μ on A sites and $-\mu$ on B sites (see also our publication of Ref. [3] reprinted in Sec. 5.3). In Fig. 4.3(c) we show the single particle ES of the ground state in this phase. There is no chiral edge mode, and the two bands in the ES are not connected.

Therefore, virtual edges lead to chiral modes in the single particle ES if and only if the model is in a topologically non-trivial phase. The chiral modes in the ES of the bulk

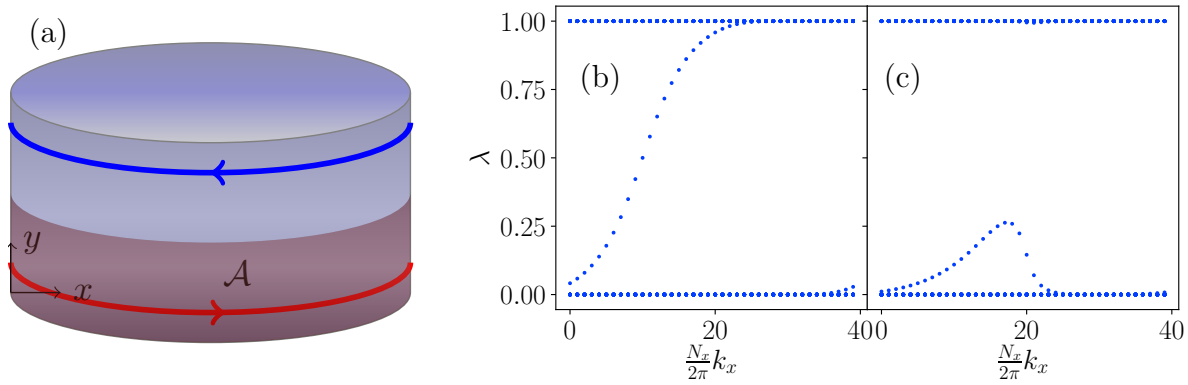

Figure 4.3: (a) Computation of the ES on the cylinder with PBC in the x direction and OBC in the y direction. The subsystem $\mathcal{A}$ marked in red consists of the lower half of the cylinder, *i.e.* all sites with $0 \leq y \leq N_y/2 - 1$ and preserves translation invariance in the x direction. (b) and (c) Single particle ES of the CI model with parameters $t = 1$ and $\Delta = 1/2$ for a system of 40×40 unit cells in the geometry sketched in (a). The spectrum is shown as a function of k_x. (b) Single particle ES in the topologically non-trivial phase of the CI model. The single chiral edge mode is due to the virtual edge of the subsystem $\mathcal{A}$. (c) Single particle ES in a trivial phase generated by addition of a strong staggered chemical potential $\mu = 2.5$ (see text). The spectrum is gapped without a mode connecting the two bands.

ground state reflect the chiral edge modes in the single particle energy spectrum created by physical edges. This exemplifies the bulk boundary correspondence for the CI model.

4.2.5 Entanglement spectrum of the Laughlin state

As a final example, let us now consider the Laughlin states for the fractional QHE, which we discussed in Chapter 3. Since these are strongly interacting systems, their entanglement Hamiltonian is not quadratic in mode operators. Hence, there is no single particle ES and we need to rely on the many body ES $\{\xi_i\}_i$.

For convenience, we consider a an infinitely long cylinder with OBC in the x direction, and a finite radius L_y and PBC in the y direction. The single particle eigenfunctions and Laughlin states in this geometry can be defined analogously to those on the disk [49]. We focus on the ES *w.r.t.* a real-space partition of the cylinder into a region $\mathcal{A}$ with $x > 0$ and its complement with $x < 0$. The dominant levels in the ES of the Laughlin state at filling $\nu = 1/2$ are shown as a function of the conserved many body momentum K_y in Fig. 4.4. These levels display a chiral dispersion with the same state counting as the edge modes, namely that of a chiral free-boson CFT given in Eq. (3.17). The exact degeneracy of the levels at the same momentum is lifted due to finite-size effects. This demonstrates the bulk boundary correspondence for the ES in chiral phases with intrinsic topological order, where the ES computed from the bulk ground state gives access to the gapless edge energy

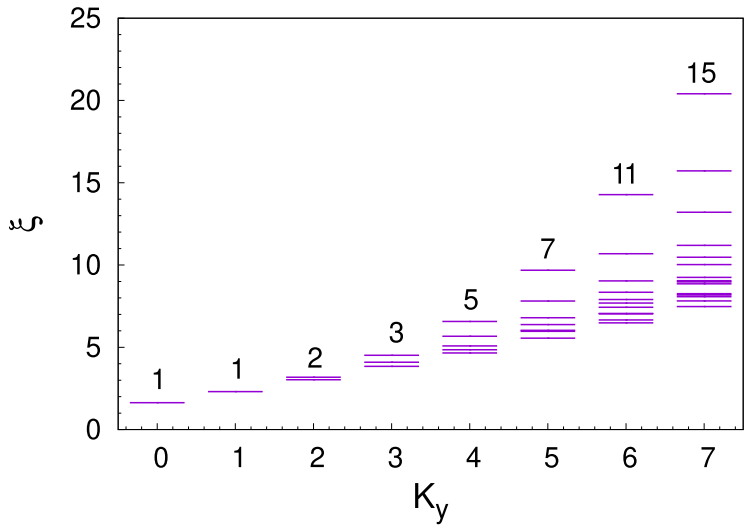

Figure 4.4: Dominant levels in the real-space ES of the Laughlin state at filling $\nu = 1/2$. We consider an infinitely long cylinder with OBC in the x direction, and a finite radius $L_y = 17l_0$ and PBC in the y direction. The spectrum is shown as a function of the conserved many body momentum K_y.

spectrum.

4.3 Tensor network states

In Sec. 4.1.2 we saw that gapped quantum ground states obey an area law for the EE. In this section we give a brief review of tensor network states (TNS) (see Ref. [116] for a review), a class of ansatz states that naturally incorporate the area law. This makes them good candidates for modeling physically relevant quantum states [117]. TNS can be seen as natural generalizations of trivial product states and allow thus a very efficient encoding of quantum many body states. They for the basis for extremely successful variational algorithms [32, 33, 34, 35, 118]. TNS are defined in terms of local building blocks that mediate the entanglement between physical constituents using virtual particles. Hence, they elucidate the entanglement patterns underlying quantum ground states and have thereby helped to understand topological phases with [36] and without [37] strong correlations.

Here, we focus on 1D matrix product states (MPS) [119, 120] and 2D projected entangled pair states (PEPS) [40]. We begin in Sec. 4.3.1 by explaining the construction of these TNS in terms of local tensors. In Sec. 4.3.2 we then show that TNS obey the area law and discuss the version of the bulk boundary correspondence applicable to TNS. Finally, in Sec. 4.3.3 we briefly review the role of symmetries in the TNS framework, and the capacity of TNS to describe different topological phases.

4.3.1 Definition

TNS are model states for quantum systems on a lattice with a finite-dimensional physical Hilbert space per lattice site. Typically, the lattice lies in real space, but TNS defined on lattices in momentum space [121] or orbital spaces [122] have also been constructed. Here we focus on bosonic TNS, for which the physical degrees of freedom are either spins or hard-core bosons. It is also possible to construct TNS for fermionic particles [123, 124] as we did in our publication of Ref. [2]; such TNS are reviewed in great detail there (see Sec. 5.2). A TNS is obtained by associating virtual particles to each physical site, which mediate the entanglement between different physical constituents. For bosonic TNS, the virtual particles obey bosonic statistics.

For a 1D MPS defined on a chain of length N we associate two virtual Hilbert spaces, denoted the left and right virtual space, to each lattice site $j \in \{0, \dots, N-1\}$. They are responsible for encoding the correlations of the physical particle with its left and right neighbors, respectively. The left and right virtual space have orthonormal bases $\{|l\rangle\}$ and $\{|r\rangle\}$, respectively, with $l, r = 0, \dots, D-1$. The dimension D of the virtual spaces is referred to as the bond dimension. For simplicity we only consider uniform TNS which have the same bond dimension for every virtual space, although more general states can be constructed. We denote by $\{|i\rangle\}$ with $i = 0, \dots, d-1$ an orthonormal basis for the physical Hilbert space with dimension d. The MPS is defined by the set of local tensors

$$A[j]^i_{lr} \tag{4.24}$$

which relate the virtual and physical particles associated to each lattice site j. For a fixed physical index i, the local tensors can be interpreted as matrices $(A[j]^i)_{lr}$ of dimension $D \times D$. Graphical representations of TNS are often very useful. In this language, the local MPS tensor is represented as shown in Fig. 4.5 by an object with three open legs, corresponding to the physical and the two virtual indices, respectively.

The many body quantum state $|\psi\rangle$ defined by the MPS is given by a linear combination of product states of the physical degrees of freedom

$$|\psi\rangle = \sum_{i_0,\dots,i_{N-1}=0}^{d-1} c_{i_0,\dots,i_{N-1}} \left[|i_0\rangle \otimes \cdots \otimes |i_{N-1}\rangle\right], \tag{4.25}$$

where $|i_j\rangle$ denotes the basis state $|i\rangle$ on the lattice site j. The coefficients $c_{i_0,\dots,i_{N-1}}$ in the expansion are obtained by contracting the local MPS tensors for all lattice sites. As indicated by the term MPS, in a 1D system this contraction can be expressed as a product of the corresponding local matrices for fixed physical indices,

$$c_{i_0,\dots,i_{N-1}} = \mathrm{Tr}\left[A[0]^{i_0} \cdots A[N-1]^{i_{N-1}}\right]. \tag{4.26}$$

Here, we assumed PBC for the chain and the trace acts on the left and right virtual spaces on sites $j = 0$ and $j = N-1$, respectively. In the graphical notation, the coefficient $c_{i_0,\dots,i_{N-1}}$ is represented as in Fig. 4.5(b) by connecting the virtual legs of different local tensors which are contracted.

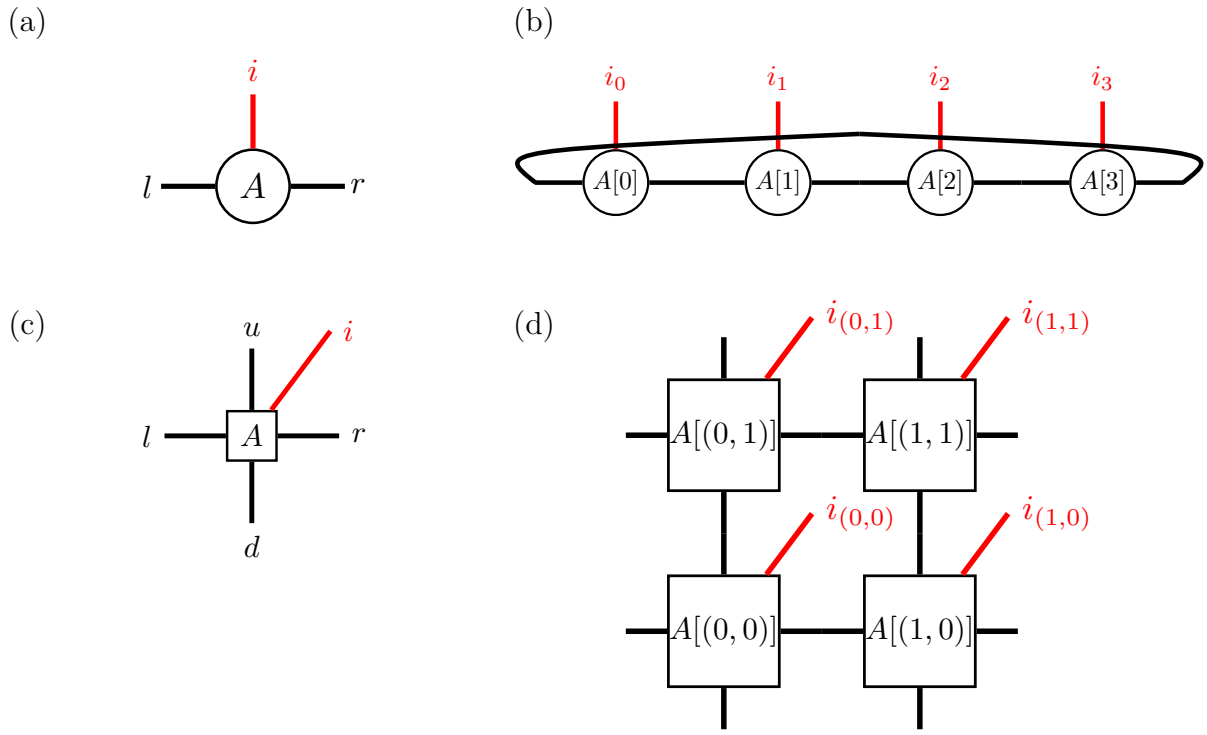

Figure 4.5: Graphical notation for TNS. (a) Local MPS tensor A with physical index i, left virtual index l and right virtual index r. (b) Contraction of several MPS tensors on a periodic chain with four sites. (c) Local PEPS tensor with physical index i, left virtual index l, up virtual index u, right virtual index r and down virtual index d. (d) Contraction of several PEPS tensors.

Similarly, 2D PEPS on the square lattice are constructed by associating four virtual spaces of bond dimension D to each site, which encode the correlations in the left, up, right and down directions. We use the same notations as above for the left and right virtual space and the physical space. The up and down virtual spaces have orthonormal bases $\{|u\rangle\}$ and $\{|d\rangle\}$, respectively, with $u, d = 0, \ldots, D-1$. The PEPS is defined by the collection of local five-index tensors

$$A[(x,y)]^{i}_{lurd} \tag{4.27}$$

for each lattice site at position (x, y). In the graphical notation, the PEPS local tensor corresponds as shown in Fig. 4.5(c) to an object with five open legs. The coefficients of the physical many body basis states are obtained by contracting the virtual indices of all local tensors (see Fig. 4.5(d) for the corresponding graphical representation). Due to the 2D space, this contraction is of much higher complexity [125] and can in general no longer be expressed as a matrix product.

MPS and PEPS are local model states which are fully defined by the set of local tensors for all lattice sites. Indeed, it can be shown that they possess parent Hamiltonians with

local interactions for which they are the exact ground states [119]. Due to their definition in terms of finite-dimensional local tensors, TNS are also very simple in the sense that they contain few variational parameters. For example, a 1D MPS with bond dimension D for a chain with N sites is determined by a polynomial number of ND^2d complex parameters. On the other hand, a generic quantum state in this physical Hilbert space is specified by an exponential number d^N of complex many body coefficients. Therefore, TNS with small bond dimension allow an extremely numerically efficient encoding of a many body quantum state.

Every many body quantum state in a finite-dimensional system can be expressed as a TNS with sufficiently large bond dimension. The usefulness of a TNS representation is the greatest when the bond dimension can be chosen small and in particular independent from the system size. As we will motivate now, whether or not a given quantum state admits such an efficient (approximate) TNS representation depends crucially on its entanglement structure [120].

4.3.2 Area law and entanglement spectrum

Let us consider an MPS defined on a periodic chain with N sites, which is partitioned into a subsystem $\mathcal{A}$ consisting of the first L sites $j = 0, \ldots, L-1$, and its complement. Due to the form of the MPS many body coefficients of Eq. (4.26), the state from Eq. (4.25) can be expressed as

$$|\psi\rangle = \sum_{l,r=0}^{D-1} |v(l,r)\rangle \otimes |w(r,l)\rangle \tag{4.28}$$

where

$$|v(l,r)\rangle = \sum_{i_0,\ldots,i_{L-1}=0}^{d-1} \left(A[0]^{i_0} \cdots A[L-1]^{i_{L-1}}\right)_{lr} \left[|i_0\rangle \otimes \cdots \otimes |i_{L-1}\rangle\right], \tag{4.29}$$

$$|w(r,l)\rangle = \sum_{i_0,\ldots,i_{L-1}=0}^{d-1} \left(A[L]^{i_L} \cdots A[N-1]^{i_{N-1}}\right)_{rl} \left[|i_L\rangle \otimes \cdots \otimes |i_{N-1}\rangle\right]. \tag{4.30}$$

This expression looks very similar to the Schmidt decomposition of Eq. (4.5). The D^2 terms originate from the possible configurations of the left virtual index of site 0 and the right virtual index of site $L-1$. As sketched in Fig. 4.6(a) these are the virtual indices of sites in $\mathcal{A}$ which cross the subsystem boundary.

In fact, Eq. (4.28) is not yet a Schmidt decomposition of the MPS because the states $|v(l,r)\rangle$ and $|w(r,l)\rangle$ are in general not orthonormal. Nonetheless, choosing an orthonormal basis from the spaces spanned by these states can only reduce the number of terms in the decomposition. Hence, the number of terms in the Schmidt decomposition of the MPS or equivalently the rank of its reduced density matrix $\rho_{\mathcal{A}}$ is at most equal to D^2. The von Neumann entropy of a reduced density matrix of rank r is at most equal to $\ln(r)$.

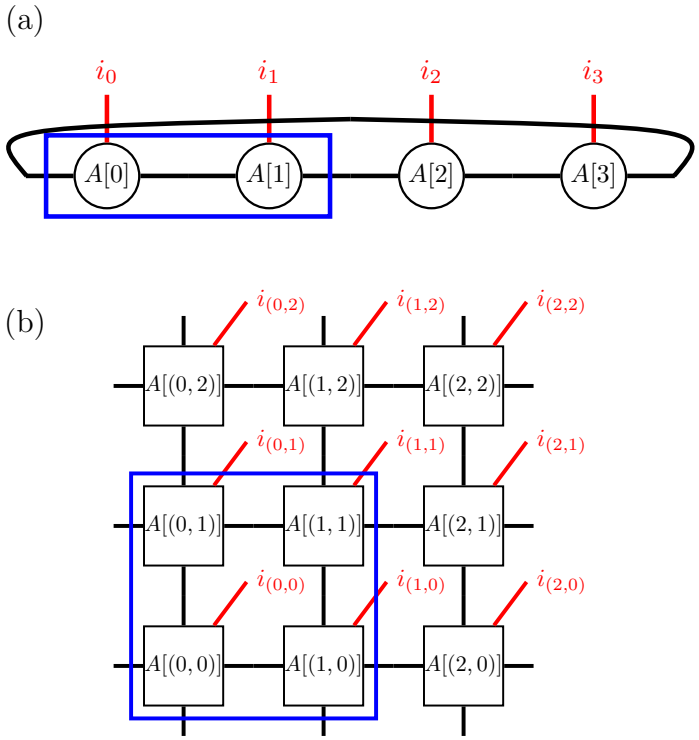

Figure 4.6: Restriction of an MPS in (a) and a PEPS in (b) to a subsystem $\mathcal{A}$ marked in blue. As explained in the text, the Hilbert space of the virtual legs of the TNS which are crossed by the boundary of $\mathcal{A}$ carries a boundary theory that can be used to compute the ES.

Therefore, the EE of the MPS satisfies

$$S^{(vN)}(\rho_{\mathcal{A}}) \leq 2\ln(D) \tag{4.31}$$

and is therefore bounded by the logarithm of the bond dimension irrespective of the size of $\mathcal{A}$. This implies that MPS with a constant bond dimension satisfy a 1D area law for the EE. Hence, they are good model states for ground states of 1D gapped Hamiltonians with exponentially decaying correlation functions. Indeed, the extremely successful density matrix renormalization group algorithm [32] can be understood in modern terms as a variational algorithm over MPS [33].

On the other hand, MPS with a constant D cannot exactly represent gapless critical models like Luttinger liquids due to their logarithmic EE scaling from Eq. (4.13). However, by increasing the bond dimension, critical states can be approximated with MPS to arbitrary precision [33]. Indeed, Eq. (4.31) implies that the bond dimension D of an MPS for a critical state with $S^{(vN)}(\rho_{\mathcal{A}}) \propto \ln(L)$ should grow as $D^2 \propto N$. Therefore, the number of complex parameters dN^3 of this MPS grows polynomially in the system size, rather than the exponential number d^N for a generic quantum state. Hence, MPS offer an extremely efficient encoding even for critical quantum states.

For 2D PEPS, an analogous argument can be made. The number of terms in the Schmidt decomposition of a given PEPS is at most equal to D to the power of the number of virtual legs crossed by the subsystem boundary. As sketched in Fig. 4.6, the number of these legs is equal to the length $|\partial\mathcal{A}|$ of the boundary of the subsystem (in units of the lattice spacing). Therefore, the EE of a PEPS is bounded as

$$S^{(vN)}(\rho_{\mathcal{A}}) \leq |\partial\mathcal{A}| \ln(D) \tag{4.32}$$

and obeys a 2D area law with the linear coefficient α from Eq. (4.10) determined by the logarithm of the bond dimension.

From Eq. (4.28) it is clear that the virtual particles at the boundary of the subsystem $\mathcal{A}$ play a decisive role in the Schmidt decomposition. They generate a set of non-orthonormal states from which the orthonormal Schmidt bases are chosen. Due to the close relation between the Schmidt decomposition and the ES (see Sec. 4.2.1), the virtual particles at the boundary can also be used to compute the ES of the TNS. Indeed, it is possible to construct an operator acting on the Hilbert space of the virtual boundary particles whose spectrum gives access to the many body ES [126]. This is referred to as the bulk boundary correspondence for TNS. For MPS on an infinite open chain and for PEPS on an infinitely long cylinder with a finite circumference, the bulk boundary correspondence allows the efficient computation of the many body ES [126]. For a more detailed review including technical details, see our publication of Ref. [1] reprinted in Sec. 5.1.

4.3.3 Symmetries

Local symmetries such as spin rotations and point group symmetries such as mirror operations have intuitive representations in the TNS formalism. For many MPS and PEPS, such physical symmetries correspond to symmetries of the local tensor involving both the physical and the virtual degrees of freedom. In Fig. 4.7 we show the example of a local symmetry acting by a unitary linear transformation U on a given site. For the local tensor A of a TNS which is invariant under this symmetry, the physical symmetry action can equivalently be expressed as the action of linear representations U_v on the virtual degrees of freedom. This understanding has led to crucial analytical results such as the classification of 1D bosonic SPT phases using MPS [37] as well as decisive speed-ups for numerical simulations [127].

An important role is played by virtual symmetries of local tensors, whose action on the physical leg is trivial. Such virtual symmetries can be used to encode intrinsic topological order in PEPS [36]. The virtual symmetries then give direct access to characteristic properties of the topological phase such as the ground state manifold, the TEE and anyonic excitations. Indeed, ground states of many models with non-chiral topological order such as Kitaev's toric code [14] or string-net models [128] have exact representations in terms of PEPS with a low bond dimension [38, 39].

The description of 2D chiral topological systems such as a non-interacting CIs or interacting FCIs with TNS is much more subtle. On one hand, PEPS with a finite bond

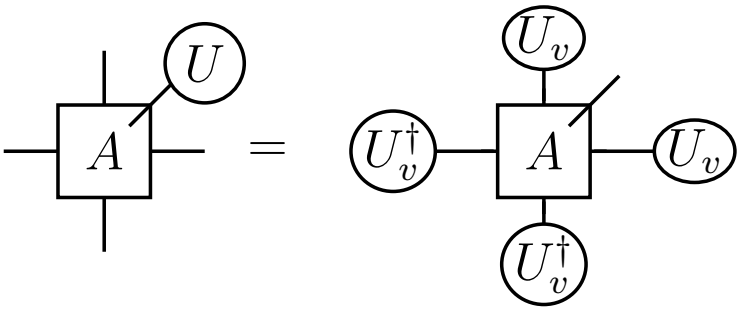

Figure 4.7: Local symmetry acting by a unitary linear transformation U on the physical leg of a PEPS tensor, which is equivalent to the action of linear maps U_v acting on the virtual legs.

dimension and features of chiral topological phases have been constructed. For example, there are PEPS for non-interacting fermionic systems which possess a non-zero Chern number and a matching chiral ES [41, 42, 43]. Their local tensors possess a virtual symmetry which can be related to the chiral edge mode [42]. On the other hand, these TNS are ground states of Hamiltonians with algebraically decaying interaction terms. Hence, they possess *algebraic* instead of exponentially decaying correlation functions and hence cannot be the ground states of gapped local Hamiltonians. Indeed, it has been proven in a no-go theorem [43, 48] that PEPS with a finite bond dimension cannot exactly represent gapped free-fermionic SPT phases.

Similarly, there are examples of interacting PEPS with features of chiral intrinsic topological order. These are constructed either by Gutzwiller projection of several copies of non-interacting chiral PEPS [44], or else from local tensors which transform under time reversal and mirror operations in a specific representation [45, 46, 47]. Such PEPS exhibit chiral ES, but also algebraically decaying correlation functions in the bulk as opposed to the exponentially decaying correlators expected for gapped phases. Indeed, it has been argued on general grounds that no interacting chiral PEPS can be the ground state of a gapped and local Hamiltonian [129]. Nonetheless, it is expected that PEPS can still serve as a numerically efficient approximate description for chiral topological phases.

Chapter 5

Publications

During my thesis, I carried out three main projects studying the entanglement signatures of different chiral topological phases. This chapter contains the reprints of the publications resulting from these projects.

In the preceding three chapters we discussed that chiral topological phases, in particular those with intrinsic topological order, give rise to fascinating phenomena that are potentially relevant for applications in quantum computing. Due to the strong correlations required for the realization of such phases, they are very difficult to study analytically and numerically. Therefore, representations using the numerically efficient tool of TNS are highly desirable. However, the nature of chiral topological phases prevents exact PEPS representations with a finite bond dimension. While there are PEPS with typical features of chiral topological phases such as a non-zero Chern number or a chiral ES, these states have algebraic bulk correlation functions. My first two projects focused on the question of how well chiral topological phases can be described approximately with PEPS.

In Sec. 5.1 we study a PEPS on the square lattice with a chiral ES reminiscent of $\mathfrak{su}(2)_1$ CFT [45, 46]. Using a careful analysis of the compatibility between the different symmetries imposed on its local tensor, we are able to explain and partially resolve some discrepancies between the ES of the PEPS and the CFT spectrum. This highlights that PEPS with a finite bond dimension can correctly reproduce certain properties of chiral topological phases despite the algebraically decaying bulk correlations.

In Sec. 5.2, we aim to give an intuitive example for the impossibility to represent a chiral topological phase exactly with a PEPS of finite bond dimension. Since the obstruction appears already for non-interacting phases, we focus on the 2D CI and a 3D HOTI with chiral hinge states. These phases can be obtained by a charge pumping interpolation of the 1D SSH model and the 2D topological quadrupole model, respectively. Using exact TNS representations of the latter two states, we construct hybrid TNS with a finite bond dimension for the CI and the 3D HOTI, where one dimension corresponds to momentum space. We show that the associated real-space TNS have an infinite bond dimension in one direction, corresponding to the non-locality of the inverse Fourier transform.

Finally, in Sec. 5.3 we revisit the 3D HOTI with chiral hinge states. We construct a wave function for a strongly correlated 3D HOTI by a Gutzwiller projection of two copies

of this state, analogous to the construction of an FCI from a CI discussed in Sec. 3.5. We show using large-scale variational Monte Carlo computations of the EE that this state has chiral hinge states of the same nature as the edge states of a Laughlin state at filling $\nu = 1/2$. We also study the bulk properties, and show that the gapped surfaces host a 2D topologically non-trivial theory whose TEE cannot be explained using topological quantum field theory.

5.1 Interplay of SU(2), point group, and translational symmetry for PEPS

This section contains a reprint of the following publication:

- Anna Hackenbroich, Antoine Sterdyniak, and Norbert Schuch. "Interplay of SU(2), point group, and translational symmetry for projected entangled pair states: Application to a chiral spin liquid". In: *Phys. Rev. B* 98 (8 Aug. 2018), p. 085151

In this publication, we study a PEPS for spin-1/2 particles on the square lattice. This TNS breaks time reversal symmetry explicitly. It is constructed in such a way that mirror operations act by a complex conjugation, akin to the application of time reversal [45, 46]. It was shown in previous publications that this state has chiral features similar to a spin liquid in the same phase as the FCI we discussed in Sec. 3.5 [45, 46]. It is thus expected to be described by the free boson CFT $\mathfrak{su}(2)_1$, which we reviewed in Sec. 3.3.4. However, certain discrepancies between the chiral ES of the PEPS and the expected spectrum of the CFT $\mathfrak{su}(2)_1$ were also observed.

The chiral PEPS has several physical symmetries including spin SU(2) rotation, the point group symmetries of the square lattice and translation symmetry with respect to a possibly enlarged unit cell. As we discussed in Sec. 4.3.3, these physical symmetries are reflected as symmetries of the local tensor. Here we investigate how the interplay of these symmetries determines which symmetry representations are allowed for the local tensor. Using the bulk boundary correspondence for TNS discussed in Sec. 4.3.2, we then show the consequences of this interplay for the ES of the PEPS on an infinite cylinder. As reviewed in Chapter 3 and Chapter 4, the ES is expected to reflect the gapless edge spectrum at physical boundaries of the system, which in turn should be described by the chiral CFT $\mathfrak{su}(2)_1$. Our results explain the discrepancies that had been observed between the ES of the PEPS and the CFT spectrum. Moreover, in a certain parameter region where the PEPS possesses an additional U(1) symmetry we can resolve these discrepancies and obtain an ES with the expected state counting of Eq. (3.17) and conformal weight $h = 1/4$ for the half-integer spin sector.

Interplay of SU(2), point group, and translational symmetry for projected entangled pair states: Application to a chiral spin liquid

Anna Hackenbroich, Antoine Sterdyniak, and Norbert Schuch
Max-Planck-Institute of Quantum Optics, Hans-Kopfermann-Str. 1, D-85748 Garching, Germany

(Received 18 May 2018; revised manuscript received 2 August 2018; published 29 August 2018)

Projected entangled pair states (PEPS) provide exact representations for many nonchiral topologically ordered states whereas their range of applicability to interacting chiral topological phases remains largely unsettled. In this context, the symmetries of the local PEPS tensors are crucial for determining the characteristic topological features of the state. In this paper we examine the constraints that arise when different symmetries are imposed simultaneously on the local tensor such as internal SU(2), point group, and translation symmetry. We show how the interplay of these symmetries manifests in the entanglement spectrum which is the main diagnostic tool for chiral topological order. We apply our results to a spin liquid PEPS introduced previously as a chiral generalization of the resonating valence bond state. Our findings explain the discrepancies observed between the entanglement spectrum of this state and the expected edge spectrum described by a chiral conformal field theory. Finally, in a certain parameter region where this PEPS possesses an additional $U(1)$ symmetry we are able to resolve these discrepancies and obtain an entanglement spectrum with the expected state countings and conformal weight.

DOI: 10.1103/PhysRevB.98.085151

I. INTRODUCTION

Topological phases are the most prominent examples of phases of matter that cannot be understood in terms of symmetry breaking and local order parameters. In the strongly interacting regime, topological order can develop where the system hosts free anyonic bulk excitations [1,2]. While global symmetries may naively seem to play a smaller role for topological than for symmetry-broken phases, they are crucial for determining the different phases a system can realize as exemplified by the classification of free-fermionic [3,4] and one-dimensional symmetry-protected [5–7] topological phases. Indeed, chiral topologically ordered phases [8] possessing gapless edge modes described by chiral conformal field theory (CFT) can only appear in the absence of time reversal symmetry. They have been observed in the paradigmatic example of the fractional quantum Hall effect [1,9] and were predicted to emerge in spin systems [10–12].

In the last decades, entanglement has emerged as a key probe for strongly correlated topological phases [13–15]. The entanglement patterns characteristic for systems with local interactions at zero temperature [16] are accurately captured by tensor network states [17] such as matrix product states (MPS) [18] in one dimension and projected entangled pair states (PEPS) [19] in two dimensions. These variational states are defined in terms of local building blocks that mediate the entanglement between physical constituents through virtual particles. Crucially, they permit both analytical understanding [6] and numerically efficient algorithms [20–22]. In one dimension, variational algorithms approximating ground states with tensor network states are extremely successful even for critical systems [20] and algorithms based on PEPS have nowadays become competitive also in two dimensions [23].

Despite their local structure, PEPS capture the physics of nonchiral topological order in a very simple and elegant manner. Indeed, ground states of many models with nonchiral topological order such as Kitaev's toric code [24] or string-net models [25] have exact representations in terms of simple PEPS [26,27]. In these examples, topological order is encoded locally in the PEPS through symmetries of the virtual degrees of freedom [28]. These virtual symmetries give direct access to characteristic properties of the topological phase such as the ground state manifold, topological entanglement entropy, and fusion rules.

In contrast, the application of the PEPS framework to chiral topological phases remains one of the open challenges in the field. It is known that Gaussian, i.e., free fermionic, PEPS can possess a nonzero Chern number [29–31]. However, they exhibit algebraically decaying correlation functions as was proven in a no-go theorem [31,32], implying that PEPS cannot exactly represent gapped chiral free-fermionic topological phases. As this no-go theorem does not apply to interacting PEPS, it is still unclear whether gapped chiral PEPS with intrinsic topological order exist. The two examples known to date are gapless: Firstly, in Ref. [33], a PEPS possessing the chiral CFT $\mathfrak{u}(1)_4$ as an edge theory was obtained by applying a Gutzwiller projection to two copies of a chiral Gaussian PEPS. Secondly, a chiral spin-liquid PEPS was constructed in Refs. [34,35] as a generalization of the square lattice resonating valence bond (RVB) state [36–39] with long-range singlets and complex amplitudes. The entanglement spectrum (ES) of this PEPS resembles the spectrum of the chiral CFT $\mathfrak{su}(2)_1$ which is the edge spectrum of the bosonic Laughlin state at filling fraction $1/2$. However, certain discrepancies were observed between the PEPS entanglement spectrum and the CFT spectrum such as mismatching conformal weights and state countings whose origin could not be resolved.

In the quest for PEPS representations of chiral topologically ordered states, the study of symmetries and their interplay

 ©2018 American Physical Society

is of particular importance: Chiral spin liquids are invariant under multiple symmetries such as spin rotations, spatial rotations, and translations. Moreover, their idealized instances transform equivalently under reflections and time reversal symmetry. For injective MPS and PEPS it is known that a given physical symmetry has to be represented locally on the virtual degrees of freedom [40,41]. This understanding has led to crucial analytical results such as the classification of one-dimensional symmetry protected topological phases [6] as well as decisive speed-ups for numerical simulations [42]. However, it has not been investigated systematically how multiple symmetries, for example spatial and internal transformations, can be implemented simultaneously and whether this leads to nontrivial constraints intrinsic to the PEPS formalism.

In this paper we analyze systematically the interplay of SU(2), translation, and point group symmetry for PEPS and then focus on the case of the chiral spin liquid PEPS which possesses an additional nonunitary symmetry, namely reflection combined with time reversal. First, we show that for half-integer physical spins one cannot simultaneously impose invariance under spin rotations, spatial rotations, and single site translation at the level of the local tensor. The states obtained from local tensors satisfying either translation invariance or point group symmetry generally differ by their flux around noncontractible loops. Furthermore, in addition to the physical symmetries the local tensors necessarily possess a virtual $\mathbb{Z}_2$ symmetry which determines the possible topological properties of the state.

In the second part of this paper, we consider the effect of the additional symmetry arising in the case of the chiral spin liquid PEPS. We show that its antiunitarity has consequences in the transfer matrix and entanglement spectra, such as the emergence of a peculiar multiplet structure. These results explain the discrepancies of the ES from the CFT spectrum which were observed in Refs. [34,35]. In particular we show that the interplay of reflection symmetry and virtual $\mathbb{Z}_2$ symmetry leads to unphysical degeneracies in the PEPS entanglement spectrum. Finally, we show that there is a region of parameter space where the PEPS exhibits an additional virtual U(1) symmetry which permits us to lift these degeneracies by considering states which break the underlying symmetry. We demonstrate numerically that within this region, the corrected low-energy ES of the PEPS is in perfect correspondence with the spectrum of the chiral CFT $\mathfrak{su}(2)_1$ including a correct value for the conformal weight.

The paper is organized as follows. In Sec. II we introduce PEPS, recalling how global symmetries of the state such as space group and SU(2) symmetries are implemented on the local tensors. We also review the role of virtual symmetries, the entanglement spectrum, and the PEPS transfer matrix. In Sec. III we discuss the formal incompatibility of translation invariance and point group symmetry in SU(2) invariant PEPS and analyze the consequences for half-integer spin. Using the example of the chiral PEPS from Ref. [34] we continue by analyzing the implications of SU(2) invariance, translation invariance, and point group symmetry for the transfer matrix and its fixed points in the case of a virtual $\mathbb{Z}_2$ symmetry in Sec. IV. Finally, in Sec. V we focus on the case where the PEPS possesses a virtual U(1) symmetry and present our numerical results establishing the correspondence between the CFT and entanglement spectra.

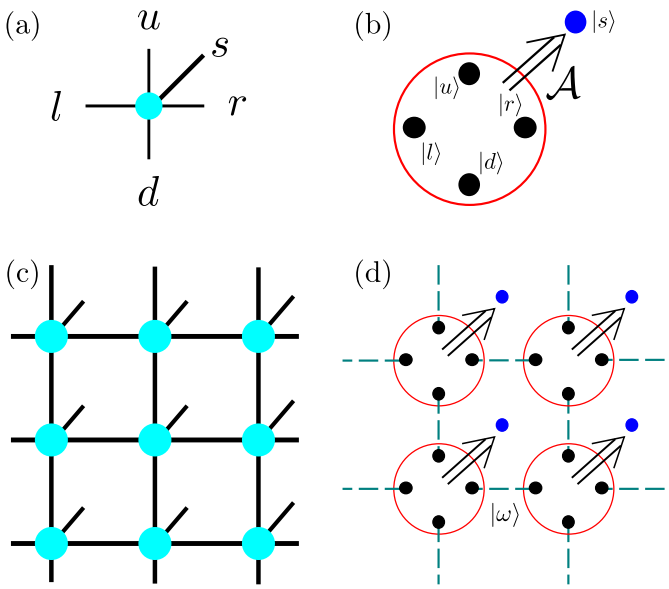

FIG. 1. Schematic description of the two different ways of defining a PEPS. (a) Four virtual spins are introduced around each physical spin. The relation between them is given by a five-index tensor. The many-body state is obtained by contracting nearest-neighbor virtual spins as shown in (c). (b) The PEPS is defined by a local projection map from the four virtual spins to the physical spin. Nearest-neighbor virtual spins are placed in a maximally entangled state $|\omega\rangle$ as shown in (d).

II. PRELIMINARIES ON PEPS

In this section we introduce our notations and review the construction of PEPS with space group symmetry, SU(2) symmetry, and virtual symmetries as well as the computation of entanglement spectra for cylinder PEPS.

A. Construction of PEPS

We study a spin system on a square lattice Λ with one spin-$\frac{1}{2}$ degree of freedom per lattice site. The local Hilbert space on every lattice site is therefore two-dimensional and spanned by the states $\{|s_{\mathbf{x}}\rangle | s_{\mathbf{x}} = 0, 1\}$ with $\mathbf{x} \in \Lambda$. For every configuration $\{\mathbf{x} \mapsto s_{\mathbf{x}}\}$ of the spins one obtains a many-body basis state $|\{\mathbf{x} \mapsto s_{\mathbf{x}}\}\rangle$ for the whole system as the tensor product $\otimes_{\mathbf{x}\in\Lambda} |s_{\mathbf{x}}\rangle$ of the corresponding local basis states on every lattice site. A generic quantum state

$$|\psi\rangle = \sum_{\{\mathbf{x}\mapsto s_{\mathbf{x}}\}} c_{\{\mathbf{x}\mapsto s_{\mathbf{x}}\}} |\{\mathbf{x} \mapsto s_{\mathbf{x}}\}\rangle \tag{1}$$

for the lattice spin system is defined by its expansion coefficients $c_{\{\mathbf{x}\mapsto s_{\mathbf{x}}\}}$ with respect to this product basis.

Projected entangled pair states (PEPS) are model states for lattice spin systems which depend only on a small number of parameters. These are given by the entries A^s_{lurd} of a five-index tensor that describes the physical spin s of one lattice site as well as four virtual spins l, u, r, d placed at the left, top, right, and bottom of each lattice site, respectively [see Fig. 1(a)]. The dimension D of the Hilbert space for each virtual spin is

called the bond dimension and is independent of the dimension $d = 2$ of the physical spin-$\frac{1}{2}$ Hilbert space on every site. The network obtained by placing a tensor $A(\mathbf{x})$ on each lattice site $\mathbf{x}$ and contracting nearest-neighbor virtual indices defines the PEPS expansion coefficient

$$c_{\{\mathbf{x}\mapsto s_\mathbf{x}\}} = \sum_{\substack{\{l_\mathbf{x} u_\mathbf{x} \\ r_\mathbf{x} d_\mathbf{x}\}}} \prod_{\mathbf{x}\in\Lambda} \delta_{l_\mathbf{x}, r_{\mathbf{x}-\mathbf{e}_1}} \delta_{u_\mathbf{x}, d_{\mathbf{x}+\mathbf{e}_2}} A(\mathbf{x})^{s_\mathbf{x}}_{l_\mathbf{x} u_\mathbf{x} r_\mathbf{x} d_\mathbf{x}}, \tag{2}$$

where $l_\mathbf{x}, u_\mathbf{x}, r_\mathbf{x}, d_\mathbf{x} = 0, \ldots, D-1$ for all lattice sites $\mathbf{x} \in \Lambda$ [see Fig. 1(c)]. In Eq. (2) we implicitly assumed periodic boundary conditions $r_\mathbf{x} = l_{\mathbf{x}+(N_h-1)\mathbf{e}_1}$ ($d_\mathbf{x} = u_{\mathbf{x}+(N_v-1)\mathbf{e}_2}$) for the virtual spins corresponding to a torus of size N_h (N_v) in the horizontal (vertical) direction. A PEPS defined on a torus therefore has no open virtual legs and is a state of the physical spins only. In the following we also study PEPS on cylinders obtained by compactifying only the vertical direction. The choice of virtual boundary conditions at the left and right edges of the cylinder may have a profound impact on the resulting physical state which persists even in the limit of an infinitely long cylinder $N_h \to \infty$. For instance whenever the local tensor possesses some symmetry the quantum numbers of the virtual boundary vectors influence the transformation behavior of the physical state. The degrees of freedom for a PEPS on the cylinder therefore consist of the physical spins and the boundary virtual spins.

Alternatively, PEPS can be defined as the result of a projection of a layer of entangled virtual spins onto the layer of physical spins. As above one associates to every lattice site four D-dimensional virtual spins placed at its left, top, right, and bottom edges which are then mapped to the physical spin of this site by the local tensor map [see Fig. 1(b)]

$$\mathcal{A} = \sum_s \sum_{l,u,r,d=0}^{D-1} \hat{A}^s_{lurd} |s\rangle[\langle l| \otimes \langle u| \otimes \langle r| \otimes \langle d|]. \tag{3}$$

Throughout this paper we also refer to $\mathcal{A}$ as a local projection map and we denote its basis entries by $\hat{A}$ in order to distinguish them from the local tensor A. Here, $\{|l\rangle | l = 0, \ldots, D-1\}$ is an orthonormal basis of the Hilbert space of the left virtual spin and similarly for $|u\rangle$ (up), $|r\rangle$ (right), and $|d\rangle$ (down). Nearest-neighbor virtual spins on adjacent lattice sites $\mathbf{x}, \mathbf{y}$ are placed in a pairwise maximally entangled state $|\omega(\mathbf{x}, \mathbf{y})\rangle = \sum_{i_\mathbf{x}, j_\mathbf{y}=0}^{D-1} \omega_{i_\mathbf{x} j_\mathbf{y}} |i_\mathbf{x}\rangle \otimes |j_\mathbf{y}\rangle$. As sketched in Fig. 1(d) the application of the product of all local projection maps to the tensor product of the virtual maximally entangled states for all nearest-neighbor bonds $\langle \mathbf{x}, \mathbf{y}\rangle$ defines the PEPS

$$|\tilde{\psi}\rangle = \left[\bigotimes_{\mathbf{x}\in\Lambda} \mathcal{A}(\mathbf{x})\right] \prod_{\langle \mathbf{x},\mathbf{y}\rangle} |\omega(\mathbf{x}, \mathbf{y})\rangle \tag{4}$$

with many-body basis coefficients

$$\tilde{c}_{\{\mathbf{x}\mapsto s_\mathbf{x}\}} = \sum_{\substack{\{l_\mathbf{x} u_\mathbf{x} \\ r_\mathbf{x} d_\mathbf{x}\}}} \prod_{\mathbf{x}\in\Lambda} \omega_{l_\mathbf{x}, r_{\mathbf{x}-\mathbf{e}_1}} \omega_{u_\mathbf{x}, d_{\mathbf{x}+\mathbf{e}_2}} \hat{A}(\mathbf{x})^{s_\mathbf{x}}_{l_\mathbf{x} u_\mathbf{x} r_\mathbf{x} d_\mathbf{x}}. \tag{5}$$

If the basis entries of the tensor map coincide with the local tensor, i.e., $\hat{A}^s_{lurd} = A^s_{lurd}$, and all virtual maximally entangled states are given by $|\omega\rangle = \sum_{i=0}^{D-1} |i\rangle \otimes |i\rangle$ with basis entries $\omega_{ij} = \delta_{ij}$ the many-body basis coefficients (2) and (5) agree such that the states $|\psi\rangle$ and $|\tilde{\psi}\rangle$ are identical. However, other options for $\hat{A}$ and $|\omega\rangle$ exist and are relevant for the construction of SU(2) spin-singlet PEPS. The PEPS in Eq. (5) can be cast into the form (2) with local tensors A defined by absorbing the virtual maximally entangled state ω_{ij} into $\hat{A}$. For the rest of this section we therefore assume w.l.o.g. that the maximally entangled state is given by $\omega_{ij} = \delta_{ij}$ and $\hat{A}^s_{lurd} = A^s_{lurd}$ unless stated otherwise.

In this paper, we consider PEPS which possess symmetries that act either nonlocally such as space group transformations or locally such as physical SU(2) rotations. Under such operations, a PEPS is mapped to another PEPS with transformed local tensors. Hence, by imposing that the new tensors are related to the original tensors in a certain way, we can ensure that the PEPS transforms in a given representation of the symmetry group. At the beginning of the next subsection Sec. II B, we describe the action of space group operations on PEPS, whereas the first paragraph of Sec. II C reviews the implementation of SU(2) symmetry for PEPS. Finally, local virtual symmetries of PEPS are considered in Sec. II D.

B. PEPS with space group symmetry

In this subsection we examine how lattice translations and point group transformations act on PEPS. All lattice rotations and reflections considered here are defined with respect to the vertices of the lattice. An element $|\{\mathbf{x} \mapsto s_\mathbf{x}\}\rangle = \otimes_{\mathbf{x}\in\Lambda} |s_\mathbf{x}\rangle$ of the many-body product basis of a lattice spin system is mapped by a space group transformation g to a different basis state $|\{\mathbf{x} \mapsto s_{g^{-1}\mathbf{x}}\}\rangle = \otimes_{\mathbf{x}\in\Lambda} |s_{g^{-1}\mathbf{x}}\rangle$. Such operations therefore map any PEPS to a different PEPS whose expansion coefficients are obtained from transformed local tensors

$$\tilde{A}(\mathbf{x})^{s_\mathbf{x}}_{lurd} = A(g^{-1}\mathbf{x})^{s_\mathbf{x}}_{g(lurd)}. \tag{6}$$

Here, the space group action on the virtual indices is trivial for translations whereas for the point group it is given by the natural two-dimensional representation of C_{4v} on the directions left, up, right, and down. For instance, the vertical mirror $\mathcal{M}_x$ acts on the indices as $lurd \mapsto ldru$, and similarly for the other group elements. In the following we consider only translation-invariant PEPS but with unit cells which can be larger than that of the underlying spin lattice Λ.

We recall that the point group C_{4v} for a site $\mathbf{x} \in \Lambda$ of the square lattice has four real one-dimensional representations which we denote by boldface letters $\mathbf{A}_1, \mathbf{A}_2, \mathbf{B}_1, \mathbf{B}_2$. The character table of these representations is shown in Table I. In the following we will be especially interested in the rotation-invariant representations $\mathbf{A}_1, \mathbf{A}_2$ that are even and odd under mirrors, respectively. Based on Eq. (6) we say that a PEPS local tensor A transforms in a one-dimensional representation σ of C_{4v} if

$$A^s_{g(lurd)} = \sigma(g) A^s_{lurd} \tag{7}$$

for all point group elements g.

Whenever the local tensor of a translation-invariant PEPS is point-group symmetric according to Eq. (7), the local representation σ also determines the transformation behavior of the PEPS under C_{4v} transformations. We denote the resulting point group representation of the PEPS by $\Sigma(\sigma)$ which generally depends also on the system size. For instance if the local

TABLE I. Character table of the one-dimensional irreducible representations of the square lattice point group C_{4v}. Here, e denotes the identity element, C_4 (resp. C_2) the rotation by $\frac{\pi}{2}$ (resp. π) and $\mathcal{M}_x$ (resp. $\mathcal{M}_{xy}$) the mirror about the horizontal axis (resp. the main diagonal).

	e	C_2	C_4	$\mathcal{M}_x$	$\mathcal{M}_{xy}$
$\mathbf{A}_1$	1	1	1	1	1
$\mathbf{A}_2$	1	1	1	−1	−1
$\mathbf{B}_1$	1	1	−1	1	−1
$\mathbf{B}_2$	1	1	−1	−1	1

tensor transforms as $\sigma = \mathbf{A}_1$ the resulting PEPS will also be invariant under rotations and reflections, i.e., $\Sigma(\mathbf{A}_1) = \mathbf{A}_1$. On the other hand, a local representation $\sigma = \mathbf{A}_2$ causes the PEPS to transform under C_{4v} in the representation $\Sigma(\mathbf{A}_2) = \mathbf{A}_1$ ($\Sigma(\mathbf{A}_2) = \mathbf{A}_2$) on a lattice with an even (odd) number of sites. These statements extend to PEPS with a checkerboard sublattice structure which are translation invariant with a bigger unit cell of 2×2 lattice sites. The checkerboard lattice is invariant under C_{4v} operations. If both local tensors of such a PEPS satisfy Eq. (7) the state will therefore transform in the same representation $\Sigma(\sigma)$ as a translation-invariant PEPS whose local tensor has the representation σ. In addition to Eq. (7) there generally are other possibilities to ensure that a PEPS transforms under the point group in a representation Σ; for instance it suffices that the local tensor transforms in the representation σ up to a local basis change of the virtual spins.

In the final sections of this paper, we study a chiral spin-liquid PEPS which is invariant under lattice translations and rotations but gets mapped to its complex conjugate by lattice mirrors. Its real (imaginary) part therefore transforms under C_{4v} in the one-dimensional representation $\mathbf{A}_1$ ($\mathbf{A}_2$) and we denote the transformation of the entire state by $\mathbf{A}_1 + i\mathbf{A}_2$. Such a state is special since the transformation behavior under time reversal and lattice symmetries which is expected for the edge modes of a chiral topological system is satisfied by the bulk of the PEPS. By analogy we say that a PEPS local tensor

$$A^s_{lurd} = (A_1)^s_{lurd} + i\,(A_2)^s_{lurd} \tag{8}$$

transforms under the point group as $\sigma = \mathbf{A}_1 + i\mathbf{A}_2$ if the real tensors A_1 and A_2 transform in the representations $\mathbf{A}_1$ and $\mathbf{A}_2$ according to Eq. (7), respectively. The local tensor A is then invariant (complex conjugated) under cyclic permutations (reflections) of its virtual indices. One can show that a translation invariant PEPS whose local tensor satisfies Eq. (8) transforms under C_{4v} in the representation $\Sigma(\mathbf{A}_1 + i\mathbf{A}_2) = \mathbf{A}_1 + i\mathbf{A}_2$ regardless of the system size.

C. Spin-singlet PEPS

Within the PEPS framework it is possible to construct quantum states which are invariant under global group transformations such as SU(2). This is the case if two conditions are met [41,43]. Firstly, the local projection map (3) should be an intertwiner between the group representation ρ_{phys} of the physical spin and some group representations $\rho_{v,l}$ ($\rho_{v,u}$, $\rho_{v,r}$, $\rho_{v,d}$) for the left (up, right, down) virtual spins such that

$$\rho_{\text{phys}}(\gamma) \circ \mathcal{A} = \mathcal{A} \circ [\rho_{v,l}(\gamma) \otimes \rho_{v,u}(\gamma) \otimes \rho_{v,r}(\gamma) \otimes \rho_{v,d}(\gamma)] \tag{9}$$

for all group elements γ. This implies that any group operation acting on the physical spins can be pushed to the virtual layer where it factorizes as a product of group operations acting on every virtual leg separately. Secondly, if a virtual particle transforms in the representation ρ_v its nearest-neighbor virtual spin has to transform in the conjugate virtual representation ρ_v^* with basis representation $\rho_v^*(\gamma)_{ij} = \rho_v(\gamma^{-1})_{ji}$ for any group element γ. The contribution of this nearest-neighbor virtual bond to the many-body basis coefficient (2) is thus invariant under group transformations since $\rho_v(\gamma)_{i'i}\delta_{ij}\rho_v^*(\gamma)_{j'j} = (\rho_v(\gamma) \circ \rho_v(\gamma^{-1}))_{i'j'} = \delta_{i'j'}$. The basis coefficient remains therefore unchanged and the PEPS transforms trivially under global group operations.

Generally, invariance of the PEPS therefore prevents nearest-neighbor virtual spins such as the left and right (up and down) tensor legs from transforming in identical group representations. However, one can reformulate a pair of nearest-neighbor virtual spins with representations (ρ_v, ρ_v^*) as two identical representations (ρ_v, ρ_v) by simultaneously changing their connecting maximally entangled state provided that ρ_v is self-conjugate. Let us exemplify this reformulation for the Lie group SU(2) whose representations are self-conjugate with the isomorphism between a representation and its conjugate given by the spin-flip operator Y,

$$\rho^*(\gamma) = Y \circ \rho(\gamma) \circ Y^{-1}. \tag{10}$$

We consider the horizontal bond between two sites $\mathbf{x}$ and $\mathbf{x}' = \mathbf{x} + \mathbf{e}_1$ with local tensors $\hat{A}(\mathbf{x})$ and $\hat{A}(\mathbf{x}')$ initially connected with an identity on the virtual bond. SU(2) invariance then requires that the right (left) virtual spin of site $\mathbf{x}$ ($\mathbf{x}'$) transforms in the representation ρ_v (ρ_v^*). Without changing the PEPS, we can insert an identity $\mathbb{1} = YY^{-1}$ into the virtual bond and define a modified right local tensor by absorbing the inverse spin flip to its left,

$$\tilde{\hat{A}}(\mathbf{x}')^{s'}_{l'u'r'd'} = \sum_{\tilde{l}'} (Y^{-1})_{l'\tilde{l}'} \hat{A}(\mathbf{x}')^{s'}_{\tilde{l}'u'r'd'}. \tag{11}$$

Due to the self-conjugacy Eq. (10) the left virtual leg of $\tilde{\hat{A}}$ transforms in the same representation ρ_v as its nearest neighbor. However, the two local tensors are now contracted with a nontrivial virtual maximally entangled state $\omega_{ij} = Y_{ij}$ that we also refer to as a virtual singlet,

$$\hat{A}(\mathbf{x})^s_{lurd}\delta_{rl'}\hat{A}(\mathbf{x}')^{s'}_{l'u'r'd'} = \hat{A}(\mathbf{x})^s_{lurd}\omega_{rl'}\tilde{\hat{A}}(\mathbf{x}')^{s'}_{l'u'r'd'}. \tag{12}$$

This reformulation is advantageous for the systematic study of PEPS with simultaneous SU(2) and space group symmetry [44]. Indeed, it allows the construction of SU(2) invariant PEPS in terms of local projection maps whose four virtual spins transform identically under spin rotations. This is the situation we will study in the following, i.e., we place virtual singlets on all bonds and moreover assume that the horizontal and vertical representations are identical. We can then investigate the symmetry properties of the local projection map and those of the virtual singlets separately. In the canonical S^z eigenbasis

the spin-flip operator is given by the unitary

$$Y = e^{i\pi S^y}. \tag{13}$$

It is symmetric (antisymmetric) and squares to $+1$ (-1) for integer (half-integer) spin representations. The virtual singlet $|\omega\rangle$ is therefore neither symmetric nor antisymmetric under exchange of the two virtual particles if ρ_v contains a mixture of integer and half-integer spin representations. As will be discussed in Sec. II D, this is a necessary condition for the realization of PEPS with half-integer physical spin. In this case there may be several distinct spin-singlet PEPS with the same local projection map and inequivalent orientations for the virtual singlets. We devote Sec. III to the study of their relations and symmetry properties. We emphasize that the singlet absorption Eq. (11) relies on the self-conjugacy of ρ_v and is therefore not always possible for groups possessing non-self-conjugate representations such as SU(3).

D. Virtual symmetries of PEPS

Many toy models with intrinsic topological order such as the $\mathbb{Z}_2$ toric code [24] possess exact representations in terms of simple PEPS [26]. For these models it has been realized that topological order is intimately related to the invariance of the local tensor under virtual symmetries which by definition do not involve the physical spin [28],

$$\mathcal{A} = \mathcal{A} \circ [\tau_{v,l}(g) \otimes \tau_{v,u}(g) \otimes \tau_{v,r}(g) \otimes \tau_{v,d}(g)]. \tag{14}$$

Here, $\tau_{v,l}$ $(\tau_{v,u}, \tau_{v,r}, \tau_{v,d})$ are representations of the virtual symmetry group G carried by the left (up, right, down) virtual legs with $\tau^*_{v,l} = \tau_{v,r}$ and $\tau^*_{v,d} = \tau_{v,u}$. For such PEPS all characteristic features of intrinsic topological order such as a topological ground state degeneracy, topological entanglement entropy, or anyonic excitations can be traced back to the virtual symmetry (14) of the local tensor. We review in particular the construction of states from the topological ground state manifold that are locally equivalent to a PEPS $|\psi\rangle$ but generally possess different eigenvalues with respect to certain nonlocal operators.

On a square lattice torus or cylinder, vertical (horizontal) flux lines of the virtual symmetry group G can be added to the PEPS $|\psi\rangle$ by inserting a group element $\tau_{v,r(u)}(g)$ on every horizontal (vertical) link crossed by a vertical (horizontal) line through the centers of plaquettes as sketched in Fig. 2(b). Due to the virtual symmetry (14) of every local tensor, these strings can be moved throughout the bulk of the tensor network. Hence they are not localized at any one position and generally cannot be detected by a local operator such as a local Hamiltonian. The number of different states that can be generated through addition of flux strings depends both on the group G and on the topology of the underlying lattice [24,25,45]. Indeed, the former determines the number of string types whereas the latter determines the number of independent noncontractible loops. However this consideration gives only the maximal dimension of the ground state manifold as some states may vanish or be linearly dependent. This notably occurs at phase transitions [46].

Let us now focus on SU(2) invariant PEPS with half-integer physical spin per unit cell which necessarily possess a virtual symmetry with symmetry group $G = \mathbb{Z}_2$.

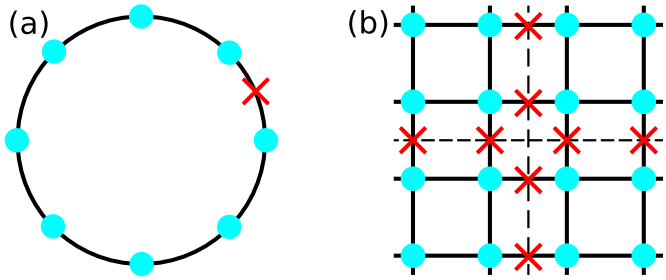

FIG. 2. Insertion of $\mathbb{Z}_2$ fluxes into one- and two-dimensional tensor network states by multiplication of certain virtual bonds with matrices Z (here represented by red crosses). The blue points represent the local tensors for which we suppressed the physical legs in the interest of readability. (a) MPS $|\psi\rangle_Z$ with a nontrivial flux through the circle. (b) PEPS $|\psi\rangle_{h,v}$ with both horizontal and vertical flux lines. Similarly there exist PEPS $|\psi\rangle_h$, $|\psi\rangle_v$ with only one horizontal or vertical flux line, respectively.

Indeed, the tensor product of two integer or two half-integer spin representations contains only integer spins. As a result, the intertwiner condition (9) between physical and virtual SU(2) representations has a solution for half-integer physical spin only if the virtual representation ρ_v contains both integer and half-integer spins. The SU(2) rotation $e^{2\pi i S^z}$ then has a nontrivial virtual representation in terms of a diagonal matrix

$$Z = \rho_v(e^{2\pi i S^z}) \tag{15}$$

equal to $+1$ (-1) on integer (half-integer) virtual spin representations such that $Z \neq \pm\mathbb{1}$ but $Z^2 = \mathbb{1}$. Due to its SU(2) invariance the local projection map for half-integer physical spin satisfies

$$(-1) \times \mathcal{A} = \mathcal{A} \circ Z^{\otimes 4} \tag{16}$$

in analogy to Eq. (14). The overall sign -1 stems from the half-integer physical spin and has no essential influence on the intrinsic topological features of the resulting PEPS.

For PEPS with a virtual $\mathbb{Z}_2$ symmetry there is only a single type of flux string that can be inserted around any noncontractible loop since two strings around the same loop annihilate each other. This leads to an expected topological degeneracy of four in a system defined on a two-dimensional torus, where the ground state manifold is spanned by the original state $|\psi\rangle$ as well as $|\psi\rangle_h$, $|\psi\rangle_v$, and $|\psi\rangle_{h,v}$ with horizontal, vertical, and both horizontal and vertical flux lines, respectively. Similar concepts apply to matrix product states (MPS) as the one-dimensional analogues of PEPS. If the local MPS tensor possesses a virtual $\mathbb{Z}_2$ symmetry one can define a state $|\psi\rangle_Z$ with a nonvanishing flux through the circle by inserting a matrix Z on one virtual bond as sketched in Fig. 2(a).

E. Entanglement spectrum for PEPS

Ever since their introduction [15], entanglement spectra have been used extensively to probe the nature of states especially in the context of topologically ordered phases [47–49]. The entanglement spectrum (ES) of a part A of a system in the state $|\psi\rangle$ is defined as the spectrum of its entanglement Hamiltonian $H_{\text{Ent}} = -\log \rho_A$ where $\rho_A = \text{Tr}_{\bar{A}} |\psi\rangle\langle\psi|$ is the corresponding reduced density matrix. In the rest of

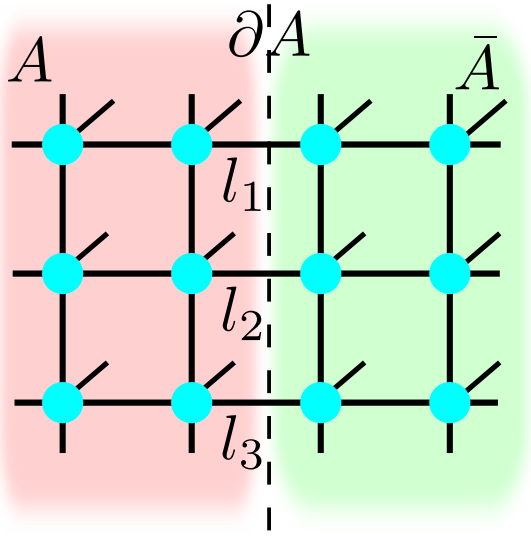

FIG. 3. Entanglement spectrum for PEPS. The lattice is divided in two disjoint regions A and $\bar{A}$. The entanglement between these regions is naturally carried by the virtual spins at the one-dimensional boundary. The entanglement Hamiltonian is obtained as an operator acting only on those spins [Eq. (18)].

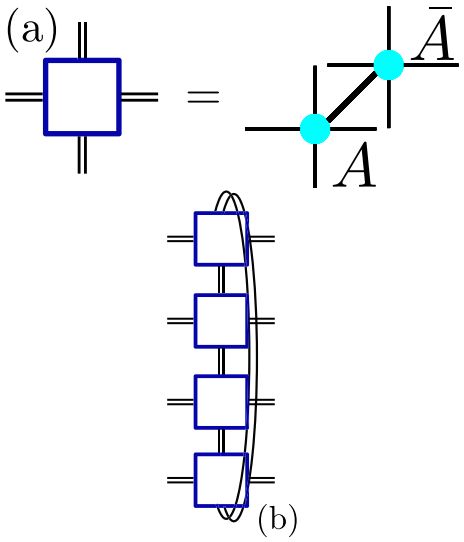

FIG. 4. Definition of the cylinder transfer matrix. (a) The local tensor is contracted with its complex conjugate to obtain the single-site transfer matrix. (b) Single-site transfer matrices are contracted along the periodic direction of the cylinder to obtain the cylinder transfer matrix.

this paper we will focus on the case where A and $\overline{A}$ form a real-space bipartition of the system. The ES is related to the spectrum of the physical edge theory as shown numerically in many cases [50–53] and analytically for noninteracting topological phases [54], certain one-dimensional symmetry protected topological phases [55], and for quantum states whose edge states are described by a chiral conformal field theory [56]. This allows, for example, us to extract conformal data such as conformal weights and thus to identify the edge conformal theory starting only from the ground state [57].

A correspondence at the level of the ES between bulk and edge degrees of freedom is very natural in the framework of PEPS. We can decompose the state for the entire system as a sum

$$|\psi\rangle = \sum_{\mathbf{l}} |\psi(\mathbf{l})\rangle_A \otimes |\psi(\mathbf{l})\rangle_{\bar{A}}, \tag{17}$$

where $|\psi(\mathbf{l})\rangle_{A(\bar{A})}$ denotes the PEPS restricted to the subsystem A ($\bar{A}$) depending explicitly on the configuration $\mathbf{l} = (l_1, l_2, l_3, \dots)$ of the virtual legs which cross the entanglement cut ∂A (see Fig. 3). Equation (17) shows that the entanglement between the physical spins in A and $\bar{A}$ is carried by the virtual spins connecting the two regions. Within the PEPS formalism it is therefore natural to interpret the entanglement Hamiltonian of a two-dimensional system as an operator for the virtual spins at the one-dimensional boundary [58].

Specifically, we consider a PEPS on a cylinder of total length N_h with subsystem A consisting of the first N_A columns starting from the left edge. The entanglement cut therefore crosses all N_v horizontal virtual bonds of one PEPS column with Hilbert space $\mathcal{H}_{sl} = (\mathbb{C}^D)^{\otimes N_v}$ where the subscript indicates that all virtual bonds lie in a single layer. We stack the PEPS with its complex conjugate, thereby forming an object with both a ket layer and a bra layer, and compute the reduced density matrix ρ_A by contracting the physical legs corresponding to sites in the complement $\bar{A}$. A detailed calculation shows that [58]

$$\rho_A = U\sqrt{(\sigma^L)^T}\sigma^R\sqrt{(\sigma^L)^T}U^\dagger, \tag{18}$$

where U is an isometry from the boundary virtual spins $\mathcal{H}_{sl}$ to the physical spins in A. On the other hand, the virtual reduced density matrix $\sigma^{L(R)}$ is an operator which maps the virtual spins at the left (right) edge of the entanglement cut from the bra layer to the ket layer. It is obtained by tracing out the physical spins in the density matrix of the restricted state $|\psi(\mathbf{l})\rangle_A$ ($|\psi(\mathbf{l})\rangle_{\bar{A}}$) while keeping the virtual legs at the entanglement cut free,

$$\sigma^L_{\mathbf{l}\tilde{\mathbf{l}}} = \mathrm{Tr}_A[|\psi(\mathbf{l})\rangle_A\ {}_A\langle\psi(\tilde{\mathbf{l}})|] \tag{19}$$

and similarly for σ^R. Here, all virtual reduced density matrices are normalized according to $\mathrm{Tr}(\sigma^{L(R)})^2 = 1$. In this paper we study reflection-symmetric PEPS for which the left and right virtual density matrices are related as $(\sigma^R)^* = \sigma^L$ such that the ES is given by the spectrum of

$$-\log[(\sigma^L)^2]. \tag{20}$$

F. Transfer matrix

An object of central importance for the study of PEPS in two dimensions is the cylinder transfer matrix Γ. As sketched in Fig. 4, Γ is obtained by stacking a single column of local PEPS tensors with their complex conjugates and contracting the physical indices of both layers. As for MPS, the transfer matrix spectrum determines the correlation length of the state. Moreover, in the presence of virtual symmetries the leading eigenvalues of Γ in different symmetry sectors determine the number of independent ground states with nonvanishing norm [46]. We will make use of this fact in Sec. V B.

In addition the transfer matrix gives access to the virtual reduced density matrices and thereby to the ES of the PEPS.

If the state has virtual boundary conditions $v^{L(R)} \in \mathcal{H}_{sl}$ at the left (right) edges of the cylinder one finds

$$\sigma^L = (\Gamma^T)^{N_A}(v^L \otimes (v^L)^*), \tag{21a}$$

$$\sigma^R = \Gamma^{N_h - N_A}(v^R \otimes (v^R)^*). \tag{21b}$$

Here we used that the transfer matrix acts equivalently on two copies $\mathcal{H}_{sl} \otimes \mathcal{H}_{sl}$ of the single-layer virtual column or on virtual density matrices $\sigma \in \mathrm{End}(\mathcal{H}_{sl})$. For an infinitely long cylinder the subleading eigenspaces of the transfer matrix are suppressed in Eq. (21) and $\sigma^{L,R}$ correspond to the leading left and right eigenvectors.

Without symmetries or fine tuning, these leading eigenvectors are nondegenerate, positive, and have nonvanishing overlap with a generic boundary vector. The ES is therefore expected to be independent of the boundary conditions in the thermodynamic limit. However, in the presence of virtual symmetries the transfer matrix is block diagonal and the ES may depend on the symmetry sector of the boundary vectors. All in all, the transfer matrix therefore contains crucial information about the topological properties of a PEPS and we devote Sec. IV B to the study of its symmetries for the chiral PEPS in which we are interested.

III. INCOMPATIBILITY OF TRANSLATION INVARIANCE AND POINT GROUP SYMMETRY IN CONSTRUCTION OF SU(2) INVARIANT PEPS

Spin liquids are states which are invariant under global SU(2) transformations and lattice translations in addition to transforming in a well-defined way under rotations and reflections about lattice sites. In order to construct spin liquid PEPS we therefore need to understand how translation invariance and point group symmetry can be implemented for SU(2) invariant PEPS. This is a subtle issue since generically either translation invariance or point group symmetry are formally broken in the construction of SU(2) invariant PEPS which we described in Sec. II C. In the present section we examine under which conditions this formal breaking of translation invariance or point group symmetry manifests at the physical level and has consequences for the transformation properties of the state. Since this question arises also in one-dimensional tensor networks we discuss the simpler MPS in parallel to two-dimensional PEPS throughout this section.

We begin with a statement of the problem in subsection III A and a summary of our findings in subsection III B before moving to a detailed analysis in subsection III C. The section concludes with the discussion of two simple MPS examples in subsection III D.

A. Statement of problem and assumptions

As described in Sec. II C, SU(2) invariant PEPS (also referred to as spin-singlet PEPS) can be defined via local projection maps which intertwine between the physical spin representation and the tensor product of representations for the virtual spins [see Eq. (9)]. If the tensor network is contracted with identities $\omega_{ij} = \delta_{ij}$ on the bonds, SU(2) invariance requires that nearest-neighbor virtual spins transform in opposite representations (ρ_v, ρ_v^*) under SU(2). For an explicitly translation-invariant PEPS with $\omega_{ij} = \delta_{ij}$ this implies that the unique local projection map cannot transform straightforwardly under reflections and rotations since its virtual spins possess nonidentical SU(2) representations.

However, the self-conjugacy of SU(2) representations permits the rewriting of a virtual nearest-neighbor pair (ρ_v, ρ_v^*) connected by $\omega_{ij} = \delta_{ij}$ as a pair of spins transforming in identical representations (ρ_v, ρ_v) and connected by a virtual singlet $\omega_{ij} = Y_{ij}$ (see Sec. II C). One can therefore consider spin-singlet PEPS with the same representation ρ_v for every virtual spin, a single local projection map

$$\mathcal{A} : \rho_v^{\otimes 4} \to \rho_{\mathrm{phys}} \tag{22}$$

valid for every lattice site and singlets $\omega_{ij} = Y_{ij}$ on the bonds. Here, the local projection map is defined on four identical virtual spins and can therefore transform in a simple way under C_{4v}, for instance in a one-dimensional representation [Eq. (7)]. The space group transformations of the PEPS are then determined both by the point group representation of $\mathcal{A}$ and by the space group transformations of the orientation pattern for the virtual singlets, where both contributions can be analyzed separately. This is the approach we follow here. Let us now specify our assumptions and notations.

For the rest of this section, $\mathcal{A}$ denotes a local tensor map of the form (22) with basis entries denoted as $\hat{A}^s_{lurd}$. As specified in Eq. (9) $\mathcal{A}$ acts as an intertwiner between the four virtual spins transforming in identical SU(2) representations ρ_v and the physical spin with representation ρ_{phys}. We assume that the physical particle has a well-defined spin $\rho_{\mathrm{phys}} = s_{\mathrm{phys}}$ whereas the virtual representation

$$\rho_v = \bigoplus_{\alpha=1}^{n} s_\alpha \tag{23}$$

is a direct sum of n irreducible representations of spin s_α for $\alpha = 1, \ldots, n$. As in Sec. II we denote by

$$Y = \bigoplus_{\alpha=1}^{n} e^{i\pi\rho_{s_\alpha}(S^y)} \tag{24}$$

the virtual spin flip operator with square

$$Z = Y^2 = \bigoplus_{\alpha=1}^{n} e^{2\pi i\rho_{s_\alpha}(S^z)} \tag{25}$$

that is equal to $+1$ (-1) on integer (half-integer) representations. Moreover we demand that the local tensor map changes in a simple manner under point group operations, i.e., under permutations of its virtual spins. Specifically, we assume that $\mathcal{A}$ transforms either in a one-dimensional representation σ as defined in Eq. (7) or else that its real and imaginary part transform in one-dimensional representations σ_1 and σ_2, respectively [cf. Eq. (8) and the subsequent discussion]. In the latter case, we abbreviate the transformation of $\mathcal{A}$ as $\sigma = \sigma_1 + i\sigma_2$. For MPS the point group C_2 has trivial and fundamental representations denoted by boldface letters **A** and **B** which are even and odd under inversion, respectively.

An SU(2) invariant PEPS is obtained from the local projection map $\mathcal{A}$ by placing virtual singlets $w_{ij} = Y_{ij}$ on

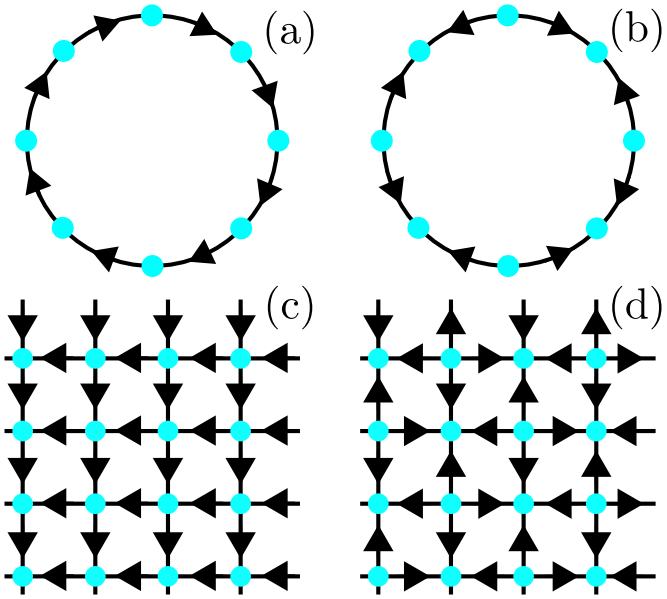

FIG. 5. Two different singlet orientation patterns for MPS in (a), (b) and PEPS in (c) and (d). The patterns in (a) and (c) are invariant under translation by one lattice site but not under point group operations, whereas the patterns (b) and (d) are invariant under the lattice point group but have an enlarged unit cell with respect to translation.

nearest-neighbor bonds. When $|\omega\rangle$ possesses an orientation (see Sec. II C), the PEPS is well defined only once we specify an orientation pattern for the singlets on all bonds. It is not possible to choose an orientation pattern for the square lattice that is simultaneously invariant under translations by one lattice site and invariant under rotations and reflections about lattice sites. In this construction either translation invariance or point group symmetry are therefore formally broken at the virtual level. We consider two natural choices for orientation patterns that are either translation invariant [see Figs. 5(a) and 5(c)] or point group invariant [see Figs. 5(b) and 5(d)]. The latter pattern has an enlarged unit cell of 2 (2×2) sites in one dimension (two dimensions) and therefore applies only to lattices with an even number of sites in every direction and sublattices $\Lambda_{A(B)} = \{\sum_i n_i \mathbf{e}_i | \sum_i n_i \text{ even (odd)}\}$, where i runs from 1 to the number of spatial dimensions. We denote the PEPS and MPS derived from these two orientation patterns by $|\psi_1\rangle$ and $|\psi_2\rangle$, respectively.

For future reference we want to express the states $|\psi_1\rangle$ and $|\psi_2\rangle$ in terms of tensor networks with identities δ_{ij} on all virtual bonds as in Eq. (2). The state $|\psi_1\rangle$ is computed from an explicitly translation invariant network with a single local tensor

$$\text{MPS}: \quad C^s_{lr} = \sum_{l'} Y_{l'l} \hat{A}^s_{l'r}, \tag{26a}$$

$$\text{PEPS}: \quad C^s_{lurd} = \sum_{l'd'} Y_{l'l} Y_{d'd} \hat{A}^s_{l'urd'}, \tag{26b}$$

that is obtained by absorbing the virtual singlet on every left (left and down) virtual leg for MPS (PEPS), respectively [see Fig. 6(a) for PEPS]. The local tensor C does not generally

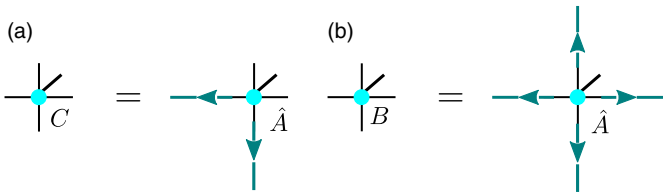

FIG. 6. Two different ways of absorbing oriented singlets into PEPS local tensors leading to (a) an explicitly translation invariant state or (b) a manifestly point group symmetric PEPS.

transform under point group operations in the representation σ as defined above. On the other hand, $|\psi_2\rangle$ has a sublattice structure with local tensors A (B) for sites on Λ_A (Λ_B), where $A^s_{lurd} = \hat{A}^s_{lurd}$ and B is obtained by absorbing the virtual singlets on all virtual legs [see Fig. 6(b) for PEPS] such that

$$\text{MPS}: \quad B^s_{lr} = \sum_{l'r'} Y_{l'l} \hat{A}^s_{l'r'} Y_{r'r}, \tag{27a}$$

$$\text{PEPS}: \quad B^s_{lurd} = \sum_{l'u'r'd'} Y_{l'l} Y_{u'u} Y_{r'r} Y_{d'd} \hat{A}^s_{l'u'r'd'}. \tag{27b}$$

Due to the SU(2) symmetry of the local projection map the local tensor B can also be obtained by applying a physical spin flip $e^{i\pi\rho_{\text{phys}}(S^y)}$ to the tensor A. Therefore both A and B transform under C_{4v} in the representation σ.

The space group transformations of the states $|\psi_1\rangle$ and $|\psi_2\rangle$ are determined both by the point group representation σ of the local tensor map and the transformation of the respective singlet orientation pattern. We denote by $\Sigma(\sigma)$ the contribution of $\mathcal{A}$ to the PEPS and MPS point group transformations. $\Sigma(\sigma)$ is a one-dimensional representation or consists of independent one-dimensional representations for the real and imaginary parts and generally also depends on the system size (cf. Sec. II B). The singlet orientation pattern for the state $|\psi_2\rangle$ is invariant under rotations and reflections about lattice sites such that $|\psi_2\rangle$ transforms under point group operations as $\Sigma(\sigma)$. However, $|\psi_2\rangle$ is not manifestly translation invariant. On the other hand, the orientation pattern for $|\psi_1\rangle$ is invariant under translations but not point group transformations. The state $|\psi_1\rangle$ is therefore manifestly translation invariant but generally transforms under point group operations in a manner different from $\Sigma(\sigma)$.

The questions we want to answer are therefore threefold:

(1) How does the translation invariant state $|\psi_1\rangle$ transform under point group operations?

(2) How does the point group symmetric state $|\psi_2\rangle$ transform under lattice translations?

(3) What is the relation between the two states $|\psi_1\rangle$ and $|\psi_2\rangle$ when both are well defined, i.e., when the number of lattice sites in every direction is even?

B. Summary of results

The answers to the questions above will depend on the system size and also on the physical and virtual spins s_{phys}, s_α. N denotes the total system size, i.e., the length of the chain for MPS and $N = N_h N_v$ for PEPS. Let us recall that N should be even for half-integer spins and Ψ_2 is defined only if both N_h

and N_v are even. We will distinguish three cases of interest to us:

Case I: The virtual spins are purely integer such that s_{phys} is integer by the SU(2) fusion rules.

Case II: The virtual spins are purely half integer such that s_{phys} is integer.

Case III: The virtual spins are mixed integer and half integer and s_{phys} is half integer such that the local tensor possesses the virtual $\mathbb{Z}_2$ symmetry defined in Eq. (16).

A fourth case exists where the physical spin is integer and the virtual spins are mixed integer and half integer. However, this situation is less relevant than Case III since the latter constitutes the only possibility to build PEPS for half-integer physical spin whereas for integer spin Case I and II provide more natural options. As the results for both cases are identical up to sign factors we focus here on Case I-III. We found the following:

(1) Point group transformations of $|\psi_1\rangle$:

Case I: $|\psi_1\rangle$ transforms as $\Sigma(\sigma)$.

Case II: $|\psi_1\rangle$ transforms as $\Sigma(\sigma)$ for N even and as $\mathbf{B}\otimes\Sigma(\sigma)$ ($\mathbf{B}_2\otimes\Sigma(\sigma)$) for MPS (PEPS) with N odd.

Case III: $|\psi_1\rangle$ transforms as $\Sigma(\sigma)$ on chains of length $N\in 4\mathbb{N}$, as $\mathbf{B}\otimes\Sigma(\sigma)$ on chains of length $N\in 4\mathbb{N}+2$ and it vanishes on odd-length chains. In two dimensions it transforms as $\Sigma(\sigma)$ on even-by-even tori and vanishes if both N_h, N_v are odd. It transforms in a two-dimensional representation on nonquadratic tori with N_h even and N_v odd such that it is mapped to the state $|\psi_1\rangle_h$ ($(-1)^{N_h/2}|\psi_1\rangle$) with a horizontal flux line under the horizontal (vertical) mirror, and analogously for N_h odd and N_v even.

(2) Translation of $|\psi_2\rangle$:

Case I: $|\psi_2\rangle$ is translation invariant.

Case II: $|\psi_2\rangle$ is translation invariant.

Case III: Translation changes $|\psi_2\rangle$ by a phase $(-1)^{N/2}$ that is nontrivial on chains of length $N\in 4\mathbb{N}+2$ but which is always trivial in two dimensions since $N\in 4\mathbb{N}$ for even-by-even tori.

(3) Relation of $|\psi_1\rangle$ and $|\psi_2\rangle$:

Case I: $|\psi_1\rangle=|\psi_2\rangle$.

Case II: $|\psi_1\rangle=(-1)^{N/2}|\psi_2\rangle$ for MPS and $|\psi_1\rangle=|\psi_2\rangle$ for PEPS.

Case III: The two states possess different $\mathbb{Z}_2$ fluxes around noncontractible loops if the system size in at least one direction is not divisible by four. For MPS

$$N\in 4\mathbb{N}: \quad |\psi_1\rangle=|\psi_2\rangle, \tag{28a}$$

$$N\in 4\mathbb{N}+2: \quad |\psi_1\rangle=|\psi_2\rangle_Z \tag{28b}$$

and for PEPS

$$N_h, N_v\in 4\mathbb{N}: \quad |\psi_2\rangle=|\psi_1\rangle, \tag{29a}$$

$$N_{h(v)}\in 4\mathbb{N},\ N_{v(h)}\in 4\mathbb{N}+2: \quad |\psi_2\rangle=|\psi_1\rangle_{h(v)}, \tag{29b}$$

$$N_h, N_v\in 4\mathbb{N}+2: \quad |\psi_2\rangle=-|\psi_1\rangle_{h,v}, \tag{29c}$$

where the states with flux insertions are as defined in Sec. II D.

C. Proofs

1. Point group transformations of $|\psi_1\rangle$

The deviations of the point group transformations of $|\psi_1\rangle$ from $\Sigma(\sigma)$ are caused by the nontrivial transformation of the corresponding singlet orientation pattern displayed in Fig. 5(a) and 5(c). The flipping of an arrow in this singlet orientation pattern corresponds to the insertion of a matrix $(Y^T)^{-1}Y=Z$ on that virtual bond.

Case I: $Z=\mathbb{1}$ such that the flipping of arrows does not manifest at the physical level.

Case II: $Z=-\mathbb{1}$ such that the flipping of arrows results in an overall phase $(-1)^N$ for horizontal and vertical reflections as well as rotations. Diagonal reflections leave the singlet pattern invariant or cause a trivial phase $(-1)^{2N}$.

Case III: $Z\neq\pm\mathbb{1}$ such that rotations and reflections cause the insertion of $\mathbb{Z}_2$ fluxes. On one-dimensional chains reflection causes the insertion of N matrices Z that cancel pairwise due to the virtual $\mathbb{Z}_2$ symmetry given by Eq. (16). The (-1) factor in this equation leads to an overall sign of $(-1)^{N/2}$ for the MPS (note that N is even for half-integer s_{phys}). For PEPS, the horizontal mirror and rotation by $\pi/2$ (vertical mirror and rotation by $-\pi/2$) cause the insertion of a Z matrix on every vertical (horizontal) bond and therefore of N_v horizontal (N_h vertical) flux lines. These can be rearranged to obtain the transformation properties stated above. Note that $|\psi_1\rangle$ vanishes if the total number of sites is odd since in this case the half-integer physical spins cannot fuse to an SU(2) invariant state.

2. Translation of $|\psi_2\rangle$

Translation of $|\psi_2\rangle$ by one lattice site exchanges the two sublattices and acts on the state as a staggered physical spin flip

$$\bigotimes_{\mathbf{x}\in\Lambda_A} e^{i\pi\rho_{\text{phys}}(S^y)}\bigotimes_{\mathbf{x}\in\Lambda_B} e^{-i\pi\rho_{\text{phys}}(S^y)}. \tag{30}$$

The physical spin flip is related to its inverse as $e^{i\pi\rho_{\text{phys}}(S^y)}=\pm e^{-i\pi\rho_{\text{phys}}(S^y)}$ for integer (half-integer) s_{phys} and $|\psi_2\rangle$ is invariant under a global spin flip. It is therefore invariant under lattice translations in Case I and Case II but changes by a phase $(-1)^{N/2}$ in Case III. This phase is always trivial for PEPS but can be relevant in MPS such as for the Majumdar-Ghosh chain, see Sec. III D.

3. Relation between $|\psi_1\rangle$ and $|\psi_2\rangle$

The singlet orientation patterns defining $|\psi_1\rangle$ and $|\psi_2\rangle$ are related by the flipping of the arrow direction on every other nearest-neighbor bond corresponding to the insertion of the matrix $(Y^T)^{-1}Y=Z$ on that link [see Fig. 7(a)]. Case I: $Z=\mathbb{1}$ such that the two states are identical. Case II: $Z=-\mathbb{1}$ such that the states are related by a phase $(-1)^{N/2}$ for MPS and $(-1)^N$ for PEPS.

For Case III the Z insertions can be rearranged using the virtual $\mathbb{Z}_2$ symmetry of every local tensor, see Fig. 7(b) for PEPS. In one dimension, the total number of such Z insertions is given by $N/2$ and thus even (odd) on chains of length $N\in 4\mathbb{N}$ ($N\in 4\mathbb{N}+2$), giving the relation (28). In two dimensions, the Z insertions on every second horizontal and

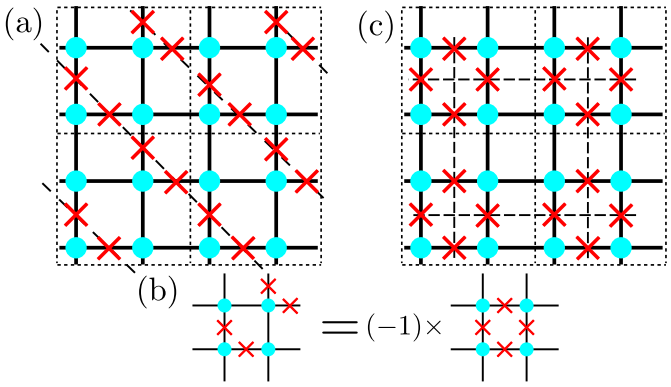

FIG. 7. (a) Schematic representation of the difference between the singlet orientation patterns defining $|\psi_1\rangle$ and $|\psi_2\rangle$. Whenever the direction of a singlet has to be exchanged this corresponds to the insertion of a matrix Z on the corresponding bond. The inserted Z matrices are represented by red crosses while the physical legs are suppressed in the interest of readability. The dotted lines delimit patches on which the graphical equation given in (b) will be applied whereas the dashed lines indicate flux lines. (b) Using the $\mathbb{Z}_2$ virtual symmetry, the two outer crosses can be moved to the interior links. (c) As a result of applying (b) to the four squares on (a), a PEPS with a flux line along every other row and every other column is obtained.

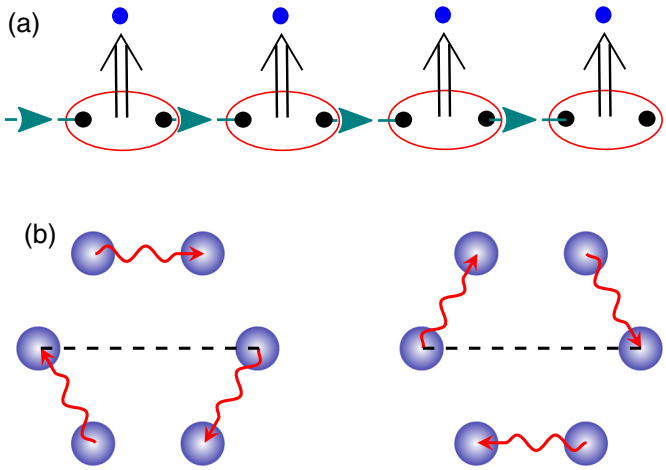

FIG. 8. (a) Schematic representation of the AKLT state: Two spin-s virtual spins are projected onto the maximal spin sector $2s$ at each site and are connected to their nearest neighbors by a singlet state. Depending on s, the singlet state is oriented (case shown here) or not. (b) Schematic description of the two degenerate Majumdar-Ghosh states $|\chi_1\rangle$ and $|\chi_2\rangle$ where the physical singlets are represented by red arrows. While they are directly related by translation, a reflection around the dashed line exchanges the two states but also flips the antisymmetric singlets giving a sign $(-1)^{N/2}$.

vertical link can be rearranged to obtain a network with a $\mathbb{Z}_2$ flux line wrapping around every other horizontal and vertical line through the centers of plaquettes such that there are a total of $N_v/2$ ($N_h/2$) horizontal (vertical) flux lines, respectively [see Fig. 7(c)]. Since flux lines around the same noncontractible loop cancel pairwise one obtains the result (29).

D. Examples

In this subsection we illustrate the previous discussion with two examples of spin-chain ground states which have an exact MPS representation: the AKLT state [59] and the Majumdar-Ghosh state [60].

1. AKLT-type MPS

A general AKLT MPS is constructed by choosing an irreducible representation $\rho_v = s$ for all virtual legs and by projecting the two virtual spins corresponding to a physical site onto the maximal spin $s_{\text{phys}} = 2s$. Thus integer (half-integer) s corresponds to Case I (Case II) of subsection III B, respectively. This construction is sketched in Fig. 8(a). The resulting local tensor map is inversion symmetric, i.e., $\hat{A}^s_{lr} = \hat{A}^s_{rl}$. On the other hand, the singlets created by the operator $Y = \rho_v(e^{i\pi S_y})$ are symmetric (antisymmetric) for integer (half-integer) virtual spin s. The local tensor of the translation invariant state $|\psi_1\rangle$ is therefore symmetric (antisymmetric) up to a local basis change

$$(C^s)^T = (-1)^{2s}\, Y^{-1} C^s Y. \tag{31}$$

The MPS $|\psi_1\rangle$ therefore transforms under the point group in the representation **A** unless s is half integer and N is odd in which case it transforms as **B**. Interestingly, the sign in Eq. (31) is a manifestation of the topologically nontrivial (trivial) nature of the AKLT state for odd (even) spin s_{phys} as pointed out in Ref. [61]. Since the singlet orientations contribute only an overall sign that is trivial for even N, $|\psi_2\rangle$ is always both translation invariant and equal to $|\psi_1\rangle$.

2. Majumdar-Ghosh MPS

The Majumdar-Ghosh state is a spin-$\frac{1}{2}$ valence bond state where every physical spin forms a singlet with one of its nearest neighbors (hence the number of sites must be even). On a periodic chain there are two possible states $|\chi_1\rangle$, $|\chi_2\rangle$ sketched in Fig. 8(b) for which the first spin forms a singlet either with the second one (on the right) or with the last one (on the left). Both translation T and inversion $\mathcal{M}$ around sites exchange the two states, $|\chi_2\rangle = T|\chi_1\rangle$ and $\mathcal{M}|\chi_1\rangle = (-1)^{N/2}|\chi_2\rangle$. Here, the sign counts the antisymmetric physical singlets flipped by inversion.

Since translation symmetry is broken in the valence bond description, a translation invariant MPS exists only for linear superpositions of $|\chi_1\rangle$ and $|\chi_2\rangle$. This MPS has virtual SU(2) representations $\rho_v = 0 \oplus \frac{1}{2}$ and the local tensor map $\hat{A}^s_{lr} = \delta_{0,l}\delta_{s,r} + \delta_{0,r}\delta_{s,l}$. Thus this example belongs to Case III of subsection III B. It is fully specified only once we choose an orientation pattern for the virtual singlets. Indeed, the orientation of a physical singlet between two sites in the resulting state corresponds to the orientation of the virtual singlet of the corresponding bond. The translation-invariant and inversion-symmetric MPS are therefore given by the linear superpositions $|\psi_1\rangle = |\chi_1\rangle + T|\chi_1\rangle$ and $|\psi_2\rangle = |\chi_1\rangle + \mathcal{M}|\chi_1\rangle$, respectively. These two states are the same for $N \in 4\mathbb{N}$ whereas $T|\chi_1\rangle = -\mathcal{M}|\chi_1\rangle$ for $N \in 4\mathbb{N}+2$ due to the odd number of physical singlets. In the tensor network language, we can account for this by multiplying one bond with the matrix Z which adds an overall phase -1 when this bond is crossed by a physical singlet. Therefore $|\psi_2\rangle = |\psi_1\rangle_Z$ for $N \in 4\mathbb{N}+2$ as shown in Eq. (28).

IV. SYMMETRIES OF CHIRAL SPIN LIQUID PEPS

From now on until the end of this paper we study the chiral PEPS for spin-$\frac{1}{2}$ on the square lattice that was introduced in Ref. [34] and subsequently studied in Ref. [35]. Unlike the chiral PEPS from Refs. [29,30,33] this state is not defined in terms of free fermions or Gutzwiller projections thereof. Instead, the PEPS is constructed from interacting bosonic spins by considering the most general local tensor map satisfying certain symmetry conditions: $\mathbf{A}_1 + i\mathbf{A}_2$ symmetry under C_{4v} and invariance under simultaneous physical and virtual SU(2) rotations, where the virtual spins are assumed to transform in the representation $\rho_v = \mathbf{0} \oplus \frac{\mathbf{1}}{\mathbf{2}}$. One thereby obtains a family of spin-singlet states parametrized by three real numbers $\lambda_1, \lambda_2, \lambda_c$. These spin liquids are deformations of the PEPS for the nearest-neighbor RVB state [37,38], where additional terms with amplitudes λ_2 and λ_c in the local tensor generate long-range singlets [39]. They provide good variational states for the square lattice Heisenberg model with additional chiral cyclic plaquette terms [62]. Moreover, for $\lambda_c = 0$ it was shown that this PEPS can be either critical or in the $\mathbb{Z}_2$ spin liquid phase [63].

The ES for the chiral PEPS presented in Refs. [34,35] resembles the spectrum of the chiral conformal field theory (CFT) $\mathfrak{su}(2)_1$. However, this correspondence is not perfect. Firstly, the ES for the state with $\mathbb{Z}_2$-even boundary conditions exhibited unambiguous chiral features only after the momentum was projected onto the region between 0 and π. Secondly, the ES for the state with $\mathbb{Z}_2$-odd boundary conditions displayed two identical modes shifted in momentum by π. Interpreted as the two sectors of the CFT $\mathfrak{su}(2)_1$, these spectra therefore do not give the expected conformal weight of $h = 1/4$ [64]. Moreover, the ES of the state with a flux line along the cylinder was found not to display any chiral features.

In this section we are going to conduct a comprehensive analysis of the symmetries possessed by the chiral spin liquid PEPS which follow from the special form of its local projection map. This understanding will permit us to explain some of the discrepancies between its ES and the CFT $\mathfrak{su}(2)_1$. In particular we show that the $\mathbb{Z}_2$-even ES is chiral in the entire Brillouin zone for the explicitly translation invariant PEPS defined in the previous section. Moreover we prove that the two branches in the $\mathbb{Z}_2$-odd ES follow from a dressed mirror symmetry. In Sec. V, this identification will allow us to resolve this issue by considering states which break this symmetry and have only a single branch in the ES. We also compute the momentum-resolved ES of the PEPS with a horizontal flux line and show that it has some chiral features even though they do not appear linked to a simple CFT.

After formally defining the chiral PEPS in Sec. IV A we analyze the symmetries of its transfer matrix and the generic form of its spectrum in Sec. IV B and Sec. IV C, respectively. We provide the same analysis for the transfer matrix with a horizontal flux line in Sec. IV D. Finally, we investigate the ES of the corresponding fixed points in Sec. IV E.

A. Definition

We study a spin liquid PEPS for particles with spin $s_{\text{phys}} = \frac{1}{2}$ on a square lattice. The state has bond dimension $D = 3$ and virtual SU(2) representations

$$\rho_v = \mathbf{0} \oplus \tfrac{\mathbf{1}}{\mathbf{2}}. \tag{32}$$

The local projection map is an intertwiner of SU(2) representations and transforms in the representation $\mathbf{A}_1 + i\mathbf{A}_2$ of C_{4v}. It therefore possesses the virtual $\mathbb{Z}_2$ symmetry from Eq. (16). Specifically, one chooses

$$\mathcal{A} = \lambda_1 \mathcal{P}\big(\mathbf{A}_1^{\varphi}\big) + \lambda_2 \mathcal{P}\big(\mathbf{A}_1^{3\varphi}\big) + i\lambda_c \mathcal{P}\big(\mathbf{A}_2^{3\varphi}\big), \tag{33}$$

where $\mathcal{P}$ are projections on irreducible C_{4v} and spin-$\frac{1}{2}$ representations in the tensor product $\rho_v^{\otimes 4}$. The coefficients λ_1, λ_2 are real for the $\mathbf{A}_1$ representations whereas $i\lambda_c$ is purely imaginary for the representation $\mathbf{A}_2$. The superscripts φ, 3φ refer to the transformation under a local U(1) action described below. The concrete form of the projection map is given in the Appendix.

We can equivalently define the local projection map (33) as a superposition of the spin-$\frac{1}{2}$ $\mathbf{B}_{1,2}$ representations in $\rho_v^{\otimes 4}$ [34]. Indeed, due to the virtual $\mathbb{Z}_2$ symmetry the two sets of local tensors corresponding to the $\mathbf{A}_{1,2}$ and $\mathbf{B}_{1,2}$ representations are related by a local gauge transformation and therefore define the same PEPS on tori and cylinders [65].

Since ρ_v is a sum of spin representations it carries a U(1) action

$$U(\varphi) : |v\rangle + |w\rangle \in \mathbf{0} \oplus \tfrac{\mathbf{1}}{\mathbf{2}} \mapsto |v\rangle + e^{i\varphi}|w\rangle \tag{34}$$

which modifies the relative phase of vectors in the spin-0 and spin-$\frac{1}{2}$ subspaces. States in the representations $\mathbf{A}_1^{\varphi}, \mathbf{A}_1^{3\varphi}, \mathbf{A}_2^{3\varphi}$ that define the local tensor have different eigenvalues φ (3φ) under this group action such that a simultaneous group action on all four virtual legs changes the parameter λ_1 relative to $\lambda_{2,c}$,

$$\mathcal{A}(\lambda_1, e^{2i\varphi}\lambda_2, e^{2i\varphi}\lambda_c) = e^{-i\varphi}\mathcal{A}(\lambda_1, \lambda_2, \lambda_c) \circ U(\varphi)^{\otimes 4}. \tag{35}$$

The transformation (35) implies that on an even-by-even torus the PEPS with parameters $(\lambda_1, \lambda_2, \lambda_c)$ is equal to the state with parameters $(\lambda_1, -\lambda_2, -\lambda_c)$. In particular it is real if either λ_2 or λ_c vanishes. For a proof we multiply all four virtual legs corresponding to tensors on the sublattice Λ_A (Λ_B) with $U(\pi/2)$ ($U(-\pi/2)$) such that the two transformations cancel each other on every bond and the tensor network remains invariant. On the other hand, according to Eq. (35) the U(1) transformations change the parameters of every local tensor as $(\lambda_1, \lambda_2, \lambda_c) \mapsto (\lambda_1, -\lambda_2, -\lambda_c)$ up to a phase which cancels on a patch of 2×1 lattice sites.

B. Transfer matrix symmetries

In this section we study the symmetries of the transfer matrix Γ of the translation invariant PEPS $|\psi_1\rangle$ on cylinders of even width N_v. Our results are summarized in Table II. Since the two transfer matrices are unitarily equivalent after blocking four columns up to the insertion of a horizontal flux line for $N_v \in 4\mathbb{N} + 2$ (see Sec. III), our results apply also to the point-group symmetric state $|\psi_2\rangle$ after corresponding transformations of the quantum numbers. The notation $\mathcal{O}_1 \otimes \mathcal{O}_2$ refers to a linear operator for a double-layer column of virtual spins that is a tensor product of two operators $\mathcal{O}_{1,2} \in \text{End}(\mathcal{H}_{sl})$ acting on the ket layer and bra layer separately. We denote by $\mathbf{l} \equiv (l_0, \ldots, l_{N_v-1}) \in \{0, \ldots, D-1\}^{N_v}$ a multi-index for the

TABLE II. Operators commuting with the transfer matrix Γ which define quantum numbers (upper part) or which create multiplets (lower part) according to Eq. (39) and Eq. (43) [we exclude the SU(2) ladder operators]. Here, $\epsilon = 0$ ($\epsilon = 1$) for the integer (half-integer) spin sector. The table is valid also for the transfer matrix $\Gamma^{(h)}$ with a horizontal flux line in both layers after substitution of the dressed translation operator $T^{dl}_{(h)}$ for T^{dl}.

Operator	Symbol	Properties	Quantum numbers
Transfer matrix	Γ	(Anti-) Hermitian for s^z_{dl} (half-)integer	E
SU(2) spin	$\sum_a \rho_{dl}(S^a)^2$, $\rho_{dl}(S^z)$	Hermitian	s_{dl}, s^z_{dl}
$\mathbb{Z}_2$ charges	$Z^{\otimes N_v} \otimes \mathbb{1}^{\otimes N_v}$, $\mathbb{1}^{\otimes N_v} \otimes Z^{\otimes N_v}$	Hermitian & unitary	Z_k, Z_b
Translation	T^{dl}	Unitary	K^{dl}
Layer inversion	I	Antiunitary	$E \mapsto (-1)^\epsilon E$, $K^{dl} \mapsto -K^{dl}$, $Z_k \leftrightarrow Z_b$
Dressed mirror	$\mathcal{R}^{dl}_x$	Antiunitary	$E \mapsto (-1)^\epsilon E$, $K^{dl} \mapsto K^{dl} + \epsilon\pi$

single-layer virtual space $\mathcal{H}_{sl}$ and by $\mathbf{L} = (\mathbf{l}, \tilde{\mathbf{l}})$ a multi-index for the double-layer space $\mathcal{H}_{sl} \otimes \mathcal{H}_{sl}$.

1. SU(2) symmetry

Spin rotations applied to the physical leg of the local tensor C can be pushed to the virtual layer and factorize as a product of representations acting on every virtual leg individually. Due to the virtual spin flips contained in the definition (26) of C, its left and down (up and right) virtual legs transform in the representation ρ^*_v (ρ_v). This may be interpreted as an ingoing (outgoing) transformation $\rho_v(g^{-1})$ ($\rho_v(g)$) acting on the left and down (up and right) virtual legs of C as sketched in Fig. 9. The complex conjugate tensor C^* for the bra layer transforms under SU(2) in a similar fashion but with conjugate representations ρ^*_{phys} for the physical leg and ρ_v (ρ^*_v) for the left and down (up and right) virtual legs. Hence, Γ commutes with simultaneous SU(2) transformations

$$\rho_{dl} = \rho_{sl} \otimes \rho^*_{sl} = \rho_v^{\otimes N_v} \otimes (\rho_v^*)^{\otimes N_v} \tag{36}$$

of all virtual spins in both layers.

2. Virtual $\mathbb{Z}_2$ symmetry

The total charge $Z^{\otimes N_v}$ of the virtual $\mathbb{Z}_2$ symmetry is conserved independently in both layers of the transfer matrix [see Eq. (16)]. We denote the eigenvalues of the ket-layer and bra-layer operators $Z^{\otimes N_v} \otimes \mathbb{1}^{\otimes N_v}$ and $\mathbb{1}^{\otimes N_v} \otimes Z^{\otimes N_v}$ by Z_k and Z_b, respectively. One has

$$Z^{\otimes N_v} = \rho_{sl}(e^{2\pi i S^z}) \tag{37a}$$

$$Z^{\otimes N_v} \otimes Z^{\otimes N_v} = \rho_{dl}(e^{2\pi i S^z}) \tag{37b}$$

such that the configurations $(Z_k, Z_b) \in \{(1,1), (-1,-1)\}$ ($\{(1,-1), (-1,1)\}$) correspond to integer (half-integer) double-layer virtual spin $\rho_{dl}(S^z)$.

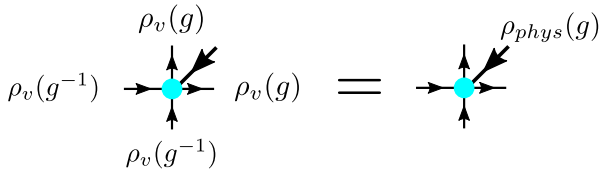

FIG. 9. Factorization of a physical spin rotation as a product of virtual SU(2) transformations for the local tensor C of the translation invariant PEPS $|\psi_1\rangle$. The arrow directionality is a consequence of the singlet absorption pattern.

3. Translation invariance

The transfer matrix Γ commutes with the unitary translation operator $T^{dl} \equiv (T^{sl})^{\otimes 2}$ defined by

$$T^{sl}_{\mathbf{lr}} = \delta_{l_0,r_1}\delta_{l_1,r_2}\cdots\delta_{l_{N_v-1},r_0}. \tag{38}$$

The single-layer (double-layer) translation operator satisfies $(T^{sl(dl)})^{N_v} = \mathbb{1}$ such that the momenta are $K^{sl(dl)} = 2\pi n/N_v$ with $n = 0, \ldots, N_v - 1$.

4. Layer inversion

The transfer matrix is complex conjugated when the indices in its ket and bra layers are exchanged, i.e., $\mathbf{L} = (\mathbf{l}, \tilde{\mathbf{l}}) \mapsto \mathbf{L}' = (\tilde{\mathbf{l}}, \mathbf{l})$. Formally, Γ commutes with an antiunitary operator $I = \mathcal{C} \circ \tilde{I}$ where $\tilde{I}$ is a unitary double-layer operator with basis elements $\tilde{I}_{\mathbf{LR}} = \delta_{\tilde{\mathbf{l}}\mathbf{r}}\delta_{\tilde{\mathbf{r}}\mathbf{l}}$ and $\mathcal{C}$ denotes complex conjugation in this basis. The layer inversion operator satisfies $I^2 = \mathbb{1}$ and commutes with spin rotations and translation. It exchanges the ket layer and bra layer $\mathbb{Z}_2$ charges,

$$I \circ (Z^{\otimes N_v} \otimes \mathbb{1}^{\otimes N_v}) = (\mathbb{1}^{\otimes N_v} \otimes Z^{\otimes N_v}) \circ I. \tag{39}$$

5. Hermiticity

The Hermitian conjugate of the transfer matrix is defined as $(\Gamma^\dagger)_{\mathbf{LR}} = (\Gamma_{\mathbf{RL}})^*$. Since the local projection map [Eq. (33)] transforms in the representation $\sigma = \mathbf{A}_1 + i\mathbf{A}_2$ of C_{4v} the local tensor C behaves under the exchange of its left and right virtual indices as $C_{ruld} = \sum_{l'r'} Y_{ll'}(C^s_{l'ur'd})^* Y_{r'r}$. Due to the SU(2) symmetry of the transfer matrix this implies

$$\Gamma^\dagger = \Gamma \circ \rho_{dl}(e^{2\pi i S^z}) \tag{40}$$

such that the transfer matrix is Hermitian (anti-Hermitian) for integer (half-integer) double-layer virtual spin $\rho_{dl}(S^z)$. Hence, the transfer matrix eigenvalues E are real (purely imaginary) for integer (half-integer) spin and complex conjugation acts as $E \mapsto (-1)^\epsilon E$ with $\epsilon = 0$ ($\epsilon = 1$), respectively.

6. Dressed mirror symmetry

We denote by $\mathcal{M}^{sl}_x$ the unitary operator that reflects the virtual spins in a single-layer column about the (nonperiodic) x axis with basis elements

$$\left(\mathcal{M}^{sl}_x\right)_{\mathbf{lr}} = \delta_{l_0,r_{N_v-1}}\delta_{l_1,r_{N_v-2}}\cdots\delta_{l_{N_v-1},r_0}, \tag{41}$$

and by $\mathcal{M}^{dl}_x = (\mathcal{M}^{sl}_x)^{\otimes 2}$ its double-layer variant. Transposition of the up and down virtual indices modifies the PEPS local tensor as $C_{ldru} = \sum_{d'u'} Y_{dd'} Y_{u'u} (C^s_{lu'rd'})^*$. The application of

$\mathcal{M}_x^{dl}$ to the virtual legs on the left and right of the transfer matrix therefore amounts to a complex conjugation of Γ as well as the insertion of a matrix $Y^2 = Z$ on every vertical bond in both layers. These insertions can be removed by multiplying every other horizontal virtual leg with Z. Hence Γ commutes with the staggered antiunitary operator

$$\mathcal{R}_x^{dl} \equiv \mathcal{C} \circ (Z \otimes \mathbb{1} \otimes \cdots \otimes Z \otimes \mathbb{1})^{\otimes 2} \circ \mathcal{M}_x^{dl} \circ \rho_{dl}(e^{i\pi S^y}), \tag{42}$$

where $\mathcal{C}$ denotes complex conjugation. We included the spin flip $\rho_{dl}(e^{i\pi S^y})$ to make sure that $\mathcal{R}_x^{dl}$ commutes with global spin rotations and that it squares to the identity $(\mathcal{R}_x^{dl})^2 = \mathbb{1}$. Due to its staggering the dressed mirror operator satisfies

$$\left(\mathcal{R}_x^{dl}\right)^{-1} \circ T^{dl} \circ \mathcal{R}_x^{dl} = (T^{dl})^\dagger \circ \rho_{dl}(e^{2\pi i S^z}), \tag{43}$$

where the last factor causes a momentum shift by π for half-integer spin. Analogous relations hold in a single-layer column with the single-layer dressed mirror operator $\mathcal{R}_x^{sl} \equiv \mathcal{C} \circ (Z \otimes \mathbb{1} \otimes \cdots \otimes Z \otimes \mathbb{1}) \circ \mathcal{M}_x^{sl} \circ \rho_{sl}(e^{i\pi S^y})$.

C. Spectrum of Γ

The spectrum of the transfer matrix Γ can be analyzed using the symmetries listed in Table II. A maximal set of Hermitian or unitary operators that commute with the transfer matrix and explains all numerically observed degeneracies is given by the spin operators, the translation operator, and the $\mathbb{Z}_2$ charges. Joint eigenstates of this set are given by

$$|X\rangle = \left|E, s_{dl}, s_{dl}^z, K^{dl}, Z_k, Z_b\right\rangle, \tag{44}$$

where $\Gamma|X\rangle = E|X\rangle$, $\sum_{a=x,y,z}(\rho_{dl}(S^a))^2|X\rangle = s_{dl}(s_{dl}+1)|X\rangle$, $\rho_{dl}(S^z)|X\rangle = s_{dl}^z|X\rangle$, and $T^{dl}|X\rangle = e^{iK^{dl}}|X\rangle$. On the other hand, the antiunitary layer inversion and dressed mirror operators commute with the transfer matrix and spin rotations but not with the translation and the $\mathbb{Z}_2$ charges, see Eq. (39) and Eq. (43). Hence they create multiplets of states with the same spin quantum numbers and whose transfer matrix eigenvalues have the same absolute value $|E|$ but which have different momenta and $\mathbb{Z}_2$ charges. These multiplets are spanned by $|X\rangle$ together with the states

$$I|X\rangle = \left|(-1)^\epsilon E, s_{dl}, s_{dl}^z, -K^{dl}, Z_b, Z_k\right\rangle, \tag{45a}$$

$$\mathcal{R}_x^{dl}|X\rangle = \left|(-1)^\epsilon E, s_{dl}, s_{dl}^z, K^{dl}+\epsilon\pi, Z_k, Z_b\right\rangle, \tag{45b}$$

$$\mathcal{R}_x^{dl} \circ I|X\rangle = \left|E, s_{dl}, s_{dl}^z, -K^{dl}+\epsilon\pi, Z_b, Z_k\right\rangle, \tag{45c}$$

where $\epsilon = 0$ ($\epsilon = 1$) and the transfer matrix eigenvalues are real (purely imaginary) for integer (half-integer) s_{dl}^z, respectively. The complex conjugation $E \mapsto (-1)^\epsilon E$ and the momentum inversion $K^{dl} \mapsto -K^{dl}$ are a consequence of the antiunitarity of I and $\mathcal{R}_x^{dl}$ whereas the momentum shift $\epsilon\pi$ is caused by the spin-dependent sign factor in Eq. (43). For half-integer spin these four states are linearly independent such that there are four redundant spectra with $Z_k \neq Z_b$.

On the other hand, for integer spin the dressed mirror symmetry does not cause any degeneracies [66]. The two-dimensional multiplet for $K^{dl} \neq 0, \pi$ is spanned by $|X\rangle$, $I|X\rangle$ whereas these two states are identical for $K^{dl} = 0, \pi$ [65].

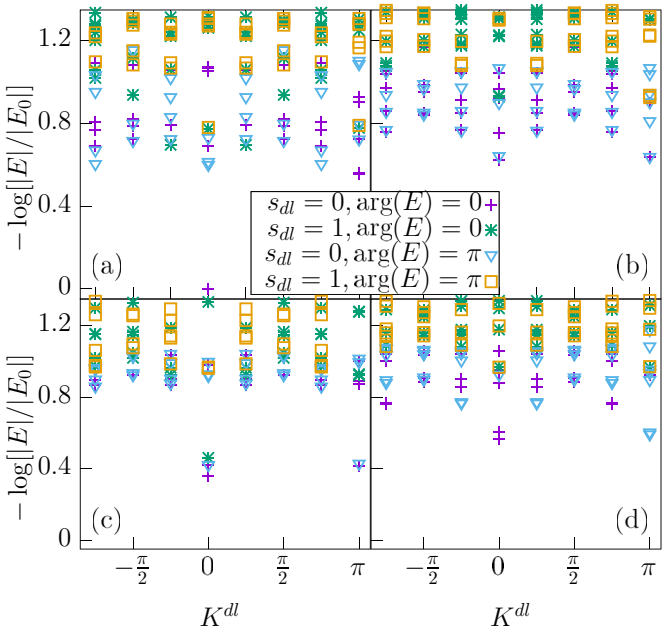

FIG. 10. Spectrum of minus the logarithm of the transfer matrix for PEPS parameters $\lambda_1 = \lambda_2 = \lambda_c = 1$, $N_v = 8$ and different topological sectors $Z_k = Z_b = 1$ in (a), $Z_k = Z_b = -1$ in (b), $Z_k = Z_b = 1$ and a vison line in both layers in (c), and $Z_k = Z_b = -1$ and a vison line in both layers in (d). These spectra are expected to give the minima of the dispersion relation of the topologically trivial excitations of a local parent Hamiltonian above the corresponding topological ground state at the point $k_x = \arg(E)$, $k_y = K^{dl}$ in the two-dimensional Brillouin zone (see main text). In all cases we show only the first few leading eigenvalues per spin and momentum sector. States with higher spin appear at higher values of $-\log[|E|/|E_0|]$ and are not shown here.

The spectrum of minus the logarithm of the transfer matrix without flux lines for $\lambda_1 = \lambda_2 = \lambda_c = 1$ and $N_v = 8$ is shown in Fig. 10(a) for $Z_k = Z_b = 1$ and Fig. 10(b) for $Z_k = Z_b = -1$. This spectrum is expected to reproduce the relative energy of the minima of the dispersion relation of a local parent Hamiltonian at the point $k_x = \arg(E)$, $k_y = K^{dl}$ in the two-dimensional Brillouin zone (BZ) [67,68]. Due to the reflection symmetry discussed in Sec. IV B 5 the transfer matrix in these sectors is Hermitian with real eigenvalues such that we probe two lines of the BZ where $k_x = 0, \pi$. Since each plot contains only states in the same topological sector of the $\mathbb{Z}_2$ symmetry the data we show describes topologically trivial excitations which are expected to be identical in every topological sector in the thermodynamic limit. Indeed, the dispersion relation for states with given spin is similar in all considered topological sectors with minima at $K^{dl} = 0, \pi$ and maxima at $K^{dl} = \pi/2, 3\pi/2$. The spectrum appears gapless without visible branches of single-particle excitations in agreement with the expectation that chiral topological PEPS are gapless [29,31]. An exception is the lowest level at zero momentum in the $\mathbb{Z}_2$-even sector whose gap to the rest of the states may be a finite-size effect [31]. The quasienergy of the lowest excitations with given spin grows with s_{dl} such that the leading states all have zero spin. For $N_v = 8$, the lowest levels in either

topological sector lie at zero momentum and we will use the corresponding states to compute the ES in the next section.

D. Transfer matrix $\Gamma^{(h)}$ with horizontal flux string

The ground state manifold for a PEPS with a virtual $\mathbb{Z}_2$ symmetry includes the state $|\psi\rangle_{(h)}$ with a horizontal flux string along the cylinder as described in Sec. II D. The transfer matrix $\Gamma^{(h)}$ for this state is obtained from Γ by the insertion of a matrix Z on the vertical virtual bond between the sites $(N_v - 1, 0)$ both in the ket and the bra layer.

$\Gamma^{(h)}$ possesses the same symmetries as Γ except for translation which is replaced by a dressed translation operator which accounts for the changing position of the flux line. Indeed, translation by one lattice site in the vertical direction causes a shift of the Z insertions from the bond $(N_v - 1, 0)$ to the bond (0,1). The insertions can be returned to their original position by multiplying the external virtual legs of site 0 in both layers with matrices Z and exploiting the virtual $\mathbb{Z}_2$ symmetry of the local tensors on that site. The transfer matrix with a flux line therefore commutes with a unitary dressed translation operator

$$T^{dl}_{(h)} = \left(T^{sl}_{(h)}\right)^{\otimes 2} = (T^{sl} \circ (Z \otimes \mathbb{1} \otimes \mathbb{1} \otimes \cdots \otimes \mathbb{1}))^{\otimes 2}. \quad (46)$$

In contrast to the usual translation operator, the dressed translation satisfies

$$\left(T^{dl}_{(h)}\right)^{N_v} = \rho_{dl}(e^{2\pi i S^z}) \quad (47)$$

and thereby imposes antiperiodic boundary conditions for half-integer virtual spins. Correspondingly, the momentum takes integer (half-integer) values in the sector of integer (half-integer) spin $\rho_{dl}(S^z)$. Analogous statements hold for the single-layer dressed translation operator and momentum. The dressed translation operator satisfies Eq. (43) with the antiunitary dressed mirror operator such that Table II applies also to $\Gamma^{(h)}$ after substitution of $T^{dl}_{(h)}$ for T^{dl}.

The spectrum of minus the logarithm of the transfer matrix with a horizontal flux line in both layers for $\lambda_1 = \lambda_2 = \lambda_c = 1$ and $N_v = 8$ is shown in Fig. 10(c) for $Z_k = Z_b = 1$ and in Fig. 10(d) for $Z_k = Z_b = -1$. In the $\mathbb{Z}_2$-odd sector the spectrum is very similar to the case without flux line. In the $\mathbb{Z}_2$-even sector the dispersion of the states in the continuum appears flatter than without flux line. The minima at $K^{dl} = 0, \pi$ split into multiple levels each and appear at almost the same quasienergy that is significantly above the lowest state without flux line. Again, the leading states in either topological sector that we will use to compute the ES lie at zero spin and momentum.

E. Entanglement spectrum

In this section we investigate the ES of the chiral PEPS on an infinite cylinder in all topological sectors of the $\mathbb{Z}_2$ symmetry. As explained in Secs. II E and II F the ES is given by the leading eigenvectors of the transfer matrix according to Eq. (20). We begin by analyzing the symmetries of the ES, thereby providing an analytical explanation for the observation of two branches in the ES corresponding to the spin-$\frac{1}{2}$ field of $\mathfrak{su}(2)_1$ [34,35].

1. Symmetries of the entanglement spectrum

Any eigenstate $|X\rangle$ of the transfer matrix defines a virtual reduced density matrix σ_X with matrix elements $(\sigma_X)_{\mathbf{l}\tilde{\mathbf{l}}} = X_{(\mathbf{l},\tilde{\mathbf{l}})}$. If $|X\rangle$ is an eigenvector with eigenvalue μ of a double-layer operator $\mathcal{O}_1 \otimes \mathcal{O}_2$ the associated σ_X satisfies the relation

$$\mathcal{O}_1 \circ \sigma_X \circ \mathcal{O}_2^T = \mu\, \sigma_X, \quad (48)$$

where $\mathcal{O}_{1,2}$ are single-layer operators. Applied to the double-layer spin (translation) Eq. (48) implies that the virtual density matrix of a double-layer eigenstate with $s_{dl} = 0$ ($K^{dl} = 0$) commutes with the single-layer spin (translation). On the other hand, $Z_{k,b}$ determine the eigenvalue of $Z^{\otimes N_v}$ on the image and support of σ_X. Equation (48) applies also to antiunitary double-layer operators such as the mirror $\mathcal{R}^{dl}_x$. Its fixed points are therefore associated with mirror-symmetric reduced density matrices $\sigma_X \mathcal{R}^{sl}_x = Z^{\otimes N_v} \mathcal{R}^{sl}_x \sigma_X$. Moreover, layer inversion maps the virtual density matrix to its Hermitian conjugate such that fixed points of I correspond to Hermitian virtual density matrices.

We now show that the ES derived from a transfer matrix eigenstate $|X\rangle$ with zero spin and momentum and $Z_k = Z_b = -1$ contains two degenerate branches related by a momentum shift $K^{sl} \mapsto K^{sl} + \pi$. Provided that there are no accidental degeneracies, we can choose the phase of $|X\rangle$ such that the density matrix σ_X is Hermitian and commutes or anticommutes with $\mathcal{R}^{sl}_x$. In the $\mathbb{Z}_2$-odd sector the dressed mirror causes a momentum shift of π according to Eq. (43). Hence, any density matrix eigenstate $\sigma_x|v\rangle = e^{-\xi/2}|v\rangle$ has an orthogonal mirror image $\mathcal{R}^{sl}_x|v\rangle$ with the same entanglement energy ξ but momentum shifted by π. As long as the dressed mirror symmetry is not broken, the ES of this state therefore contains two exactly degenerate branches shifted in momentum by π.

2. Numerical results

The ES of the leading eigenstates is shown in Fig. 11 for $\lambda_1 = \lambda_2 = \lambda_c = 1$ and $N_v = 8$. The ES for the PEPS without flux line in (a) and (b) display a linear dispersion relation where the number of low-lying states per momentum sector is that expected for the chiral CFT $\mathfrak{su}(2)_1$. Due to the dressed mirror symmetry of the transfer matrix the spectrum (b) in the half-integer spin sector possesses two branches shifted in momentum by π as discussed above. Moreover, the estimated conformal weight of the half-integer sector is much larger than the expected value of 1/4. In the half-integer spin sector the ES in Fig. 11(d) with a flux line looks very similar to the ES without flux line up to an overall momentum shift of 1/2 due to the antiperiodic boundary conditions. However, the ES with a horizontal flux line in the integer spin sector has some chiral features but does not possess a single mode with the state counting of $\mathfrak{su}(2)_1$. Up to now, we were not able to find a simple CFT with the state counting of this ES.

V. CHIRAL SPIN LIQUID PEPS FOR $\lambda_1 = 0$

In this section we study the chiral spin-$\frac{1}{2}$ liquid PEPS for $\lambda_1 = 0$. This case is interesting since the PEPS possesses an additional virtual U(1) symmetry provided that the lattice is bipartite. Such a symmetry appears also for the nearest-neighbor RVB PEPS [38] albeit with a different charge per

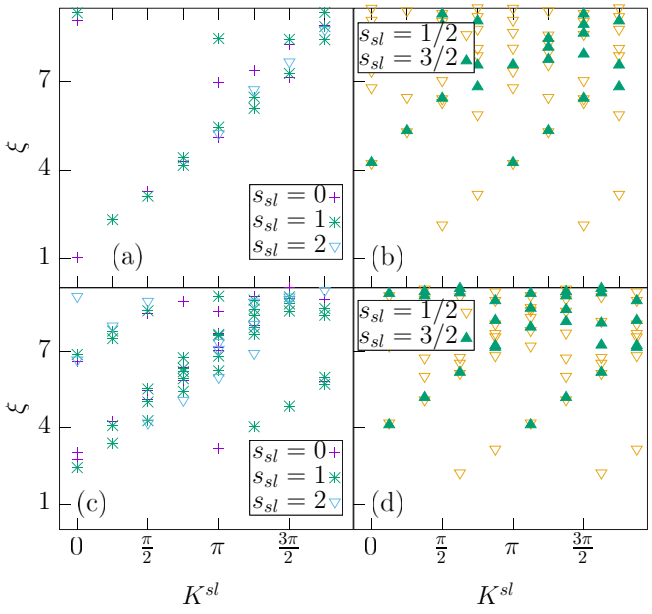

FIG. 11. Entanglement spectrum for the leading eigenvectors of the transfer matrix with $\lambda_1 = \lambda_2 = \lambda_c = 1$ and $N_v = 8$ in the diagonal sectors with $Z_k = Z_b = 1$ in (a), (c) and $Z_k = Z_b = -1$ in (b), (d) and a vison line in both layers for (c), (d). The ES in (a) has a single chiral mode with the integer-spin state counting of the chiral CFT $\mathfrak{su}(2)_1$. The ES in (b) and (d) are very similar and are symmetric under a momentum shift of π caused by the dressed mirror operator. In the region $0 \leqslant K^{sl} \leqslant \pi$ they have a single chiral mode with the half-integer-spin state counting of $\mathfrak{su}(2)_1$. The ES in (c) has some chiral features but possesses multiple branches whose state counting could not be related to a simple CFT.

unit cell. After defining the U(1) symmetry in Sec. V A we analyze its implications for the transfer matrix spectrum in Sec. V B. Moreover we provide numerical evidence that not all charge sectors lead to independent physical states and identify the dominant sectors. In Sec. V C we compute the ES of the leading independent states with fixed charge and show that the half-integer spin sector has a single chiral branch and does not contain any degeneracies created by the dressed mirror symmetry. Furthermore we show that the estimated conformal weight is very close to the value expected for $\mathfrak{su}(2)_1$ when $\lambda_c \approx \lambda_2$.

A. Staggered virtual U(1) symmetry

The virtual Hilbert space $\mathbf{0} \oplus \frac{\mathbf{1}}{\mathbf{2}}$ carries a virtual U(1) action $U(\varphi)$ defined in Eq. (34) that changes the relative phase of vectors in the two spin subspaces. Generically this phase rotation maps the local PEPS tensor to a different point in the parameter space, $(\lambda_1, \lambda_2, \lambda_c) \mapsto (\lambda_1, e^{2i\varphi}\lambda_2, e^{2i\varphi}\lambda_c)$ [see Eq. (35)]. However, if either $\lambda_2 = \lambda_c = 0$ or $\lambda_1 = 0$ all non-vanishing configurations in the local tensor acquire the same phase under this operation such that

$$\mathcal{A} \circ U(\varphi)^{\otimes 4} = e^{in\varphi}\mathcal{A}, \tag{49}$$

where the charge is $n = 3$ ($n = 1$) for $\lambda_1 = 0$ ($\lambda_2 = \lambda_c = 0$). This identity is very similar to the definition of the virtual $\mathbb{Z}_2$ symmetry in Eq. (16). However, Eq. (49) implies the existence of a global virtual U(1) symmetry for the PEPS only if the lattice is bipartite. Indeed, invariance of the state requires that the left and right (top and bottom) virtual legs of every unit cell transform in mutually conjugate representations. On a bipartite lattice with a unit cell of 2×2 sites one can therefore construct a staggered symmetry by combining transformations $U(\varphi)$ and $U(-\varphi)$ for sites on Λ_A and Λ_B, respectively. This staggering of the U(1) symmetry will become crucial in order to obtain an ES with only a single branch in the half-integer sector.

When expressed in terms of the generator

$$Q = -i(\partial_\varphi U(\varphi))|_{\varphi=0} = \begin{pmatrix} 0 & 0 & 0 \\ 0 & 1 & 0 \\ 0 & 0 & 1 \end{pmatrix} \tag{50}$$

which counts the number of virtual legs in the spin-$\frac{1}{2}$ virtual representation, the relation (49) translates into a virtual Gauss law

$$\mathcal{A} \circ \big[Q \otimes \mathbb{1} \otimes \mathbb{1} \otimes \mathbb{1} + \mathbb{1} \otimes Q \otimes \mathbb{1} \otimes \mathbb{1} + \mathbb{1} \otimes \mathbb{1} \otimes Q \otimes \mathbb{1} + \mathbb{1} \otimes \mathbb{1} \otimes \mathbb{1} \otimes Q\big] = n\,\mathcal{A}. \tag{51}$$

For $\lambda_1 = 0$, $n = 3$ in Eq. (51) implying that exactly three virtual legs of every local tensor are in the spin-$\frac{1}{2}$ state. On the other hand, for the nearest-neighbor RVB state obtained at $\lambda_2 = \lambda_c = 0$ one finds $n = 1$ such that exactly one virtual leg is in the spin-$\frac{1}{2}$ state [38].

Similarly to the case of discrete virtual symmetries one can consider states obtained from the chiral PEPS by inserting strings of virtual U(1) operators along noncontractible loops of the manifold. For any local parent Hamiltonians these states are indistinguishable from the original PEPS when $\lambda_1 = 0$. On a cylinder the minimally entangled states with respect to a vertical entanglement cut are generated by insertion of flux strings in the horizontal direction on one hand and projection on sectors of fixed charge in the vertical direction on the other hand. The conserved charge of the staggered virtual U(1) symmetry acting on one column of virtual boundary legs is

$$Q_{sl} = \sum_{i=0}^{N_v-1} (-1)^i Q_{(i)} \tag{52}$$

with integer eigenvalues q in the range $-N_v/2 \leqslant q \leqslant N_v/2$. In Eq. (52), the subscript i indicates on which virtual spin the local generator (50) acts and the factor $(-1)^i$ accounts for the staggering of the virtual symmetry. The local $\mathbb{Z}_2$ matrix is a special case of a U(1) rotation, $Z = U(\pi)$. Therefore, even (odd) charges q correspond to trivial (nontrivial) $\mathbb{Z}_2$ charge. Moreover, the single-layer spin in a given charge sector is constrained as

$$\left|2s^z_{sl}\right| \leqslant N_v - |q|. \tag{53}$$

In the following we focus on analyzing the PEPS with fixed vertical charge q and without horizontal U(1) flux strings.

B. Transfer matrix

In this section we analyze the consequences of the staggered virtual U(1) symmetry at $\lambda_1 = 0$ for the spectrum of the transfer matrix Γ on a cylinder of even N_v.

1. Quantum numbers

Due to the virtual Gauss law (51) the single-column transfer matrix anticommutes with the generator (52) applied to both the ket and bra layer separately,

$$Q_k = Q_{sl} \otimes \mathbb{1}, \tag{54a}$$

$$Q_b = \mathbb{1} \otimes Q_{sl}. \tag{54b}$$

As discussed above, the corresponding charges q_k and q_b in the ket and bra layer take values $-N_v/2 \leqslant q_k, q_b \leqslant N_v/2$ and define a bound for the double-layer spin,

$$\left|2s^z_{dl}\right| \leqslant |2N_v - |q_k| - |q_b||. \tag{55}$$

The double-column transfer matrix Γ^2 for the PEPS on a patch of size $2 \times N_v$ therefore commutes with $Q_{k,b}$ and thus possesses a U(1) × U(1) symmetry with generators (54).

It is natural to analyze the spectrum of the transfer matrix in terms of the U(1) charges q_k, q_b. However, this is not compatible with the set of quantum numbers from Table II that we used for the single-column transfer matrix at arbitrary PEPS parameters $\lambda_1, \lambda_2, \lambda_c$. Indeed, due to their staggering the generators $Q_{k,b}$ generally anticommute both with the translation operator and the single-column transfer matrix. We therefore pass to a modified set of quantum numbers given by the double-column transfer matrix Γ^2, the U(1) generators Q_k, Q_b, the SU(2) spin operators, double-step translation $(T^{dl})^2$, and the product ΓT^{dl} of the single-column transfer matrix and single-step translation (individually, both of these operators anticommute with the U(1) generators). We refer to joint eigenstates of this commuting set as

$$|\tilde{X}\rangle = \left|E^2, s_{dl}, s^z_{dl}, \tilde{K}^{dl}, \mu, q_k, q_b\right\rangle, \tag{56}$$

where $\Gamma^2|\tilde{X}\rangle = E^2|\tilde{X}\rangle$, the spin quantum numbers are as defined above, and the momentum of the double-step translation takes values $\tilde{K}^{dl} = 2\pi n/(N_v/2)$ with $0 \leqslant n \leqslant N_v/2 - 1$. The quantum number μ is defined as the eigenvalue of ΓT^{dl} and satisfies $\mu^2 = E^2 e^{i\tilde{K}^{dl}}$ so that it can take only two values once the transfer matrix weight and double-step momentum are fixed.

Alternatively one can use the set of quantum numbers from Table II extended by the products $q_k^2, q_b^2, q_k q_b$ which are compatible with single-step translation. The resulting joint eigenstates

$$|X\rangle = \left|E, s_{dl}, s^z_{dl}, K^{dl}, q_k^2, q_b^2, q_k q_b\right\rangle \tag{57}$$

generally are linear superpositions of multiple eigenstates $|\tilde{X}\rangle$ defined in Eq. (56).

In the following we will use the basis given by Eq. (56) to analyze the transfer matrix spectrum. A special situation arises in the sector with $q_k = q_b = 0$ where $Q_{k,b}$ are identically zero and therefore commute with the single-column transfer matrix and single-step translation operator. In this case we recover the single-step momentum as a quantum number and the eigenstates Eq. (57) are in one-to-one correspondence with the states Eq. (56).

2. Multiplets

The spectrum of the square of the transfer matrix contains multiplets of states with the same weight E^2 and spin quantum numbers but different values for the momentum, U(1) charges or quantum number μ. In terms of the eigenstates defined in Eq. (56) these multiplets are created by layer inversion I, the dressed mirror symmetry $\mathcal{R}^{dl}_x$, and their combination which act on the quantum numbers as [69]

$$I: \quad \tilde{K}^{dl} \mapsto -\tilde{K}^{dl},\ \mu \mapsto \mu^*,\ q_k \leftrightarrow q_b \tag{58a}$$

$$\mathcal{R}^{dl}_x: \quad \tilde{K}^{dl} \mapsto \tilde{K}^{dl},\ \mu \mapsto \mu,\ q_{k,b} \mapsto -q_{k,b}. \tag{58b}$$

Hence there are four degenerate states whenever (i) $|q_k| \neq |q_b|$ or (ii) $|q_k| = |q_b| \neq 0$ and $\tilde{K}^{dl} \neq 0$. Similarly one finds that there are two degenerate states when (iii) $|q_k| = |q_b| \neq 0$ and $\tilde{K}^{dl} = 0$ or (iv) $q_k = q_b = 0$ and $\tilde{K}^{dl} \neq 0$. Compared to general values of the parameters $(\lambda_1, \lambda_2, \lambda_c)$ the spectrum at $\lambda_1 = 0$ therefore contains larger multiplets of degenerate states.

For any given diagonal sector with nonzero charge $q_k = q_b = q$ this discussion implies that the leading transfer matrix eigenstate

$$|\tilde{X}_0\rangle_{(q,q)} \tag{59}$$

is exactly degenerate with the leading state with opposite charge $q_k = q_b = -q$. Numerically we found that these leading states have zero spin as well as zero momentum with respect to the double-step translation operator. Therefore they are invariant under layer inversion I, and their degeneracy is due to the dressed reflection symmetry of the transfer matrix. Numerically we observe that there are no additional degeneracies. Since single-step translation also reverses the sign of the charges, $q_{k,b} \mapsto -q_{k,b}$, we can therefore choose a basis such that

$$|\tilde{X}_0\rangle_{(-q,-q)} = T^{dl}\,|\tilde{X}_0\rangle_{(q,q)}. \tag{60}$$

Thus we can construct eigenstates with well-defined single-step momentum $K^{dl} = 0, \pi$ and $q_k^2 = q_b^2 = q_k q_b = q^2$ as linear superpositions

$$|X_0\rangle_{K^{dl}=0,N} = \frac{1}{\sqrt{2}}[|\tilde{X}_0\rangle_{(q,q)} \pm |\tilde{X}_0\rangle_{(-q,-q)}] \tag{61}$$

of the two degenerate states with well-defined charges. The states (59) and (60) are not stable under perturbations of the PEPS induced by small nonvanishing values of λ_1 due to the breaking of the U(1) symmetry for any nonvanishing λ_1. On the other hand we expect that to first order in λ_1 the states (61) remain eigenstates of the transfer matrix although degeneracy will be lifted.

3. Dominant sectors on finite-site cylinders

The chiral PEPS at $\lambda_1 = 0$ gives rise to an extensive number of states obtained by projecting the virtual boundary vector at one end of the cylinder onto a given eigenvalue sector of the conserved charge Q_{sl}. However, it is not clear whether all of these boundary sectors correspond to independent physical states in the thermodynamic limit. Indeed, some of these states may have vanishing norm or correspond to a linear superposition of other states in the limit $N_v \to \infty$ as has been observed for free fermionic chiral PEPS [30]. For long cylinders the quotient of the norm of two states $|\psi_q\rangle$ and $|\psi_p\rangle$ with fixed boundary charges q and p is expected to

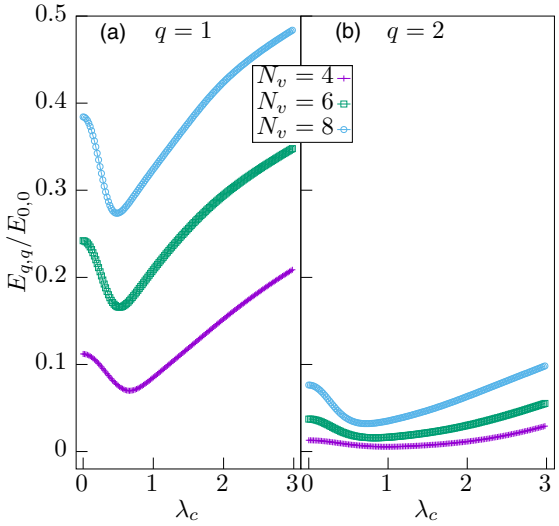

FIG. 12. Normalized leading eigenvalue $E_{q,q}/E_{0,0}$ of the double column transfer matrix in the diagonal sector $q_k = q_b = q$ as a function of λ_c for $\lambda_1 = 0$, $\lambda_2 = 1$, different cylinder widths N_v, and $q = 1$ in (a) and $q = 2$ in (b). On long cylinders, this ratio is expected to determine the relative norm of the states in different U(1) sectors according to Eq. (62).

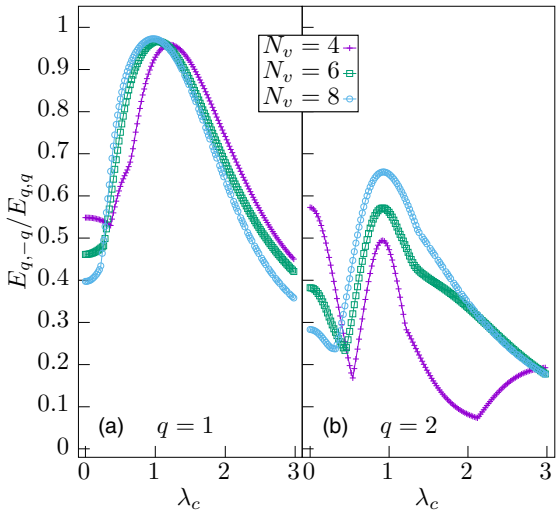

FIG. 13. Ratio of the leading transfer matrix eigenvalues in the off-diagonal and diagonal sectors with $q_k = -q_b = q$ and $q_k = q_b = q$ as a function of λ_c for $\lambda_1 = 0$, $\lambda_2 = 1$, different cylinder widths N_v and $q = 1$ in (a) and $q = 2$ in (b). On long cylinders, this ratio is expected to determine the overlap of the states in different U(1) sectors according to Eq. (63). Since the normalized overlap for $q = 1$ is very close to unity when $\lambda_c \approx \lambda_2$ we expect that the states $|\psi_1\rangle$ and $|\psi_{-1}\rangle$ become identical in the thermodynamic limit in this region.

approach [46]

$$\langle\psi_q|\psi_q\rangle/\langle\psi_p|\psi_p\rangle \approx \left(\frac{E_{q,q}}{E_{p,p}}\right)^{N_h/2}, \tag{62}$$

where $E_{q,q}$ refers to the dominant eigenvalue of the double-column transfer matrix in the diagonal sector where the bra-layer and ket-layer charges are $q_b = q_k = q$. Moreover, the dominant eigenvalues of the transfer matrix in the off-diagonal sectors with $q_k \neq q_b$ determine the overlap of two normalized states [46]

$$\langle\psi_q|\psi_p\rangle \approx \left(\frac{E_{q,p}}{\sqrt{E_{q,q}E_{p,p}}}\right)^{N_h/2}. \tag{63}$$

In order to study the overlap and weight of different sectors we have performed exact diagonalization of the double-column cylinder transfer matrix including the quantum numbers q_k, q_b for the numerically accessible values of the cylinder width N_v. The normalized leading eigenvalue $E_{q,q}/E_{0,0}$ in the diagonal sector for U(1) charges $q = 1, 2$ is displayed in Fig. 12 as a function of the PEPS parameter λ_c for $\lambda_2 = 1$ and for system sizes $N_v = 4, 6, 8$. For all considered values of λ_c and N_v, the ratio $E_{q,q}/E_{0,0}$ decreases with increasing q and is much smaller than unity if $|q| > 1$ (for $N_v = 8$ we find that $E_{3,3}/E_{0,0} \sim 10^{-3}$ and $E_{4,4}/E_{0,0} \sim 10^{-4}$, respectively). The normalized overlap $E_{q,-q}/E_{q,q}$ for $q = 1, 2$ and $N_v = 4, 6, 8$ is displayed as a function of λ_c in Fig. 13. For both values of q and all system sizes the overlap increases rapidly for $0.5 \leqslant \lambda_c \leqslant 1$, has a maximum in the vicinity of $\lambda_c = 1$, and decreases again for bigger values of λ_c. The overlap for $q = 1$ ($q = 2$) appears to increase with N_v for $\lambda_c \leqslant 1.3$ ($\lambda_c \leqslant 2$). For $N_v = 8$ the maximal overlap for $q = 1$ is above 97% whereas for $q = 2$ the maximal value is around 65% but does not appear to be converged as a function of the system size. All in all, the dominant sectors for small cylinder width N_v are therefore those with small U(1) charges $|q| \leqslant 1$ where the states with $q = 1$ and $q = -1$ that are related by a single-step translation have a very large overlap above 97%. Since we are restricted to small systems the finite-size scaling in Figs. 12 and 13 is not conclusive. However, it is consistent with the hypothesis that the only two independent leading sectors in the thermodynamic limit are those with $q = 0$ and $q = 1$.

C. Entanglement spectrum

The ES for a PEPS on an infinite cylinder is obtained from all transfer matrix eigenstates whose eigenvalues approach the leading eigenvalue in the limit $N_v \to \infty$. Here, the contributing states should form an orthogonal set. If the PEPS has a virtual symmetry the correct relative weight for the leading states in different symmetry sectors in the ES is *a priori* not known and should be chosen such that the entanglement Hamiltonian as an operator for the one-dimensional spin chain at the virtual cut is as local as possible [46]. As discussed in the previous subsection the leading sectors at finite cylinder width for the chiral PEPS at $\lambda_1 = 0$ are those with conserved U(1) charge $q = -1, 0, 1$. In particular we exclude sectors with charge $|q| \geqslant 2$ since their transfer matrix eigenvalues are far suppressed. Moreover we include only one of the states with $q = \pm 1$ since we expect that they become identical in the thermodynamic limit. The virtual reduced density matrix is then a linear superposition of the density matrices σ_q for the leading states in the sectors $q = 0, 1$ which are individually normalized to $\mathrm{Tr}\,\sigma_q^2 = 1$. The relative weight in this linear superposition determines the overall shift in entanglement energy between levels with integer and half-integer spin and thereby also the conformal weight of the spin-1/2 field. We

expect that the ansatz

$$\sigma = \sigma_0 + \sigma_1 \tag{64}$$

for the virtual reduced density matrix correctly reproduces the low-lying levels in the ES. Indeed, the linear superposition (64) possesses equal weight on the $\mathbb{Z}_2$ even and odd sectors as expected for a PEPS with a virtual $\mathbb{Z}_2$ symmetry [46].

In the following subsection (Sec. V C 1) we further motivate the ansatz Eq. (64) for the virtual reduced density matrix by showing analytically that the two density matrices $\sigma_{\pm q}$ possess an identical ES without any degeneracies caused by the dressed mirror symmetry. On the other hand the ES of the translation invariant linear superposition Eq. (61) contains two copies of the ES of $\sigma_{\pm q}$ shifted in momentum by π. Finally, in Sec. V C 2 we discuss the chirality of the ES derived from Eq. (64) for $N_v = 8$ and show that the conformal weight of the spin-1/2 sector is very close to the expected value of 1/4 when $\lambda_c \approx \lambda_2$.

1. ES for $q \neq 0$

For any value of the U(1) charge q, the transfer matrix eigenstate $|\tilde{X}_0\rangle_{(q,q)}$ corresponds to a virtual reduced density matrix σ_q that maps the virtual spins in the bra layer of the entanglement cut to those in the ket layer as explained in Sec. IV E 1. Due to the fixed charge the support and image of σ_q consist of the subspace of the single-layer virtual space with $Q_{sl} = q$ such that

$$Q_{sl}\,\sigma_q = \sigma_q\,Q_{sl} = q\,\sigma_q. \tag{65}$$

Since $|\tilde{X}_0\rangle_{(q,q)}$ is invariant under double-step translation, the virtual reduced density matrix σ_q commutes with the single-layer double-step translation $(T^{sl})^2$.

Whenever the leading states $|\tilde{X}_0\rangle_{(\pm q,\pm q)}$ with opposite nonvanishing charges are related by single-step translation as in Eq. (60) their virtual reduced density matrices are unitarily equivalent with the basis change given by single-layer single-step translation,

$$\sigma_q = T^{sl}\,\sigma_{-q}\,(T^{sl})^\dagger. \tag{66}$$

Hence the ES of $|\tilde{X}_0\rangle_{(\pm q,\pm q)}$ given by the spectra of $-\log\sigma^2_{\pm q}$ are identical. This ES does not possess any degeneracies caused by the antiunitary dressed mirror symmetry since $\mathcal{R}^{sl}_x$ does not act within a subspace of fixed nonzero U(1) charge q.

On the other hand the virtual reduced density matrix of the momentum eigenstate $|X_0\rangle_{K^{sl}=0}$ defined in Eq. (61) is given by the sum

$$\sigma_+ = \frac{1}{\sqrt{2}}[\sigma_q + \sigma_{-q}] \tag{67}$$

which has support on both the $Q_{sl} = \pm q$ subspaces. Eigenstates of σ_+ with well-defined single-step momentum K^{sl} are given by linear superpositions of eigenstates of $\sigma_{\pm q}$ with well-defined double-step momentum $\tilde{K}^{sl}$. For a relative phase of ± 1 in the linear superposition one finds either $K^{sl} = \tilde{K}^{sl}$ or $K^{sl} = \tilde{K}^{sl} + \pi$. Therefore the ES of $|X_0\rangle_{K^{sl}=0}$ consists of two copies of the ES of $|\tilde{X}_0\rangle_{(\pm q,\pm q)}$ shifted in momentum by π. Note that the normalized ES of $|X_0\rangle_{K^{sl}=0}$ is shifted by $\ln 2$ compared to that of $|\tilde{X}_0\rangle_{(q,q)}$ due to the factor of $\frac{1}{\sqrt{2}}$ in Eq. (67).

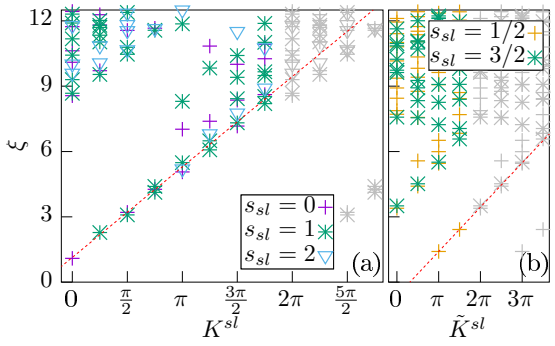

FIG. 14. Entanglement spectrum for the chiral PEPS with fixed virtual U(1) charge in (a) for $q = 0$ corresponding to integer spin and in (b) for $q = 1$ corresponding to half-integer spin. The dotted lines are linear fits obtained from the averaged multiplets in the lowest four and three levels for (a) and (b), respectively. We plotted parts of the second BZ in gray to show the chirality of the branches extending for more than a single BZ. The parameter values are $\lambda_1 = 0, \lambda_2 = \lambda_c = 1$ and the system size is $N_v = 8$.

2. Conformal weight

In Fig. 14 we display the ES derived from the virtual reduced density matrix Eq. (64) for the chiral PEPS on a cylinder of width $N_v = 8$ with parameters $\lambda_1 = 0$ and $\lambda_2 = \lambda_c = 1$ which is close to the point where the overlap between the states with charges $q = \pm 1$ is maximal. We used the maximal set of quantum numbers such that the ES is computed using the single-step (double-step) translation in the sector $q = 0$ ($q = 1$). The low-lying entanglement energies in either sector lie on a chiral branch where the dispersion velocity is nearly the same in both sectors and the counting of the SU(2) multiplets is precisely that of the CFT $\mathfrak{su}(2)_1$ up to the first four levels [64].

We studied different properties of the ES in order to quantify how closely it resembles the CFT $\mathfrak{su}(2)_1$ spectrum for different values of λ_c. Firstly, we computed the conformal weight of the half-integer spin sector using two different methods. On one hand, we used a simple estimate

$$h_{se} \approx \frac{\xi_0^{(1/2)} - \xi_0^{(0)}}{\xi_1^{(0)} - \xi_0^{(0)}}, \tag{68}$$

where $\xi_i^{(s)}$ is the entanglement energy of the ith level in the sector with spin $s = 0$ or $s = 1/2$. On the other hand, we approximated the average entanglement energy of the multiplets corresponding to the lowest four (three) levels of the chiral branch in the ES of the spin-0 (spin-1/2) sector using a linear fit with the offset a_s and dispersion velocity v_s as free parameters. The conformal weight is then given by

$$h_{\text{fit}} \approx \frac{2}{v_0 + v_{1/2}}(a_{1/2} - a_0). \tag{69}$$

Secondly, we compared the ratio $v_{1/2}/v_0$ of the dispersion velocities for the two sectors as obtained from the linear

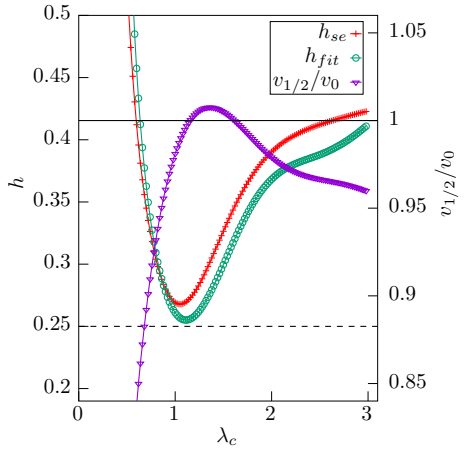

FIG. 15. Numerical estimates for the conformal weight of the spin-1/2 sector and the ratio of the half-integer and integer spin dispersion velocities as a function of λ_c. In the vicinity of $\lambda_c = 1$, the conformal weight approaches the expected value of 1/4 and the dispersion velocities are approximately equal as required by conformal invariance. The expected values for these quantities are indicated by dashed lines. Here, the data was analyzed using a linear fit and the estimates for the conformal weight are obtained using Eqs. (68) and (69), respectively. The PEPS parameters are $\lambda_1 = 0$ and $\lambda_2 = 1$ and the cylinder width is $N_v = 8$.

fits. Since a CFT has no mass scale, these velocities are equal for $\mathfrak{su}(2)_1$. A third measure for the chirality of the ES is given by the difference in entanglement energy between the second-lowest level at $K^{sl} = 0$ and the lowest state at momentum $K^{sl} = 7$. This difference should be positive if the chiral branch wraps more than once around the BZ. We observe that this criterion is fulfilled for $0.6 \leqslant \lambda_c \leqslant 1.12$, showing that the correspondence to the CFT is closest inside this region. In Fig. 15 we show the conformal weight and the ratio of the two dispersion velocities for $N_v = 8$ as a function of λ_c. The conformal weight derived from either estimate has a clear minimum in the vicinity of $\lambda_c = 1$ with values of $h \approx 0.27$ for the simple estimate and $h \approx 0.25$ for the linear fit. This is in very good agreement with the value of $h = 1/4$ expected for $\mathfrak{su}(2)_1$ [64]. For small and very large values of λ_c the estimated conformal weight grows rapidly as the ES becomes gapped. This is expected as we showed in Sec. IV A that the PEPS is real both for $\lambda_c = 0$ approached in the limit $\lambda_c \ll \lambda_2$ and for $\lambda_2 = 0$ which up to an overall normalization is the state we obtain in the limit $\lambda_c \gg \lambda_2$. Moreover, the ratio of estimated dispersion velocities for the half-integer and integer spin sectors is very close to unity in the vicinity of $\lambda_c = 1$ whereas it decreases rapidly for $\lambda_c < 1$. All in all, for $0.8 \leqslant \lambda_c \leqslant 1.12$ the estimated conformal weight is less than 0.3, the ratio of the two dispersion velocities deviates by less than 10% from the expected value, and the chiral branch in the integer spin sector wraps more than once around the BZ. We therefore conclude that the chiral PEPS in this parameter region possesses an ES whose low-lying levels correspond very closely to the spectrum of the chiral CFT $\mathfrak{su}(2)_1$ since it has the correct state counting, conformal weight, and identical dispersion velocities in both sectors.

VI. CONCLUSION

In this paper we investigated the interplay of point group symmetry and translation symmetry for SU(2) invariant PEPS. We showed that for half-integer physical spins it is not possible to simultaneously impose both translation invariance and point group symmetry at the level of the local tensors. Depending on which symmetry is imposed one obtains generically distinct PEPS that are related by the insertion of virtual $\mathbb{Z}_2$ flux strings. This understanding enabled us to explain the discrepancies between the spectrum of the chiral CFT $\mathfrak{su}(2)_1$ and the ES of the chiral spin liquid PEPS introduced in Refs. [34,35]. Moreover, we were able to identify a region of the parameter space where these discrepancies can be lifted due to a staggered virtual U(1) symmetry of the PEPS and presented numerical data establishing a correspondence between the ES and the CFT spectrum. Many questions remain open in the application of PEPS to chiral topologically ordered states. A crucial missing ingredient is an analytical understanding of the link between the symmetry structure of the local tensors and the CFT obtained in the entanglement spectrum. Such an understanding would permit the generalization of the PEPS we analyzed in this paper to other edge CFTs. Another important direction would be the development of additional probes to detect the edge chirality and to identify the precise nature of the edge CFT. These would allow for more precise disambiguation of regimes with chiral and gapped entanglement spectra.

ACKNOWLEDGMENTS

We are grateful to F. Alet, J. Dubail, D. Poilblanc, G. Sierra, H.-H. Tu, F. Verstraete, and E. Zohar for fruitful discussions. This work was supported by the European Union through the ERC Starting Grant WASCOSYS (No. 636201). A.S. acknowledges funding by the Alexander von Humboldt Foundation.

APPENDIX: TENSOR ELEMENTS

In this Appendix we provide an explicit expression for the local projection map Eq. (33) of the chiral spin liquid PEPS. In contrast to Refs. [34,35] we use a representation where the local tensor transforms under the point group as $\mathbf{A}_1 + i\mathbf{A}_2$ rather than $\mathbf{B}_1 + i\mathbf{B}_2$. As explained in Sec. IV A, both representations for the local tensor define the same state. We denote by $|0\rangle, |1\rangle$ the eigenstates of the spin-$\frac{1}{2}$ representation with S^z eigenvalue $\pm\frac{1}{2}$ both on the physical and virtual legs whereas $|2\rangle$ corresponds to the virtual spin-0 state. In this basis, the nonvanishing tensor elements are given by

$$A^s_{s222} = A^s_{2s22} = A^s_{22s2} = A^s_{222s} = \lambda_1, \tag{A1}$$

$$A^s_{s\bar{s}s2} = A^s_{\bar{s}s2s} = A^s_{s2s\bar{s}} = A^s_{2s\bar{s}s} = -2(-1)^s\lambda_2, \tag{A2}$$

$$A^s_{ss\bar{s}2} = A^s_{s\bar{s}2s} = A^s_{\bar{s}2ss} = A^s_{2s2\bar{s}} = (-1)^s[\lambda_2 + i\lambda_c], \tag{A3}$$

$$A^s_{\bar{s}ss2} = A^s_{ss2\bar{s}} = A^s_{s2\bar{s}s} = A^s_{2\bar{s}ss} = (-1)^s[\lambda_2 - i\lambda_c], \tag{A4}$$

where $s = 0, 1$.

[1] R. B. Laughlin, Phys. Rev. Lett. **50**, 1395 (1983).
[2] G. Moore and N. Read, Nucl. Phys. B **360**, 362 (1991).
[3] A. P. Schnyder, S. Ryu, A. Furusaki, and A. W. W. Ludwig, Phys. Rev. B **78**, 195125 (2008).
[4] A. Kitaev, AIP Conf. Proc. **1134**, 22 (2009).
[5] A. M. Turner, F. Pollmann, and E. Berg, Phys. Rev. B **83**, 075102 (2011).
[6] N. Schuch, D. Pérez-García, and I. Cirac, Phys. Rev. B **84**, 165139 (2011).
[7] X. Chen, Z.-C. Gu, Z.-X. Liu, and X.-G. Wen, Science **338**, 1604 (2012).
[8] X.-G. Wen, Int. J. Mod. Phys. B **04**, 239 (1990).
[9] D. C. Tsui, H. L. Stormer, and A. C. Gossard, Phys. Rev. Lett. **48**, 1559 (1982).
[10] V. Kalmeyer and R. B. Laughlin, Phys. Rev. Lett. **59**, 2095 (1987).
[11] B. Bauer, L. Cincio, B. P. Keller, M. Dolfi, G. Vidal, S. Trebst, and A. W. Ludwig, Nat. Commun. **5**, 5137 (2014).
[12] S.-S. Gong, W. Zhu, and D. Sheng, Sci. Rep. **4**, 6317 (2014).
[13] A. Kitaev and J. Preskill, Phys. Rev. Lett. **96**, 110404 (2006).
[14] M. Levin and X.-G. Wen, Phys. Rev. Lett. **96**, 110405 (2006).
[15] H. Li and F. D. M. Haldane, Phys. Rev. Lett. **101**, 010504 (2008).
[16] M. B. Hastings, J. Stat. Mech.: Theory Exp. (2007) P08024.
[17] M. M. Wolf, F. Verstraete, M. B. Hastings, and J. I. Cirac, Phys. Rev. Lett. **100**, 070502 (2008).
[18] M. Fannes, B. Nachtergaele, and R. F. Werner, Commun. Math. Phys. **144**, 443 (1992).
[19] F. Verstraete and J. I. Cirac, arXiv:cond-mat/0407066.
[20] U. Schollwöck, Ann. Phys. **326**, 96 (2011).
[21] P. Corboz, Phys. Rev. B **94**, 035133 (2016).
[22] V. Zauner-Stauber, L. Vanderstraeten, M. T. Fishman, F. Verstraete, and J. Haegeman, Phys. Rev. B **97**, 045145 (2018).
[23] B.-X. Zheng, C.-M. Chung, P. Corboz, G. Ehlers, M.-P. Qin, R. M. Noack, H. Shi, S. R. White, S. Zhang, and G. K.-L. Chan, Science **358**, 1155 (2017).
[24] A. Kitaev, Ann. Phys. **303**, 2 (2003).
[25] M. A. Levin and X.-G. Wen, Phys. Rev. B **71**, 045110 (2005).
[26] F. Verstraete, M. M. Wolf, D. Perez-Garcia, and J. I. Cirac, Phys. Rev. Lett. **96**, 220601 (2006).
[27] Z.-C. Gu, M. Levin, B. Swingle, and X.-G. Wen, Phys. Rev. B **79**, 085118 (2009).
[28] N. Schuch, I. Cirac, and D. Pérez-García, Ann. Phys. **325**, 2153 (2010).
[29] T. B. Wahl, H.-H. Tu, N. Schuch, and J. I. Cirac, Phys. Rev. Lett. **111**, 236805 (2013).
[30] T. B. Wahl, S. T. Haßler, H.-H. Tu, J. I. Cirac, and N. Schuch, Phys. Rev. B **90**, 115133 (2014).
[31] J. Dubail and N. Read, Phys. Rev. B **92**, 205307 (2015).
[32] N. Read, Phys. Rev. B **95**, 115309 (2017).
[33] S. Yang, T. B. Wahl, H.-H. Tu, N. Schuch, and J. I. Cirac, Phys. Rev. Lett. **114**, 106803 (2015).
[34] D. Poilblanc, J. I. Cirac, and N. Schuch, Phys. Rev. B **91**, 224431 (2015).
[35] D. Poilblanc, N. Schuch, and I. Affleck, Phys. Rev. B **93**, 174414 (2016).
[36] P. W. Anderson, Science **235**, 1196 (1987).
[37] N. Schuch, D. Poilblanc, J. I. Cirac, and D. Pérez-García, Phys. Rev. B **86**, 115108 (2012).
[38] D. Poilblanc, N. Schuch, D. Pérez-García, and J. I. Cirac, Phys. Rev. B **86**, 014404 (2012).
[39] L. Wang, D. Poilblanc, Z.-C. Gu, X.-G. Wen, and F. Verstraete, Phys. Rev. Lett. **111**, 037202 (2013).
[40] D. Perez-Garcia, F. Verstraete, M. M. Wolf, and J. I. Cirac, Quantum Inf. Comput. **7**, 401 (2007).
[41] D. Perez-Garcia, M. Sanz, C. Gonzalez-Guillen, M. M. Wolf, and J. I. Cirac, New J. Phys. **12**, 025010 (2010).
[42] I. P. McCulloch and M. Gulácsi, Europhys. Lett. **57**, 852 (2002).
[43] A. Molnar, J. Garre-Rubio, D. Pérez-García, N. Schuch, and J. I. Cirac, arXiv:1804.04964.
[44] M. Mambrini, R. Orús, and D. Poilblanc, Phys. Rev. B **94**, 205124 (2016).
[45] X. G. Wen and Q. Niu, Phys. Rev. B **41**, 9377 (1990).
[46] N. Schuch, D. Poilblanc, J. I. Cirac, and D. Pérez-García, Phys. Rev. Lett. **111**, 090501 (2013).
[47] A. Sterdyniak, N. Regnault, and B. A. Bernevig, Phys. Rev. Lett. **106**, 100405 (2011).
[48] A. Sterdyniak, C. Repellin, B. A. Bernevig, and N. Regnault, Phys. Rev. B **87**, 205137 (2013).
[49] N. Regnault and B. A. Bernevig, Phys. Rev. X **1**, 021014 (2011).
[50] R. Thomale, A. Sterdyniak, N. Regnault, and B. A. Bernevig, Phys. Rev. Lett. **104**, 180502 (2010).
[51] A. Sterdyniak, A. Chandran, N. Regnault, B. A. Bernevig, and P. Bonderson, Phys. Rev. B **85**, 125308 (2012).
[52] J. Dubail, N. Read, and E. H. Rezayi, Phys. Rev. B **85**, 115321 (2012).
[53] Y.-C. He, S. Bhattacharjee, R. Moessner, and F. Pollmann, Phys. Rev. Lett. **115**, 116803 (2015).
[54] L. Fidkowski, Phys. Rev. Lett. **104**, 130502 (2010).
[55] F. Pollmann, A. M. Turner, E. Berg, and M. Oshikawa, Phys. Rev. B **81**, 064439 (2010).
[56] X.-L. Qi, H. Katsura, and A. W. W. Ludwig, Phys. Rev. Lett. **108**, 196402 (2012).
[57] A. M. Läuchli, arXiv:1303.0741.
[58] J. I. Cirac, D. Poilblanc, N. Schuch, and F. Verstraete, Phys. Rev. B **83**, 245134 (2011).
[59] I. Affleck, T. Kennedy, E. H. Lieb, and H. Tasaki, Phys. Rev. Lett. **59**, 799 (1987).
[60] C. K. Majumdar and D. K. Ghosh, J. Math. Phys. **10**, 1388 (1969).
[61] F. Pollmann, E. Berg, A. M. Turner, and M. Oshikawa, Phys. Rev. B **85**, 075125 (2012).
[62] D. Poilblanc, Phys. Rev. B **96**, 121118 (2017).
[63] J.-Y. Chen and D. Poilblanc, Phys. Rev. B **97**, 161107 (2018).
[64] P. Francesco, P. Mathieu, and D. Sénéchal, *Conformal Field Theory* (Springer Science & Business Media, New York, 2012).
[65] Given a local tensor transforming in the $\mathbf{A}_{1,2}$ representation, one obtains a tensor transforming as $\mathbf{B}_{1,2}$ by multiplying either both horizontal or both vertical virtual legs with the matrix Z from Eq. (16).
[66] Since $(\mathcal{R}_x^{dl})^2 = \mathbb{1}$ and $I^2 = \mathbb{1}$ Kramer's theorem for antiunitary operators does not apply such that the mirror symmetry and layer

inversion do not cause any degeneracies whenever they do not change any quantum numbers.

[67] V. Zauner, D. Draxler, L. Vanderstraeten, M. Degroote, J. Haegeman, M. M. Rams, V. Stojevic, N. Schuch, and F. Verstraete, New J. Phys. **17**, 053002 (2015).

[68] J. Haegeman, V. Zauner, N. Schuch, and F. Verstraete, Nat. Commun. **6**, 8284 (2015).

[69] For system sizes $N_v \in 4\mathbb{N}$ the quantum number μ permits us to distinguish the two points $\tilde{K}^{dl} = 0$ and $\tilde{K}^{dl} = \pi$ which are both invariant under inversion of the double-step momentum $\tilde{K}^{dl}$ whereas only $\tilde{K}^{dl} = 0$ corresponds to inversion-symmetric single-step momenta $K^{dl} = 0, \pi$. Indeed, μ is real for $\tilde{K}^{dl} = 0$ and purely imaginary for $\tilde{K}^{dl} = \pi$.

5.2 Fermionic tensor networks for HOTIs from charge pumping

This section contains a reprint of the following publication:

- Anna Hackenbroich, B. Andrei Bernevig, Norbert Schuch, and Nicolas Regnault. "Fermionic tensor networks for higher-order topological insulators from charge pumping". In: *Phys. Rev. B* 101 (11 Mar. 2020), p. 115134

In the previous section we showed that PEPS can have features of chiral topological phases such as a chiral ES with the state counting of a CFT. However, as we discussed in Sec. 4.3.3, these TNS cannot be the ground states of gapped and local Hamiltonians. Here we want to give an illustration of this statement using an intuitive example. Since this obstruction appears already for non-interacting SPT phases, we consider two free-fermionic systems with chiral boundary modes. On one hand, we consider the 2D CI discussed in Sec. 2.3, and on the other hand, the 3D chiral hinge insulator discussed in Sec. 2.5.3. Both of these models can be obtained from charge pumping interpolations between trivial and topological phases of lower-dimensional systems: the 1D SSH model we discussed in Sec. 2.2 in the case of the CI, and the 2D topological quadrupole model we reviewed in Sec. 2.5.1 in the case of the 3D chiral hinge insulator.

In order to construct TNS for the chiral models we therefore proceed by first deriving TNS representations of the ground states of the lower-dimensional models along the dipole pumping interpolations. Here we make use of the formalism of Gaussian TNS, which offers a very efficient description of free-fermionic systems and which is reviewed in great detail in the appendices of this publication. We thus find a Gaussian MPS with bond dimension 2 which interpolates between the trivial and the topological dimerized limits of the SSH model. The parent Hamiltonian of this MPS is a gapped next-nearest neighbor Hamiltonian interpolating between the trivial and topological phases of the fully dimerized SSH model. Similarly, we obtain a Gaussian PEPS with bond dimension 2 which interpolates between the trivial and the topological dimerized limits of the topological quadrupole model. The parent Hamiltonian of this PEPS is a gapped next-nearest neighbor Hamiltonian interpolating between the trivial and topological phases of the fully dimerized topological quadrupole model.

The TNS representations of the lower-dimensional models allow us to express the ground states of the chiral models as TNS in a hybrid real-momentum-space lattice with a finite constant bond dimension in all directions. Here, the single momentum-space direction corresponds to the interpolation parameter of the charge pumping cycles. After an inverse Fourier transform in this direction, the PEPS with only real-space coordinates requires an exponentially growing Hilbert space dimension for these bonds, whereas the bond dimension in the other directions remains finite. This confirms that it is not possible to express the ground states of the chiral models as real-space TNS with a constant and finite bond dimension.

Fermionic tensor networks for higher-order topological insulators from charge pumping

Anna Hackenbroich,[1,2] B. Andrei Bernevig,[3,4] Norbert Schuch,[1,2] and Nicolas Regnault[3,5]
[1]*Max-Planck-Institute of Quantum Optics, Hans-Kopfermann-Str. 1, 85748 Garching, Germany*
[2]*Munich Center for Quantum Science and Technology, Schellingstraße 4, 80799 München, Germany*
[3]*Joseph Henry Laboratories and Department of Physics, Princeton University, Princeton, New Jersey 08544, USA*
[4]*Max-Planck-Institute of Microstructure Physics, 06120 Halle, Germany*
[5]*Laboratoire de Physique de l'École normale supérieure, ENS, Université PSL, CNRS, Sorbonne Université, Université Paris-Diderot, Sorbonne Paris Cité, 75005 Paris, France*

(Received 24 December 2019; revised manuscript received 19 February 2020; accepted 19 February 2020; published 19 March 2020)

We apply the charge-pumping argument to fermionic tensor network representations of d-dimensional topological insulators (TIs) to obtain tensor network states (TNSs) for $(d+1)$-dimensional TIs. We exemplify the method by constructing a two-dimensional projected entangled pair state (PEPS) for a Chern insulator starting from a matrix product state (MPS) in $d=1$ describing pumping in the Su-Schrieffer-Heeger (SSH) model. In extending the argument to second-order TIs, we build a three-dimensional TNS for a chiral hinge TI from a PEPS in $d=2$ for the obstructed atomic insulator (OAI) of the quadrupole model. The $(d+1)$-dimensional TNSs obtained in this way have a constant bond dimension inherited from the d-dimensional TNSs in all but one spatial direction, making them candidates for numerical applications. From the d-dimensional models, we identify gapped next-nearest-neighbor Hamiltonians interpolating between the trivial and OAI phases of the fully dimerized SSH and quadrupole models, whose ground states are given by an MPS and a PEPS with a constant bond dimension equal to 2, respectively.

DOI: 10.1103/PhysRevB.101.115134

I. INTRODUCTION

Higher-order TIs [1–4] have recently been introduced as a new class of symmetry-protected topological systems generalizing the framework of TIs with surface states [5]. According to one definition, a TI of order n in d spatial dimensions has topological boundary modes at the $(d-n)$-dimensional intersection of n crystal faces. In this terminology, conventional TIs such as Chern insulators [6] are of order $n=1$ with protected boundary modes at $(d-1)$-dimensional edges. On the other hand, second-order TIs protected by mirror or rotation symmetries have zero-dimensional corner states in $d=2$ dimensions (in which case they may exemplify obstructed atomic limits [7] with local Wannier states) and one-dimensional chiral or helical hinge states in $d=3$ dimensions (and bulk bands without a local Wannier description). Prototypical examples of second-order topological phases include the two-dimensional quadrupole model of Ref. [1], a natural extension [8] of the Su-Schrieffer-Heeger (SSH) model [9], and the three-dimensional chiral hinge insulator of Ref. [2], both of which have been experimentally observed in either materials [10] or mechanical [11], acoustic [12,13], photonic [14–17], and electrical [18–20] systems.

The bulk-boundary correspondence states that the topological properties of a system are reflected in the excitations at its physical boundary. For instance, a two-dimensional Chern insulator is characterized by an integer number of gapless chiral edge modes [21]. Similarly, second-order TIs in two dimensions possess gapless corner modes at the intersection of two edges compatible with the crystal symmetry [1]. In three dimensions, one type of second order TI is characterized by the presence or absence of a chiral hinge mode [2]. For strong TIs [22] as well as chiral topological phases, the universal features in the boundary energy spectrum are encoded in its entanglement spectrum (ES) [23] characterizing the bulk entanglement properties. The convenience of this bulk characterization makes the ES an important tool for the numerical analysis of topological phases. Recently, it was also observed, as expected, that the ES of higher-order TIs displays characteristic $(d-n)$-dimensional boundary states as long as the entanglement cut preserves the crystal symmetries of the phase [24–26].

A natural platform for the bulk-boundary correspondence is provided by tensor network states (TNSs) [27] in which the entanglement between physical particles is mediated through virtual particles hosting the lower-dimensional boundary theory [28]. Physical and virtual particles are related by a local tensor whose bond dimension determines the maximal amount of entanglement in the state [29,30]. The structure of the local tensor encodes the topological properties of the quantum state, and an analysis of this relation has led to valuable insight for the systematic understanding of one-dimensional symmetry-protected topological (SPT) phases [31] and intrinsically ordered topological phases [32]. Free-fermion systems

Published by the American Physical Society under the terms of the Creative Commons Attribution 4.0 International license. Further distribution of this work must maintain attribution to the author(s) and the published article's title, journal citation, and DOI. Open access publication funded by the Max Planck Society.

can be described using Gaussian fermionic TNSs (GfTNSs) that are defined purely in terms of two-point correlation functions [33]. Starting from such Gaussian TNSs, interacting states can be constructed, whose topological properties derive from the features of the initial Gaussian model [34].

Many nonchiral topologically ordered phases in two dimensions [35,36] have a simple representation in terms of projected entangled pair states (PEPSs) [37] with a finite and constant bond dimension [38,39]. However, Gaussian PEPSs with chiral topological properties do not adequately describe the bulk of a gapped phase since their correlation functions decay algebraically [40,41]. Indeed, the existence of gapped Gaussian PEPSs with finite bond dimension for SPT phases of free fermions is forbidden in dimensions $d > 1$ [41,42]. The no-go theorem states that only Wannierizable phases corresponding to the product of one- and zero-dimensional systems can be exactly represented as a Gaussian TNS.

This no-go theorem does not prevent TNSs from being a useful numerical description at finite system size for chiral topological phases like the fractional quantum Hall effect [43]. Hence, numerically efficient TNSs for such phases are valuable, especially in two and three dimensions. One method for the construction of TIs in $d+1$ dimensions from d-dimensional TIs is given by charge pumping [44]. For instance, a two-dimensional Chern insulator is obtained from a charge-pumping interpolation in the one-dimensional SSH model when the periodic time direction is identified with the momentum in the second spatial direction [45]. For second-order TIs, dipole pumping in the quadrupole model defines a three-dimensional chiral hinge insulator [2,3]. In both cases, the zero-dimensional boundary modes of the d-dimensional model give rise to one-dimensional chiral boundary modes in the $(d+1)$-dimensional system.

In this paper, we exemplify how the charge-pumping argument applied to d-dimensional GfTNSs with constant bond dimension yields gapped GfTNSs for TIs in $d+1$ dimensions. By construction, the $(d+1)$-dimensional TNS has a constant finite bond dimension in a hybrid coordinate system with d real-space axes and one momentum axis in the additional dimension. In order to obtain a real-space tensor network for the $(d+1)$-dimensional state, we apply to the hybrid TNS an inverse Fourier transform (FT) in the direction $d+1$. As a result, the bond dimension of the real-space local tensor in this direction generically grows with the system size due to the nonlocality of the FT, whereas it is identical to the finite bond dimension of the d-dimensional TNS in the other d directions. We apply this construction both to a matrix product state (MPS) [46] for the SSH model in order to obtain a PEPS for a Chern insulator, and to a Gaussian PEPS with finite bond dimension for the topological quadrupole model in order to obtain a three-dimensional GfTNS for the second-order chiral hinge state TI of Refs. [2,3]. Therefore, our approach provides us with a gapped TNS with one-dimensional chiral boundary states and a constant finite bond dimension in all but one of the spatial directions. This representation is therefore potentially useful for tensor network algorithms.

This paper is structured as follows: In Sec. II we begin with a brief overview of charge pumping in the SSH model and fermionic TNSs, and continue by studying an MPS for the SSH ground state along the charge-pumping interpolation. In the following Sec. III, we employ this MPS to construct a two-dimensional PEPS describing a Chern insulator. In Sec. IV we extend our method to the two-dimensional second-order quadrupole insulator and the construction of a three-dimensional PEPS for the chiral hinge state higher-order TI. Finally, we summarize our results and discuss remaining open questions in Sec. V.

II. FERMIONIC MPS FOR CHARGE PUMPING IN THE SSH MODEL

In this section we introduce a fermionic MPS that describes a charge-pumping cycle in the SSH model corresponding to a Chern insulator with Chern number $\mathcal{C} = 1$ in two spatial dimensions. We begin by briefly reviewing the SSH model, the charge-pumping argument, and its relation to Chern insulators in Sec. II A. We continue with a short introduction to fermionic MPSs in Sec. II B. In Sec. II C, we construct the MPS for the SSH model and study its parent Hamiltonian.

A. Chern insulator from charge pumping in the SSH model

The SSH model describes a one-dimensional chain of spinless fermions with two orbitals denoted A and B per unit cell [9]. We consider the model at half-filling where the number of particles is equal to the number N_x of unit cells. For open boundary conditions, the Hamiltonian reads as

$$H_{\mathrm{SSH}} = t^{(0)} \sum_{x=0}^{N_x-1} (\hat{a}^\dagger_{A,x}\hat{a}_{B,x} + \mathrm{H.c.}) + t^{(1)} \sum_{x=1}^{N_x-1} (\hat{a}^\dagger_{B,x-1}\hat{a}_{A,x} + \mathrm{H.c.}), \tag{1}$$

where we use the notation $\hat{a}_{A,x}$ and $\hat{a}_{B,x}$ for the fermionic annihilation operators of the orbitals A and B in unit cell x with $x = 0, \ldots, N_x - 1$, respectively. Here, $t^{(0)}$ denotes the hopping amplitude between A and B orbitals within the same unit cell, and $t^{(1)}$ the hopping amplitude between sites on neighboring unit cells [see Fig. 1(a)]. For $|t^{(1)}| > |t^{(0)}|$, the hopping between unit cells dominates the hopping within unit cells and the SSH model is in a phase topologically different from the case $|t^{(0)}| > |t^{(1)}|$. This phase is protected by spatial inversion symmetry and characterized by fermionic edge modes [45] and a "filling anomaly" [8]. It is called obstructed atomic insulator (OAI) [7]. When the intracell hopping $t^{(0)}$ vanishes in the deep OAI phase, the system is dimerized since its bulk splits into decoupled two-site blocks. In this case, the edge excitations are created by the mode operators $\hat{a}^\dagger_{A,0}$ and $\hat{a}^\dagger_{B,N_x-1}$ and have exactly zero energy in this specific model, but can generally be moved in energy. On the other hand, for $|t^{(0)}| > |t^{(1)}|$ the SSH model is trivial, with a dimerized point at $t^{(1)} = 0$ and no state at zero energy.

A gapped interpolation between the trivial and OAI phases of the SSH model can be constructed by adding to the Hamiltonian H_{SSH} the term

$$\sum_{x=0}^{N_x-1} (\mu_A \hat{a}^\dagger_{A,x}\hat{a}_{A,x} + \mu_B \hat{a}^\dagger_{B,x}\hat{a}_{B,x}) \tag{2}$$

introducing a staggered chemical potential $\mu_A = -\mu_B = \mu$ which breaks the inversion symmetry as shown in Fig. 1(a).

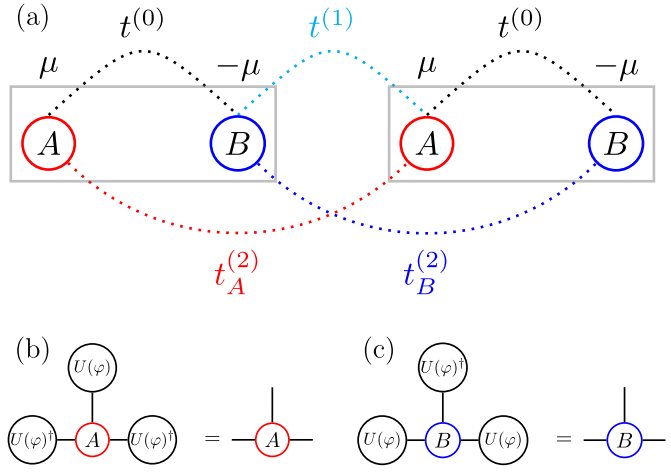

FIG. 1. (a) Extended SSH model with a staggered chemical potential μ, nearest-neighbor hoppings $t^{(0)}$ and $t^{(1)}$ within and between unit cells, and next-nearest-neighbor hoppings $t_A^{(2)}$ and $t_B^{(2)}$ on the A and B sublattices, respectively. The unit cells consisting of one site of each sublattice are marked by gray rectangles. (b) Action on the local MPS tensors of the U(1) symmetry ensuring that the MPS of Eq. (11) lies at half filling of the chain.

In Ref. [3], the authors consider the periodic time-dependent Hamiltonian $H_{\text{pump}}(t)$ with time $t \in (-\pi, \pi]$ defined by the couplings

$$(\mu, t^{(1)}, t^{(0)}) = \begin{cases} (\cos(t), 0, -\sin(t)), & -\pi < t \leqslant 0 \\ (\cos(t), \sin(t), 0), & 0 < t \leqslant \pi. \end{cases} \tag{3}$$

At $t = -\pi$ (equivalent to $t = \pi$), the system is in an atomic phase with only the A orbitals occupied. For $-\pi < t < 0$, the coupling between A and B sites in the same unit cell is nonzero and the charge is transferred from left to right by the changing chemical potential until only the B orbitals are occupied at $t = 0$. At $t = -\pi/2$, the staggered chemical potential vanishes and the system is in the trivial dimerized phase of the SSH model. For $0 < t < \pi$, the intra-unit-cell coupling vanishes whereas the hopping between different unit cells is nonzero and the charge is transferred from left to right such that at $t = \pi$ the system returns to the state with all A orbitals occupied. At $t = \pi/2$, the chemical potential vanishes and the system is in the OAI dimerized phase of the SSH model. The ground state of the pumping Hamiltonian $H_{\text{pump}}(t)$ is continuous as a function of time t if the chain has periodic and antiperiodic boundary conditions for N_x odd and even, respectively.

The charge-pumping interpolation of Eq. (3) can be used to generate a lattice model in one dimension higher with the topology of a Chern insulator [3]. Indeed, $H_{\text{pump}}(t)$ corresponds to the time-dependent Bloch Hamiltonian

$$\mathcal{H}_{\text{pump}}(k_x, t) = [t^{(0)}(t) + t^{(1)}(t)\cos k_x]\sigma_1 + t^{(1)}(t)\sin k_x \times \sigma_2 + \mu(t)\sigma_3, \tag{4}$$

where $\sigma_1 = \left(\begin{smallmatrix} 0 & 1 \\ 1 & 0 \end{smallmatrix}\right)$, $\sigma_2 = \left(\begin{smallmatrix} 0 & -i \\ i & 0 \end{smallmatrix}\right)$, and $\sigma_3 = \left(\begin{smallmatrix} 1 & 0 \\ 0 & -1 \end{smallmatrix}\right)$ are the Pauli matrices and $k_x = \frac{\pi}{N_x}(2j - N_x) \in [-\pi, \pi]$ for $0 \leqslant j \leqslant N_x - 1$ the lattice momentum. Since the interpolation is cyclic, the time $t \in [-\pi, \pi]$ may be interpreted as the lattice momentum k_y of a second spatial direction y and Eq. (4) as the Bloch Hamiltonian of a two-dimensional system with closed boundaries in both directions. This Hamiltonian has a Chern number $\mathcal{C} = 1$ due to the charge transport between unit cells induced by the interpolation for $t \in [0, \pi]$ [3].

We note that the cycle of Eq. (3) can be deformed to a smooth charge-pumping interpolation, *without changing the topology or breaking the dimerization*. In this cycle, the couplings $\mu(t)$, $t^{(1)}(t)$, and $t^{(0)}(t)$ and hence the Bloch Hamiltonian are smooth functions of the time t, i.e., they are infinitely often continuously differentiable with respect to t. As explained in the previous paragraph, a two-dimensional Chern insulator model is obtained by identifying the time t and the momentum k_y. Due to the smoothness of the cycle, the real-space representation of the Chern insulator has couplings which decay faster than any polynomial [47]. The smooth cycle is obtained by smoothing out the nonanalyticities of Eq. (3) at $t = 0, \pi$ using smooth functions that interpolate between 0 and 1. This can be done in such a way that, like in Eq. (3), at each time t the smooth couplings satisfy $\mu(t)^2 + t^{(1)}(t)^2 + t^{(0)}(t)^2 = 1$ [48].

B. Fermionic MPSs for a half-filled lattice

Similarly to bosonic MPSs for spin chains, fermionic MPSs describing chains of electrons are obtained by associating virtual particles to each physical particle which mediate the entanglement between different physical constituents [33]. In the case of fermionic tensor networks, the virtual particles obey fermionic statistics. A fermionic MPS with f physical complex fermionic modes per site and ξ virtual complex fermionic modes per lattice site and nearest-neighbor bond has physical dimension $d_p = 2^f$ and bond dimension $D = 2^\xi$. The state is fully characterized by the set of local maps which relate the virtual and physical particles associated to one lattice site. With respect to orthonormal bases $\{|i\rangle\}$ with $i = 0, \ldots, d_p - 1$ for the physical Hilbert space and $\{|l\rangle\}$, $\{|r\rangle\}$ with $l, r = 0, \ldots, D - 1$ for the left and right virtual spaces on one site, respectively, the local maps are represented by d_p local matrices A^i_{lr} of dimension $D \times D$ [49].

In order to fix the global parity of the state, we restrict ourselves to parity-even local tensors which preserve the fermion parity between the physical and virtual layers [49]. We choose the orthonormal basis for the physical Hilbert space such that all basis states $|i\rangle$ have either even fermion parity $|i| = 0$ or odd fermion parity $|i| = 1$, and similarly for the virtual Hilbert spaces. A local tensor is parity even if for all nonvanishing elements $A^i_{lr} \neq 0$, the total fermion parity $|i| + |l| + |r| = 0$ is even, such that

$$(-1)^{|i|}A^i_{lr} = (-1)^{|l|}A^i_{lr}(-1)^{|r|} \tag{5}$$

for all configurations of i, l, and r (where no summation is implied). If the MPS is constructed from tensors $A[j]$ at each site j with this property, the state on a closed chain with N_x sites is given by

$$|\psi\rangle = \sum_{i_0, \ldots, i_{N_x-1}} \sum_{l} (-1)^{\epsilon|l|} \times (A[0]^{i_0} \ldots A[N_x - 1]^{i_{N_x-1}})_{ll} |i_0, \ldots, i_{N_x-1}\rangle. \tag{6}$$

Here, $|l|$ is the parity of the virtual basis state on the link between the first and last site, and $\epsilon = 1$ or 0 corresponding to periodic and antiperiodic boundary conditions for the many-body state, respectively [49].

Below, we construct a fermionic MPS with parity-even local tensors for the ground state of the SSH model along the dimerized charge-pumping interpolation. Due to the parity symmetry of Eq. (5), this MPS necessarily has an even number of physical particles on a closed chain where all virtual bonds are contracted. On the other hand, the ground state of the SSH model is half-filled such that the number of particles is odd if the number of unit cells is odd. Therefore, to construct the parity-even SSH MPS we use a many-body basis built by acting with creation operators on the state $|\Omega\rangle$ that contains N_x physical particles. To that end, we define new mode operators $a_{A,x}$ and $a_{B,x}$ for the physical fermions by performing a particle-hole transformation on all B orbitals of the SSH chain while leaving the A orbitals unaltered,

$$a_{A,x} \equiv \hat{a}_{A,x}, \tag{7a}$$

$$a_{B,x} \equiv \hat{a}^\dagger_{B,x}. \tag{7b}$$

The state $|\Omega\rangle$ is the vacuum of the new operators, given in terms of the original vacuum state $|\hat{\Omega}\rangle$ with $\hat{a}_{A,x}|\hat{\Omega}\rangle = \hat{a}_{B,x}|\hat{\Omega}\rangle = 0$ as

$$|\Omega\rangle = \prod_x \hat{a}^\dagger_{B,x}|\hat{\Omega}\rangle. \tag{8}$$

It satisfies $a_{A,x}|\Omega\rangle = a_{B,x}|\Omega\rangle = 0$. Therefore, the new vacuum contains N_x of the original fermions and thus is half-filled. The MPS of the SSH model along the interpolation is then defined with respect to the Fock states constructed from the modes $a^\dagger_{A,x}$ and $a^\dagger_{B,x}$ acting on the new vacuum $|\Omega\rangle$. This particle-hole transformation is motived by our desire to write the MPS in terms of parity-even local tensors, which will in turn enable us to express the state as a GfTNS and thereby compute a Bloch parent Hamiltonian analytically.

C. MPS for the SSH model

In this section, we study a fermionic MPS for the SSH model. In Sec. II C 1, we define the state in terms of its local tensors and identify the U(1) symmetry leading to a conserved number of particles. In Sec. II C 2, we derive a parent Hamiltonian for the MPS, allowing us to conclude in Sec. II C 3 that the MPS describes the SSH model along the charge-pumping cycle of Eq. (3).

1. Local tensors and U(1) *symmetry*

In order to describe the ground state of the SSH model along the dimerized charge-pumping interpolation, we consider a fermionic MPS with physical dimension $d_p = 2$ corresponding to one fermionic mode per site and bond dimension $D_{\mathrm{SSH}} = 2$. This is the minimal bond dimension for an MPS along the charge-pumping cycle since the ES of an open SSH chain in the OAI and trivial dimerized phases has two degenerate levels with respect to all cuts between and within unit cells, respectively.

The fermionic MPS is translation invariant with a unit cell of two sites. It is therefore fully specified by the local matrices A^i_{lr} and B^i_{lr} with $i, l, r \in \{0, 1\}$ for sites on the A and B sublattices, respectively. In terms of the local tensors the physical state on a closed chain is given as

$$|\psi\rangle = \sum_{\substack{i_{A,0},\ldots,i_{A,N_x-1}\\ i_{B,0},\ldots,i_{B,N_x-1}}} |i_{A,0}, i_{B,0}, i_{A,1}, \ldots, i_{B,N_x-1}\rangle \times \sum_l (-1)^{\epsilon|l|} \times (A^{i_{A,0}} B^{i_{B,0}} A^{i_{A,1}} \ldots B^{i_{B,N_x-1}})_{ll}, \tag{9}$$

where $\epsilon = 1$ or 0 for periodic and antiperiodic boundary conditions. The physical many-body basis state is

$$\left|i_{A,0}, i_{B,0}, i_{A,1}, \ldots, i_{B,N_x-1}\right\rangle = (a^\dagger_{A,0})^{i_{A,0}} (a^\dagger_{B,0})^{i_{B,0}} (a^\dagger_{A,1})^{i_{A,1}} \ldots \left(a^\dagger_{B,N_x-1}\right)^{i_{B,N_x-1}} |\Omega\rangle \tag{10}$$

with the vacuum $|\Omega\rangle$ from Eq. (8). Guided by the dimerized limits to be discussed below, for the local MPS matrices we make the ansatz

$$A^0 = \begin{pmatrix} \gamma & 0 \\ 0 & 0 \end{pmatrix}, \; A^1 = \begin{pmatrix} 0 & \beta \\ -\alpha & 0 \end{pmatrix}, \tag{11a}$$

$$B^0 = \begin{pmatrix} \gamma & 0 \\ 0 & 0 \end{pmatrix}, \; B^1 = \begin{pmatrix} 0 & -\alpha \\ -\beta & 0 \end{pmatrix}, \tag{11b}$$

depending on parameters $\alpha, \beta, \gamma \in \mathbb{R}$. Note that the normalized quantum state defined by these local MPS matrices depends only on the two quotients α/γ and β/γ. Nonetheless, we choose to work with the parametrization of Eq. (11) since the case $\gamma = 0$ can be treated more conveniently without divergences.

In order to motivate the ansatz of Eq. (11) for the local matrices, let us see how the MPS from Eq. (9) can describe the ground state of the SSH model both in the trivial and the OAI dimerized phases with appropriate choices for the parameters α, β, and γ. In the trivial dimerized phase of the SSH model, each unit cell decouples from the rest of the system and is in the state $(a^\dagger_A a^\dagger_B - 1)|\Omega\rangle$. In order to ensure the absence of entanglement on the bonds between unit cells, the blocked MPS matrices $(A^{i_A} B^{i_B})_{lr}$ for one unit cell should be nonzero only if $l = r = 0$. Then, the restriction of the MPS to the unit cell, $\sum_{i_A,i_B} (A^{i_A} B^{i_B})_{00} |i_A, i_B\rangle$, is proportional to $(a^\dagger_A a^\dagger_B - 1)|\Omega\rangle$ if the blocked MPS matrices have only two nonzero entries $(A^0 B^0)_{00} = -(A^1 B^1)_{00}$. Therefore, the MPS represents the trivial dimerized phase of the SSH model if the parameters are chosen as $\alpha = 0$ and $|\beta| = |\gamma| \neq 0$. Similarly, in the OAI dimerized phase the chain splits into decoupled plaquettes composed of two adjacent sites from different unit cells. The state on each of the plaquettes is given by the superposition $(a^\dagger_B a^\dagger_A + 1)|\Omega\rangle$ such that the blocked MPS matrices for the plaquette should have only two nonzero entries $(B^0 A^0)_{00} = (B^1 A^1)_{00}$. This is achieved if $\beta = 0$ and $|\alpha| = |\gamma| \neq 0$. The ansatz of Eq. (11) is chosen such as to allow an interpolation between these two cases.

The MPS of Eq. (9) with the parametrization of Eq. (11) has a U(1) symmetry which ensures that the physical state lies at half-filling of the chain. The U(1) rotation acts on a single complex fermion with the matrix $U(\varphi) = \left(\begin{smallmatrix} 1 & 0 \\ 0 & e^{i\varphi} \end{smallmatrix}\right)$. The local tensors for the two sublattices are invariant under a combination of U(1) rotations of the physical and virtual legs

as sketched in Figs. 1(b) and 1(c) (see for instance Ref. [50] for MPSs with physical symmetries):

$$A^i_{lr} = \sum_j \sum_{l'r'} U(\varphi)_{ij} U(\varphi)^\dagger_{ll'} A^j_{l'r'} U(\varphi)^\dagger_{r'r}, \tag{12a}$$

$$B^i_{lr} = \sum_j \sum_{l'r'} U(\varphi)^\dagger_{ij} U(\varphi)_{ll'} B^j_{l'r'} U(\varphi)_{r'r}. \tag{12b}$$

If we choose $\varphi = \pi$, these identities correspond to the parity symmetry of Eq. (5), showing that the local MPS tensors are parity even. For each nearest-neighbor bond, one virtual leg transforms with $U(\varphi)$ and the other with $U(\varphi)^\dagger$ in Eq. (12), such that the two U(1) rotations cancel if the bond is contracted. Therefore, the state on a chain with closed boundaries after the contraction of all virtual bonds is invariant under the physical part of the U(1) rotations of Eq. (12), given by staggered transformations $U(\varphi)$ and $U(\varphi)^\dagger$ on A and B orbitals, respectively. Invariance under this global symmetry implies that

$$\begin{aligned} 0 &= \left\langle \sum_x [a^\dagger_{A,x} a_{A,x} - a^\dagger_{B,x} a_{B,x}] \right\rangle \\ &= \left\langle \sum_x [\hat{a}^\dagger_{A,x} \hat{a}_{A,x} + \hat{a}^\dagger_{B,x} \hat{a}_{B,x}] \right\rangle - N_x, \end{aligned} \tag{13}$$

forcing the number of particles measured in terms of the original physical modes to be equal to the number of unit cells as required for the SSH ground state. In Eq. (12), the physical legs on the A and B sublattices transform as particles and holes, respectively, as expected due to the particle-hole transformation of Eq. (7). In addition, Eq. (12) implies that the virtual legs on the A and B sublattices transform as holelike and particlelike degrees of freedom (DOFs), respectively.

In order to gain a better understanding of the parameters α, β, and γ as well as of the systems described by the MPS from Eq. (9), it is helpful to consider a parent Hamiltonian for which it is the exact ground state. This Hamiltonian can be computed directly in terms of its Bloch representation once the MPS of Eq. (9) is expressed as a Gaussian fermionic TNS.

2. Parent Hamiltonian

Since the charge-pumping Hamiltonian of Eq. (3) describes noninteracting fermions, its ground state is a fermionic Gaussian state. It is thus fully characterized by its covariance matrix (CM) (see Appendix A for a summary of our conventions) [51]. As we review in Appendix B, the tensor network formalism may be used to construct Gaussian fermionic TNSs which are ground states of free-fermion Hamiltonians [33]. The CM in Fourier space of a translationally invariant Gaussian TNS is given by a simple expression which can often be evaluated analytically. Then, any positive function $\epsilon(\mathbf{k}) > 0$ on the Brillouin zone gives rise to a parent Hamiltonian with dispersion relation $\epsilon(\mathbf{k})$, whose Bloch representation is obtained by multiplying the CM by $\epsilon(\mathbf{k})$.

For all values of the parameters α, β, and γ, the MPS of Eq. (11) corresponds to a Gaussian fermionic TNS whose Fourier CM is computed analytically in Appendix E. We show that this MPS with bond dimension $D = 2$ is the unique ground state of a longer-range SSH-like model with a staggered chemical potential μ and next-nearest-neighbor hoppings $t^{(2)}_A$ and $t^{(2)}_B$ on the A and B sublattices, respectively, as sketched in Fig. 1(a). The coupling constants of the parent Hamiltonian H_{MPS} depend on the parameters of the MPS as

$$\mu = \frac{\gamma^4 - \alpha^4 - \beta^4}{\alpha^4 + \beta^4 + \gamma^4}, \tag{14a}$$

$$t^{(0)} = \frac{2\beta^2\gamma^2}{\alpha^4 + \beta^4 + \gamma^4}, \tag{14b}$$

$$t^{(1)} = \frac{2\alpha^2\gamma^2}{\alpha^4 + \beta^4 + \gamma^4}, \tag{14c}$$

$$t^{(2)}_A = -t^{(2)}_B = \frac{-2\alpha^2\beta^2}{\alpha^4 + \beta^4 + \gamma^4}, \tag{14d}$$

where $t^{(0)}$ and $t^{(1)}$ denote the hopping amplitudes between nearest-neighbor sites on the same and adjacent unit cells, respectively.

Depending on the parameter values, H_{MPS} describes different phases of the fermionic chain. If any two out of the three parameters α, β, γ vanish, the system is in an atomic state without entanglement between different sites. Indeed, if only γ is nonzero, all hopping constants vanish and the chemical potential is $\mu = +1$ such that we obtain the state with all B sites occupied. On the other hand, if either only α or only β is nonzero, all hopping constants vanish and the chemical potential is $\mu = -1$ such that the MPS is equal to the state with all A sites occupied. This implies that the atomic state with occupied A orbitals is obtained from two distinct parameter configurations $(\alpha, \beta, \gamma) = (1, 0, 0)$ and $(\alpha, \beta, \gamma) = (0, 1, 0)$ whose corresponding local MPS matrices are related by a virtual unitary gauge transformation with representation matrix σ_1.

On the other hand, if only γ and β are nonzero, the system is in a dimerized phase where the next-nearest-neighbor hopping as well as the nearest-neighbor hopping between unit cells vanishes, whereas the nearest-neighbor hopping within unit cells is finite. Unless $|\gamma| = |\beta|$, inversion symmetry is broken by the nonzero chemical potential. For $|\gamma| = |\beta|$, we obtain the trivial dimerized phase of the SSH model. Similarly, if only γ and α are nonzero, all couplings vanish except for the nearest-neighbor hopping between unit cells and the chemical potential. For $|\gamma| = |\alpha|$, inversion symmetry is restored and we obtain the OAI dimerized phase of the SSH model. Finally, if all three parameters are nonzero, both nearest-neighbor hopping constants $t^{(0)}$ and $t^{(1)}$ are nonzero and there is an additional next-nearest-neighbor hopping $t^{(2)}_A = -t^{(2)}_B$ which is odd under inversion.

3. Charge-pumping interpolation

We now use the MPS of Eq. (11) to describe charge pumping by considering the evolving state obtained from time-dependent parameters $\alpha(t)$, $\beta(t)$, and $\gamma(t)$ with time $t \in (-\pi, \pi]$. In Eq. (14) we saw that the MPS can represent charge pumping with a dimerized nearest-neighbor as well as a longer-range nondimerized Hamiltonian. For simplicity, we focus on the dimerized case. For the MPS given by the

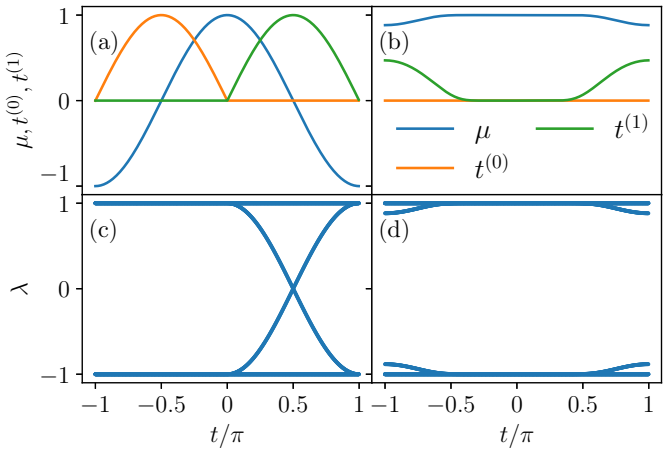

FIG. 2. (a), (b) Coupling constants of H_{MPS} and (c), (d) single-particle ES for the MPS of Eq. (11) along topologically nontrivial and trivial interpolations. In (a) and (c), along the charge-pumping interpolation of Eq. (15) corresponding to a Chern insulator with Chern number $\mathcal{C} = 1$. In (b) and (d), along the topologically trivial interpolation of Eq. (17). In both (a) and (b), the vanishing next-nearest-neighbor coupling $t_A^{(2)} = t_B^{(2)} = 0$ of H_{MPS} is not shown. The ES in (c) and (d) was computed on half of a periodic chain with $N_x = 10$ unit cells.

parametrization

$$\phi_{\mathrm{pump}} : (\alpha(t), \beta(t), \gamma(t)) = \begin{cases} (0, \sqrt{|\sin t/2|}, \sqrt{|\cos t/2|}), & -\pi < t \leqslant 0 \\ (\sqrt{|\sin t/2|}, 0, \sqrt{|\cos t/2|}), & 0 < t \leqslant \pi \end{cases} \tag{15}$$

the parent Hamiltonian H_{MPS} is exactly equal to the time-dependent Hamiltonian $H_{\mathrm{pump}}(t)$ of the dimerized charge-pumping cycle of Eq. (3). The evolution of the couplings in H_{MPS} along the parametrization is shown in Fig. 2(a). Hence, the MPS of Eq. (11) can describe the ground state of the pumping model of Eq. (3) with the topology of a Chern insulator for all times $t \in (-\pi, \pi]$.

The ground state of the charge-pumping cycle $H_{\mathrm{pump}}(t)$ and its correlation functions are continuous along the entire interpolation. However, the local MPS tensors parametrized by ϕ_{pump} are discontinuous at the point $t = \pm\pi$ along the cycle: $\alpha \to 0$ and $\beta \to 1$ as $t \to -\pi$ from above, whereas $\alpha \to 1$ and $\beta \to 0$ as $t \to \pi$ from below. In fact, at $t = \pm\pi$ the system is in the atomic state with all A orbitals occupied. As discussed in the paragraph beneath Eq. (14), there are two distinct configurations for the MPS parameters corresponding to this state which are attained for $t = \pm\pi$.

For the MPS we are considering, the discontinuity in the parametrization ϕ_{pump} is related to the chiral edge mode of the Chern insulator defined by the interpolation. Indeed, charge pumping in the SSH model with open boundaries corresponds to a Chern insulator on a cylinder with periodic and open boundaries in the vertical and horizontal directions, respectively. In the topological phase with Chern number $\mathcal{C} = 1$, each edge of the cylinder hosts a one-dimensional chiral mode [21]. These modes are reflected in the ES of the SSH chain along the charge-pumping cycle. For instance, the single-particle ES [52] of half the chain with periodic boundaries computed from the representation of the state as a Gaussian fermionic TNS along ϕ_{pump} is shown in Fig. 2(c). It has both a left- and a right-moving mode which are localized at the two virtual edges and which are degenerate in the SSH topological phase at $t = \pi/2$.

Using the representation of the MPS in terms of local tensors, we can also compute the many-body ES of half of an infinite chain with open boundaries. Indeed, the many-body ES is isometric to the spectrum of the logarithm of the normalized and symmetrized left and right fixed points of the MPS transfer matrix [28]. In the case of the MPS from Eq. (11), the fixed point is a matrix of dimension 2×2 with eigenvalues

$$\frac{1}{2} \pm \frac{-\alpha^4 + \beta^4 + \gamma^4}{2\sqrt{(-\alpha^4 + \beta^4 + \gamma^4)^2 + 4\alpha^2\beta^2\gamma^4}}. \tag{16}$$

Therefore, the many-body ES has two nontrivial levels that are related by normalization and which describe the spinless fermion at the single virtual boundary of the half-infinite chain. If and only if $\alpha^4 = \beta^4 + \gamma^4$, the two eigenvalues from Eq. (16) are degenerate. This corresponds to a crossing of the Fermi level by the edge fermion. If the interpolation describes a Chern insulator with Chern number $\mathcal{C} = 1$, a degeneracy of the eigenvalues from Eq. (16) should therefore occur exactly once along the cycle. For the parametrization ϕ_{pump} this happens in the SSH topological phase at $t = \pi/2$ with $\alpha = \gamma$ and $\beta = 0$. Indeed, $\alpha^4 < \beta^4 + \gamma^4$ for $t < \pi/2$ and $\alpha^4 > \beta^4 + \gamma^4$ for $t > \pi/2$. Hence, the nontrivial Chern number implies that for MPS of the form of Eq. (11) the parametrization has to be discontinuous along the cycle in order to combine the two parts of the interpolation where $\alpha^4 \gtrless \beta^4 + \gamma^4$ with only a single degenerate point.

We emphasize that this discontinuity in the MPS interpolation is required by the topology of the charge-pumping cycle, even if the pumping cycle itself is infinitely often continuously differentiable. For example, the smooth deformation of the topological pumping cycle, whose existence is discussed in Sec. II A, has an MPS ground state of the form of Eq. (11). Due to the nontrivial topology of the cycle, this MPS has a discontinuous interpolation despite the smoothness of its Bloch Hamiltonian.

The MPS of Eq. (11) can also describe cyclic interpolations corresponding to topologically trivial two-dimensional models. For instance, the MPS with parametrization

$$\phi_{\mathrm{triv}} : (\alpha(t), \beta(t), \gamma(t)) = \left(\tfrac{1}{2} e^{-(\tan\frac{|t|}{2})^{-2}}, 0, 1\right) \tag{17}$$

for $t \in (-\pi, \pi]$ corresponds to the ground state of a model with finite chemical potential and nearest-neighbor hopping $t^{(1)}$ between unit cells, whereas the hopping within unit cells and the next-nearest-neighbor hopping vanish [see Fig. 2(b)]. From the single-particle ES in Fig. 2(d) we see that the conduction and valence bands in this system are not connected by the edge modes such that the Chern number is zero. Indeed, both the MPS parametrization ϕ_{triv} and the

corresponding Bloch parent Hamiltonian are smooth along the cycle.

III. CHERN INSULATOR PEPS FROM SSH CHARGE PUMPING

In this section we discuss how charge pumping can be used to construct tensor networks in $d+1$ dimensions starting from d-dimensional TNSs. Specifically, we show how the MPS from Sec. II for the SSH model along a charge-pumping cycle leads to a two-dimensional PEPS for a Chern insulator. In Sec. III B we define a hybrid real-momentum space PEPS with finite bond dimension for the Chern insulator. In Sec. III C, we perform an inverse FT in the direction $d+1$ required to transform the state to a fully real-space representation. In Sec. III D we study how the resulting state can be expressed as a real-space PEPS, whose bond dimension is investigated in Sec. III E.

A. $(d+1)$-dimensional TIs from charge pumping

Charge pumping provides a systematic method to obtain a TI in $d+1$ spatial dimensions from a d-dimensional TI. Indeed, if the Bloch Hamiltonian of the d-dimensional model is smooth along the charge-pumping interpolation as a function of the cyclic time $t \in (-\pi, \pi]$, t can be identified with the momentum k_{d+1} in the $(d+1)$st direction of the $(d+1)$-dimensional system. The time-dependent Hamiltonian of the d-dimensional model then gives the Bloch Hamiltonian of the $(d+1)$-dimensional system as a function of k_{d+1}. For instance, charge pumping in the SSH model with $d=1$ defines a two-dimensional Chern insulator with Chern number $\mathcal{C}=1$ (cf. Sec. II A).

We discretize the $(d+1)$st dimension with a finite number N_{d+1} of lattice sites. The discrete momentum values in $(-\pi, \pi]$ are $k_{d+1}^{(j)} = \frac{\pi}{N_{d+1}}(2j - N_{d+1})$ for even N_{d+1}, and $k_{d+1}^{(j)} = \frac{\pi}{N_{d+1}}(2j - N_{d+1} + 1)$ for odd N_{d+1}. They are identified with discrete times $t^{(j)} = k_{d+1}^{(j)}$ for $j = 0, \ldots, N_{d+1} - 1$.

Let us express the identification of time t and momentum k_{d+1} as a relation between the mode operators of the hybrid and real-space systems. The d-dimensional system has annihilation operators $\hat{a}_{\tau,\mathbf{x}}(t^{(j)})$ for the physical fermion on the orbital $\tau = 1, \ldots, f$ on the unit cell $\mathbf{x} \in \mathbb{Z}^d$, where f is the number of orbitals per unit cell. They depend on the discretized time value $t^{(j)}$ along the pumping interpolation at which the d-dimensional model is evaluated. For example, in the SSH model we have mode operators $\hat{a}_{A,x}(t^{(j)}), \hat{a}_{B,x}(t^{(j)})$ with $x = 0, \ldots, N_x - 1$.

The $(d+1)$-dimensional model obtained from charge pumping has the same number of orbitals as the d-dimensional model it is derived from. For instance, the Chern insulator constructed from the SSH model also has sublattices A and B. Therefore, the physical creation operators of the $(d+1)$-dimensional system in real space are $\hat{a}_{\tau,(\mathbf{x},x_{d+1})}$, where $x_{d+1} = 0, \ldots, N_{d+1} - 1$ is the real-space coordinate in the $(d+1)$st direction and $\tau = 1, \ldots, f$. The charge-pumping construction of the $(d+1)$-dimensional model requires periodic boundary conditions in the direction $d+1$. We may therefore consider the FT of the mode operators in the direction $d+1$, while keeping the real-space coordinate $\mathbf{x}$ in the other d dimensions, given by

$$\hat{a}_{\tau,(\mathbf{x},k_{d+1}^{(j)})} = \sum_{x_{d+1}=0}^{N_{d+1}-1} \mathcal{F}_{k_{d+1}^{(j)} x_{d+1}} \hat{a}_{\tau,(\mathbf{x},x_{d+1})} \tag{18a}$$

with

$$\mathcal{F}_{k_{d+1}^{(j)} x_{d+1}} = \frac{e^{-ik_{d+1}^{(j)} x_{d+1}}}{\sqrt{N_{d+1}}}. \tag{18b}$$

In terms of these mode operators, the identification of time t and momentum k_{d+1} is the expressed by the identity

$$\hat{a}_{\tau,\mathbf{x}}(t^{(j)}) = \hat{a}_{\tau,(\mathbf{x},k_{d+1}^{(j)})} \tag{19}$$

for all d-dimensional unit cells $\mathbf{x}$ and sublattices $\tau = 1, \ldots, f$. For example, in the case of the SSH charge pumping we have $\hat{a}_{\tau,x}(t^{(j)}) = \hat{a}_{\tau,(x,k_y^{(j)})}$ for $\tau = A, B$ and $x = 0, \ldots, N_x - 1$.

The Bloch Hamiltonian of the $(d+1)$-dimensional model is the time-dependent Hamiltonian of the d-dimensional system. Hence, with the identification of Eq. (19), the $(d+1)$-dimensional ground state is given by the direct product

$$|\psi_{d+1}\rangle = \bigotimes_{j=0}^{N_{d+1}-1} |\psi_d(t^{(j)})\rangle \tag{20}$$

of the many-body ground states $|\psi_d(t)\rangle$ of the d-dimensional model evaluated at the N_{d+1} discrete times along the interpolation. From Eq. (19) it is clear that this defines the ground state with respect to hybrid $(d+1)$-dimensional real-momentum space coordinates $(\mathbf{x}, k_{d+1}^{(j)})$.

In order to obtain the state in terms of $(d+1)$-dimensional real-space coordinates $(\mathbf{x}, x_{d+1})$, we need to apply the inverse of the FT of Eq. (18) to the hybrid state of Eq. (20). If the d-dimensional pumping Bloch Hamiltonian is smooth as a function of time, the real-space correlation functions are guaranteed to decay faster than any polynomial [47].

B. Hybrid real-momentum-space Chern PEPS

We now specialize this construction, which we explained above in terms of generic free-fermionic TIs, to d-dimensional TIs which are described by a GfTNS at all times along their charge-pumping cycle. We will thereby obtain a GfTNS for the $(d+1)$-dimensional TI.

For the remainder of this section and for pedagogical purposes, we will focus on the one-dimensional case (i.e., $d=1$) and the corresponding notation. We will mostly rely on charge pumping in the SSH model which is described by the MPS with bond dimension $D_{\mathrm{SSH}} = 2$ from Eq. (9). Hence, we will obtain a Gaussian fermionic PEPS for the Chern insulator with Chern number $\mathcal{C}=1$. Extensions to other models and higher dimensions are straightforward.

In case the d-dimensional ground state along the pumping cycle is given as a GfTNS, Eq. (20) allows to define the $(d+1)$-dimensional ground state as a hybrid TNS, where the first d dimensions correspond to real space and the $(d+1)$st dimension is expressed in momentum space. Indeed, the local tensor of the hybrid TNS at the position $(\mathbf{x}, k_{d+1}^{(j)})$ is given

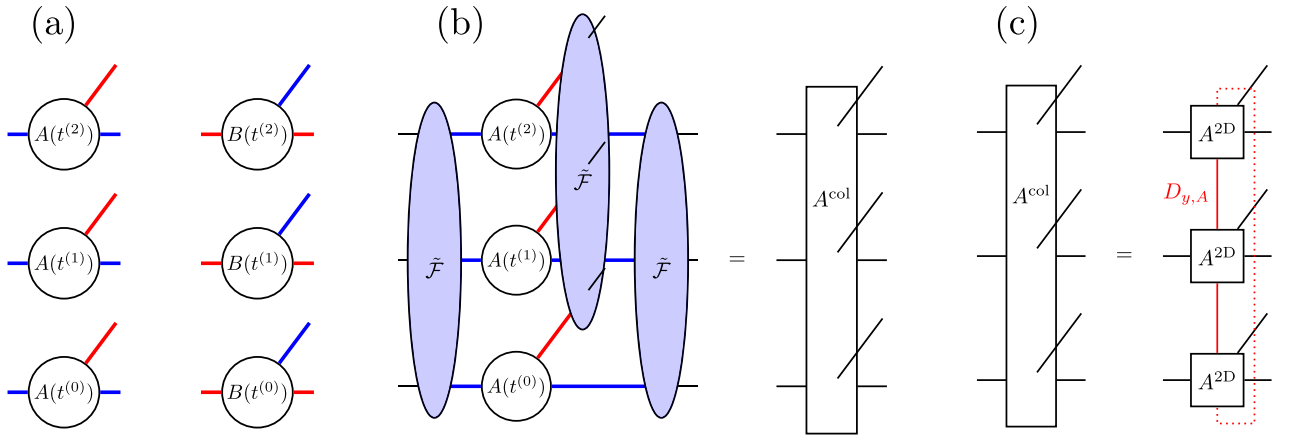

FIG. 3. (a) Hybrid real-momentum-space PEPS for $N_y = 3$ sites in the vertical direction obtained by stacking rows of the MPS of Eq. (11) evaluated at different times $t^{(j)}$ along the charge-pumping interpolation. Physical and virtual legs transforming as particles and holes under the U(1) symmetry of Eq. (12) are marked in red and blue, respectively. Since the vertical bond dimension is trivial, i.e., equal to one, it is omitted in this sketch. (b) Inverse FT $\tilde{\mathcal{F}}$ acting separately on the physical and horizontal virtual legs of one column of A sites of the hybrid PEPS. The result defines the column tensor A^{col} for the real-space PEPS. (c) Decomposition of the column tensor A^{col} into the contraction of local PEPS tensors A^{2D} for the two-dimensional state. The vertical virtual legs of A^{2D} marked in red have a bond dimension $D_{y,A}$ which generally grows with the system size N_y due to the nonlocality of the inverse FT. The inverse FT and decomposition of a column of B sites is analogous.

by the local tensor of the d-dimensional model at the d-dimensional real-space position $\mathbf{x}$ and time $t^{(j)}$.

Thus, the virtual DOFs of the hybrid TNS in the first d directions are identical to those of the d-dimensional model. In other words, the identification of time and momentum from Eq. (19) holds not just for the physical mode operators, but also for the virtual mode operators in the first d dimensions.

On the other hand, due to the direct product in the direction of k_{d+1} in Eq. (20), the hybrid TNS does not need virtual legs in the direction $d+1$, and we say that the bond dimension in this direction is equal to one (implying that the contraction of this direction corresponds trivially to a product).

The hybrid Chern PEPS obtained from the SSH charge pumping MPS of Eq. (9) is sketched in Fig. 3(a) in the hybrid coordinate system where the horizontal axis describes x and the vertical axis corresponds to $k_y \equiv k_{d+1}$. The local tensor for a site on the A sublattice at the position $(x, k_y^{(j)})$ is given by the SSH local tensor $A^i_{lr}(t^{(j)})$ at the time $t^{(j)}$ along the cycle, and similarly for the B sublattice. In the horizontal direction, the two-dimensional hybrid state hence inherits both the translation invariance and the constant finite bond dimension D_{SSH} of the MPS. As discussed in the previous paragraph, virtual legs in the vertical direction are not needed for the hybrid Chern PEPS and are hence not shown in Fig. 3(a).

C. Inverse Fourier transform

As discussed below Eq. (20), the hybrid state obtained from charge pumping is mapped to a $(d+1)$-dimensional real-space coordinate system by applying an inverse FT in the direction $d+1$ to the fermionic mode operators. For GfTNSs, which have virtual in addition to physical DOFs, the inverse FT should be applied to both the physical mode operators and the virtual fermionic mode operators in the first d directions. For the hybrid Chern PEPS, we therefore apply the inverse FT in the vertical direction to the physical and the horizontal virtual legs. The extension of the FT to the horizontal virtual modes amounts to a virtual basis change and does not alter the physical state, but ensures that the real-space PEPS is invariant under vertical translations $y \mapsto y+1$ of its physical and virtual legs (see also Appendix F).

For the hybrid Chern PEPS, the correct definition of the inverse FT in the vertical direction y entails a subtlety. Indeed, recall that the SSH charge-pumping MPS from Eq. (9) is defined with respect to mode operators $a_{\tau,x}(t^{(j)})$ related to the $\hat{a}_{\tau,x}(t^{(j)})$ used in Eq. (19) by the particle-hole transformation of Eq. (7). For the Chern PEPS, we perform an analogous particle-hole transformation in two-dimensional real space and define new mode operators

$$a_{A,(x,y)} = \hat{a}_{A,(x,y)}, \tag{21a}$$

$$a_{B,(x,y)} = \hat{a}^\dagger_{B,(x,y)}. \tag{21b}$$

The operators $a_{A,(x,y)}, a^\dagger_{A,(x,y)}, a_{B,(x,y)}, a^\dagger_{B,(x,y)}$ span the basis in which we want to express the real-space Chern PEPS.

The SSH particle-hole transformation of Eq. (7) acts within the set of operators at time $t^{(j)}$. Since we identify time and momentum, this is equivalent to a particle-hole transformation acting on the modes of the Chern PEPS in momentum space rather than real space like in Eq. (21). Due to the antiunitarity of the particle-hole transformation, the inverse FT relating the modes $a_{B,x}(t^{(j)})$ and $a_{B,(x,y)}$ on the B sublattice therefore contains an additional complex conjugation. Hence, the physical mode operators $a_{\tau,x}(t^{(j)})$ of the SSH models, providing the basis for the hybrid Chern PEPS, and the mode operators $a_{\tau,(x,y)}$ for the real-space Chern PEPS are related as

$$a_{\tau,(x,y)} = \sum_{j=0}^{N_y-1} \tilde{\mathcal{F}}_{\tau,\tau;y,t^{(j)}} a_{\tau,x}(t^{(j)}) \tag{22a}$$

with the inverse vertical FT

$$\tilde{\mathcal{F}}_{\tau,\tau';y,t^{(j)}} = \frac{\delta_{\tau,\tau'}}{\sqrt{N_y}} e^{i\eta_\tau y t^{(j)}}. \tag{22b}$$

Here, $\eta_A = 1$ and $\eta_B = -1$ for the physical modes which are particlelike on the A sublattice and holelike on the B sublattice.

The inverse FT of the horizontal virtual legs of the hybrid PEPS is analogous to Eq. (22) for the physical modes. Here, the particlelike or holelike character of the virtual modes is determined by their transformation under the U(1) symmetry of Eq. (12). Specifically, the left and right virtual legs on the A sublattice transform as holes, i.e., $\eta_{L,A} = \eta_{R,A} = -1$, whereas the left and right virtual legs on the B sublattice transform as particles such that $\eta_{L,B} = \eta_{R,B} = 1$.

Let us now study how the inverse vertical FT $\tilde{\mathcal{F}}$ acts on the hybrid Chern PEPS. Due to the translation invariance in the horizontal direction, it is enough to consider one column of the hybrid state given by the sites $(x, k_y^{(j)})$ for a fixed horizontal position x and $j = 0, \ldots, N_y - 1$ [see Fig. 3(a)]. Under $\tilde{\mathcal{F}}$, the hybrid column is mapped to one column of the two-dimensional real-space state, given by the sites (x, y) with $y = 0, \ldots, N_y - 1$.

Since the inverse FT $\tilde{\mathcal{F}}$ is nonlocal, for a generic interpolation there are long-range correlations in the real-space column $\{(x, y)\}_{0 \leqslant y \leqslant N_y - 1}$ of the PEPS. In the tensor network language, the real-space column is therefore described by a single tensor obtained from the application of $\tilde{\mathcal{F}}$ to one column of the hybrid PEPS [in contrast to the hybrid column $\{(x, k_y^{(j)})\}_{0 \leqslant j \leqslant N_y - 1}$ which is described by a product of individual tensors for each $k_y^{(j)}$, signifying the absence of correlations in the vertical direction]. For a real-space column of A sites, we denote this tensor by A^{col} as shown in Fig. 3(b). Similarly, we define a tensor B^{col} for a real-space column of B sites. The tensors A^{col} and B^{col} have N_y physical legs of dimension $d_p = 2$ and N_y left and right virtual legs of dimension $D_{\mathrm{SSH}} = 2$, which describe the physical and horizontal virtual DOFs of the real-space PEPS.

The SSH pumping MPS is a Gaussian MPS for free fermions. Thus, the column tensors A^{col} and B^{col} are also Gaussian states, which can be described by their covariance matrices (CMs). These CMs are computed in Appendix F for the general d-dimensional case. There we show that the CMs of the real-space columns A^{col} and B^{col}, defined by the application of the inverse FT of Eq. (22) to the physical and horizontal virtual legs of the hybrid columns, are given by the inverse FT of the time-dependent CMs describing the local SSH tensors $A^i_{lr}(t^{(j)})$ and $B^i_{lr}(t^{(j)})$ along the pumping cycle. This result fully characterizes the column tensors A^{col} and B^{col}.

D. Translation-invariant real-space PEPS

From the previous subsections, we are now ready to discuss how the two-dimensional real-space state can be expressed as a TNS with local tensors for each site. For that purpose, the column tensors A^{col} and B^{col} have to be decomposed into a column of local PEPS tensors A^{2D} and B^{2D} with both horizontal virtual legs of dimension D_{SSH} and vertical virtual legs with dimension $D_{y,A}$ and $D_{y,B}$, respectively. We require the local PEPS tensors to be identical on all sites of the same sublattice as shown in Fig. 3(c) in order to make the invariance under real-space translations explicit.

The decomposition of the column into PEPS tensors can be achieved using tools developed for one-dimensional MPSs [53,54]. To that end, we define one-dimensional pure states $|\psi_{\mathrm{1D}}(A^{\mathrm{col}})\rangle$ and $|\psi_{\mathrm{1D}}(B^{\mathrm{col}})\rangle$, whose many-body wave functions are the tensor elements of A^{col} and B^{col}, respectively. Therefore, $|\psi_{\mathrm{1D}}(A^{\mathrm{col}})\rangle$ effectively describes a chain of length N_y, where the local Hilbert space at each site of the fictitious chain is the tensor product of the physical and horizontal virtual Hilbert spaces of A^{col} at the corresponding physical site (and similarly for $|\psi_{\mathrm{1D}}(B^{\mathrm{col}})\rangle$ and B^{col}). Pictorially, $|\psi_{\mathrm{1D}}(A^{\mathrm{col}})\rangle$ and $|\psi_{\mathrm{1D}}(B^{\mathrm{col}})\rangle$ are obtained by merging at each site the physical and horizontal virtual legs of A^{col} and B^{col} into an effective physical index of dimension $\tilde{d}_p = d_p D_{\mathrm{SSH}}^2$ per site.

Our goal is now to express $|\psi_{\mathrm{1D}}(A^{\mathrm{col}})\rangle$ and $|\psi_{\mathrm{1D}}(B^{\mathrm{col}})\rangle$ as translation-invariant MPSs with periodic boundary conditions. Then, after unfolding the effective physical index into the physical and horizontal virtual indices of the PEPS, the local tensors of these MPSs will define the PEPS tensors A^{2D} and B^{2D}, respectively. Similarly, the MPS bond dimensions $D_{y,A}$ and $D_{y,B}$ are equal to the vertical bond dimensions of the PEPS local tensors A^{2D} and B^{2D}, respectively.

Numerically, the translation-invariant MPSs for $|\psi_{\mathrm{1D}}(A^{\mathrm{col}})\rangle$ and $|\psi_{\mathrm{1D}}(B^{\mathrm{col}})\rangle$ can be obtained as follows. Multiple steps are necessary since the common and stable MPS algorithms rely on the presence of open boundary conditions and do not directly find a periodic translation-invariant MPS for a translation-invariant state. Instead, in a first step the Gaussian states $|\psi_{\mathrm{1D}}(A^{\mathrm{col}})\rangle$ and $|\psi_{\mathrm{1D}}(B^{\mathrm{col}})\rangle$ can be decomposed into non-translation-invariant Gaussian MPSs with open boundary conditions by performing successive Schmidt decompositions of the system [53,55]. We are not aware of any method to transform a Gaussian open-boundary MPS into a Gaussian translation-invariant MPS. We therefore interpret the Gaussian MPSs for $|\psi_{\mathrm{1D}}(A^{\mathrm{col}})\rangle$ and $|\psi_{\mathrm{1D}}(B^{\mathrm{col}})\rangle$ as regular fermionic open-boundary MPSs by choosing physical and virtual basis states and computing the local MPS tensors for each site. Finally, these open-boundary MPSs are transformed into translation-invariant and generically non-Gaussian MPSs with periodic boundary conditions following the standard procedure described in Ref. [54]. This approach leads to the bond dimension of the translation-invariant MPS being given by the sum of the bond dimensions of the open-boundary MPS for each site. Therefore, the bond dimension grows at least linearly with the system size [54].

E. Vertical PEPS bond dimension

Above, we showed that the inverse FT of the hybrid PEPS can be decomposed into a $(d+1)$-dimensional real-space TNS, where the bond dimension in the first d directions is equal to that of the original d-dimensional state. The core question is the scaling of the bond dimension in the $(d+1)^{\mathrm{st}}$ real- space dimension with respect to the system size in this direction.

1. Lower bound from ES

The bond dimension of a tensor network is intimately related to the entanglement between its physical particles: For

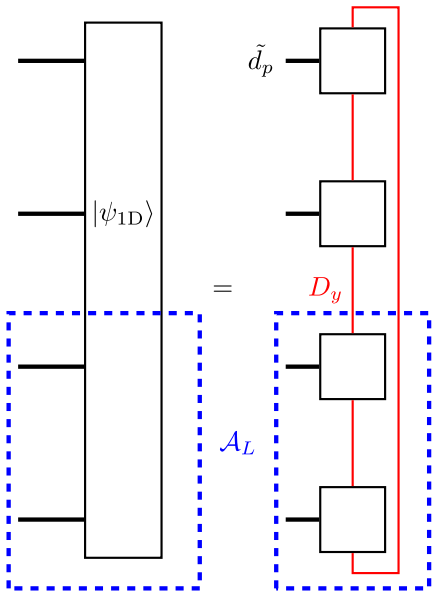

FIG. 4. Schmidt decomposition of the one-dimensional effective state $|\psi_{1D}\rangle$ for the PEPS column with physical dimension $\tilde{d}_p$ into the subsystem $\mathcal{A}_L$ of the first L sites and its complement. When $|\psi_{1D}\rangle$ is written as a translation-invariant MPS with bond dimension D_y, the virtual boundary of the subsystem $\mathcal{A}_L$, marked in blue, crosses two bonds of the MPS.

a TNS describing a physical system with a subsystem $\mathcal{A}$, the total dimension of all virtual legs at the boundary $\partial\mathcal{A}$ can be no smaller than the rank of the state's Schmidt decomposition into the DOFs of $\mathcal{A}$ and its complement. This constraint allows us to infer a lower bound for the vertical bond dimension of the real-space PEPS from the ES of the one-dimensional column states.

We consider a generic one-dimensional effective column state denoted $|\psi_{1D}\rangle$ with an effective physical dimension $\tilde{d}_p$. Below, we will choose either $|\psi_{1D}\rangle = |\psi_{1D}(A^{\text{col}})\rangle$ or $|\psi_{1D}\rangle = |\psi_{1D}(B^{\text{col}})\rangle$ with $\tilde{d}_p = d_p D_{\text{SSH}}^2$. We assume that $|\psi_{1D}\rangle$ is expressed as a translation-invariant MPS with a bond dimension D_y corresponding to the vertical PEPS bond dimension (see Fig. 4). Such a representation can be obtained for instance using the procedure described in the previous subsection. We now perform a Schmidt decomposition of the pure state $|\psi_{1D}\rangle$ with respect to the subsystem $\mathcal{A}_L$ of the first L sites $0 \leqslant y \leqslant L-1$, and denote the rank of the decomposition by $r_L(|\psi_{1D}\rangle)$. As sketched in Fig. 4, the cut between $\mathcal{A}_L$ and its complement crosses exactly two virtual bonds of the MPS, namely, those between sites $(L-1, L)$ and $(N_y-1, 0)$, each of dimension D_y. Since the virtual dimension can be no smaller than the Schmidt rank for any subsystem size L, we obtain the bound

$$D_y^2 \geqslant \max_{1\leqslant L\leqslant N_y-1} r_L(|\psi_{1D}\rangle). \tag{23}$$

The Schmidt rank $r_L(|\psi_{1D}\rangle)$ may be obtained by counting the nontrivial levels in the single-particle ES of the Gaussian column state $|\psi_{1D}\rangle$. This ES can be computed numerically based on the explicit result for the CM of $|\psi_{1D}\rangle$ given in Appendix F. Since the state $|\psi_{1D}\rangle$ with physical dimension $\tilde{d}_p$ has $\log_2(\tilde{d}_p)$ free-fermionic modes per lattice site, its single-particle ES with respect to the subsystem $\mathcal{A}_L$ consists of levels $0 \leqslant |\lambda_i(L)| \leqslant 1$ with $1 \leqslant i \leqslant L\log_2(\tilde{d}_p)$ [see Eq. (A5) for a definition of the single-particle ES and its levels $|\lambda_j|$]. For an improved numerical stability, we actually compute $\mu_i(L) = \sqrt{1-\lambda_i(L)^2}$ that may be conveniently extracted from the CM [see Eq. (A6)]. Here, values $\mu_i(L) = 1$ and $\mu_i(L) = 0$ correspond to maximally entangled and nonentangled modes, respectively. The many-body Schmidt rank of the state $|\psi_{1D}\rangle$ is therefore given by the exponential

$$r_L(|\psi_{1D}\rangle) = 2^{\#\{\mu_i(L)>0\}} \tag{24}$$

of the number of entangled modes in the single-particle ES with $\mu_i(L)$ bigger than zero.

2. *Exponential growth*

The number of entangled modes in the single-particle ES of a column A^{col} of unit cells of the real-space PEPS is displayed in Fig. 5(a) for two different cyclic interpolations of the MPS from Eq. (11): on one hand, the parametrization ϕ_{pump} of Eq. (15) giving rise to a two-dimensional Chern insulator, and on the other hand the parametrization ϕ_{triv} of Eq. (17) corresponding to a topologically trivial two-dimensional state. The corresponding data of the column B^{col} is identical.

For ϕ_{pump} the number of entangled modes is equal to

$$\#\{\mu_i(L) > 0\} = \min\{3L, N_y\} \tag{25}$$

when $L \leqslant N_y/2$ (the spectra for L and $N_y - L$ are identical). In Appendix G we show that this is the maximal number of entangled modes which is compatible with the global U(1) symmetry of A^{col} inherited from the SSH model MPS. Here, the factor 3 in Eq. (25) is a consequence of the column tensor having three fermions (one physical fermion and two virtual fermions) per site. The validity of Eq. (25) can be seen in Fig. 5(a) for the smallest system size $N_y = 28$. For larger system sizes, the number of entangled modes shown in Fig. 5(a) is lower than Eq. (25) because of the finite numerical resolution, as shown by the ES in Fig. 5(b). We have checked that for the Chern PEPS obtained from the MPS corresponding to the smooth charge-pumping cycle described in Sec. II A, the number of entangled modes is also given by Eq. (25).

For ϕ_{triv}, the number of entangled modes is given by $2L$ when $L \leqslant N_y/2$. This is lower than Eq. (25) for ϕ_{pump} except at $L = N_y/2$, where both numbers agree. As discussed in Appendix G, this reduction of entangled modes is due to the decoupling of all right virtual legs and is not related to topology. Indeed, for the trivial cycle, the parameter $\beta(t) = 0$ vanishes for the entire duration of the interpolation ϕ_{triv}. Any small perturbation of ϕ_{triv} by a nonzero β increases the number of entangled modes to Eq. (25). Moreover, these additional decoupled modes disappear when blocking the two columns A^{col} and B^{col}, i.e., by contracting the bonds connecting them. Hence, the column for AB unit cells has the same Schmidt rank for both ϕ_{pump} and ϕ_{triv}.

The number of entangled modes from Eq. (25) corresponds to a maximal Schmidt rank

$$\max_{1\leqslant L\leqslant N_y-1} r_L[|\psi_{1D}(A^{\text{col}})\rangle] = 2^{N_y} \tag{26}$$

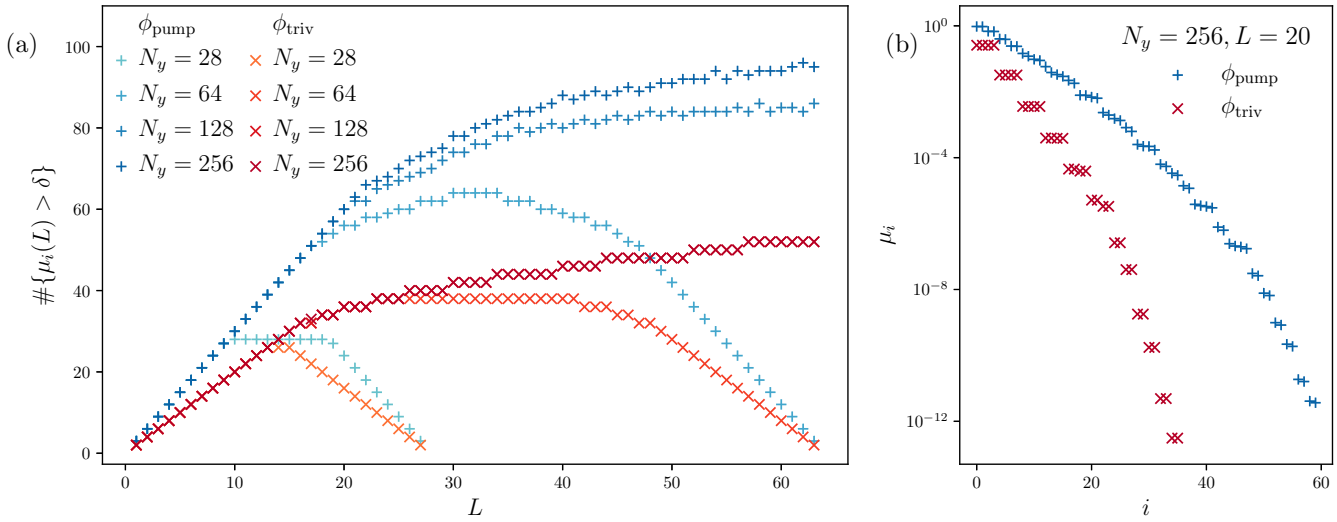

FIG. 5. Single-particle ES of a column A^{col} of the two-dimensional real-space TNSs defined by two different parametrizations for the MPS of Eq. (11): the charge-pumping interpolation ϕ_{pump} of Eq. (15) leading to a Chern insulator, and the parametrization ϕ_{triv} of Eq. (17) leading to a topologically trivial two-dimensional state. (a) Number of modes in the single-particle ES with a finite entanglement corresponding to a value $\mu_i > \delta$ with $\delta = 10^{-13}$ the numerical accuracy for different system sizes N_y as a function of the subsystem size L. (b) Single-particle ES for a column with $N_y = 256$ sites with respect to the subsystem $\mathcal{A}_L$ with $L = 20$. The double degeneracy in the ES corresponding to ϕ_{triv} is due to the decoupling of all right virtual legs since $\beta(t) = 0$ along ϕ_{triv}.

for the state $|\psi_{\text{1D}}(A^{\text{col}})\rangle$, and similarly for $|\psi_{\text{1D}}(B^{\text{col}})\rangle$. The bound of Eq. (23) therefore implies that the vertical bond dimensions $D_{y,A}$ and $D_{y,B}$ grow exponentially as a function of N_y. This is a generic feature of our construction and *not* related to the topology of the state: It originates in the nonlocality of the inverse FT which couples all states in the exponentially growing Hilbert space of one column. Indeed, a generic quantum state requires an exponentially growing bond dimension to be represented *exactly* as a TNS.

Despite the faster decay of the single-particle entanglement energies for the topologically trivial state than for the Chern insulator in Fig. 5(b), this does not allow us to make any statement about differences in the growth of the vertical bond dimension required for an *approximative* PEPS for the two systems.

IV. FERMIONIC PEPS FOR TWO-DIMENSIONAL HIGHER-ORDER TI

In this section, we study a Gaussian fermionic PEPS for the topological quadrupole model from Ref. [1], which is reviewed in Sec. IV A. The PEPS is defined in Sec. IV B, where we also provide its parent Hamiltonian. In Sec. IV C we discuss a three-dimensional PEPS with chiral hinge states obtained from a dipole-pumping interpolation of the quadrupole model [2,3].

A. Second-order quadrupole insulator

A two-dimensional second-order topological phase with a quantized bulk quadrupole moment was recently proposed theoretically [1] and has subsequently been observed experimentally in mechanical [11], photonic [14–17], and electrical [18,19] systems. This phase is described by a microscopic free-fermionic model with one spinless fermionic mode per site and a unit cell of 2×2 sites depicted in Fig. 6(a). We consider the system at half-filling where only the lowest two bands are occupied. With open boundary conditions, the nearest-neighbor Hamiltonian is given by

$$H_{\text{Quad}} = \sum_{\mathbf{x}} \sum_{j=0,1} \left[t_x^{(j)} (\hat{a}^\dagger_{1,\mathbf{x}} \hat{a}_{3,\mathbf{x}+j\hat{\mathbf{x}}} + \hat{a}^\dagger_{4,\mathbf{x}} \hat{a}_{2,\mathbf{x}+j\hat{\mathbf{x}}}) + t_y^{(j)} (\hat{a}^\dagger_{1,\mathbf{x}} \hat{a}_{4,\mathbf{x}+j\hat{\mathbf{y}}} - \hat{a}^\dagger_{3,\mathbf{x}} \hat{a}_{2,\mathbf{x}+j\hat{\mathbf{y}}}) + \text{H.c.} \right], \quad (27)$$

where $\hat{\mathbf{x}}$ and $\hat{\mathbf{y}}$ denote the unit vectors in the horizontal and vertical direction, respectively. The positions of the unit cells are $\mathbf{x} = x\hat{\mathbf{x}} + y\hat{\mathbf{y}}$ with $0 \leqslant x \leqslant N_x - 1$ and $0 \leqslant y \leqslant N_y - 1$ on a lattice with N_x and N_y unit cells in the horizontal and vertical directions. For $\tau = 1, \ldots, 4$, $\hat{a}^\dagger_{\tau,\mathbf{x}}$ denotes the creation operator for a fermion in orbital τ and unit cell at position $\mathbf{x}$. The Hamiltonian of Eq. (27) contains four nearest-neighbor hopping amplitudes $t_x^{(0)}, t_y^{(0)}, t_x^{(1)}$, and $t_y^{(1)}$, where the subscripts x and y refer to hoppings in the horizontal and vertical directions, and the superscripts (0) and (1) indicate hopping between sites on the same and adjacent unit cells, respectively. The signs of the hopping amplitudes ensure that there is a flux π through every plaquette of the square lattice.

The quadrupole model of Eq. (27) is in a second-order topological OAI phase protected by the horizontal and vertical mirror symmetries M_x and M_y if $t_x^{(0)}/t_x^{(1)} \in]-11[$ and $t_y^{(0)}/t_y^{(1)} \in]-11[$ [1,56]. In this phase, corners host gapless protected states at the intersection of two gapped edges. Moreover, the system possesses a quantized bulk quadrupole moment, edge dipole moment, and corner charge [3]. When the hopping amplitudes $t_x^{(0)}$ and $t_y^{(0)}$ within unit cells vanish in the OAI phase, the model is in a dimerized OAI phase where every site in the bulk is contained in a decoupled plaquette shifted from the unit cell by one site in the horizontal and vertical directions. Hence, the corner modes are fully localized on the four corner sites of a rectangular patch. On

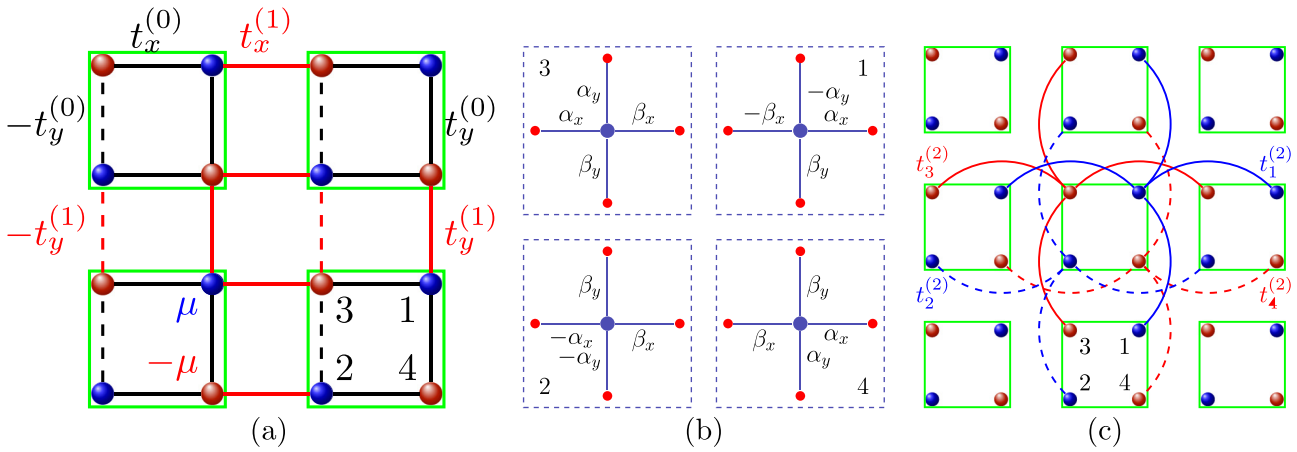

FIG. 6. (a) Sketch of the quadrupole model from Ref. [3]. A unit cell (marked with a green square) contains four sites. The horizontal and vertical nearest-neighbor hoppings $t_x^{(0)}$ and $t_y^{(0)}$ within unit cells are sketched in black, whereas the nearest-neighbor hoppings $t_x^{(1)}$ and $t_y^{(1)}$ between unit cells are sketched in red. The couplings corresponding to dashed bonds carry a negative sign to ensure a flux π through every plaquette. Lattice sites marked in blue and red have a chemical potential μ and $-\mu$, respectively. (b) Sketch of a unit cell of the quadrupole PEPS from Eq. (29). For each site 1, 2, 3, or 4 marked by a dashed blue square, the blue (red) circles denote its physical (virtual) fermions. Each edge connecting a physical and virtual fermion is labeled with the amplitude of the local tensor when these two fermions are in state $|1\rangle$ and all other virtual fermions of the same site are in state $|0\rangle$. (c) Next-to-nearest-neighbor hopping terms of Eq. (32) in the parent Hamiltonian H_{PEPS}.

the other hand, for $|t_x^{(0)}/t_x^{(1)}| > 1$ or $|t_y^{(0)}/t_y^{(1)}| > 1$ the model of Eq. (27) is in a trivial phase with gapped edges and corners. If the hoppings $t_x^{(1)}$ and $t_y^{(1)}$ between adjacent unit cells vanish, the system is in a trivial dimerized phase where each unit cell decouples from the rest of the system.

Similarly to the charge-pumping cycle discussed in Sec. II A, a dipole-pumping cycle interpolating between the trivial and OAI dimerized phases of the quadrupole model can be defined by adding the chemical potential μ to all sites on the sublattices 1 and 2 and $-\mu$ to all sites on the sublattices 3 and 4 [3]. Therefore, the staggering pattern breaks the symmetries protecting the topological phase but preserves the C_2 rotation symmetry [see Fig. 6(a)]. The dipole-pumping cycle is obtained from C_4-symmetric hopping amplitudes $t^{(0)} \equiv t_x^{(0)} = t_y^{(0)}$ and $t^{(1)} \equiv t_x^{(1)} = t_y^{(1)}$ and a chemical potential μ evolving according to the same cyclic interpolation of Eq. (3) as for the SSH charge pump.

The properties of the dipole-pumping cycle for the quadrupole model are analogous to those of the charge-pumping cycle for the SSH model. In particular, the system remains in a dimerized state throughout the interpolation since at all times $t \in [-\pi, \pi]$ only one of the two hopping amplitudes $t^{(0)}(t)$ and $t^{(1)}(t)$ is nonzero. At $t = \pm\pi$ and $t = 0$, the system is in an atomic state with only the orbitals 1 and 2 occupied at $t = \pm\pi$ and only the orbitals 3 and 4 occupied at $t = 0$. For $-\pi < t < 0$, the hopping within unit cells is nonzero, whereas the hopping between unit cells is nonzero for $0 < t < \pi$. In both cases, charge gets transferred by the changing chemical potential. At $t = -\pi/2$ and $\pi/2$, the chemical potential vanishes such that the mirror symmetries are restored and the Hamiltonian corresponds to the trivial and OAI dimerized phase of the quadrupole model, respectively.

In the same manner as charge pumping relates the SSH model to a Chern insulator, dipole pumping induces a model with chiral hinge states from the quadrupole model [2,3]. The chiral hinge model is a three-dimensional second-order topological insulator whose one-dimensional protected boundary modes occur at the intersection of a pair of two-dimensional faces. The topology of the hinge model obeys a $\mathbb{Z}_2$ classification protected by the product $M_x M_y \mathcal{T}$ of the horizontal and vertical mirror symmetries and time reversal $\mathcal{T}$ [2].

B. PEPS for the quadrupole model

In this section, we provide a Gaussian fermionic PEPS for the ground state of the quadrupole model. After giving the details of the construction in Sec. IV B 1, we compute its parent Hamiltonian in Sec. IV B 2 and discuss its ES in Sec. IV B 3.

1. Construction

In order to construct a Gaussian PEPS for the ground state of the quadrupole model, we use similar ideas as in the SSH model MPS derived in Sec. II. In analogy to the particle-hole transformation of Eq. (7) on the B sublattice of the SSH chain, we define new physical modes $a_{\tau,\mathbf{x}}$ by performing a particle-hole transformation on the sublattices 3 and 4 while leaving the sublattices 1 and 2 unaffected,

$$a_{1,\mathbf{x}} = \hat{a}_{1,\mathbf{x}}, \quad a_{2,\mathbf{x}} = \hat{a}_{2,\mathbf{x}}, \tag{28a}$$

$$a_{3,\mathbf{x}} = \hat{a}_{3,\mathbf{x}}^\dagger, \quad a_{4,\mathbf{x}} = \hat{a}_{4,\mathbf{x}}^\dagger. \tag{28b}$$

The vacuum $|\Omega\rangle$ of the new modes, satisfying $a_{\tau,\mathbf{x}}|\Omega\rangle = 0$ for $\tau = 1, \ldots, 4$, contains exactly $2N_xN_y$ physical particles as required for the quadrupole model at half-filling. Thus, the particle-hole transformation allows us to express the quadrupole PEPS in terms of a separate and parity-even local tensor for each lattice site. Parity evenness is required in order to ensure that the state is independent of the order of contractions in the network [57].

The quadrupole PEPS has bond dimension $D_{\text{Quad}} = 2$ and is constructed from four local tensors $A^{[\tau]i}{}_{\text{lurd}}$ for sites on the four sublattices $\tau = 1, \ldots, 4$, respectively. Here, $i \in \{0, 1\}$ corresponds to the physical index and $l, u, r, d \in \{0, 1\}$ to the left, up, right, and down virtual indices, respectively. The physical basis states $|0\rangle = |\Omega\rangle$ and $|1\rangle = a^\dagger_{\tau,\mathbf{x}}|\Omega\rangle$ are obtained from the transformed mode operators of Eq. (28).

Due to the close relation between the SSH and the quadrupole models, we are guided in our ansatz for the local tensors of the quadrupole PEPS by the MPS tensors of Eq. (11). This can be most easily seen from Fig. 6(b). We obtain the quadrupole model by coupling neighboring sites both horizontally and vertically according to the pattern of an SSH chain. In the PEPS tensors, the couplings of the horizontal SSH chains are transmitted by the left and right virtual fermions associated to parameters α_x, β_x analogous to Eq. (11). Similarly, the vertical SSH chains are implemented using the top and bottom virtual fermions associated to the parameters α_y, β_y. Using the analogy to Eq. (11), we therefore obtain local PEPS tensors whose nonvanishing elements are given in terms of five real parameters γ, α_x, α_y, β_x, and β_y as

$$A^{[1]0}{}_{0000} = A^{[2]0}{}_{0000} = A^{[3]0}{}_{0000} = A^{[4]0}{}_{0000} = \gamma, \tag{29a}$$

$$-A^{[1]1}{}_{1000} = A^{[2]1}{}_{0010} = A^{[3]1}{}_{0010} = A^{[4]1}{}_{1000} = \beta_x, \tag{29b}$$

$$A^{[1]1}{}_{0001} = A^{[2]1}{}_{0100} = A^{[3]1}{}_{0001} = A^{[4]1}{}_{0100} = \beta_y, \tag{29c}$$

$$A^{[1]1}{}_{0010} = -A^{[2]1}{}_{1000} = A^{[3]1}{}_{1000} = A^{[4]1}{}_{0010} = \alpha_x, \tag{29d}$$

$$-A^{[1]1}{}_{0100} = -A^{[2]1}{}_{0001} = A^{[3]1}{}_{0100} = A^{[4]1}{}_{0000} = \alpha_y. \tag{29e}$$

All the other tensor elements are equal to zero. The phases in Eq. (29) were chosen such as to ensure that there is a flux π through every plaquette. As sketched in Fig. 6(b), the parameters β_x and β_y represent the coupling of the physical leg to the virtual legs corresponding to the horizontal and vertical bonds pointing into the unit cell, respectively. Similarly, α_x and α_y control the coupling of the physical leg to the virtual legs pointing out of the unit cell.

The PEPS of Eq. (29) has a global U(1) symmetry analogous to Eq. (12) for the SSH MPS. Indeed, the local tensors are invariant under a combination of U(1) rotations of the physical and virtual legs given by

$$A^{[\tau]i}{}_{\text{lurd}} = \sum_j \sum_{l'u'r'd'} U(\varphi)_{ij} U(\varphi)^\dagger_{ll'} U(\varphi)^\dagger_{uu'} \times A^{[\tau]j}{}_{l'u'r'd'} U(\varphi)^\dagger_{r'r} U(\varphi)^\dagger{}_{d'd} \tag{30a}$$

for sites on the sublattices $\tau = 1, 2$, and

$$A^{[\tau]i}{}_{\text{lurd}} = \sum_j \sum_{l'u'r'd'} U(\varphi)^\dagger_{ij} U(\varphi)_{ll'} U(\varphi)_{uu'} \times A^{[\tau]j}{}_{l'u'r'd'} U(\varphi)_{r'r} U(\varphi)_{d'd} \tag{30b}$$

for sites on the sublattices $\tau = 3, 4$. Here, $U(\varphi) = \left(\begin{smallmatrix} 1 & 0 \\ 0 & e^{i\varphi} \end{smallmatrix}\right)$ is the U(1) rotation acting on a single fermion. Equation (30) implies that the virtual legs for the local tensors on the sublattices $\tau = 1, 2$ and $\tau = 3, 4$ transform as holes and particles. Hence, each pair of virtual legs associated with the same nearest-neighbor bond transforms oppositely under the U(1) rotation, such that the PEPS is invariant under the physical part of Eq. (30). The charge associated with this symmetry is

$$\sum_{\mathbf{x}} \left[\sum_{\tau=1,2} a^\dagger_{\tau,\mathbf{x}} a_{\tau,\mathbf{x}} - \sum_{\tau=3,4} a^\dagger_{\tau,\mathbf{x}} a_{\tau,\mathbf{x}} \right] = \sum_{\mathbf{x}} \sum_{\tau=1}^{4} \hat{a}^\dagger_{\tau,\mathbf{x}} \hat{a}_{\tau,\mathbf{x}} - \frac{1}{2} N_x N_y \tag{31}$$

such that the U(1) symmetry ensures that the state lies exactly at half-filling of the lattice just as in the one-dimensional case.

2. Parent Hamiltonian

For all values of the parameters γ, α_x, α_y, β_x, and β_y, the PEPS from Eq. (29) can be expressed as a Gaussian TNS for free fermions. In Appendix H, we show that the PEPS with parameters $\alpha \equiv \alpha_x = \alpha_y$ and $\beta \equiv \beta_x = \beta_y$ is the unique ground state of an extended version of the quadrupole model H_{PEPS} with C_4-symmetric hoppings, with a staggered chemical potential that breaks C_4 symmetry and with an additional next-to-nearest-neighbor hopping

$$\sum_\tau \sum_{\mathbf{x}} t^{(2)}_\tau [\hat{a}^\dagger_{\tau,\mathbf{x}} \hat{a}_{\tau,\mathbf{x}+\hat{\mathbf{x}}} + \hat{a}^\dagger_{\tau,\mathbf{x}} \hat{a}_{\tau,\mathbf{x}+\hat{\mathbf{y}}} + \text{H.c.}] \tag{32}$$

between sites on the same sublattice τ with amplitude $t^{(2)}_\tau$. The pattern of next-to-nearest-neighbor hoppings is shown in Fig. 6(c). The couplings of H_{PEPS} depend on the parameters of the PEPS as

$$\mu = \frac{\gamma^4 - \alpha^4 - \beta^4}{\alpha^4 + \beta^4 + \gamma^4}, \tag{33a}$$

$$t^{(0)}_x = t^{(0)}_y = \frac{\sqrt{2}\beta^2\gamma^2}{\alpha^4 + \beta^4 + \gamma^4}, \tag{33b}$$

$$t^{(1)}_x = t^{(1)}_y = \frac{\sqrt{2}\alpha^2\gamma^2}{\alpha^4 + \beta^4 + \gamma^4}, \tag{33c}$$

$$t^{(2)}_1 = t^{(2)}_2 = -t^{(2)}_3 = -t^{(2)}_4 = -\frac{1}{2}\frac{\alpha^2\beta^2}{\alpha^4 + \beta^4 + \gamma^4}. \tag{33d}$$

Similarly to the parent Hamiltonian H_{MPS} of the SSH model MPS of Eq. (11), H_{PEPS} describes different phases depending on the values of the parameters α, β, and γ. When two out of the three parameters vanish, the system is in an atomic insulator state: If $\alpha = \beta = 0$, the particles are localized on the orbitals $\tau = 3, 4$, whereas they are localized on the orbitals $\tau = 1, 2$ if $\alpha = \gamma = 0$ or $\beta = \gamma = 0$. In contrast, when $\alpha = 0$ and $\beta, \gamma \neq 0$, all hoppings of the parent Hamiltonian vanish except for the nearest-neighbor hopping within unit cells. Similarly, when $\beta = 0$ and $\alpha, \gamma \neq 0$, the only nonzero hopping is the nearest-neighbor hopping between unit cells. In both cases, the system is in a dimerized phase with a staggered chemical potential. Setting $\beta = \gamma$ and $\alpha = \gamma$, respectively, we recover the trivial and OAI dimerized phases of the quadrupole model with vanishing chemical potential. Finally, when all three parameters are nonzero, the system has a nonvanishing nearest- and

next-nearest-neighbor hopping as well as a finite staggered chemical potential.

3. Corner states and entanglement spectrum

The characteristic $(d-1)$-dimensional gapless edge states of a conventional d-dimensional TI are reflected in the state's bulk ES [22]. Similarly, the ES of the quadrupole model in its dimerized OAI phase hosts gapless corner states as long as the virtual cut is compatible with the protecting symmetries [24]. In order to further characterize the different phases described by the PEPS from Eq. (29), we therefore study the ES of the state defined on a torus with respect to a rectangular subsystem $\mathcal{A}_{L_x\times L_y}$ of L_x and L_y unit cells in the horizontal and vertical direction.

For $\beta = 0$, the PEPS from Eq. (29) is in a dimerized phase where the system splits into four-site plaquettes shifted from the unit cell by one site in the horizontal and vertical directions. For $\alpha = \gamma$, we obtain the OAI dimerized phase of the quadrupole model, whereas for $\alpha \neq \gamma$ there is a nonzero staggered chemical potential that breaks the symmetries protecting the OAI phase. Due to the dimerization, with open boundaries the system has SSH chains with a staggered chemical potential at the edges, and corner sites which decouple from each other and the bulk. Correspondingly, the single-particle ES of the PEPS with respect to the subsystem $\mathcal{A}_{L_x\times L_y}$ has three distinct contributions from the bulk, the edges, and the corners as sketched in Fig. 7. The bulk consists of $(L_x-1)(L_y-1)$ plaquettes decoupled from the rest of the system, which contribute $4(L_x-1)(L_y-1)$ nonentangled modes with levels $|\lambda_{\text{bulk}}| = 1$ (in the dimerized limit) to the single-particle ES.

On the other hand, the corner and edge sites belong to plaquettes crossed by the boundary of the subsystem $\mathcal{A}_{L_x\times L_y}$. In Appendix H 3 we show that the four boundaries provide $4(L_x-1+L_y-1)$ entangled modes with levels $\pm\lambda_{\text{edge}}$, where

$$\lambda_{\text{edge}} = \frac{\sqrt{\gamma^8+\alpha^8}}{\gamma^4+\alpha^4}. \tag{34a}$$

Since the number of these entangled modes grows linearly with the size of the edge, the boundary leads to an area-law term in the entanglement entropy.

Furthermore, each corner site hosts exactly one mode corresponding to a level $\mp\lambda_{\text{corner}}$ with

$$\lambda_{\text{corner}} = \frac{\gamma^4-\alpha^4}{\gamma^4+\alpha^4}. \tag{34b}$$

Here, the negative sign holds for the top right and bottom left corner sites on the sublattices $\tau = 1$ and 2, respectively, whereas the positive signs applies to the top left and bottom right corner sites on the sublattices $\tau = 3$ and 4, respectively.

For $\alpha = \gamma$, the PEPS of Eq. (29) describes the OAI phase of the quadrupole model. Indeed, in this case the edges have entanglement levels $\lambda_{\text{edge}} = 1/\sqrt{2}$ and the four corners have degenerate levels $\lambda_{\text{corner}} = 0$ corresponding to maximally entangled corner modes. On the other hand, for $\alpha = 0$, both $\lambda_{\text{edge}} = 1$ and $\lambda_{\text{corner}} = 1$ such that the TNS describes an atomic state.

Finally, if the OAI dimerized phase is perturbed by a small nonzero value $\beta \neq 0$, one can check numerically that the corner modes acquire a finite splitting $\lambda_{\text{corner}} \neq 0$ and are no longer perfectly localized at the corner sites. This confirms that the TNS with $\beta \neq 0$ is not in the OAI phase of the quadrupole model as expected from the breaking of the mirror symmetries and C_4 symmetry by the next-nearest-neighbor hopping and the chemical potential.

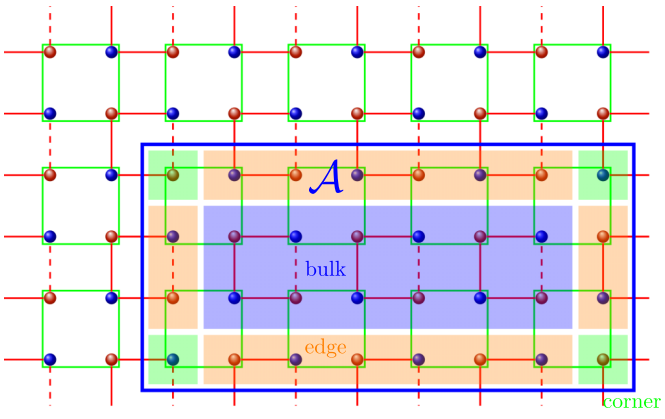

FIG. 7. Quadrupole model in the dimerized OAI phase with a rectangular subsystem $\mathcal{A}$ marked by a blue rectangle. The four-site plaquettes coupled by the nearest-neighbor hopping $t^{(1)}$ (drawn in red) are shifted from the unit cells (denoted by green squares) by one site in both directions. The decoupled plaquettes in the bulk of $\mathcal{A}$ (marked in blue) do not contribute to the ES. In contrast, nontrivial levels in the ES come from both the plaquettes at the corners with a single site in $\mathcal{A}$ (marked in green), and from those at the edges with two sites in $\mathcal{A}$ (marked in orange).

C. 3D chiral hinge PEPS from dipole pumping

The PEPS of Eq. (29) with parameters $\alpha = \alpha_x = \alpha_y$ and $\beta = \beta_x = \beta_y$ describes a dimerized dipole-pumping cycle of the quadrupole model if α, β, and γ follow the parametrization ϕ_{pump} which we found for the dimerized charge-pumping cycle of the SSH model MPS. The coupling constants of the parent Hamiltonian H_{PEPS} derived from the parametrization ϕ_{pump} are shown in Fig. 8(a). They differ from those of the dipole-pumping Hamiltonian of Ref. [3] only by a factor of $1/\sqrt{2}$ for the hopping amplitudes, which does not affect the topology of the interpolation. The single-particle ES of the PEPS along ϕ_{pump} is shown in Fig. 8(b). In the first half of the cycle, the system is in a dimerized phase with each unit cell decoupled from the rest of the system. Hence, the single-particle ES contains only the bulk bands with $\lambda = \pm 1$. However, in the second half of the cycle for $0 < t < \pi$, the contributions from the edges and corners can be clearly distinguished. The four corner modes connect the bands with $\lambda = \pm 1$ and are degenerate in the OAI dimerized phase of the quadrupole model obtained for $t = \pi/2$. In the three-dimensional second-order TI of Ref. [2] obtained by the identification of the time t along the dipole-pumping cycle with the momentum k_z in the third direction, these corner modes generate the chiral modes localized at the hinges.

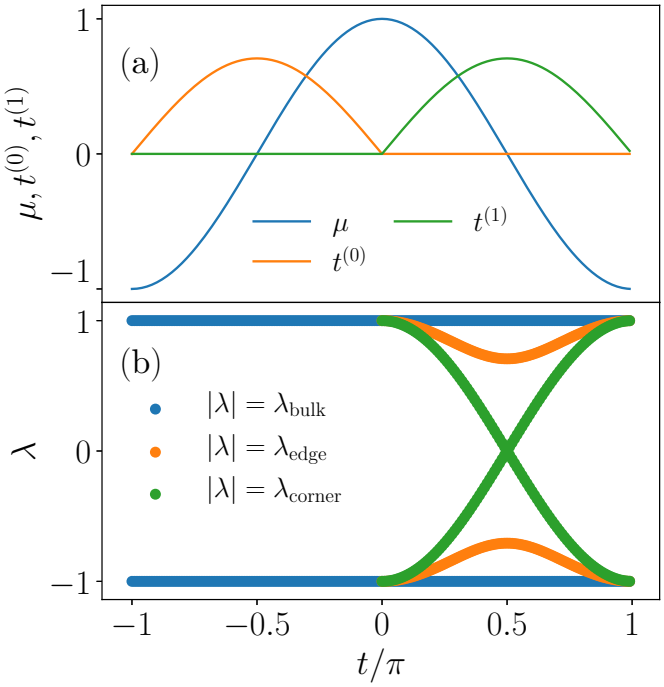

FIG. 8. (a) Coupling constants of the parent Hamiltonian H_{PEPS} and (b) single-particle ES of the PEPS of Eq. (29) along the dipole-pumping interpolation generated by the parametrization ϕ_{pump}. In (a), the vanishing of the next-nearest-neighbor coupling $t_\tau^{(2)} = 0$ of H_{PEPS} is not shown. In (b), we marked the bulk contribution in blue and for times $t \in [0, \pi]$ with $\beta(t) = 0$, the edge contribution in orange and the corner contribution in green. The ES was computed on a torus with $N_x = N_y = 10$ unit cells with respect to the subsystem $\mathcal{A}_{L_x \times L_y}$ with $L_x = L_y = 5$.

Following the steps described in Sec. III, we may use the PEPS of Eq. (29) along the interpolation ϕ_{pump} to define a three-dimensional PEPS for the second-order hinge TI. Moreover, we can construct a topologically trivial three-dimensional state from the interpolation ϕ_{triv} from Eq. (17). These PEPSs have a finite bond dimension $D_{\text{Quad}} = 2$ in the x and y directions. In the hybrid real-momentum space where the third dimension corresponds to the momentum k_z or time t, the states have a finite bond dimension equal to one also in the third direction.

On the other hand, due to the nonlocality of the inverse FT, in real space their bond dimension $D_{z,\tau}$ in the third direction for sites on the sublattice τ for $\tau = 1, \ldots, 4$ grows with the system size N_z. As in Sec. III E, we can estimate $D_{z,\tau}$ from the ES of a column of sites on the sublattice τ with respect to the subsystem $\mathcal{A}_L$ of the first L sites.

The number of entangled levels in the single-particle ES of a column of sites on the sublattice $\tau = 1$ of the three-dimensional PEPSs is shown in Fig. 9(a). As we can see from the smallest system size $N_z = 28$, for both ϕ_{pump} and ϕ_{triv} the number of entangled modes is *identical* to the two-dimensional case from Sec. III when replacing N_y with N_z. Moreover, the spectra displayed in Fig. 9(b) are similar, although not identical, to the corresponding results for the two-dimensional PEPSs.

As we show in Appendix G, for ϕ_{pump} this number of entangled modes is the maximal number compatible with the symmetries of the quadrupole PEPS, here the U(1) symmetry from Eq. (30), and the mirror symmetry M_{xy} of the local tensor on the sublattice $\tau = 1$. Indeed, the latter causes the decoupling of one superposition of the left and down virtual legs, and similarly for the up and right virtual legs. For ϕ_{triv},

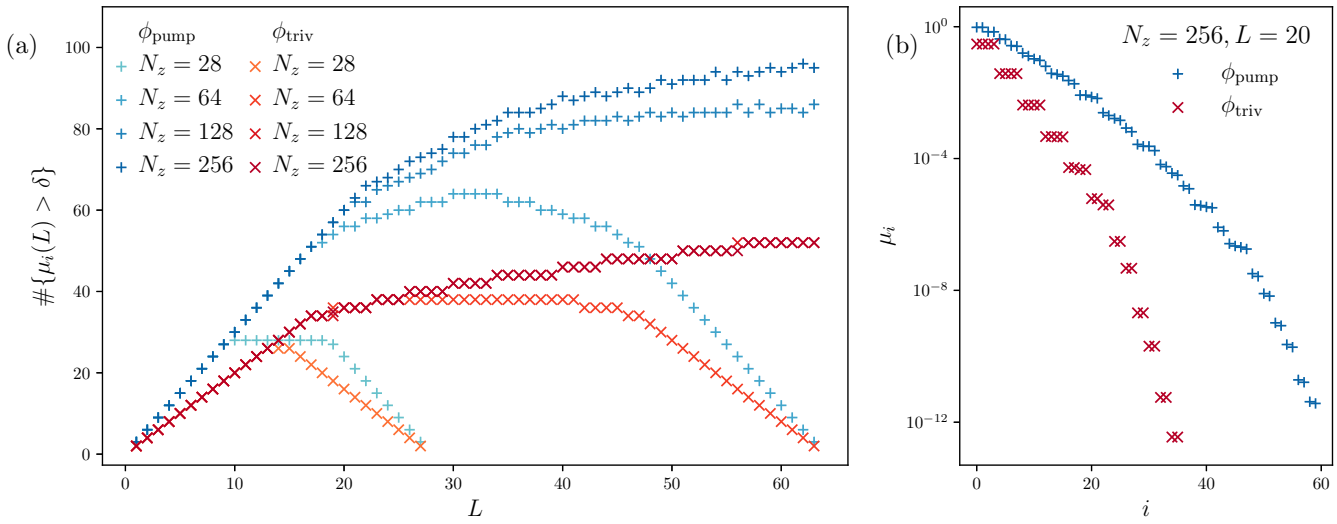

FIG. 9. Single-particle ES of a column of sites on the sublattice $\tau = 1$ of the three-dimensional real-space TNSs defined by two different parametrizations for the quadrupole PEPS of Eq. (29): the charge-pumping interpolation ϕ_{pump} of Eq. (15) leading to a chiral hinge insulator (blue) and the parametrization ϕ_{triv} of Eq. (17) leading to a topologically trivial three-dimensional state (red). (a) Number of modes in the single-particle ES with a finite entanglement corresponding to a value $\mu_i > \delta$ with $\delta = 10^{-13}$ the numerical accuracy for different system sizes N_z as a function of the subsystem size L. Due to the mirror symmetry M_{xy} of the quadrupole PEPS tensor on the sublattice $\tau = 1$, the number of entangled modes for both parametrizations is identical to the two-dimensional case shown in Fig. 5(a). (b) Single-particle ES for a column with $N_z = 256$ sites with respect to the subsystem $\mathcal{A}_L$ with $L = 20$. The double degeneracy in the ES corresponding to ϕ_{triv} is due to the decoupling of the left and down virtual legs since $\beta(t) = 0$ along ϕ_{triv} (see Appendix G). The spectra are similar, with the same number of entangled modes, but not strictly identical to those of the two-dimensional state shown in Fig. 5(b).

there is an additional reduction of the number of entangled modes since the left and down virtual legs decouple due to the vanishing parameter $\beta = 0$ along the trivial interpolation (see Appendix G).

Analogously to Sec. III E, we therefore conclude that the bond dimension $D_{z,\tau}$ in the third direction grows exponentially with N_z for $\tau = 1, 2, 3, 4$. Due to the mirror symmetries of the quadrupole model, $D_{z,\tau}$ has the same value as the vertical bond dimension of the two-dimensional PEPSs obtained from cyclic interpolations of the SSH model. The increase in spatial dimensionality therefore does not cause an increase of the bond dimension in the $(d+1)$st direction.

V. CONCLUSION

In this paper, we showed how to use charge pumping to define TNSs for $(d+1)$-dimensional conventional or higher-order TIs starting from TNSs of TIs in d-space dimensions. To that end, we constructed a Gaussian fermionic MPS for the SSH model with bond dimension $D_{\mathrm{SSH}} = 2$ in $d = 1$ dimension, and a Gaussian fermionic PEPS for the topological quadrupole model with bond dimension $D_{\mathrm{Quad}} = 2$ in $d = 2$ dimensions. We proved that these TNSs have local gapped parent Hamiltonians with up to next-nearest-neighbor hopping, and thereby showed that they describe the SSH model along a charge-pumping cycle and the quadrupole model along a dipole-pumping cycle, respectively. We employed these TNSs to construct a two-dimensional PEPS for a Chern insulator and a three-dimensional PEPS for a chiral hinge higher-order topological insulator (HOTI), respectively. The $(d+1)$-dimensional TNSs inherit the finite bond dimension D_{SSH} and D_{Quad} in the first d dimensions, respectively. In a hybrid coordinate system where the $(d+1)$st dimension corresponds to momentum, the $(d+1)$-dimensional TNSs have a finite bond dimension in this direction. In contrast, we showed that the bond dimension in the $(d+1)$st direction grows exponentially in a real-space coordinate system.

Our results suggest several directions for future work. On one hand, it would be interesting to study if a real-space PEPS for the Chern insulator with a polynomially growing bond dimension can be found by truncating the Schmidt values of the real-space column in our construction. Such a result could potentially provide insight into the physical origin for the obstructions preventing the existence of chiral PEPSs with a finite bond dimension. On the other hand, we expect the TNSs constructed here to be useful for finite-size simulations despite their growing bond dimension since the bond dimension is finite in all but one direction. By their local nature, they could be employed as the building block of interacting $(d+1)$-dimensional TIs obtained by Gutzwiller projection or parton constructions [58–61].

ACKNOWLEDGMENTS

We thank I. Cirac, C. Hubig, A. Molnar, S. Pinon, A. Sterdyniak, and E. Zohar for discussions. A.H. and N.S. acknowledge support by the European Research Council (ERC) under the European Union's Horizon 2020 research and innovation programme through the ERC Starting Grant WASCOSYS (Grant No. 636201), and by the Deutsche Forschungsgemeinschaft (DFG) under Germany's Excellence Strategy (Grant No. EXC-2111–390814868). A.H. and N.R. were supported by Grants No. ANR-17-CE30-0013-01 and No. ANR-16-CE30-0025. B.A.B. was supported by the Department of Energy Grant No. DE-SC0016239, the National Science Foundation EAGER Grant No. DMR 1643312, Simons Investigator Grant No. 404513, ONR Grant No.N00014-14-1-0330, the Packard Foundation, the Schmidt Fund for Innovative Research, ARO MURI Grant No. W911NF-12-1-0461 and by the NSF through the Princeton Center for Complex Materials, a Materials Research Science and Engineering Center DMR-1420541.

APPENDIX A: COVARIANCE MATRICES OF GAUSSIAN FERMIONIC STATES

Eigenstates and thermal states of free-fermion systems are given by Gaussian states which satisfy Wick's theorem. They are hence fully characterized by their covariance matrix (CM) of two-point correlation functions [51]. In this Appendix, we review the definitions of the complex and real CM for pure and mixed states in Appendix A 1. We summarize the relation with the entanglement spectrum in Appendix A 2 and provide the concrete expression for the CM of a Gaussian state parametrized as the exponential of a fermion bilinear in Appendix A 4.

1. Definitions

We consider a generic system of N fermionic DOFs with annihilation operators a_j and creation operators $a_j^\dagger$ for $j = 1, \ldots, N$. In a pure or mixed state of this system, its covariance matrix is defined as

$$G_{\mu\nu} = \frac{i}{2}\langle[\chi_\mu^\dagger, \chi_\nu]\rangle = \begin{pmatrix} R^* & Q^* \\ Q & R \end{pmatrix}, \tag{A1}$$

where $\mu, \nu = 1, \ldots, 2N$ and $\chi = (a_1, \ldots, a_N, a_1^\dagger, \ldots, a_N^\dagger)$ is the mode vector. The blocks R and Q of dimension $N \times N$ in Eq. (A1) are anti-Hermitian and antisymmetric, respectively, i.e., $R^\dagger = -R$ and $Q^T = -Q$, such that G is anti-Hermitian. For a generic mixed state, G satisfies the inequality $GG^\dagger \leqslant \frac{1}{4}\mathbb{1}$ and its eigenvalues come in complex-conjugate pairs $\pm\frac{i}{2}|\lambda_j|$ with $0 \leqslant |\lambda_j| \leqslant 1$ for $1 \leqslant j \leqslant N$. For pure states, $GG^\dagger = \frac{1}{4}\mathbb{1}$ such that its eigenvalues are given by $|\lambda_j| = 1$.

For a state with charge conservation, the levels $-1 \leqslant \lambda_j \leqslant 1$ can be computed directly including their sign [62]: Since $\langle a_j^\dagger a_k^\dagger\rangle = 0$ for all $1 \leqslant j, k \leqslant N$, the off-diagonal block Q^* vanishes in the complex CM G of Eq. (A1), and the eigenvalues of the diagonal block R^* are given by $\frac{i}{2}\lambda_j$.

For a generic system with pair creation and annihilation, it is convenient to define Majorana fermionic modes $c_{2j} = a_j^\dagger + a_j$, $c_{2j-1} = (-i)(a_j^\dagger - a_j)$ for $j = 1, \ldots, N$ with $\{c_\mu, c_\nu\} = 2\delta_{\mu\nu}$ [63]. We denote the matrix corresponding to this basis change by

$$S_{\mu\nu} = \begin{cases} \delta_{\nu,\mu/2} + \delta_{\nu,\mu/2+N}, & \mu \text{ even} \\ i(\delta_{\nu,(\mu+1)/2} - \delta_{\nu,(\mu+1)/2+N}), & \mu \text{ odd} \end{cases} \tag{A2}$$

with $c_\mu = \sum_\nu S_{\mu\nu}\chi_\nu$ and $S^\dagger = 2S^{-1}$. In terms of the Majorana modes, the CM

$$\Gamma_{\mu\nu} = \frac{i}{2}\langle [c_\mu, c_\nu]\rangle = [S^* G S^T]_{\mu\nu} \tag{A3}$$

of size $2N \times 2N$ is real and antisymmetric. Hence, each of its singular values $|\lambda_j|$ with $1 \leqslant j \leqslant N$ is doubly degenerate. Moreover, Γ satisfies $\Gamma\Gamma^\dagger \leqslant \mathbb{1}$ with equality for a pure state.

2. Relation to entanglement spectrum

We frequently consider the restriction of a pure quantum state $|\psi\rangle$ to a subsystem $\mathcal{A}$ of the entire system, which is described by the reduced density matrix $\rho_\mathcal{A} = \mathrm{tr}_{\bar{\mathcal{A}}}[|\psi\rangle\langle\psi|]$ obtained by tracing over the DOFs in the complement $\bar{\mathcal{A}}$ of $\mathcal{A}$. The many-body entanglement Hamiltonian H_Ent with respect to this partition is given by the logarithm of the reduced density matrix as [23]

$$\rho_\mathcal{A} = \frac{1}{Z} e^{-H_\mathrm{Ent}}, \tag{A4}$$

where $Z = \mathrm{tr}(e^{-H_\mathrm{Ent}})$.

If $|\psi\rangle$ is a Gaussian state with CM G, then $\rho_\mathcal{A}$ is Gaussian with its CM $G_\mathcal{A} = (G_{\mu\nu})_{\mu,\nu\in\mathcal{A}}$ given by the restriction of G to the modes of $\mathcal{A}$. In this case, the many-body entanglement Hamiltonian is a bilinear function of the fermionic mode operators defined by a square matrix referred to as the single-particle entanglement Hamiltonian. The eigenvalues β_j of the single-particle entanglement Hamiltonian are related to the eigenvalues $\pm\frac{i}{2}|\lambda_j|$ of $G_\mathcal{A}$ as $|\lambda_j| = \tanh\frac{\beta_j}{2}$, where $1 \leqslant j \leqslant L$ and L is the number of modes in the subsystem $\mathcal{A}$ [52]. We therefore refer to the collection

$$\{|\lambda_j|\}_{1\leqslant j\leqslant L} \tag{A5}$$

as the single-particle ES of $\rho_\mathcal{A}$.

The single-particle ES can also be computed from the Majorana CM Γ of Eq. (A3) for the Gaussian state $|\psi\rangle$. One obtains the levels $|\lambda_j|$ for $1 \leqslant j \leqslant L$ directly as the singular values of the block $(\Gamma_{\mu\nu})_{\mu,\nu\in\mathcal{A}}$ associated with the DOFs in $\mathcal{A}$. On the other hand, the levels can be computed indirectly from the off-diagonal block $(\Gamma_{\mu\nu})_{\mu\in\mathcal{A},\nu\in\bar{\mathcal{A}}}$ describing the correlations between $\mathcal{A}$ and its complement $\bar{\mathcal{A}}$. Indeed, the two blocks are coupled by the constraint $\Gamma\Gamma^T = \mathbb{1}$ originating in the purity of the state $|\psi\rangle$. Concretely, the singular values of the off-diagonal block are given by

$$\mu_j = \sqrt{1-\lambda_j^2} \tag{A6}$$

for $1 \leqslant j \leqslant L$ [64]. This allows to infer the single-particle entanglement energies for weakly entangled modes $|\lambda_j| \approx 1$ with an improved numerical accuracy.

3. Gaussian projections and Schur complements

In the construction of GfTNSs to be discussed in Appendix B, we will frequently encounter the following situation: Let us take a total system of $N+M$ fermionic modes with mode operators $a_j, a_j^\dagger$ for $j = 1, \ldots, N+M$, and consider the subsystem defined by the M last modes $j = N+1, \ldots, N+M$. Let $|Q\rangle$ be a Gaussian pure state of the total system and $|\omega\rangle$ a Gaussian pure state of the subsystem of the last M modes. Then, the projection

$$|\psi\rangle = \langle\omega|Q\rangle, \tag{A7}$$

which is a state of only the first N modes, is again a Gaussian state. The Majorana CMs Γ_ψ, Γ_Q, and Γ_ω of the three Gaussian states are given by the expression in Eq. (A3), where the expectation values are taken in the states $|\psi\rangle$, $|Q\rangle$, and $|\omega\rangle$, respectively.

Γ_ψ can be computed from Γ_Q and Γ_ω using a Schur complement coming from the Gaussian integration over the last M modes [51,65–67]. Indeed, we can write the antisymmetric Majorana CM Γ_Q of the unprojected state of the total system as

$$\Gamma_Q = \begin{pmatrix} \mathbf{A} & \mathbf{B} \\ -\mathbf{B}^T & \mathbf{D} \end{pmatrix}, \tag{A8}$$

where the block $\mathbf{A}$ of size $2N \times 2N$ refers to the Majorana modes corresponding to $a_j, a_j^\dagger$ for $j = 1, \ldots, N$, and the block $\mathbf{D}$ of size $2M \times 2M$ refers to the Majorana modes corresponding to $a_j, a_j^\dagger$ for $j = N+1, \ldots, N+M$. The block $\mathbf{B}$ of size $2N \times 2M$ encodes the correlations between the first N and last M modes. In terms of these blocks and the CM Γ_ω of size $2M \times 2M$, the CM of the projected state is

$$\Gamma_\psi = \mathbf{A} + \mathbf{B}\,[\mathbf{D} + \Gamma_\omega]^{-1}\,\mathbf{B}^T. \tag{A9}$$

Mathematically, this is the Schur complement of the block corresponding to the last M modes.

4. Parametrization of Gaussian states

We consider a normalized Gaussian state with even fermionic parity which, anticipating Appendix B, we will denote by $|\psi\rangle = |Q\rangle$. $|Q\rangle$ is parametrized in terms of the antisymmetric complex matrix M of dimension $N \times N$ as [51,68]

$$|Q\rangle = \mathcal{N} \times e^{\sum_{ij} M_{ij} a_i^\dagger a_j^\dagger}|\Omega\rangle, \tag{A10}$$

where $|\Omega\rangle$ is the fermionic vacuum and $\mathcal{N}$ is a normalization factor.

A relevant case is given by states whose parametrization matrices have nonzero entries only in the first row and column (or more generally, in the nth row and column). In particular, we will see in Appendices E and H that the local tensors of the MPS of Eq. (11) and the PEPS of Eq. (29) define Gaussian states of this form. In this case, $M_{ij}M_{kl}\,a_i^\dagger a_j^\dagger a_k^\dagger a_l^\dagger = 0$ for all $1 \leqslant i, j, k, l \leqslant N$ since all nonvanishing terms contain the factor $(a_1^\dagger)^2 = 0$ [$(a_n^\dagger)^2 = 0$ in the general case]. Therefore, the series expression of the exponential in Eq. (A10) terminates after first order such that

$$|Q\rangle = \mathcal{N}\left[1 + \sum_{i,j=1}^{N} M_{ij} a_i^\dagger a_j^\dagger\right]|\Omega\rangle, \tag{A11}$$

leading to the CM

$$G = \frac{i}{2}\begin{pmatrix} -\mathbb{1}_N + 8\mathcal{N}^2 \times M^\dagger M & -4\mathcal{N}^2 \times M^\dagger \\ -4\mathcal{N}^2 \times M & \mathbb{1}_N - 8\mathcal{N}^2 \times MM^\dagger \end{pmatrix}, \tag{A12}$$

where the normalization is $\mathcal{N}^{-2} = 1 + 2\,\mathrm{tr}(MM^\dagger)$.

APPENDIX B: CONSTRUCTION OF GfTNS

Gaussian fermionic tensor network states (GfTNS) describe free-fermion systems. They have the advantage that the contraction of the network can be performed in terms of covariance matrices, allowing efficient computations even for large systems. In this Appendix, we review the construction of Gaussian TNSs in one and two spatial dimensions. We begin in Appendix B 1 by illustrating the construction of a TNS via fiducial states using the simple example of a bosonic MPS, where we do not need to take care of fermionic signs in tensor products. In Appendix B 2, we move to the case of fermionic physical and virtual particles. In Appendix E, the concepts introduced here are illustrated using the pedagogical example of the SSH model MPS from Sec. II C.

1. Fiducial state approach

We recall that the construction of a TNS can be performed in several different but equivalent ways. Within the most well-known approach, the local information on the state is encoded in the local tensor with physical and virtual legs. For example, for a one-dimensional bosonic MPS $|\psi_{\mathrm{bMPS}}\rangle$ the local tensor at position x takes the form $A[x]^{i_x}_{l_x r_x}$, where i_x is the physical index, l_x is the left virtual index, and r_x is the right virtual index. The global state is obtained by contracting, for each nearest-neighbor bond, the two virtual legs associated with this bond which belong to neighboring tensors. This is done by identifying and summing over the corresponding virtual indices. For example, the contraction of two neighboring MPS tensors gives $\sum_{r_x,l_{x+1}} A[x]^{i_x}_{l_x r_x}\delta_{r_x l_{x+1}} A[x+1]^{i_{x+1}}_{l_{x+1} r_{x+1}}$.

More formally, this can be expressed as follows: First, we create a total maximally entangled state in the virtual layer whose role it is to implement the contraction of bonds. The total maximally entangled state is the tensor product over all nearest-neighbor bonds of a maximally entangled state of the two virtual particles for this bond. In our MPS example, the maximally entangled state for the bond between sites x and $x+1$ is

$$|\omega_{x,x+1}\rangle = \sum_{r_x,l_{x+1}} \delta_{r_x l_{x+1}} |r_x, l_{x+1}\rangle. \tag{B1}$$

Second, at each site we translate the local tensor into a local projection map, which maps the virtual particles onto the physical particle at this site. The representation matrix of the local projection map is given by the local tensor. For instance, the MPS local projection map at site x is

$$\hat{A}[x] = \sum_{i_x,l_x,r_x} A[x]^{i_x}_{l_x r_x} |i_x\rangle\langle l_x, r_x|. \tag{B2}$$

The bond between sites x and $x+1$ is contracted by applying the projection maps $\hat{A}[x]$ and $\hat{A}[x+1]$ to $|\omega_{x,x+1}\rangle$, giving

$$\begin{aligned}&\hat{A}[x]\hat{A}[x+1]|\omega_{x,x+1}\rangle\\ &= \sum_{\substack{i_x,\, i_{x+1}\\ l_x,\, r_{x+1}}} |i_x, i_{x+1}\rangle\langle l_x, r_{x+1}|\\ &\quad\times \sum_{r_x,l_{x+1}} A[x]^{i_x}_{l_x r_x}\delta_{r_x l_{x+1}} A[x+1]^{i_{x+1}}_{l_{x+1} r_{x+1}}.\end{aligned} \tag{B3}$$

The global state is then obtained by contracting all bonds, i.e., by applying the product of all local projection maps to the total virtual maximally entangled state. For instance, the MPS on a chain with N_x sites and periodic boundaries takes the form

$$|\psi_{\mathrm{bMPS}}\rangle = \prod_{x=0}^{N_x-1} \hat{A}[x] \bigotimes_{x=0}^{N_x-1} |\omega_{x,x+1}\rangle, \tag{B4}$$

where the lattice site indices are $x = 0, \ldots, N_x - 1$. This is a state of only the physical particles.

For GfTNSs, we will deal with fermionic particles and therefore follow a slightly different, but equivalent, approach to construct the TNSs using so-called fiducial states (see Refs. [47,68] for pedagogical introductions). In this approach, we consider fiducial states instead of local projection maps, which contain only creation operators. The fiducial state on each lattice site lies in the joint Hilbert space of the physical and virtual particles on this site. Its basis coefficients are given by the entries of the local tensor. For example, the local fiducial states of the MPS are

$$|Q_x\rangle = \sum_{i_x,l_x,r_x} A[x]^{i_x}_{l_x r_x} |i_x\rangle|l_x, r_x\rangle. \tag{B5}$$

Hence, the fiducial states are equivalent to the local projection maps or local tensors; in particular, they contain all the local information about the TNSs. The total state is obtained by projecting the tensor product of all local fiducial states on the total virtual maximally entangled state. For the MPS, we have

$$|\psi_{\mathrm{bMPS}}\rangle = \bigotimes_{x=0}^{N_x-1} \langle\omega_{x,x+1}| \bigotimes_{x=0}^{N_x-1} |Q_x\rangle \tag{B6}$$

which is equivalent to the expression in Eq. (B4). We are now ready to generalize the fiducial state formalism to fermionic physical and virtual particles.

2. Fermionic particles

We consider a one- or two-dimensional lattice system of free fermions with f fermionic modes per lattice site $\mathbf{x}$, which are associated to the physical creation operators $a^\dagger_{\tau,\mathbf{x}}$ with $\tau = 1, \ldots, f$. A Gaussian fermionic TNS for this system with physical dimension 2^f and bond dimension 2^ξ is obtained by associating ξ complex virtual fermionic modes with each physical lattice site $\mathbf{x}$ and nearest-neighbor direction α, where $\alpha = L, R$ for one-dimensional MPSs with left and right nearest-neighbor bonds and $\alpha = L, U, R, D$ for two-dimensional PEPSs on the square lattice with left, up, right, and down nearest-neighbor bonds [33,68]. We denote the creation operators for these virtual modes by $b^\dagger_{\alpha,j,\mathbf{x}}$ where $j = 1, \ldots, \xi$ labels the different modes per bond and lattice site. For each lattice site, there are hence $n_{\mathrm{modes}} = f + 2\xi$ modes for a fermionic MPS and $n_{\mathrm{modes}} = f + 4\xi$ modes for a two-dimensional fermionic PEPS. The mode operators needed for the construction of the SSH MPS are discussed in the first paragraph of Appendix E.

We collect the mode operators associated with one lattice site into a mode vector

$$\begin{aligned}\chi_{\mathbf{x}} = (&a_{1,\mathbf{x}}, a_{2,\mathbf{x}}, \ldots, a_{f,\mathbf{x}}, b_{L,1,\mathbf{x}}, b_{L,2,\mathbf{x}}, \ldots, b_{R,1,\mathbf{x}}, \ldots,\\ &a^\dagger_{1,\mathbf{x}}, \ldots, b^\dagger_{L,1,\mathbf{x}}, \ldots, b^\dagger_{R,1,\mathbf{x}}, \ldots)^T\end{aligned} \tag{B7}$$

of length $2n_{\text{modes}}$. The physical and virtual mode operators obey canonical anticommutation relations

$$\{(\chi_{\mathbf{x}})_\mu, (\chi_{\mathbf{x}'})_\nu\} = \delta_{\mathbf{x},\mathbf{x}'}\delta_{|\mu-\nu|,n_{\text{modes}}} \tag{B8}$$

for $1 \leqslant \mu, \nu \leqslant 2n_{\text{modes}}$. Their joint vacuum state $|\Omega\rangle$ satisfies

$$a_{\tau,\mathbf{x}}|\Omega\rangle = b_{\alpha,j,\mathbf{x}}|\Omega\rangle = 0 \tag{B9}$$

for all $\mathbf{x}$, $\tau = 1, \ldots, f$, α, and $j = 1, \ldots, \xi$.

The local information about the TNS is contained in the local fiducial states $|Q_{\mathbf{x}}\rangle$, introduced in Eq. (B5), which are equivalent to the local tensors $A[\mathbf{x}]$ used in the main text. We can easily translate between the two approaches since the basis elements of the local fiducial state are by definition equal to the local tensors [cf. Eq. (B5)]. For fermions, we write $|Q_{\mathbf{x}}\rangle = Q_{\mathbf{x}}|\Omega\rangle$ where $Q_{\mathbf{x}}$ is a polynomial of creation operators which acts on the vacuum to create the fiducial state. For fermionic MPSs and PEPSs in one and two dimensions we have [49,57]

$$A[\mathbf{x}]^i_{lr} = [\langle r| \otimes \langle i| \otimes \langle l|]Q_{\mathbf{x}}|\Omega\rangle, \tag{B10}$$

$$A[\mathbf{x}]^i_{\text{lurd}} = [\langle d| \otimes \langle r| \otimes \langle u| \otimes \langle l| \otimes \langle i|]Q_{\mathbf{x}}|\Omega\rangle, \tag{B11}$$

where $|i\rangle$ with $i = 0, \ldots, 2^f - 1$ is a basis for the Fock space associated with the physical mode operators $\{a^\dagger_{\tau,\mathbf{x}}\}_{1\leqslant\tau\leqslant f}$, and $|l\rangle$ with $l = 0, \ldots, 2^\xi - 1$ is a basis of the Fock space associated with the left virtual mode operators $\{b^\dagger_{L,j,\mathbf{x}}\}_{1\leqslant j\leqslant\xi}$ on site $\mathbf{x}$ (similarly $|u\rangle$ for the up mode operators $\{b^\dagger_{U,j,\mathbf{x}}\}_{1\leqslant j\leqslant\xi}$, $|r\rangle$ for the right mode operators $\{b^\dagger_{R,j,\mathbf{x}}\}_{1\leqslant j\leqslant\xi}$, and $|d\rangle$ for the down mode operators $\{b^\dagger_{D,j,\mathbf{x}}\}_{1\leqslant j\leqslant\xi}$). For the SSH model MPS, the fiducial states obtained thus are given in Eq. (E1).

A Gaussian fermionic TNS has the property that all local fiducial states $|Q_{\mathbf{x}}\rangle$ satisfy Wick's theorem. In this case, the global physical state $|\psi\rangle$ is also Gaussian [33,51]. We denote by Γ_Q the Majorana CM of the product of all fiducial states, $\prod_{\mathbf{x}} Q_{\mathbf{x}}|\Omega\rangle$, also referred to as total fiducial state. From now onward, we consider GfTNSs with parity-even local tensors as discussed in Sec. II B, whose local fiducial states therefore have an even number of physical and virtual fermions. The maps $Q_{\mathbf{x}}$ can thus be expressed as in Eq. (A10) as the exponential of a quadratic form of the physical and virtual creation operators on the site $\mathbf{x}$, which are contained in the last n_{modes} entries $[(\chi_{\mathbf{x}})_{n_{\text{modes}}+m}]_{1\leqslant m\leqslant n_{\text{modes}}}$ of the mode vector of Eq. (B7) [51,68]. Concretely, the local fiducial state is parametrized as

$$Q_{\mathbf{x}} = \exp\left[\sum_{m,m'=1}^{n_{\text{modes}}} (M_{\mathbf{x}})_{mm'}(\chi_{\mathbf{x}})_{n_{\text{modes}}+m}(\chi_{\mathbf{x}})_{n_{\text{modes}}+m'}\right], \tag{B12}$$

with an antisymmetric square matrix $M_{\mathbf{x}}$ of dimension n_{modes}. For the SSH model MPS, this matrix is given in Eq. (E2).

In order to illustrate the concepts introduced above, let us construct a Gaussian maximally entangled state of the virtual fermions for each nearest-neighbor bond $\langle \mathbf{x}'\mathbf{x}''\rangle$. Let us denote by α' and α'' the type of virtual fermion involved in the bond $\langle \mathbf{x}'\mathbf{x}''\rangle$ on the site $\mathbf{x}'$ and $\mathbf{x}''$, respectively. For instance, if $\mathbf{x}'' = \mathbf{x}' + \hat{\mathbf{x}}$, then $\alpha' = R$ and $\alpha'' = L$. A fermionic maximally entangled state for this bond is then given by [33]

$$|\omega_{\mathbf{x}'\mathbf{x}''}\rangle = \prod_{j=1}^{\xi} \frac{1}{\sqrt{2}}(1 + b^\dagger_{\alpha',j,\mathbf{x}'}b^\dagger_{\alpha'',j,\mathbf{x}''})|\Omega\rangle. \tag{B13}$$

Due to the fermionic anticommutation relations, this expression is not symmetric under exchange of $(\alpha', \mathbf{x}')$ and $(\alpha'', \mathbf{x}'')$; we say that the bond points from the initial site $\mathbf{x}'$ to the final site $\mathbf{x}''$.

The state $|\omega_{\mathbf{x}'\mathbf{x}''}\rangle$ is a Gaussian state satisfying Wick's theorem. To see this, we first consider the simple case of a one-dimensional MPS with $\xi = 1$ virtual fermion per nearest-neighbor bond and lattice site. In this case, the virtual maximally entangled state from Eq. (B13) for the bond $\langle \mathbf{x}, \mathbf{x} + \hat{\mathbf{x}}\rangle$ becomes

$$\begin{aligned}|\omega_{\mathbf{x},\mathbf{x}+\hat{\mathbf{x}}}\rangle &= \frac{1}{\sqrt{2}}[1 + b^\dagger_{R,\mathbf{x}}b^\dagger_{L,\mathbf{x}+\hat{\mathbf{x}}}]|\Omega\rangle \\ &= \frac{1}{\sqrt{2}}\left[1 + (b^\dagger_{R,\mathbf{x}}\, b^\dagger_{L,\mathbf{x}+\hat{\mathbf{x}}})\frac{1}{2}\begin{pmatrix}0 & 1\\ -1 & 0\end{pmatrix}\begin{pmatrix}b^\dagger_{R,\mathbf{x}}\\ b^\dagger_{L,\mathbf{x}+\hat{\mathbf{x}}}\end{pmatrix}\right]|\Omega\rangle,\end{aligned} \tag{B14}$$

where the bond points from site $\mathbf{x}$ to site $\mathbf{x} + \hat{\mathbf{x}}$. This is a Gaussian state of the form of Eq. (A11) parametrized by the antisymmetric matrix $M = (i/2)\sigma_2$. Hence, its complex CM G can be computed from Eq. (A12) and is given by

$$G = -\frac{1}{2}\begin{pmatrix}0 & \sigma_2\\ -\sigma_2 & 0\end{pmatrix}, \tag{B15}$$

where $\sigma_2 = \left(\begin{smallmatrix}0 & -i\\ i & 0\end{smallmatrix}\right)$ denotes the second Pauli matrix. According to Eq. (A3), the corresponding Majorana CM Γ is obtained by conjugation with the matrix S, and is found to be

$$\Gamma = \begin{pmatrix}0 & \sigma_1\\ -\sigma_1 & 0\end{pmatrix}, \tag{B16}$$

where $\sigma_1 = \left(\begin{smallmatrix}0 & 1\\ 1 & 0\end{smallmatrix}\right)$ denotes the first Pauli matrix. For a two-dimensional TNS with $\xi = 1$, the real CM of the virtual state for the vertical nearest-neighbor bond $\langle \mathbf{x}, \mathbf{x} - \hat{\mathbf{y}}\rangle$ is also given by Eq. (B16). In this case, we choose the bond to be oriented downward from $\mathbf{x}$ to $\mathbf{x} - \hat{\mathbf{y}}$ to comply with our ordering of the virtual legs as L, U, R, D. For TNS with more virtual fermions, $\xi > 1$, the virtual maximally entangled state from Eq. (B13) is a tensor product of multiple states of the form of Eq. (B14). Hence, the corresponding real CM is a direct sum of multiple copies of the Γ from Eq. (B16). We denote by Γ_ω the Majorana CM of the total virtual maximally entangled state $\otimes_{\langle \mathbf{x}'\mathbf{x}''\rangle}|\omega_{\mathbf{x}'\mathbf{x}''}\rangle$. Since the total virtual maximally entangled state is a tensor product over all bonds, Γ_ω is a direct sum of multiple copies of the Γ from Eq. (B16).

As explained in Appendix B 1, the global physical state $|\psi\rangle$ is obtained from the constituents introduced above by projecting the total fiducial state onto the virtual maximally entangled state

$$|\psi\rangle = \left[\bigotimes_{\langle \mathbf{x}'\mathbf{x}''\rangle} \langle\omega_{\mathbf{x}'\mathbf{x}''}|\right]\prod_{\mathbf{x}} Q_{\mathbf{x}}|\Omega\rangle. \tag{B17}$$

We recall from Appendix A 3 that for Gaussian states, this projection can be formulated in terms of CMs and gives rise to a Schur complement. This is the approach we take in the following.

Let us see how we can apply the general Schur complement expression of Eq. (A9) in order to compute the Majorana

CM $\Gamma_{|\psi\rangle}$ for the physical state from the CMs Γ_Q and Γ_ω defined above for the fiducial and virtual maximally entangled states. We introduce the symbols p and v to collectively refer to all Majorana mode operators for the physical and virtual fermions. Therefore, $(\Gamma_Q)_{pp}$ and $(\Gamma_Q)_{vv}$ denote the blocks of the CM of the total fiducial state that describe the reduced state of only the physical and virtual degrees of freedom (DOFs), respectively. On the other hand, the blocks $(\Gamma_Q)_{pv} = -(\Gamma_Q)_{vp}^T$ encode the correlations between physical and virtual fermions. In Eq. (B17), we are projecting the fiducial state of physical and virtual modes onto a maximally entangled state of the virtual modes in order to obtain a state of only the physical modes. According to Eq. (A9), this is represented by the Schur complement of the virtual block (vv) given by

$$\Gamma_{|\psi\rangle} = (\Gamma_Q)_{pp} + (\Gamma_Q)_{pv}[(\Gamma_Q)_{vv} + \Gamma_\omega]^{-1}(\Gamma_Q)_{pv}^T. \tag{B18}$$

Note that the CM on the left-hand side of this equation tracks every physical mode independently. Hence, its dimension is proportional to the system size and becomes large for our cases of interest. We will now specialize Eq. (B18) to translation-invariant states, where we can achieve a massive reduction of the size of the physical CM down to the number of Bloch bands independent of the system size.

APPENDIX C: TRANSLATION-INVARIANT GfTNSs

In this Appendix, we specialize the formalism reviewed in Appendix B to translation-invariant GfTNSs, where the contraction of the network can often be performed analytically. In Appendix C 1, we compute the CM of a translation-invariant GfTNS, which we then use in Appendix C 2 to construct a parent Hamiltonian for the state.

1. Covariance matrix

For translation-invariant Gaussian TNSs, we introduce the Fourier transform (FT) of the physical and virtual mode operators as

$$a_{\tau,\mathbf{k}} = \sum_{\mathbf{x}} \mathcal{F}_{\mathbf{k},\mathbf{x}} a_{\tau,\mathbf{x}}, \tag{C1a}$$

$$b_{\alpha,j,\mathbf{k}} = \sum_{\mathbf{x}} \mathcal{F}_{\mathbf{k},\mathbf{x}} b_{\alpha,j,\mathbf{x}} \tag{C1b}$$

for all $\tau = 1, \ldots, f$, $j = 1, \ldots, \xi$, $\alpha = L, R$ for MPSs, and $\alpha = L, U, R, D$ for two-dimensional PEPSs. Here, the FT in two spatial dimensions with N_x and N_y sites in the horizontal and vertical direction, respectively, position vector $\mathbf{x} = (x, y)$ and momentum vector $\mathbf{k} = (k_x, k_y)$, is given by

$$\mathcal{F}_{\mathbf{k},\mathbf{x}} = \frac{1}{\sqrt{N_x N_y}} e^{-i\mathbf{k}\mathbf{x}}. \tag{C1c}$$

The momenta in the horizontal (k_x) and vertical (k_y) direction take values $k_x = \frac{2\pi j}{N_x}$ with $0 \leqslant j \leqslant N_x - 1$ and $k_y = \frac{2\pi j}{N_y}$ with $0 \leqslant j \leqslant N_y - 1$. The FT for a single spatial direction is analogous.

We define the FT of the mode vector $\chi_{\mathbf{x}}$ from Eq. (B7) to be

$$\chi_{\mathbf{k}} = \sum_{\mathbf{x}} \mathcal{F}_{\mathbf{k},\mathbf{x}} \chi_{\mathbf{x}}. \tag{C2}$$

Therefore,

$$\chi_{\mathbf{k}} = (a_{1,\mathbf{k}}, a_{2,\mathbf{k}}, \ldots, a_{f,\mathbf{k}}, b_{L,1,\mathbf{k}}, b_{L,2,\mathbf{k}}, \ldots, b_{R,1,\mathbf{k}}, \ldots, a^\dagger_{1,-\mathbf{k}}, \ldots, b^\dagger_{L,1,-\mathbf{k}}, \ldots, b^\dagger_{R,1,-\mathbf{k}}, \ldots)^T \tag{C3}$$

mixes mode operators at momenta $\mathbf{k}$ and $-\mathbf{k}$ similarly to a Nambu spinor.

Due to the translation invariance of the GfTNS, the FT brings the CMs of the physical state, the total fiducial state, and the total virtual maximally entangled state into a block-diagonal form. We denote the Majorana CM of the total fiducial state with respect to the Fourier transform of the mode operators by

$$(\Gamma_Q)_{\mu,\nu;\mathbf{k}\mathbf{q}} = \sum_{\mathbf{x},\mathbf{x}'} \mathcal{F}^*_{\mathbf{k},\mathbf{x}} (\Gamma_Q)_{\mu,\nu;\mathbf{x}\mathbf{x}'} \mathcal{F}_{\mathbf{q},\mathbf{x}'} = \delta_{\mathbf{k}\mathbf{q}} (\tilde{\Gamma}_Q(\mathbf{k}))_{\mu,\nu}, \tag{C4}$$

where the last equality defines the Majorana CM $\tilde{\Gamma}_Q(\mathbf{k})$ restricted to the block of momentum $\mathbf{k}$. Note that the size of $\tilde{\Gamma}_Q(\mathbf{k})$ is given by twice the number of Bloch bands, $2 \times n_{\text{modes}}$, and therefore no longer grows with the system size. Analogous statements hold for the physical CM $\Gamma_{|\psi\rangle}$ with the Fourier block matrix $\tilde{\Gamma}_{|\psi\rangle}(\mathbf{k})$ of size $2f$, and for the CM of the total virtual maximally entangled state Γ_ω with Fourier block $\tilde{\Gamma}_\omega(\mathbf{k})$ of size $2(n_{\text{modes}} - f)$.

Since the TNS is translation invariant, the local fiducial state $|Q_{\mathbf{x}}\rangle$ is the same on every unit cell. Hence, the Fourier CM of the total fiducial state is localized at momentum $\mathbf{k} = 0$,

$$\tilde{\Gamma}_Q(\mathbf{k}) = \Gamma_{Q_{\mathbf{x}}} \times \delta_{\mathbf{k},0}. \tag{C5}$$

Here, $\Gamma_{Q_{\mathbf{x}}}$ is the CM of the local fiducial state $|Q_{\mathbf{x}}\rangle$ on a single site of dimension $2n_{\text{modes}}$. It has the block structure

$$\Gamma_{Q_{\mathbf{x}}} = \begin{pmatrix} \mathbf{A} & \mathbf{B} \\ -\mathbf{B}^T & \mathbf{D} \end{pmatrix}, \tag{C6}$$

where the real antisymmetric blocks $\mathbf{A}$ and $\mathbf{D}$ of dimension $2f$ and $2(n_{\text{modes}} - f)$ describe the physical and virtual subspaces, respectively, whereas the block $\mathbf{B}$ encodes the coupling between physical and virtual modes.

On the other hand, the CM of the total virtual maximally entangled state $\tilde{\Gamma}_\omega(\mathbf{k})$ has a nontrivial momentum dependence since the maximally entangled states from Eq. (B13) connect different unit cells. It is a direct sum of the contributions from the different spatial directions. For a single virtual fermion with $\xi = 1$, the Majorana Fourier CM of the horizontal bonds oriented from left to right is the Fourier transform of the matrix Γ from Eq. (B16). It reads as [40]

$$\tilde{\Gamma}_\omega(k_x) = \begin{pmatrix} 0 & -\sigma_1 e^{-ik_x} \\ \sigma_1 e^{ik_x} & 0 \end{pmatrix}. \tag{C7}$$

This matrix is written in the basis of the FT of the Majorana operators constructed from the complex modes $(b_{L,\mathbf{x}}, b_{R,\mathbf{x}}, b^\dagger_{L,\mathbf{x}}, b^\dagger_{R,\mathbf{x}})$ where we have omitted the index j since $\xi = 1$. The contribution from the vertical bonds is given by Eq. (C7) with $k_x \mapsto -k_y$ since the vertical bonds are oriented downward and hence in the direction of negative k_y. Therefore, the Fourier CM of the virtual bonds is anti-Hermitian and satisfies the identities $\tilde{\Gamma}_\omega(\mathbf{k})^* = \tilde{\Gamma}_\omega(-\mathbf{k})$ and $\tilde{\Gamma}_\omega(\mathbf{k})^T = -\tilde{\Gamma}_\omega(-\mathbf{k})$.

We are now in a position to compute the physical Majorana CM in momentum space by taking the FT of Eq. (B18). In momentum space, the right-hand side simplifies significantly due to the expression for the fiducial state CM given in Eqs. (C5) and (C6). We thus find [33]

$$\tilde{\Gamma}_{|\psi\rangle}(\mathbf{k}) = \mathbf{A} + \mathbf{B}[\mathbf{D} + \tilde{\Gamma}_{\omega}(\mathbf{k})]^{-1}\mathbf{B}^{T}. \tag{C8}$$

The physical state is well defined if the matrix inversion can be carried out, i.e., if the determinant

$$q(\mathbf{k}) = \det[\mathbf{D} + \tilde{\Gamma}_{\omega}(\mathbf{k})] \tag{C9}$$

is not equal to zero. We emphasize that the matrices in Eq. (C8) have a constant size given by the number of Bloch bands, such that Eq. (C8) can typically be evaluated analytically. In Appendix E, we use Eq. (C8) to evaluate the Bloch CM of the SSH model MPS from Sec. II A, and in Appendix H, we use Eq. (C8) to evaluate the Bloch CM of the quadrupole model PEPS of Sec. IV B.

2. Parent Hamiltonian

A translation-invariant Gaussian fermionic TNS $|\psi\rangle$ has an infinite number of parent Hamiltonians for which it is an exact ground state. For any non-negative scalar function $\epsilon(\mathbf{k}) \geqslant 0$ on the Brillouin zone,

$$H_{\epsilon} = \frac{i}{4}\sum_{\mathbf{k}} \epsilon(\mathbf{k}) \left(\chi_{\mathbf{k}}^{(p)}\right)^{\dagger}[S^{T}\tilde{\Gamma}_{|\psi\rangle}(\mathbf{k})S^{*}]\chi_{\mathbf{k}}^{(p)} \tag{C10}$$

is a parent Hamiltonian for the Gaussian fermionic TNS $|\psi\rangle$ [33,40]. Here,

$$\chi_{\mathbf{k}}^{(p)} = (a_{1,\mathbf{k}}, \ldots, a_{f,\mathbf{k}}, a_{1,-\mathbf{k}}^{\dagger}, \ldots, a_{f,-\mathbf{k}}^{\dagger})^{T} \tag{C11}$$

is the physical part of the mode vector of Eq. (C3), and S is the transformation matrix defined in Eq. (A2) from the Majorana fermions to the complex fermions.

The properties of the parent Hamiltonian H_{ϵ} depend on the dispersion function $\epsilon(\mathbf{k})$. If $\epsilon(\mathbf{k}) > 0$ is strictly positive throughout the Brillouin zone, H_{ϵ} is gapped. Moreover, if all matrix entries of the product $\epsilon(\mathbf{k})\tilde{\Gamma}_{|\psi\rangle}(\mathbf{k})$ are polynomials in $e^{\pm ik_x}$ and $e^{\pm ik_y}$, the parent Hamiltonian is strictly local.

A natural, *but not unique*, choice for the dispersion function is given by $\epsilon(\mathbf{k}) = q(\mathbf{k})$ from Eq. (C9). Indeed, since D and $\tilde{\Gamma}_{\omega}(\mathbf{k})$ are anti-Hermitian and of even dimension [see Eqs. (C6) and (C7)], it follows that $q(\mathbf{k})$ is real. If moreover $q(\mathbf{k})$ is strictly positive throughout the Brillouin zone, implying that the PEPS has exponentially decaying real-space correlations, the parent Hamiltonian H_q is gapped and strictly local with all terms acting on at most 2ξ successive unit cells [40,47].

APPENDIX D: GfTNSs WITH CONSERVED PARTICLE NUMBER

In the main text, we consider Gaussian fermionic TNSs with a conserved particle number: the ground states of both the SSH model and the quadrupole model lie at half-filling. The TNSs are written in a basis related to the physical basis by a staggered particle-hole conjugation [cf. Eq. (7) for the SSH MPS and Eq. (28) for the quadrupole PEPS]. Hence, the U(1) symmetry of the local tensors, which imposes the conservation of the physical particle number, also takes a staggered form [cf. Eq. (12) for the SSH MPS and Eq. (30) for the quadrupole PEPS]. In this Appendix, we rephrase this U(1) symmetry in the language of fiducial states, and show that it enforces many vanishing elements for the CM of the local fiducial state. These are equivalent to the vanishing of the off-diagonal block $Q = 0$ of the complex CM of a state with conserved particle number (see Appendix A 1), but expressed in the basis after the staggered particle-hole transformation. We focus on the one-dimensional case since the computation for two-dimensional GfTNSs is analogous.

For one-dimensional Gaussian fermionic MPS, we consider a U(1) symmetry of the local tensor of the general form

$$A[\mathbf{x}]^{i}_{lr} = \sum_{i'l'r'} \left(\bigotimes_{\tau=0}^{f} U(\eta_{\tau,\mathbf{x}}\varphi)\right)_{ii'} \left(\bigotimes_{j=0}^{\xi} U(\eta_{L,j,\mathbf{x}}\varphi)\right)_{ll'} \times \left(\bigotimes_{j=0}^{\xi} U(\eta_{R,j,\mathbf{x}}\varphi)\right)_{rr'} A[\mathbf{x}]^{i'}_{l'r'}, \tag{D1}$$

where $\eta_{\tau,\mathbf{x}}, \eta_{L,j,\mathbf{x}}, \eta_{R,j,\mathbf{x}} \in \{\pm 1\}$ for $\tau = 1, \ldots, f$ and $j = 1, \ldots, \xi$. Here,

$$U(\varphi) = \begin{pmatrix} 1 & 0 \\ 0 & e^{i\varphi} \end{pmatrix} \tag{D2}$$

is the U(1) rotation acting on a single spinless fermion. Positive and negative values for η indicate that the corresponding physical or virtual modes transform as particles and holes, respectively. The symmetries of Eq. (12) for the local tensors on the A and B sublattices of the SSH charge-pumping MPS are examples with $f = \xi = 1$.

Since the elements of the local tensor $A[\mathbf{x}]$ are the basis coefficients of the local fiducial state $|Q_{\mathbf{x}}\rangle$ [cf. Eq. (B10)], Eq. (D1) is equivalent to the invariance of the local fiducial state under the U(1) symmetry

$$\hat{U}_{\mathbf{x}}(\varphi) = \prod_{\tau=0}^{f} \hat{U}_{\tau,\mathbf{x}}(\eta_{\tau,\mathbf{x}}\varphi) \prod_{j=0}^{\xi} \hat{U}_{L,j,\mathbf{x}}(\eta_{L,j,\mathbf{x}}\varphi)\hat{U}_{R,j,\mathbf{x}}(\eta_{R,j,\mathbf{x}}\varphi) \tag{D3}$$

whose many-body basis representation is given in Eq. (D1). Here, each individual operator $\hat{U}$ in the product acts on exactly one fermion. For instance, the operator acting on the physical fermion τ is given by

$$\hat{U}_{\tau,\mathbf{x}}(\eta_{\tau,\mathbf{x}}\varphi) = e^{i\eta_{\tau,\mathbf{x}}\varphi}a_{\tau,\mathbf{x}}^{\dagger}a_{\tau,\mathbf{x}} + a_{\tau,\mathbf{x}}a_{\tau,\mathbf{x}}^{\dagger} \tag{D4}$$

and similarly for the virtual fermions. This agrees with the matrix representation of the U(1) rotation acting on a single mode given in Eq. (D2).

We observe that the U(1) operator of the physical fermion τ from Eq. (D4) satisfies $a_{\tau,\mathbf{x}}\hat{U}_{\tau,\mathbf{x}}(\eta_{\tau,\mathbf{x}}\varphi) = e^{i\eta_{\tau,\mathbf{x}}\varphi}\hat{U}_{\tau,\mathbf{x}}(\eta_{\tau,\mathbf{x}}\varphi)a_{\tau,\mathbf{x}}$ and $a_{\tau,\mathbf{x}}^{\dagger}\hat{U}_{\tau,\mathbf{x}}(\eta_{\tau,\mathbf{x}}\varphi) = e^{-i\eta_{\tau,\mathbf{x}}\varphi}\hat{U}_{\tau,\mathbf{x}}(\eta_{\tau,\mathbf{x}}\varphi)a_{\tau,\mathbf{x}}^{\dagger}$. Extending this to all of the modes in the mode operator of Eq. (B7), we find that

$$(\chi_{\mathbf{x}})_{\mu}\hat{U}_{\mathbf{x}}(\varphi) = e^{i\varphi(\eta_{\mathbf{x}})_{\mu}}\hat{U}_{\mathbf{x}}(\varphi)(\chi_{\mathbf{x}})_{\mu}, \tag{D5}$$

where $1 \leqslant \mu, \nu \leqslant 2n_{\text{modes}}$. Here, we collected all the parameters η into a vector of length $2n_{\text{modes}}$ using the same ordering

as in the mode vector of Eq. (B7),

$$\eta_{\mathbf{x}} = (\eta_{1,\mathbf{x}}, \eta_{2,\mathbf{x}}, \ldots, \eta_{f,\mathbf{x}}, \eta_{L,1,\mathbf{x}}, \eta_{L,2,\mathbf{x}}, \ldots, \eta_{R,1,\mathbf{x}}, \ldots, -\eta_{1,\mathbf{x}}, \ldots, -\eta_{L,1,\mathbf{x}}, \ldots, -\eta_{R,1,\mathbf{x}}, \ldots), \tag{D6}$$

where the last n_{modes} entries describe the creation operators which transform with the opposite sign under the U(1) symmetry.

We are now ready to infer the consequences of the local fiducial state's invariance under the U(1) symmetry from Eq. (D3) for its complex CM. Indeed, due to the relation of Eq. (D5), correlation functions transform under the symmetry as

$$\begin{aligned}\langle Q_{\mathbf{x}}|(\chi_{\mathbf{x}}^{\dagger})_{\nu}(\chi_{\mathbf{x}})_{\mu}|Q_{\mathbf{x}}\rangle &= \langle Q_{\mathbf{x}}|\hat{U}_{\mathbf{x}}^{\dagger}(\varphi)(\chi_{\mathbf{x}}^{\dagger})_{\nu}(\chi_{\mathbf{x}})_{\mu}\hat{U}_{\mathbf{x}}(\varphi)|Q_{\mathbf{x}}\rangle \\ &= e^{i\varphi[(\eta_{\mathbf{x}})_{\mu}-(\eta_{\mathbf{x}})_{\nu}]}\langle Q_{\mathbf{x}}|(\chi_{\mathbf{x}}^{\dagger})_{\nu}(\chi_{\mathbf{x}})_{\mu}|Q_{\mathbf{x}}\rangle.\end{aligned} \tag{D7}$$

Therefore, they vanish unless $(\eta_{\mathbf{x}})_{\mu} = (\eta_{\mathbf{x}})_{\nu}$. This shows that the symmetry of Eq. (D1) forces the vanishing of half the elements of the complex CM of the local fiducial state

$$(G_{\mathbf{x}})_{\mu\nu} = 0 \quad \text{if } (\eta_{\mathbf{x}})_{\mu} \neq (\eta_{\mathbf{x}})_{\nu}, \tag{D8}$$

where $1 \leqslant \mu, \nu \leqslant 2n_{\text{modes}}$.

APPENDIX E: COVARIANCE MATRIX FOR SSH MPS

In this Appendix, we illustrate the formalism of GfTNS introduced in Appendices B and C using the example of the MPS from Eq. (11) describing charge pumping in the SSH model. After expressing the state as a GfTNS in Appendix E 1, we demonstrate the computation of its Bloch CM and parent Hamiltonian in Appendix E 2.

1. Expression as GfTNS

Our goal is to express the SSH charge-pumping MPS, which is already fully defined by Eq. (11) in the language of local tensors, as a GfTNS using the formalism from Appendix B. Since the MPS has physical dimension 2 and bond dimension 2, it is described by $f = 1$ physical fermion and $\xi = 1$ virtual fermion per nearest-neighbor bond and lattice site (cf. the first paragraph of Appendix B 2). On the A sublattice, the annihilation operators for the physical, left virtual, and right virtual modes are $a_{A,x}$, $b_{L,A,x}$, and $b_{R,A,x}$, respectively, and similarly for the B sublattice. Following the recipe given above, we need to find the local fiducial states $|Q_{A,x}\rangle = Q_{A,x}|\Omega\rangle$ and $|Q_{B,x}\rangle = Q_{B,x}|\Omega\rangle$ that match the local tensors A and B from Eq. (11) at each unit cell x. The link between the local tensors and fiducial states is then given by Eq. (B10) stating that the local tensor entries are the basis coefficients of the fiducial state. For example, the tensor element $A^1_{01} = \beta$ tells us that the local fiducial map $Q_{A,x}$ contains a term $\beta a^{\dagger}_{A,x} b^{\dagger}_{R,A,x}$. Performing this matching for every nonzero tensor entry, we find that the fiducial maps are given by

$$Q_{A,x} = \gamma + \alpha a^{\dagger}_{A,x} b^{\dagger}_{L,A,x} + \beta a^{\dagger}_{A,x} b^{\dagger}_{R,A,x}, \tag{E1a}$$

$$Q_{B,x} = \gamma + \beta a^{\dagger}_{B,x} b^{\dagger}_{L,B,x} - \alpha a^{\dagger}_{B,x} b^{\dagger}_{R,B,x}. \tag{E1b}$$

In a second step, we want to write the local fiducial states as Gaussian states satisfying Wick's theorem in order to express the MPS as a GfTNS. Since the local tensors are parity even, the local fiducial states $|Q_{A,x}\rangle$ and $|Q_{B,x}\rangle$ can be parametrized as in Eq. (B12) using the exponential of antisymmetric coefficient matrices $M_{A,x}$ and $M_{B,x}$. In the case of the SSH pumping MPS, this is very simple since the fiducial states we derived in Eq. (E1) have the form of Eq. (A11), allowing us to directly read off $M_{A,x}$ and $M_{B,x}$ (imposing antisymmetry). We find that the coefficient matrices are given by

$$M_{A,x} = \frac{1}{2}\begin{pmatrix} 0 & a & b \\ -a & 0 & 0 \\ -b & 0 & 0 \end{pmatrix}, \tag{E2a}$$

$$M_{B,x} = \frac{1}{2}\begin{pmatrix} 0 & b & -a \\ -b & 0 & 0 \\ a & 0 & 0 \end{pmatrix}. \tag{E2b}$$

Here, we defined the quotients $a = \alpha/\gamma$ and $b = \beta/\gamma$ of the parameters used in Eq. (11), and we absorbed the remaining factor γ into the normalization constant $\mathcal{N}$ in Eq. (A11). The complex CMs of these local fiducial states are computed from $M_{A,x}$ and $M_{B,x}$ using Eq. (A12), and are then transformed to the Majorana representation using Eq. (A3). One finds that the Majorana CM $\Gamma_{Q_{A,x}}$ is

$$\Gamma_{Q_{A,x}} = \frac{1}{c}\begin{pmatrix} (c-2)i\sigma_2 & 4a\sigma_1 & 4b\sigma_1 \\ -4a\sigma_1 & (8a^2-c)i\sigma_2 & 8abi\sigma_2 \\ -4b\sigma_1 & 8abi\sigma_2 & (8b^2-c)i\sigma_2 \end{pmatrix}, \tag{E3}$$

where we introduced the shorthand notation $c \equiv 1 + 4a^2 + 4b^2$, and the basis is the Majorana basis derived from $(a_{A,x}, b_{L,A,x}, b_{R,A,x}, a^{\dagger}_{A,x}, b^{\dagger}_{L,A,x}, b^{\dagger}_{R,A,x})$. The Majorana CM $\Gamma_{Q_{B,x}}$ in the Majorana basis derived from $(a_{B,x}, b_{L,B,x}, b_{R,B,x}, a^{\dagger}_{B,x}, b^{\dagger}_{L,B,x}, b^{\dagger}_{R,B,x})$ is given by Eq. (E3) with the replacements $a \mapsto b$ and $b \mapsto -a$. We have thus successfully expressed the MPS from Eq. (11) as a GfTNS.

The virtual maximally entangled states for the SSH MPS are of the form discussed in Appendix B 2. In particular, the Majorana CM $\Gamma_{|\omega_{A,x,B,x}\rangle}$ of the state $|\omega_{A,x,B,x}\rangle$ within a unit cell is given by Eq. (B16) in the Majorana basis obtained from $(b_{R,A,x}, b_{L,B,x}, b^{\dagger}_{R,A,x}, b^{\dagger}_{L,B,x})$. Similarly, the Majorana CM of the state $|\omega_{B,x,A,x+1}\rangle$ between unit cells is given by Eq. (B16) in the Majorana basis obtained from $(b_{R,B,x}, b_{L,A,x+1}, b^{\dagger}_{R,B,x}, b^{\dagger}_{L,A,x+1})$.

2. Bloch CM and parent Hamiltonian

Now that we have expressed the MPS from Eq. (11) as a GfTNS, we want to use the power of the formalism introduced in Appendix C to derive its CM and parent Hamiltonian on a chain with periodic boundary conditions. We will compute the Bloch CM by evaluating Eq. (C8), and from there obtain the parent Hamiltonian via Eq. (C10).

a. CM for a unit cell

The expression for the Bloch CM from Eq. (C8) is valid for a translation-invariant GfTNS. In particular, the CM Γ_{Q_x} with its blocks **A**, **B**, and **D** from Eq. (C5) is the Majorana CM of the fiducial state of a *unit cell*, not a single site. In

order to proceed, we therefore need to derive the fiducial state of an entire unit cell by contracting the virtual bond within a unit cell. In the language of GfTNSs, this is described by projecting the fiducial states $Q_{A,x}Q_{B,x}|\Omega\rangle$ of the two sites in one unit cell onto the virtual maximally entangled state connecting them:

$$\langle\omega_{AB}|[Q_{A,x}Q_{B,x}|\Omega\rangle]. \tag{E4}$$

This projection is a special case of Eq. (A7). Hence, the CM Γ_{Q_x} of the resulting state is given, as in Eq. (A9), by the Schur complement of the block of size 4×4 corresponding to the Majorana mode operators constructed from $(b_{R,A}, b_{L,B}, b^\dagger_{R,A}, b^\dagger_{L,B})$:

$$\Gamma_{Q_x} = \mathbf{A}' + \mathbf{B}'\,[\mathbf{D}' + \Gamma_{|\omega_{A,x,B,x}\rangle}]^{-1}\,\mathbf{B}'^{T}. \tag{E5}$$

Here, $\mathbf{A}'$ and $\mathbf{D}'$ are the blocks on the diagonal of the direct sum $\Gamma_{Q_{A,x}}\oplus\Gamma_{Q_{B,x}}$ corresponding to the Majorana modes derived from $(a_{A,x}, a_{B,x}, b_{L,A,x}, b_{R,B,x}, a^\dagger_{A,x}, a^\dagger_{B,x}, b^\dagger_{L,A,x}, b^\dagger_{R,B,x})$ and $(b_{R,A,x}, b_{L,B,x}, b^\dagger_{R,A,x}, b^\dagger_{L,B,x})$, respectively. Correspondingly, $\mathbf{B}'$ is the off-diagonal block.

Γ_{Q_x} has the block form

$$\Gamma_{Q_x} = \begin{pmatrix} \mathbf{A} & \mathbf{B} \\ -\mathbf{B}^T & \mathbf{D} \end{pmatrix}, \tag{E6}$$

where $\mathbf{A}$ and $\mathbf{D}$ are real antisymmetric blocks of size 4×4, and $\mathbf{B}$ is a real block of size 4×4. We find that the diagonal blocks $\mathbf{A}$ and $\mathbf{D}$ are of the form

$$Z^{(1)}(r,s) = \begin{pmatrix} 0 & -r & 0 & -s \\ r & 0 & -s & 0 \\ 0 & s^* & 0 & -r \\ s^* & 0 & r & 0 \end{pmatrix}, \tag{E7}$$

where r and s are parameters. Specifically, the physical and virtual blocks are

$$\mathbf{A} = Z^{(1)}(r_p, s_p), \tag{E8a}$$

$$\mathbf{D} = Z^{(1)}(r_v, s_v) \tag{E8b}$$

with

$$r_p = \frac{1-a^4-b^4}{1+2a^2+a^4+b^4}, \tag{E8c}$$

$$s_p = \frac{2b^2}{1+2a^2+a^4+b^4}, \tag{E8d}$$

$$r_v = \frac{1-a^4+b^4}{1+2a^2+a^4+b^4}, \tag{E8e}$$

$$s_v = \frac{2a^2b^2}{1+2a^2+a^4+b^4}. \tag{E8f}$$

Here, the denominator is a consequence of the matrix inverse in Eq. (E5). In addition, the block containing the coupling between physical and virtual fermions is

$$\mathbf{B} = a\begin{pmatrix} 0 & r_p+1 & 0 & -s_p \\ r_p+1 & 0 & s_p & 0 \\ 0 & -s_p & 0 & -r_p-1 \\ s_p & 0 & -r_p-1 & 0 \end{pmatrix}. \tag{E9}$$

b. Bloch CM

We can now directly compute the Fourier Majorana CM $\tilde\Gamma_{|\psi\rangle}(k_x)$ of the physical state defined by the MPS on a chain with N_x sites and periodic boundary conditions. $\tilde\Gamma_{|\psi\rangle}(k_x)$ is given by the Schur complement in Eq. (C8), where the Fourier Majorana CM $\tilde\Gamma_\omega(k_x)$ for the virtual bonds is given by Eq. (C7), and $\mathbf{A}$, $\mathbf{B}$, and $\mathbf{D}$ are given in the previous section.

For the SSH pumping MPS, Eq. (C8) is a matrix equation of size 4×4 since there are two physical Bloch bands. The matrix inverse can be evaluated analytically using the special parametrization $Z^{(1)}(r,s)$ from Eq. (E7). Indeed, the Fourier Majorana CM for the virtual bonds from Eq. (C7) can be written as $\tilde\Gamma_\omega(k_x) = Z^{(1)}(0, e^{ik_x})$. One easily checks that

$$Z^{(1)}(r,s) + Z^{(1)}(r',s') = Z^{(1)}(r+r', s+s'), \tag{E10a}$$

$$\det[Z^{(1)}(r,s)] = (r^2+ss^*)^2, \tag{E10b}$$

$$(Z^{(1)}(r,s))^{-1} = -\frac{Z^{(1)}(r,s)}{\sqrt{\det[Z^{(1)}(r,s)]}}. \tag{E10c}$$

Using these identities, the matrix inverse in Eq. (C8) can be performed by hand,

$$\begin{aligned}(\mathbf{D}+\tilde\Gamma_\omega(k_x))^{-1} &= (Z^{(1)}(r_v, s_v+e^{ik_x}))^{-1} \\ &= -\frac{Z^{(1)}(r_v, s_v+e^{ik_x})}{\sqrt{r_v^2+(s_v+e^{ik_x})^2}},\end{aligned} \tag{E11}$$

and we evaluate the determinant $q(k_x)$ from Eq. (C9) as

$$\begin{aligned}q(k_x) &= \left[r_v^2+(s_v+e^{ik_x})^2\right]^2 \\ &= \frac{4(1+a^4+b^4+2a^2b^2\cos k_x)^2}{((a^2+1)^2+b^4)^2}.\end{aligned} \tag{E12}$$

Unless $\gamma = 0$ and $|\alpha| = |\beta|$, $q(k_x)$ is strictly positive such that the MPS is well defined everywhere except for these parameter values.

After the matrix inversion in Eq. (C8), the remaining matrix multiplications in Eq. (C8) can be performed using a computer algebra system. We thus find that the Fourier Majorana CM $\tilde\Gamma_{|\psi\rangle}(k_x)$ of the physical state is again of the form of Eq. (E7):

$$\tilde\Gamma_{|\psi\rangle}(k_x) = Z^{(1)}(r(k_x), s(k_x)) \tag{E13a}$$

with parameters

$$r(k_x) = \frac{1-a^4-b^4-2a^2b^2\cos k_x}{1+a^4+b^4+2a^2b^2\cos k_x}, \tag{E13b}$$

$$s(k_x) = \frac{2(b^2+a^2e^{-ik_x})}{1+a^4+b^4+2a^2b^2\cos k_x}. \tag{E13c}$$

c. Parent Hamiltonian

Using Eq. (C10), we can now find a Bloch parent Hamiltonian H_ϵ for the MPS from its Majorana Fourier CM which we computed in Eq. (E13). In order to gain a physical understanding of the parent Hamiltonian, we express it in terms of the original complex physical modes before the particle-hole transformation of Eq. (7) given by

$$\hat a_{A,\mathbf{k}} = a_{A,\mathbf{k}}, \tag{E14a}$$

$$\hat a_{B,\mathbf{k}} = a^\dagger_{B,-\mathbf{k}} \tag{E14b}$$

after the FT of Eq. (C1). We find

$$H_\epsilon = \sum_{k_x} \epsilon(k_x) \begin{pmatrix} \hat{a}_{A,k_x} \\ \hat{a}_{B,k_x} \end{pmatrix}^\dagger \begin{pmatrix} r(k_x) & s(k_x) \\ s(k_x)^* & -r(k_x) \end{pmatrix} \begin{pmatrix} \hat{a}_{A,k_x} \\ \hat{a}_{B,k_x} \end{pmatrix}, \quad \text{(E15)}$$

where the functions $s(k_x)$ and $r(k_x)$ are defined in Eq. (E13).

In order for H_ϵ to be gapped and strictly local, we need to find a dispersion function $\epsilon(k_x)$ which is strictly positive such that $\epsilon(k_x)s(k_x)$ and $\epsilon(k_x)r(k_x)$ are polynomials in $e^{\pm ik_x}$. As explained in Appendix C 2, a natural choice is $\epsilon(k_x) = q(k_x)$. Indeed, $q(k_x)$ computed in Eq. (E12) cancels the denominator of Eq. (E13). Since $q(k_x)s(k_x)$ and $q(k_x)r(k_x)$ contain the factor $e^{\pm ik_x}$ up to second order, the parent Hamiltonian H_q contains hopping terms between up to second-nearest-neighbor unit cells.

Due to the special structure of Eq. (E8), we can in fact obtain a more short-ranged parent Hamiltonian from the choice

$$\epsilon(k_x) = \frac{1 + a^4 + b^4 + 2a^2b^2 \cos k_x}{a^4 + b^4 + 1} \quad \text{(E16)}$$

proportional to $\sqrt{q(k_x)}$, which is in turn proportional to the denominator of r and s from Eq. (E13b). $\epsilon(k_x)$ is strictly positive for all parameter values that lead to a well-defined state. The factor $1/(a^4 + b^4 + 1)$ is a normalization ensuring that the parent Hamiltonian matches Eq. (3) if the MPS is given by the parametrization ϕ_{pump} of Eq. (15). We see that the parent Hamiltonian H_ϵ with Bloch representation

$$H_\epsilon(k_x) = \frac{1}{a^4 + b^4 + 1}[(1 - a^4 - b^4 - 2a^2b^2 \cos k_x)\sigma_3 + 2(b^2 + a^2 \cos k_x)\sigma_1 + 2a^2 \sin k_x \sigma_2] \quad \text{(E17)}$$

with respect to the original complex physical modes has hopping only up to nearest-neighbor unit cells.

APPENDIX F: COLUMN COVARIANCE MATRIX OF REAL-SPACE $(d+1)$-DIMENSIONAL TNS FROM CHARGE PUMPING OF d-DIMENSIONAL TNS WITH CONSERVED PARTICLE NUMBER

In Sec. III C, we introduced the tensors A^{col} and B^{col} describing the real-space Chern PEPS restricted to a column of sites on the A and B sublattices at positions $\{(x, y)\}_{0 \leqslant y \leqslant N_y - 1}$. A^{col} and B^{col} are defined by the application of the inverse FT of Eq. (22) to the physical and horizontal virtual legs of a column of the hybrid Chern PEPS at positions $\{(x, k_y^{(j)})\}_{0 \leqslant j \leqslant N_y - 1}$. In this Appendix, using the representation of the SSH pumping MPS as a GfTNS from Appendix E, we compute A^{col} and B^{col} explicitly in terms of their CMs. In order to demonstrate the generality of the result, we will consider a general $(d+1)$-dimensional TNS constructed from charge pumping of a d-dimensional TNS, which is assumed to have a conserved number of physical particles, and hence possess a U(1) symmetry of the form discussed in Appendix D.

Thus, let $|\psi_d(t)\rangle$ be the Gaussian fermionic TNS in d spatial dimensions along a cyclic interpolation parametrized by the time $t \in (-\pi, \pi]$. With the same basis as in Eq. (B7), we collect the physical and virtual mode operators for one unit cell $\mathbf{x} \in \mathbb{Z}^d$ of $|\psi_d(t)\rangle$ into the mode vector

$$\chi_{\mathbf{x}}(t) = (a_{1,\mathbf{x}}(t), a_{2,\mathbf{x}}(t), \ldots, a_{f,\mathbf{x}}(t), b_{L,1,\mathbf{x}}(t), b_{L,2,\mathbf{x}}(t), \ldots, b_{R,1,\mathbf{x}}(t), \ldots, a^\dagger_{1,\mathbf{x}}(t), \ldots, b^\dagger_{L,1,\mathbf{x}}(t), \ldots, b^\dagger_{R,1,\mathbf{x}}(t), \ldots)^T \quad \text{(F1)}$$

of length $2n_{\text{modes}}$. The physical and virtual mode operators now depend on the time t along the interpolation. As explained in Appendix B, the d-dimensional TNS is defined by its Gaussian local fiducial state $Q_{\mathbf{x}}(t)|\Omega\rangle$, which is characterized by its complex CM $G_{\mathbf{x}}(t)$ of dimension $2n_{\text{modes}}$.

We assume that the TNS has a conserved number of particles, such that the local fiducial state $Q_{\mathbf{x}}(t)|\Omega\rangle$ of $|\psi_d(t)\rangle$ has a U(1) symmetry of the form discussed in Appendix D. This symmetry determines which physical and virtual modes correspond to holes and particles: for each $1 \leqslant \mu \leqslant n_{\text{modes}}$, an entry $(\eta_{\mathbf{x}})_\mu = 1$ or $(\eta_{\mathbf{x}})_\mu = -1$ in the vector $\eta_{\mathbf{x}}$ from Eq. (D6) indicates that the mode μ has a particlelike or holelike character, respectively. Note that $\eta_{\mathbf{x}}$ does not depend on the time t, such that the holelike or particlelike character of the modes remains unchanged along the interpolation.

We can now move to the hybrid $(d+1)$-dimensional TNS, which is defined by Eq. (20) of the main text. From Sec. III B we recall that the local fiducial state (equivalent to the local tensor) of the hybrid state at the position $(\mathbf{x}, k_{d+1}^{(j)})$ is given by $Q_{\mathbf{x}}(t^{(j)})|\Omega\rangle$ containing the modes $\chi_{\mathbf{x}}(t^{(j)})$ from Eq. (F1). In particular, due to the tensor product in the $(d+1)$st direction, virtual fermions in this direction are not needed.

We can now easily write the CM of one column of the hybrid $(d+1)$-dimensional TNS, given by the sites at positions $\{(\mathbf{x}, k_{d+1}^{(j)})\}_{0 \leqslant j \leqslant N_{d+1}-1}$. Indeed, due to the absence of virtual legs in the direction $d+1$, the contraction of the bonds in this direction of the hybrid column amounts to a trivial tensor product in the language of local tensors. In terms of fiducial states, this corresponds to a direct sum of CMs. Hence, the complex CM $G_{\mathbf{x}}^{\text{hybrid}}$ of the column $\{(\mathbf{x}, k_{d+1}^{(j)})\}_{0 \leqslant j \leqslant N_{d+1}-1}$ of the hybrid state is block diagonal:

$$\left(G_{\mathbf{x}}^{\text{hybrid}}\right)_{\mu,\mu';t^{(j)},t^{(j')}} = \delta_{j,j'} (G_{\mathbf{x}}(t^{(j)}))_{\mu,\mu'}. \quad \text{(F2)}$$

Here, $G_{\mathbf{x}}^{\text{hybrid}}$ is written in the basis $\{(\chi_{\mathbf{x}})_\mu (t^{(j)})\}_{1 \leqslant \mu \leqslant 2n_{\text{modes}}, 0 \leqslant j \leqslant N_{d+1}-1}$ of all operators for the physical and virtual modes in the first d directions in the column.

We now consider the $(d+1)$-dimensional real-space state restricted to a column $\{(\mathbf{x}, x_{d+1})\}_{0 \leqslant x_{d+1} \leqslant N_{d+1}-1}$, which is obtained by applying the inverse FT $\tilde{\mathcal{F}}$ in direction $d+1$ to the physical and virtual legs of the hybrid column. The complex CM $G_{\mathbf{x}}^{\text{col}}$ of this at position $\mathbf{x}$ is therefore given by

$$G_{\mathbf{x}}^{\text{col}} = \tilde{\mathcal{F}}^* G_{\mathbf{x}}^{\text{hybrid}} \tilde{\mathcal{F}}^T. \quad \text{(F3)}$$

The inverse FT is the d-dimensional generalization of Eq. (22),

$$\tilde{\mathcal{F}}_{\mu,\mu';x_{d+1},t^{(j)}} = \frac{\delta_{\mu,\mu'}}{\sqrt{N_{d+1}}} e^{i(\eta_{\mathbf{x}})_\mu x_{d+1} t^{(j)}} \quad \text{(F4)}$$

with $0 \leqslant j, x_{d+1} \leqslant N_{d+1} - 1$.

From Eqs. (F2), (F3), and (F4), $G_{\mathbf{x}}^{\mathrm{col}}$ becomes

$$\left(G_{\mathbf{x}}^{\mathrm{col}}\right)_{\mu,\mu';x_{d+1},x'_{d+1}} = \frac{1}{N_{d+1}} \sum_{j=0}^{N_{d+1}-1} e^{-i[(\eta_{\mathbf{x}})_{\mu} x_{d+1} - (\eta_{\mathbf{x}})_{\mu'} x'_{d+1}]t^{(j)}} (G_{\mathbf{x}}(t^{(j)}))_{\mu,\mu'}. \quad \text{(F5)}$$

This expression can be further simplified due to the constraint of Eq. (D8) imposed on $G_{\mathbf{x}}(t^{(j)})$ by its U(1) symmetry, implying $G_{\mathbf{x}}(t^{(j)})_{\mu,\mu'} = 0$ unless $(\eta_{\mathbf{x}})_{\mu} = (\eta_{\mathbf{x}})_{\mu'}$. Indeed, we may thus define the matrix

$$\tilde{G}_{\mathbf{x}}(t^{(j)})_{\mu,\mu'} \equiv G_{\mathbf{x}}((\eta_{\mathbf{x}})_{\mu} t^{(j)})_{\mu,\mu'} \quad \text{(F6)}$$

that mixes elements of the complex CM of the d-dimensional state at times $t^{(j)}$ and $-t^{(j)}$ according to whether the modes μ and μ' transform as particles or holes, respectively. The $2n_{\mathrm{modes}}$-dimensional blocks of the column CM $G_{\mathbf{x}}^{\mathrm{col}}$ are then given by the FT of this matrix:

$$\left(G_{\mathbf{x}}^{\mathrm{col}}\right)_{x_{d+1},x'_{d+1}} = \sum_{j=0}^{N_{d+1}-1} \frac{e^{-i[x_{d+1}-x'_{d+1}]t^{(j)}}}{N_{d+1}} \tilde{G}_{\mathbf{x}}(t^{(j)}). \quad \text{(F7)}$$

This expression is explicitly invariant under real-space translations $x_{d+1} \mapsto x_{d+1} + 1$ acting on both the physical modes and the virtual modes in the first d directions. Hence, the inverse FT of Eq. (F4) guarantees the translation invariance of the column CM $G_{\mathbf{x}}^{\mathrm{col}}$ in the direction $d+1$.

Finally, we want to investigate which form the global U(1) symmetry related to particle-number conservation takes for $G_{\mathbf{x}}^{\mathrm{col}}$. This result will be used in Appendix G. The U(1) is inherited from the invariance of each fiducial state $Q_{\mathbf{x}}(t)|\Omega\rangle$ under the U(1) symmetry of Eq. (D3), which is independent of t. From the expression of the latter in second quantization [cf. Eq. (D4)], we see that the generator of the global U(1) symmetry of the column state is

$$\left\langle \sum_{x_{d+1}=0}^{N_{d+1}-1} \left[\sum_{\tau=0}^{f} \eta_{\tau,\mathbf{x}} a^{\dagger}_{\tau,(\mathbf{x},x_{d+1})} a_{\tau,(\mathbf{x},x_{d+1})} + \sum_{\alpha} \sum_{j=0}^{\xi} \eta_{\alpha,j,\mathbf{x}} b^{\dagger}_{\alpha,j,(\mathbf{x},x_{d+1})} b_{\alpha,j,(\mathbf{x},x_{d+1})} \right] \right\rangle = 0, \quad \text{(F8)}$$

whose expectation value vanishes.

APPENDIX G: DISENTANGLED MODES IN SINGLE-PARTICLE ES AT FIXED PARTICLE NUMBER

In this Appendix, we show that as stated in Eq. (25), the maximal number of entangled modes compatible with the U(1) symmetry of the SSH model MPS in the ES of the Chern PEPS column state is given by $\max\{3L, N_y\}$, where L is the number of sites in the subsystem. We proceed by deriving a lower bound on the number of disentangled modes in the ES of a state with a conserved particle number (and therefore an upper bound on the number of entangled modes). We first consider a generic state in Appendix G 1, before specializing to the fiducial state of a real-space column of the $(d+1)$-dimensional TNS in Appendix G 2.

1. Insulator with filling fraction q

We consider a noninteracting system of N fermionic DOFs with creation and annihilation operators $a_j^{\dagger}$, a_j for $j = 1, \ldots, N$. We define a bipartition of the system into the subsystem $\mathcal{A}$ and its complement $\bar{\mathcal{A}}$, where the DOFs of $\mathcal{A}$ are described by the first $N_{\mathcal{A}}$ modes $j = 1, \ldots, N_{\mathcal{A}}$. Let $|\psi\rangle$ be a pure state of this system with a conserved particle number and filling fraction q, such that the total number of occupied modes in $|\psi\rangle$ is qN. We denote by $n_{\mathcal{A}}^{\lambda=1}$ the number of entanglement levels with the value $\lambda = 1$ in the single-particle ES of $|\psi\rangle$ restricted to $\mathcal{A}$. We now want to show that this number is bounded below by the filling fraction as

$$n_{\mathcal{A}}^{\lambda=1} \geqslant \max\{qN - (N - N_{\mathcal{A}}),\ 0\}. \quad \text{(G1)}$$

Proof. Let $H = \sum_{i,j=1}^{N} h_{ij} a_i^{\dagger} a_j$ be a noninteracting flat-band Hamiltonian whose ground state is $|\psi\rangle$, where h is a Hermitian matrix of dimension $N \times N$. The occupied modes in $|\psi\rangle$ are given by the qN orthogonal eigenstates $u^{(k)}$ of h with energy -1, i.e.,

$$\sum_{j=1}^{N} h_{ij} u_j^{(k)} = -u_i^{(k)}, \quad \text{(G2)}$$

where $k = 1, \ldots, qN$.

With respect to the bipartition into $\mathcal{A}, \bar{\mathcal{A}}$, each basis state $u^{(k)}$ falls into exactly one of the following three categories (assuming that the eigenstates are ordered accordingly):

(1) For $k = 1, \ldots, m_1$, the states satisfy $u_i^{(k)} = 0$ for $i = N_{\mathcal{A}} + 1, \ldots, N$ such that the corresponding occupied modes are composed of DOFs of the subsystem $\mathcal{A}$. According to Theorem 1 of Ref. [69], each such state leads to an entanglement level $\lambda = 1$ in the single-particle ES of $|\psi\rangle$ restricted to $\mathcal{A}$. Hence, $m_1 \leqslant n_{\mathcal{A}}^{\lambda=1}$.

(2) For $k = m_1 + 1, \ldots, m_2$, $u_i^{(k)} = 0$ for $i = 1, \ldots, N_{\mathcal{A}}$ such that the corresponding occupied modes are localized in $\bar{\mathcal{A}}$.

(3) For $k = m_2 + 1, \ldots, qN$, $u_i^{(k)} \neq 0$ both for some $i \in \{1, \ldots, N_{\mathcal{A}}\}$ and some $i \in \{N_{\mathcal{A}} + 1, \ldots, N\}$ such that the corresponding occupied modes are localized neither in $\mathcal{A}$ nor in $\bar{\mathcal{A}}$.

The numbers m_1, m_2 are assumed to be maximal in the sense that no linear combination of eigenstates of the category (3) lies either purely in $\mathcal{A}$ or purely in $\bar{\mathcal{A}}$.

In the next paragraph, we will show that the number $qN - m_1$ of states from the categories (2) and (3) is no larger than the number $N - N_{\mathcal{A}}$ of DOFs in $\bar{\mathcal{A}}$. This proves the claim since the number of states from the different categories can then be estimated as

$$qN = m_1 + (qN - m_1) \leqslant n_{\mathcal{A}}^{\lambda=1} + (N - N_{\mathcal{A}}), \quad \text{(G3)}$$

leading to Eq. (G1).

As a final step, we need to show that $qN - m_1 \leqslant N - N_{\mathcal{A}}$. This follows from the linear independence of the $qN - m_1$ vectors $\{\tilde{u}^{(k)}\}_{k>m_1}$ of dimension $N - N_{\mathcal{A}}$, where $\tilde{u}_i^{(k)} = u_{N_{\mathcal{A}}+i}^{(k)}$ for $i = N_{\mathcal{A}} + 1, \ldots, N$ is the restriction of the eigenvector to the DOFs of $\bar{\mathcal{A}}$. Indeed, let us assume that we have a vanishing

linear combination

$$0 = \sum_{k=m_1+1}^{qN} \mu_k \tilde{u}^{(k)} \tag{G4}$$

with coefficients μ_k. The scalar product with $\tilde{u}^{(l)}$ shows that $0 = \mu_l$ for $l = m_1 + 1, \ldots, m_2$: indeed, the orthogonality of the $u^{(k)}$ implies $\sum_{i>N_A} \tilde{u}_i^{(l)} \tilde{u}_i^{(k)} = \sum_{i\geqslant 1} u_i^{(l)} u_i^{(k)} = \delta_{kl}$. Equation (G4) therefore implies $0 = \sum_{k>m_2}^{qN} \mu_k \tilde{u}^{(k)}$ where the sum runs only over category (3). Due to the maximality of m_1, m_2 as defined above just below point (3), we then have $0 = \sum_{k>m_2}^{qN} \mu_k u^{(k)}$. Otherwise, this would be a linear combination purely in $\mathcal{A}$ since the part in $\bar{\mathcal{A}}$ vanishes by assumption. We thus also get $0 = \mu_l$ for $l = m_2 + 1, \ldots, qN$, proving that $qN - m_1 \leqslant N - N_{\mathcal{A}}$.

2. Real-space column of $(d+1)$-dimensional TNS

We now apply Eq. (G1) to the case where $|\psi\rangle$ is the fiducial state of one real-space column of the $(d+1)$-dimensional pumping TNS, whose CM is computed in Eq. (F5). The column state has $N = n_{\text{modes}} N_{d+1}$ degrees of freedom, where N_{d+1} is the number of sites in the direction $d+1$ and n_{modes} the number of physical and virtual particles per lattice site of the d-dimensional TNS. Below we will show that in a suitable basis, the column state has a conserved particle number $qN = N_{d+1} n_{\eta_-}$, where n_{η_-} is the number of values -1 in the first n_{modes} entries of the vector $\eta_{\mathbf{x}}$ from Eq. (D6). We consider the single-particle ES of the column state with respect to the subsystem $\mathcal{A}_L$ of the first L sites $0 \leqslant x_{d+1} \leqslant L-1$ of the column, which has $N_{\mathcal{A}_L} = L n_{\text{modes}}$ DOFs. By Eq. (G1), the number $n_{\mathcal{A}_L}^{\lambda=1}$ of entanglement levels with the value $\lambda = 1$ in this spectrum is lower bounded as

$$n_{\mathcal{A}_L}^{\lambda=1} \geqslant \max\{N_{d+1} n_{\eta_-} - (N_{d+1} - L) n_{\text{modes}},\ 0\}. \tag{G5}$$

We now show that with a suitable particle-hole transformation we can find a single-particle basis with respect to which the column state has a conserved particle number $N_{d+1} n_{\eta_-}$. In Eq. (F5) the state is expressed in a basis where the CM $G_{\mathbf{x}}^{\text{col}}$ has a nonvanishing off-diagonal block Q corresponding to superconducting correlations, such that only the parity of the particle number is conserved [cf. Eq. (A1)]. Below Eq. (F5) we note that half the entries of $G_{\mathbf{x}}^{\text{col}}$ vanish, namely, those with $(\eta_{\mathbf{x}})_\mu \neq (\eta_{\mathbf{x}})_{\mu'}$. A new basis, in which the complex CM has only a diagonal block R and hence a fixed particle number, is created as follows: For those modes $1 \leqslant m \leqslant n_{\text{modes}}$ with $(\eta_{\mathbf{x}})_m = -1$, we exchange annihilation and creation operators since the latter have $(\eta_{\mathbf{x}})_{m+n_{\text{modes}}} = 1$. This is a particle-hole transformation corresponding to the mapping

$$a_{\tau,(\mathbf{x},x_{d+1})} \mapsto a_{\tau,(\mathbf{x},x_{d+1})}^\dagger \tag{G6}$$

for all physical modes with $\eta_{\tau,\mathbf{x}} = -1$ while leaving modes with $\eta_{\tau,\mathbf{x}} = 1$ unchanged, and similarly for the virtual modes.

The number of particles in the column state is given by the expectation value from Eq. (F8) of the generator of its global U(1) symmetry. Note that this is not the physical particle number, but rather the number of particles in the system composed of the physical legs and the virtual legs in the first d spatial dimensions. Under the transformation of Eq. (G6), the particle-number expectation value from Eq. (F8) transforms as explained in Eq. (13). We thus find that in the new basis of modes the particle number is $N_{d+1} n_{\eta_-}$ as claimed above.

a. Chern PEPS

Let us apply these results to the Chern PEPS derived from the SSH pumping MPS. For simplicity, we restrict ourselves to a column A^{col} of A sites with $n_{\text{modes}} = 3$ DOFs per site and $\eta_A = 1$ and $\eta_{L,A} = \eta_{R,A} = -1$ [cf. the discussion below Eq. (13)]. Therefore, $n_{\eta_-} = 2$ and Eq. (G5) becomes

$$n_{\mathcal{A}_L}^{\lambda=1} \geqslant \max\{3L - N_y,\ 0\}. \tag{G7}$$

This shows that Eq. (25) gives the maximal number of entangled modes compatible with the U(1) symmetry of the SSH model MPS.

For the PEPS defined by the trivial cycle ϕ_{triv} from Eq. (17), the discussion above can be refined: since $\beta = 0$ throughout the interpolation, all right virtual modes decouple from the column tensor such that there trivially are N_y entanglement levels $|\lambda| = 1$. Let us investigate if the U(1) symmetry causes additional decoupled levels in the system of the coupled physical and left virtual particles. This system has only two DOFs per site, namely, the physical leg with $\eta_A = 1$ and the left virtual leg with $\eta_{L,A} = -1$. In this case, Eq. (G5) gives a trivial lower bound for the number of decoupled modes with levels $\lambda = 1$:

$$n_{\mathcal{A}_L}^{\lambda=1} \geqslant \max\{2L - N_y,\ 0\} = 0 \quad \text{for } L \leqslant N_y/2. \tag{G8}$$

Hence, the U(1) symmetry does not cause any additional decoupled modes, and the number of entangled modes is given by $2L$ as discussed in the main text.

b. Chiral hinge PEPS

The discussion for the three-dimensional chiral hinge PEPS from Sec. IV C is analogous, where a column of sites on the sublattice 1 has $n_{\text{modes}} = 5$ DOFs per site with $\eta_1 = 1$ and $\eta_{L,1} = \eta_{U,1} = \eta_{R,1} = \eta_{D,1} = -1$. Therefore, $n_{\eta_-} = 4$ and Eq. (G5) implies $n_{\mathcal{A}_L}^{\lambda=1} \geqslant \max\{5L - N_z,\ 0\}$.

For the mirror-symmetric case with couplings $\alpha = \alpha_x = \alpha_y$ and $\beta = \beta_x = \beta_y$, this bound can be refined. Indeed, by defining the linear combinations $b_{\pm,1}^{LD} = (b_{L,1} \pm b_{D,1})/\sqrt{2}$ and $b_{\pm,1}^{UR} = (b_{R,1} \pm b_{R,1})/\sqrt{2}$, the local fiducial state $|Q^{[1]}\rangle$ from Eq. (H1) below can be written as

$$|Q^{[1]}\rangle = \left[\gamma - \sqrt{2}\beta a_1^\dagger \left(b_{-,1}^{LD}\right)^\dagger - \sqrt{2}\alpha a_1^\dagger \left(b_{-,1}^{UR}\right)^\dagger\right]|\Omega\rangle. \tag{G9}$$

Therefore, when considering only one column of sites on the sublattice 1, two virtual fermionic modes decouple from the local tensor on each site. Effectively, the remaining coupled system therefore has only $n_{\text{modes}} = 3$ DOFs per site with $\eta_1 = 1$ and $\eta_{-,1}^{LD} = \eta_{-,1}^{UR} = -1$, such that the number of additional disentangled modes due to the U(1) symmetry can be estimated as above for the Chern PEPS. Hence, with the identification $N_y \mapsto N_z$, the bound on the number of disentangled modes is given by Eqs. (G7) and (G8) for the PEPSs derived from ϕ_{pump} and ϕ_{triv}, respectively.

APPENDIX H: QUADRUPOLE PEPS AS GfTNS

In this Appendix we apply the formalism of GfTNSs to the quadrupole model pumping PEPS of Eq. (29). In Appendix H 1, we show how the state can be expressed as a GfTNS. This allows us to compute its Bloch CM and a Bloch parent Hamiltonian on the torus in Appendix H 2. These sections are completely analogous to Appendix E for the SSH pumping MPS. We therefore refer the reader to this Appendix for a detailed explanation of each step. Finally, in Appendix H 3 we discuss the ES of the PEPS when the parameters are chosen such that the state represents the OAI dimerized phase of the quadrupole model.

1. Expression as GfTNS

The quadrupole model pumping PEPS is defined in Eq. (29) of the main text in the language of local tensors. Here, we want to reexpress this state in the formalism of GfTNSs. We recall that each unit cell consists of 2×2 lattice sites, and that the PEPS has physical dimension 2 and bond dimension 2. This corresponds to $f = 1$ physical fermion per lattice site and $\xi = 1$ virtual fermion per nearest-neighbor bond and lattice site, represented in Fig. 6(b) by blue and red circles, respectively.

As explained in Appendix B, the local PEPS tensors $A^{[\tau]}$ on the four sublattices $\tau = 1, 2, 3, 4$ from the main text correspond to local fiducial states $|Q^{[\tau]}\rangle$, whose basis coefficients are given by the local tensors [see Eq. (B10)]. We write a_τ for the annihilation operator of the physical fermion and $b_{L,\tau}$, $b_{U,\tau}$, $b_{R,\tau}$, $b_{D,\tau}$ for the annihilation operators of the left, up, right, down virtual fermions on the sublattice τ (we dropped the unit-cell index due to the translation invariance). Let $|\Omega\rangle$ denote the vacuum annihilated by all these operators. Applying Eq. (B10), we see that the local fiducial states on the four sublattices derived from the local tensors of Eq. (29) are

$$|Q^{[1]}\rangle = [\gamma - \beta_x a_1^\dagger b_{L,1}^\dagger - \alpha_y a_1^\dagger b_{U,1}^\dagger + \alpha_x a_1^\dagger b_{R,1}^\dagger + \beta_y a_1^\dagger b_{D,1}^\dagger]|\Omega\rangle, \tag{H1a}$$

$$|Q^{[2]}\rangle = [\gamma - \alpha_x a_2^\dagger b_{L,2}^\dagger + \beta_y a_2^\dagger b_{U,2}^\dagger + \beta_x a_2^\dagger b_{R,2}^\dagger - \alpha_y a_2^\dagger b_{D,2}^\dagger]|\Omega\rangle, \tag{H1b}$$

$$|Q^{[3]}\rangle = [\gamma + \alpha_x a_3^\dagger b_{L,3}^\dagger + \alpha_y a_3^\dagger b_{U,3}^\dagger + \beta_x a_3^\dagger b_{R,3}^\dagger + \beta_y a_3^\dagger b_{D,3}^\dagger]|\Omega\rangle, \tag{H1c}$$

$$|Q^{[4]}\rangle = [\gamma + \beta_x a_4^\dagger b_{L,4}^\dagger + \beta_y a_4^\dagger b_{U,4}^\dagger + \alpha_x a_4^\dagger b_{R,4}^\dagger + \alpha_y a_4^\dagger b_{D,4}^\dagger]|\Omega\rangle. \tag{H1d}$$

These fiducial states are of the form of Eq. (A11) with only zero- and second-order terms in the creation operators. Hence, the fiducial states are Gaussian and can be parametrized as in Eqs. (A10) and (B12) with antisymmetric coefficient matrices

$$M_1 = \frac{1}{2 \times 2^{1/4}} \begin{pmatrix} 0 & -b_x & -a_y & a_x & b_y \\ b_x & 0 & 0 & 0 & 0 \\ a_y & 0 & 0 & 0 & 0 \\ -a_x & 0 & 0 & 0 & 0 \\ -b_y & 0 & 0 & 0 & 0 \end{pmatrix}, \tag{H2a}$$

$$M_2 = \frac{1}{2 \times 2^{1/4}} \begin{pmatrix} 0 & -a_x & b_y & b_x & -a_y \\ a_x & 0 & 0 & 0 & 0 \\ -b_y & 0 & 0 & 0 & 0 \\ -b_x & 0 & 0 & 0 & 0 \\ a_y & 0 & 0 & 0 & 0 \end{pmatrix}, \tag{H2b}$$

$$M_3 = \frac{1}{2 \times 2^{1/4}} \begin{pmatrix} 0 & a_x & a_y & b_x & b_y \\ -a_x & 0 & 0 & 0 & 0 \\ -a_y & 0 & 0 & 0 & 0 \\ -b_x & 0 & 0 & 0 & 0 \\ -b_y & 0 & 0 & 0 & 0 \end{pmatrix}, \tag{H2c}$$

$$M_4 = \frac{1}{2 \times 2^{1/4}} \begin{pmatrix} 0 & b_x & b_y & a_x & a_y \\ -b_x & 0 & 0 & 0 & 0 \\ -b_y & 0 & 0 & 0 & 0 \\ -a_x & 0 & 0 & 0 & 0 \\ -a_y & 0 & 0 & 0 & 0 \end{pmatrix}. \tag{H2d}$$

Here, we defined the quotients $a_x = \alpha_x/\gamma$, $a_y = \alpha_y/\gamma$, $b_x = \beta_x/\gamma$, and $b_y = \beta_y/\gamma$ of the parameters from Eq. (29). We absorbed the remaining factor γ into the normalization constant $\mathcal{N}$ in Eq. (A11).

We have thus successfully written the PEPS from Eq. (29) as a GfTNS. Before proceeding, we choose the orientation of the virtual bonds as follows: all horizontal bonds are oriented from left to right and all vertical bonds are oriented from top to bottom.

2. Bloch CM and parent Hamiltonian

Having expressed the quadrupole model pumping PEPS as a GfTNS, we now want to use the formalism from Appendix C to compute the Bloch CM and a Bloch parent Hamiltonian for the state on a torus. We will compute the Bloch CM by evaluating Eq. (C8), and from there obtain the parent Hamiltonian via Eq. (C10).

a. CM of unit cell

The Majorana CM $\Gamma_{Q_\mathbf{x}}$ in Eq. (C8) refers to the fiducial state of a unit cell, not that of a single site. We therefore need to compute $\Gamma_{Q_\mathbf{x}}$ from the fiducial states for each individual sublattice given in Eq. (H1). This is done by contracting the four virtual bonds within one unit cell. In the language of fiducial states, we project the tensor product $|Q^{[1]}\rangle \otimes |Q^{[2]}\rangle \otimes |Q^{[3]}\rangle \otimes |Q^{[4]}\rangle$ of the fiducial states for a unit cell on the product of the maximally entangled states of the four virtual bonds connecting the lattice sites within this unit cell. This is analogous to the computation leading to Eq. (E13), and we refer the reader to Appendix E 2 a for details. Here, we will only state the result for the Majorana CM $\Gamma_{Q_\mathbf{x}}$.

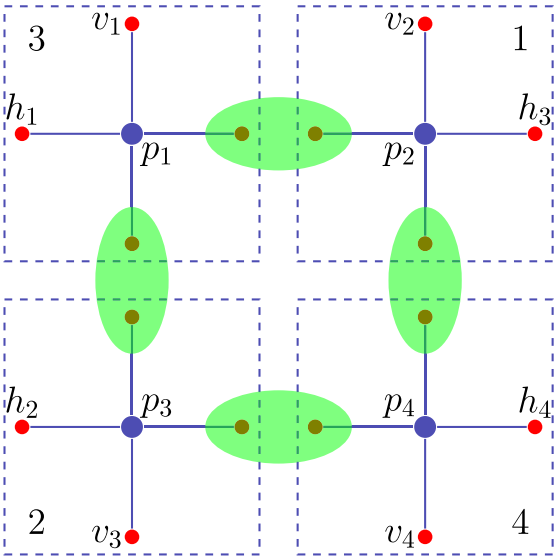

FIG. 10. Unit cell of the quadrupole model pumping PEPS after projection of the virtual fermions corresponding to the bonds within the unit cell (marked by green ellipses) onto maximally entangled states. This results in a fiducial state with four physical fermions (blue circles) collected into the block p, four horizontal virtual fermions in the block v_h, and four virtual fermions in the block v_v (red circles for both). The order of the individual fermions within these blocks is indicated by the labels next to each circle.

The fiducial state of one unit cell, after contraction of the virtual bonds within the plaquette, describes four physical fermions and two virtual fermions per direction left, up, right, down (see Fig. 10). We collect the four physical, horizontal virtual and vertical virtual fermions into blocks labeled p, v_h, and v_v. The order of the individual fermions within these blocks is indicated in Fig. 10. Since the Majorana CM $\Gamma_{Q_\mathbf{x}}$ of the fiducial state of a unit cell is antisymmetric (see Appendix A 1), we can then separate it into 8×8 blocks as

$$\Gamma_{Q_\mathbf{x}} = \begin{pmatrix} \mathbf{A}_p & \mathbf{B}_{pv_h} & \mathbf{B}_{pv_v} \\ -\mathbf{B}_{pv_h}^T & \mathbf{D}_{v_h} & \mathbf{B}_{v_h v_v} \\ -\mathbf{B}_{pv_v}^T & -\mathbf{B}_{v_h v_v}^T & \mathbf{D}_{v_v} \end{pmatrix}. \tag{H3}$$

The blocks $\mathbf{A}_p$, $\mathbf{D}_{v_h}$, and $\mathbf{D}_{v_v}$ describe the reduced fiducial state of the physical, horizontal virtual and vertical virtual subsystem, respectively. The off-diagonal blocks describe the coupling between these three subsystems. Equation (H3) is a generalization of Eq. (C6) with

$$\mathbf{A} = \mathbf{A}_p, \tag{H4a}$$

$$\mathbf{B} = \left(\mathbf{B}_{pv_h}\, \mathbf{B}_{pv_v}\right), \tag{H4b}$$

$$\mathbf{D} = \begin{pmatrix} \mathbf{D}_{v_h} & \mathbf{B}_{v_h v_v} \\ -\mathbf{B}_{v_h v_v}^T & \mathbf{D}_{v_v} \end{pmatrix} \tag{H4c}$$

which we find useful since we want to treat horizontal and vertical virtual fermions separately.

We are now ready to give the expression for the Majorana CM $\Gamma_{Q_\mathbf{x}}$ of the fiducial state of a unit cell. For simplicity, we set $\alpha_x = \alpha_y \equiv \alpha$ and $\beta_x = \beta_y \equiv \beta$ from now on, corresponding to parameters $a_x = a_y \equiv a$ and $b_x = b_y \equiv b$ in Eq. (H2). The diagonal blocks $\mathbf{A}_p$, $\mathbf{D}_{v_h}$, and $\mathbf{D}_{v_v}$ of $\Gamma_{Q_\mathbf{x}}$ take the form

$$Z^{(2)}(r,s,u) = \begin{pmatrix} 0 & -r & 0 & -u & 0 & -s & 0 & 0 \\ r & 0 & -u & 0 & -s & 0 & 0 & 0 \\ 0 & u^* & 0 & -r & 0 & 0 & 0 & -s \\ u^* & 0 & r & 0 & 0 & 0 & -s & 0 \\ 0 & s^* & 0 & 0 & 0 & -r & 0 & u \\ s^* & 0 & 0 & 0 & r & 0 & u & 0 \\ 0 & 0 & 0 & s^* & 0 & -u^* & 0 & -r \\ 0 & 0 & s^* & 0 & -u^* & 0 & r & 0 \end{pmatrix} \tag{H5}$$

with parameters $r \in \mathbb{R}$ and $s, u \in \mathbb{C}$. Specifically,

$$\mathbf{A}_p = Z^{(2)}(r_p, -s_p, s_p), \tag{H6a}$$

$$\mathbf{D}_{v_h} = Z^{(2)}(r_v, s_v, s_v), \tag{H6b}$$

$$\mathbf{D}_{v_v} = Z^{(2)}(r_v, -s_v, s_v) \tag{H6c}$$

with parameters

$$r_p = -\frac{\sqrt{2}(2a^4 + b^4 - 1)}{4a^2 + 2\sqrt{2}a^4 + \sqrt{2}(1+b^4)}, \tag{H7a}$$

$$s_p = \frac{2b^2}{4a^2 + 2\sqrt{2}a^4 + \sqrt{2}(1+b^4)}, \tag{H7b}$$

$$r_v = \frac{2a^2 + \sqrt{2}(b^4+1)}{4a^2 + 2\sqrt{2}a^4 + \sqrt{2}(1+b^4)}, \tag{H7c}$$

$$s_v = \frac{\sqrt{2}a^2b^2}{4a^2 + 2\sqrt{2}a^4 + \sqrt{2}(1+b^4)}, \tag{H7d}$$

where the denominator stems from the matrix inversion in the Schur complements used to evaluate the projection on the virtual bonds within one unit cell. The off-diagonal blocks of $\Gamma_{Q_\mathbf{x}}$ are

$$\mathbf{B}_{v_h v_v} = \begin{pmatrix} 0 & 1-r_v & 0 & s_v & 0 & -s_v & 0 & 0 \\ r_v - 1 & 0 & s_v & 0 & -s_v & 0 & 0 & 0 \\ 0 & s_v & 0 & 0 & 0 & 1-r_v & 0 & -s_v \\ s_v & 0 & 0 & 0 & r_v - 1 & 0 & -s_v & 0 \\ 0 & s_v & 0 & r_v - 1 & 0 & 0 & 0 & s_v \\ s_v & 0 & 1-r_v & 0 & 0 & 0 & s_v & 0 \\ 0 & 0 & 0 & s & 0 & s_v & 0 & 1-r_v \\ 0 & 0 & s_v & 0 & s_v & 0 & r_v - 1 & 0 \end{pmatrix}, \tag{H8a}$$

$$\mathbf{B}_{pv_h} = \frac{a}{2^{1/4}} \begin{pmatrix} 0 & r_p+1 & 0 & -s_p & 0 & -s_p & 0 & 0 \\ r_p+1 & 0 & s_p & 0 & s_p & 0 & 0 & 0 \\ 0 & s_p & 0 & 0 & 0 & r_p+1 & 0 & s_p \\ -s_p & 0 & 0 & 0 & r_p+1 & 0 & -s_p & 0 \\ 0 & -s_p & 0 & -r_p-1 & 0 & 0 & 0 & s_p \\ s_p & 0 & -r_p-1 & 0 & 0 & 0 & -s_p & 0 \\ 0 & 0 & 0 & s_p & 0 & -s_p & 0 & r_p+1 \\ 0 & 0 & -s_p & 0 & s_p & 0 & r_p+1 & 0 \end{pmatrix}, \tag{H8b}$$

$$\mathbf{B}_{pv_v} = \frac{a}{2^{1/4}} \begin{pmatrix} 0 & r_p+1 & 0 & s_p & 0 & -s_p & 0 & 0 \\ r_p+1 & 0 & -s_p & 0 & s_p & 0 & 0 & 0 \\ 0 & s_p & 0 & -r_p-1 & 0 & 0 & 0 & s_p \\ -s_p & 0 & -r_p-1 & 0 & 0 & 0 & -s_p & 0 \\ 0 & -s_p & 0 & 0 & 0 & -r_p-1 & 0 & s_p \\ s_p & 0 & 0 & 0 & -r_p-1 & 0 & -s_p & 0 \\ 0 & 0 & 0 & s_p & 0 & s_p & 0 & r_p+1 \\ 0 & 0 & -s_p & 0 & -s_p & 0 & r_p+1 & 0 \end{pmatrix}. \tag{H8c}$$

b. Bloch CM

We can now compute the Bloch CM $\tilde{\Gamma}_{|\psi\rangle}(\mathbf{k})$ of the physical state on a torus by evaluating Eq. (C8). Here, the Majorana CM of the local fiducial state of the unit cell with its blocks **A**, **B**, and **D** is given in the previous subsection.

In the same basis as **D**, the Bloch CM $\tilde{\Gamma}_{\omega}(\mathbf{k})$ of the total virtual maximally entangled state of size 16×16 is

$$\tilde{\Gamma}_{\omega}(\mathbf{k}) = \begin{pmatrix} \tilde{\Gamma}_{\omega,v_h}(\mathbf{k}) & 0 \\ 0 & \tilde{\Gamma}_{\omega,v_v}(\mathbf{k}) \end{pmatrix}, \tag{H9a}$$

where the blocks $\tilde{\Gamma}_{\omega,v_h}(\mathbf{k})$ and $\tilde{\Gamma}_{\omega,v_v}(\mathbf{k})$ refer to the horizontal and vertical virtual fermions, respectively. Since the horizontal fermions on the sublattice 1 couple only to the horizontal fermions on sublattice 3 (and similarly for 2 and 4), the CM $\tilde{\Gamma}_{\omega,v_h}(\mathbf{k})$ is given by a sum of two copies of the CM from Eq. (C7) for an MPS with $\xi = 1$. Hence,

$$\tilde{\Gamma}_{\omega,v_h}(\mathbf{k}) = \begin{pmatrix} 0 & 0 & -\sigma_1 e^{-ik_x} & 0 \\ 0 & 0 & 0 & -\sigma_1 e^{-ik_x} \\ \sigma_1 e^{ik_x} & 0 & 0 & 0 \\ 0 & \sigma_1 e^{ik_x} & 0 & 0 \end{pmatrix}. \tag{H9b}$$

The expression for $\tilde{\Gamma}_{\omega,v_v}(\mathbf{k})$ is analogous with $k_x \to -k_y$ (where the negative sign indicates that the bonds are oriented from top to bottom and hence point in the direction of negative y). Note that $\tilde{\Gamma}_{\omega,v_h}(\mathbf{k}) = Z^{(2)}(0, e^{-ik_x}, 0)$ and $\tilde{\Gamma}_{\omega,v_v}(\mathbf{k}) = Z^{(2)}(0, e^{ik_y}, 0)$ are of the form of Eq. (H5).

For the quadrupole model pumping PEPS, the evaluation of Eq. (C8) requires the inversion of the matrix $\mathbf{D} + \tilde{\Gamma}_{\omega}(\mathbf{k})$ of size 16×16. This can be done analytically using the special representation from Eq. (H5). Indeed, one can show that the matrix $Z^{(2)}$ has the properties

$$Z^{(2)}(r, s, u) + Z^{(2)}(r', s', u') = Z^{(2)}(r + r', s + s', u + u'), \tag{H10a}$$

$$\det[Z^{(2)}(r, s, u)] = (r^2 + ss^* + uu^*)^4, \tag{H10b}$$

$$[Z^{(2)}(r, s, u)]^{-1} = -\frac{Z^{(2)}(r, s, u)}{[\det Z^{(2)}(r, s, u)]^{1/4}}. \tag{H10c}$$

Moreover, conjugation with the matrix $\mathbf{B}_{v_h v_v}$ from Eq. (H8a), which gives the off-diagonal block of **D**, returns a matrix of the form of Eq. (H5),

$$\mathbf{B}_{v_h v_v} Z^{(2)}(r, s, u) \mathbf{B}^T_{v_h v_v} = Z^{(2)}(r', s', u'), \tag{H11}$$

where $r' = r[(1 - r_v)^2 - 2s_v^2] + 2(1 - r_v)s_v \mathrm{Re}(s - u)$, $s' = -s(1 - r_v)^2 + 2rs_v(r_v - 1) - 2s_v^2[\mathrm{Re}(u) + i\mathrm{Im}(s)]$, and $u' = u(1-r_v)^2 + 2rs_v(r_v-1) + 2s_v^2[\mathrm{Re}(s) + i\mathrm{Im}(u)]$. Using these identities, the inverse of $\mathbf{D} + \tilde{\Gamma}_{\omega}(\mathbf{k})$ can be evaluated blockwise, and we compute the determinant in Eq. (C9) as

$$q(\mathbf{k}) = \frac{2^8(1 + a^4 + b^4 + a^2b^2 \cos k_x + a^2b^2 \cos k_y)^4}{(1 + 2\sqrt{2}a^2 + 2a^4 + b^4)^4}. \tag{H12}$$

This is strictly positive unless $\gamma = 0$ and $|\alpha| = |\beta|$, such that the PEPS is well defined everywhere except for these parameter values.

Proceeding thus, we find that the Bloch Majorana CM $\tilde{\Gamma}_{|\psi\rangle}(\mathbf{k})$ of the physical state is also of the form of Eq. (H5),

$$\tilde{\Gamma}_{|\psi\rangle} = Z^{(2)}(r(\mathbf{k}), s(\mathbf{k}), u(\mathbf{k})), \tag{H13a}$$

where the parameters are

$$r(\mathbf{k}) = \frac{1 - a^4 - b^4 - a^2b^2 \cos k_x - a^2b^2 \cos k_y}{1 + a^4 + b^4 + a^2b^2 \cos k_x + a^2b^2 \cos k_y}, \tag{H13b}$$

$$s(\mathbf{k}) = \frac{-\sqrt{2}(b^2 + a^2 e^{-ik_x})}{1 + a^4 + b^4 + a^2b^2 \cos k_x + a^2b^2 \cos k_y}, \tag{H13c}$$

$$u(\mathbf{k}) = \frac{\sqrt{2}(b^2 + a^2 e^{ik_y})}{1 + a^4 + b^4 + a^2b^2 \cos k_x + a^2b^2 \cos k_y}. \tag{H13d}$$

In the denominator, we recognize the fourth root $q(\mathbf{k})^{1/4}$ coming from the matrix inversion according to Eq. (H10c).

c. Parent Hamiltonian

We are now in a position to find a parent Hamiltonian for the physical state on a torus, using Eq. (C10) and the result for the Bloch Majorana CM $\tilde{\Gamma}_{|\psi\rangle}$ from Eq. (H13). To

get an intuitive understanding of the Hamiltonian, we find it useful to express it in terms of the original fermionic modes before the particle-hole transformation of Eq. (28). Their FT is related to the FT of the new modes as $\hat{a}_{\tau,\mathbf{k}} = a_{\tau,\mathbf{k}}$ for $\tau = 1, 2$ and $\hat{a}_{\tau,\mathbf{k}} = a^{\dagger}_{\tau,-\mathbf{k}}$ for $\tau = 3, 4$. With respect to the original fermionic modes, Eq. (C10) is given by

$$H_{\epsilon} = \sum_{\mathbf{k}} \epsilon(\mathbf{k}) \times \hat{a}^{\dagger}_{\tau,\mathbf{k}} \begin{pmatrix} r(\mathbf{k}) & 0 & -s(\mathbf{k})^* & u(\mathbf{k}) \\ 0 & r(\mathbf{k}) & -u(\mathbf{k})^* & -s(\mathbf{k}) \\ -s(\mathbf{k}) & -u(\mathbf{k}) & -r(\mathbf{k}) & 0 \\ u(\mathbf{k})^* & -s(\mathbf{k})^* & 0 & -r(\mathbf{k}) \end{pmatrix}_{\tau\tau'} \hat{a}_{\tau',\mathbf{k}}, \tag{H14}$$

where a summation over τ, τ' is implied in the second line.

As discussed in Appendix H 2 c, the properties of the parent Hamiltonian are determined by our choice of dispersion relation $\epsilon(\mathbf{k})$. By setting $\epsilon(\mathbf{k}) = q(\mathbf{k})$, we would obtain a gapped parent Hamiltonian with coupling between up to fourth-nearest-neighbor unit cells. However, we can find a more short-ranged parent Hamiltonian due to the special form of the fiducial state CM using Eq. (H5). Indeed, by choosing the dispersion function

$$\epsilon(\mathbf{k}) = \frac{1 + a^4 + b^4 + a^2 b^2 \cos k_x + a^2 b^2 \cos k_y}{a^4 + b^4 + 1} \tag{H15}$$

which is proportional to the denominator of r, s, and u from Eq. (H13), we obtain a second-nearest-neighbor parent Hamiltonian with Bloch representation

$$\begin{aligned} H_{\epsilon}(\mathbf{k}) = \frac{1}{a^4 + b^4 + 1} & \\ \times [(1 - a^4 - b^4 - a^2 b^2 \cos k_x - a^2 b^2 \cos k_y)\sigma_3 \otimes \sigma_0 & \\ + \sqrt{2}(b^2 + a^2 \cos k_x)\sigma_1 \otimes \sigma_0 & \\ + \sqrt{2} a^2 \sin k_x (-\sigma_2 \otimes \sigma_3) & \\ + \sqrt{2}(b^2 + a^2 \cos k_y)(-\sigma_2 \otimes \sigma_2) & \\ + \sqrt{2} a^2 \sin k_y (-\sigma_2 \otimes \sigma_1)], & \end{aligned} \tag{H16}$$

where σ_0 is the identity matrix of dimension two.

3. ES in topological quadrupole phase

When $b = 0$, the system described by the PEPS of Eq. (H2) splits into decoupled four-site plaquettes shifted from the unit cell by one site in both directions, corresponding to the OAI dimerized phase of the quadrupole model if $a = 1$. The Majorana CM $\Gamma_{\text{Plaquette}}$ describing the physical state of one such decoupled plaquette takes the form of Eq. (H5) with

$$r = \frac{1 - a^4}{1 + a^4}, \tag{H17a}$$

$$u = s = -\frac{\sqrt{2} a^2}{1 + a^4}. \tag{H17b}$$

As an application, we will derive the ES contributions from the edges and corners given in Eqs. (34a) and (34b), respectively.

We begin with the four corners. The Majorana CM $\Gamma_{\text{corner},\tau}$ for a single corner site on the sublattice τ is given by the corresponding block of dimension 2 on the diagonal of $\Gamma_{\text{Plaquette}}$. Specifically,

$$\Gamma_{\text{corner},\tau} = \begin{pmatrix} 0 & -r \\ r & 0 \end{pmatrix} \tag{H18}$$

for $\tau = 1, 2, 3, 4$. We now transform $\Gamma_{\text{corner},\tau}$ to the basis of the original complex fermionic modes before the particle-hole transformation of Eq. (28). Then, the CM of the corner site has a vanishing off-diagonal block $\hat{Q}^*_{\text{corner},\tau} = 0$ and a diagonal block $\hat{R}^*_{\text{corner},\tau} = \mp \frac{i}{2} \lambda_{\text{corner}}$ with $\lambda_{\text{corner}} = r$, where the negative and positive signs hold for the sublattices $\tau = 1, 2$ and $\tau = 3, 4$, respectively. Using the expression for r from Eq. (H17a) and $a = \alpha/\gamma$, we obtain the formula for the corner ES level given in Eq. (34b) with one level per corner.

Similarly, the Majorana CM $\Gamma_{\text{edge},\tau_1,\tau_2}$ for two decoupled edge sites on the sublattices τ_1 and τ_2 is given by a block of dimension 4 of $\Gamma_{\text{Plaquette}}$. Concretely,

$$\Gamma_{\text{edge},\tau_1\tau_2} = \begin{pmatrix} 0 & -r & 0 & -s \\ r & 0 & -s & 0 \\ 0 & s & 0 & -r \\ s & 0 & r & 0 \end{pmatrix} \tag{H19}$$

for $(\tau_1, \tau_2) \in \{(3, 1), (4, 2), (4, 1), (2, 3)\}$. In the basis of the original complex fermionic modes before the particle-hole transformation of Eq. (28), $\Gamma_{\text{edge},\tau_1,\tau_2}$ takes the following form: it has a vanishing off-diagonal block $\hat{Q}^*_{\text{edge},\tau_1\tau_2} = 0$ and a nonzero diagonal block $\hat{R}^*_{\text{edge},\tau_1\tau_2}$ with doubly degenerate eigenvalues $\pm \frac{i}{2} \lambda_{\text{edge}}$ and

$$\lambda_{\text{edge}} = \sqrt{r^2 + s^2} = \frac{\sqrt{1 + a^8}}{1 + a^4}. \tag{H20}$$

This corresponds to the formula given in Eq. (34a).

[1] W. A. Benalcazar, B. A. Bernevig, and T. L. Hughes, Science **357**, 61 (2017).

[2] F. Schindler, A. M. Cook, M. G. Vergniory, Z. Wang, S. S. Parkin, B. A. Bernevig, and T. Neupert, Sci. Adv. **4**, eaat0346 (2018).

[3] W. A. Benalcazar, B. A. Bernevig, and T. L. Hughes, Phys. Rev. B **96**, 245115 (2017).

[4] J. Langbehn, Y. Peng, L. Trifunovic, F. von Oppen, and P. W. Brouwer, Phys. Rev. Lett. **119**, 246401 (2017).

[5] M. Z. Hasan and C. L. Kane, Rev. Mod. Phys. **82**, 3045 (2010).

[6] F. D. M. Haldane, Phys. Rev. Lett. **61**, 2015 (1988).

[7] B. Bradlyn, L. Elcoro, J. Cano, M. Vergniory, Z. Wang, C. Felser, M. Aroyo, and B. A. Bernevig, Nature (London) **547**, 298 (2017).

[8] B. J. Wieder and B. A. Bernevig, arXiv:1810.02373.

[9] W. P. Su, J. R. Schrieffer, and A. J. Heeger, Phys. Rev. B **22**, 2099 (1980).

[10] F. Schindler, Z. Wang, M. G. Vergniory, A. M. Cook, A. Murani, S. Sengupta, A. Y. Kasumov, R. Deblock, S. Jeon, I. Drozdov, H. Bouchiat, S. Guéron, A. Yazdani, B. A. Bernevig, and T. Neupert, Nat. Phys. **14**, 918 (2018).

[11] M. Serra-Garcia, V. Peri, R. Süsstrunk, O. R. Bilal, T. Larsen, L. G. Villanueva, and S. D. Huber, Nature (London) **555**, 342 (2018).

[12] H. Xue, Y. Yang, F. Gao, Y. Chong, and B. Zhang, Nat. Mater. **18**, 108 (2019).

[13] X. Ni, M. Weiner, A. Alù, and A. B. Khanikaev, Nat. Mater. **18**, 113 (2019).

[14] S. Mittal, V. V. Orre, G. Zhu, M. A. Gorlach, A. Poddubny, and M. Hafezi, Nat. Photonics **13**, 692 (2019).

[15] A. E. Hassan, F. K. Kunst, A. Moritz, G. Andler, E. J. Bergholtz, and M. Bourennane, Nat. Photonics **13**, 697 (2019).

[16] B.-Y. Xie, G.-X. Su, H.-F. Wang, H. Su, X.-P. Shen, P. Zhan, M.-H. Lu, Z.-L. Wang, and Y.-F. Chen, Phys. Rev. Lett. **122**, 233903 (2019).

[17] Y. Yang, Z. Jia, Y. Wu, R.-C. Xiao, Z. H. Hang, H. Jiang, and X. C. Xie, Sci. Bulletin (2020), doi:10.1016/j.scib.2020.01.024.

[18] C. W. Peterson, W. A. Benalcazar, T. L. Hughes, and G. Bahl, Nature (London) **555**, 346 (2018).

[19] S. Imhof, C. Berger, F. Bayer, J. Brehm, L. W. Molenkamp, T. Kiessling, F. Schindler, C. H. Lee, M. Greiter, T. Neupert, and R. Thomale, Nat. Phys. **14**, 925 (2018).

[20] M. Serra-Garcia, R. Süsstrunk, and S. D. Huber, Phys. Rev. B **99**, 020304(R) (2019).

[21] B. A. Bernevig and T. L. Hughes, *Topological Insulators and Topological Superconductors* (Princeton University Press, Princeton, 2013).

[22] L. Fidkowski, Phys. Rev. Lett. **104**, 130502 (2010).

[23] H. Li and F. D. M. Haldane, Phys. Rev. Lett. **101**, 010504 (2008).

[24] Q. Wang, D. Wang, and Q.-H. Wang, Europhys. Lett. **124**, 50005 (2018).

[25] P. Zhu, K. Loehr, and T. L. Hughes, arXiv:1910.10180.

[26] R. Takahashi, Y. Tanaka, and S. Murakami, Phys. Rev. Research **2**, 013300 (2020).

[27] J. I. Cirac and F. Verstraete, J. Phys. A: Math. Theor. **42**, 504004 (2009).

[28] J. I. Cirac, D. Poilblanc, N. Schuch, and F. Verstraete, Phys. Rev. B **83**, 245134 (2011).

[29] M. B. Hastings, Phys. Rev. B **73**, 085115 (2006).

[30] M. M. Wolf, F. Verstraete, M. B. Hastings, and J. I. Cirac, Phys. Rev. Lett. **100**, 070502 (2008).

[31] N. Schuch, D. Pérez-García, and I. Cirac, Phys. Rev. B **84**, 165139 (2011).

[32] N. Schuch, I. Cirac, and D. Pérez-García, Ann. Phys. **325**, 2153 (2010).

[33] C. V. Kraus, N. Schuch, F. Verstraete, and J. I. Cirac, Phys. Rev. A **81**, 052338 (2010).

[34] S. Yang, T. B. Wahl, H.-H. Tu, N. Schuch, and J. I. Cirac, Phys. Rev. Lett. **114**, 106803 (2015).

[35] A. Kitaev, Ann. Phys. **303**, 2 (2003).

[36] M. A. Levin and X.-G. Wen, Phys. Rev. B **71**, 045110 (2005).

[37] F. Verstraete and J. I. Cirac, arXiv:cond-mat/0407066.

[38] F. Verstraete, M. M. Wolf, D. Perez-Garcia, and J. I. Cirac, Phys. Rev. Lett. **96**, 220601 (2006).

[39] Z.-C. Gu, M. Levin, B. Swingle, and X.-G. Wen, Phys. Rev. B **79**, 085118 (2009).

[40] T. B. Wahl, H.-H. Tu, N. Schuch, and J. I. Cirac, Phys. Rev. Lett. **111**, 236805 (2013).

[41] J. Dubail and N. Read, Phys. Rev. B **92**, 205307 (2015).

[42] N. Read, Phys. Rev. B **95**, 115309 (2017).

[43] M. P. Zaletel and R. S. K. Mong, Phys. Rev. B **86**, 245305 (2012).

[44] D. J. Thouless, Phys. Rev. B **27**, 6083 (1983).

[45] A. J. Károly, *A Short Course on Topological Insulators: Band-structure Topology and Edge States in One and Two Dimensions* (Springer, Berlin, 2016).

[46] M. Fannes, B. Nachtergaele, and R. F. Werner, Commun. Math. Phys. **144**, 443 (1992).

[47] T. B. Wahl, S. T. Haßler, H.-H. Tu, J. I. Cirac, and N. Schuch, Phys. Rev. B **90**, 115133 (2014).

[48] A. Deitmar and S. Echterhoff, *Principles of Harmonic Analysis* (Springer, Berlin, 2014).

[49] N. Bultinck, D. J. Williamson, J. Haegeman, and F. Verstraete, Phys. Rev. B **95**, 075108 (2017).

[50] D. Pérez-García, M. M. Wolf, M. Sanz, F. Verstraete, and J. I. Cirac, Phys. Rev. Lett. **100**, 167202 (2008).

[51] S. Bravyi, Quantum Inf. Comput. **5**, 216 (2005).

[52] I. Peschel, J. Phys. A: Math. Gen. **36**, L205 (2003).

[53] N. Schuch and B. Bauer, Phys. Rev. B **100**, 245121 (2019).

[54] D. Perez-Garcia, F. Verstraete, M. M. Wolf, and J. I. Cirac, Quantum Inf. Comput. **7**, 401 (2007).

[55] M. T. Fishman and S. R. White, Phys. Rev. B **92**, 075132 (2015).

[56] B. J. Wieder, Z. Wang, J. Cano, X. Dai, L. M. Schoop, B. Bradlyn, and B. A. Bernevig, Strong and "fragile" topological dirac semimetals with higher-order fermi arcs, Nat. Commun. **11**, 627 (2020).

[57] N. Bultinck, D. J. Williamson, J. Haegeman, and F. Verstraete, J. Phys. A: Math. Theor. **51**, 025202 (2017).

[58] Y. Zhang, T. Grover, and A. Vishwanath, Phys. Rev. B **84**, 075128 (2011).

[59] Y. Zhang and A. Vishwanath, Phys. Rev. B **87**, 161113(R) (2013).

[60] S. A. Parameswaran, R. Roy, and S. L. Sondhi, C. R. Phys. **14**, 816 (2013), topological insulators / Isolants topologiques.

[61] Y.-H. Wu, L. Wang, and H.-H. Tu, arXiv:1910.11011.

[62] I. Peschel and V. Eisler, J. Phys. A: Math. Theor. **42**, 504003 (2009).

[63] A. Kitaev, Ann. Phys. **321**, 2 (2006).

[64] A. Botero and B. Reznik, Phys. Rev. A **67**, 052311 (2003).

[65] G. Giedke and J. Ignacio Cirac, Phys. Rev. A **66**, 032316 (2002).

[66] J. Eisert, S. Scheel, and M. B. Plenio, Phys. Rev. Lett. **89**, 137903 (2002).

[67] J. Fiurášek, Phys. Rev. Lett. **89**, 137904 (2002).

[68] E. Zohar, M. Burrello, T. B. Wahl, and J. I. Cirac, Ann. Phys. **363**, 385 (2015).

[69] A. Alexandradinata, T. L. Hughes, and B. A. Bernevig, Phys. Rev. B **84**, 195103 (2011).

5.3 Fractional chiral hinge insulator

This section contains a reprint of the following publication:

- Anna Hackenbroich, Ana Hudomal, Norbert Schuch, B. Andrei Bernevig, and Nicolas Regnault. "Fractional Chiral Hinge Insulator". In: *arXiv e-prints* (Oct. 2020). arXiv: 2010.09728 [cond-mat.str-el]

In this publication, we study a model wave function for a strongly correlated 3D HOTI with chiral hinge states. This wave function is obtained from Gutzwiller projection of two copies of the ground state of the chiral hinge insulator discussed in Sec. 2.5.3 with different spin orientations. This is analogous to the construction of the ground state of the FCI discussed in Sec. 3.5 for the case of an infinitely strong on-site repulsion U between electrons with different spin.

We analyze this model wave function using large-scale variational Monte Carlo simulations. Analogous to the fractional quantum Hall edge modes discussed in Sec. 3.3.4, the chiral hinge modes are described by chiral Luttinger liquids. From the logarithmic scaling of the EE, we extract the central charge of the Luttinger CFT as discussed Sec. 4.1.2. A similar scaling analysis of the spin fluctuations allows us to extract the Luttinger parameter K. We are thus able to show that the chiral hinge modes are of the same nature as the edge modes of the Laughlin state at filling $\nu = 1/2$ discussed in Chapter 3.

We also study the bulk properties of the model wave function, in particular its topological degeneracy and TEE. To that end, we employ a Kitaev-Preskill subtraction scheme as discussed in Sec. 4.1.2. While the TEE in the bulk vanishes for the model wave function, we show that the gapped surfaces host a 2D topologically non-trivial theory whose TEE cannot be explained using topological quantum field theory.

Fractional Chiral Hinge Insulator

Anna Hackenbroich,[1,2] Ana Hudomal,[3,4] Norbert Schuch,[1,2,5,6] B. Andrei Bernevig,[7] and Nicolas Regnault[7,8]

[1] *Max-Planck-Institute of Quantum Optics, Hans-Kopfermann-Straße 1, 85748 Garching, Germany*
[2] *Munich Center for Quantum Science and Technology, Schellingstraße 4, 80799 München, Germany*
[3] *Institute of Physics Belgrade, University of Belgrade, 11080 Belgrade, Serbia*
[4] *School of Physics and Astronomy, University of Leeds, Leeds, LS2 9JT, United Kingdom*
[5] *University of Vienna, Department of Physics, Boltzmanngasse 5, 1090 Wien, Austria*
[6] *University of Vienna, Department of Mathematics, Oskar-Morgenstern-Platz 1, 1090 Wien, Austria*
[7] *Joseph Henry Laboratories and Department of Physics, Princeton University, Princeton, New Jersey 08544, USA*
[8] *Laboratoire de Physique de l'Ecole normale supérieure, ENS, Université PSL, CNRS, Sorbonne Université, Université Paris-Diderot, Sorbonne Paris Cité, Paris, France*

arXiv:2010.09728v1 [cond-mat.str-el] 19 Oct 2020

We propose and study a wave function describing an interacting three-dimensional fractional chiral hinge insulator (FCHI) constructed by Gutzwiller projection of two non-interacting second order topological insulators with chiral hinge modes at half filling. We use large-scale variational Monte Carlo computations to characterize the model states via the entanglement entropy and charge-spin-fluctuations. We show that the FCHI possesses fractional chiral hinge modes characterized by a central charge $c = 1$ and Luttinger parameter $K = 1/2$, like the edge modes of a Laughlin 1/2 state. By changing the boundary conditions for the underlying fermions, we investigate the topological degeneracy of the FCHI. Within the range of the numerically accessible system sizes, we observe a non-trivial topological degeneracy. A more numerically pristine characterization of the bulk topology is provided by the topological entanglement entropy (TEE) correction to the area law. While our computations indicate a vanishing bulk TEE, we show that the gapped surfaces host a two-dimensional topological order with a TEE per surface compatible with half that of a Laughlin 1/2 state, a value that cannot be obtained from topological quantum field theory.

I. INTRODUCTION

Strong interactions in condensed matter systems can lead to fascinating emergent phenomena. In two-dimensional (2D) systems, strong interactions may lead to the emergence of topological order (TO), such as experimentally observed in the fractional quantum Hall effect. Features of TO in 2D include a non-trivial ground state degeneracy on certain surfaces and the appearance of itinerant excitations with fractional quantum numbers and braiding statistics. It has long been an active field of study to extend this rich physics to three-dimensional (3D) strongly interacting systems, where the emergent physics can be even more diverse, including systems with fractonic excitations [1, 2]. Whereas many microscopic models based on interacting spin systems have been proposed to exhibit TO in 3D, such as the 3D toric code [3] and 3D Kitaev models [4–7], there is a scarcity of electronic or realistic examples that could be experimentally relevant.

Among the 3D electronic topological insulators (TIs), an entirely new class has recently been discovered: certain TIs protected by crystalline symmetries, now dubbed higher order TIs [8–23], possess a much richer bulk-boundary correspondence than conventional, or first order, TIs. For example, there exists a 3D chiral hinge insulator (CHI), whose gapped surfaces are connected by gapless chiral hinge modes [10]. Higher order TIs in two and three dimensions have been experimentally observed in either materials [24], mechanical [25], acoustic [26, 27], photonic [28–31] or electrical [32–34] systems.

In this letter, we provide a first stepping stone in the realization of a full-fledged electronic 3D fractional TI by building a 3D fractional chiral hinge insulator (FCHI) model wave function. Indeed, the hinge modes of the non-interacting CHI are of the same nature as the edge modes of a Chern insulator, two copies of which at fractional filling and with strong interactions form a fractional Chern insulator (FCI) hosting fractional quantum Hall physics [35–37]. Therefore, we may speculate that under similar conditions the FCHI will also display non-trivial topology with fractionalized excitations at least at the hinges or surfaces. The FCHI could also represent another lane between higher order TI and fractonic systems [38].

Numerical computations and especially exact diagonalizations for interacting electronic systems in 3D are notoriously difficult due to the spatial dimensionality. To partially circumvent this challenge, we will rely on a model wave function, a fruitful approach for TO, to capture the FCHI. This approach has been extensively applied in the realm of the fractional quantum Hall effect [39, 40] and FCIs [41]. In order to define the FCHI wave function, we will make use of Gutzwiller projection, a systematic method to construct interacting model wave functions starting from copies of non-interacting ground states. Large-scale variational Monte Carlo (MC) simulations then allow us to analyze this wave function for bigger system sizes than possible with other methods.

To probe the topological content of the wave function, we will study the entanglement entropy (EE), which can

be evaluated in MC simulations [41–43], and follows an area law with characteristic subleading corrections [44]. In two dimensions there are logarithmic corrections for gapless edge modes [45–47] which along with the constant topological entanglement entropy (TEE) correction to the bulk area law [48, 49] provide information on the system's topology. In three dimensions, corrections to the bulk area law include the TEE and possible size-dependent corrections for fractonic systems and layered constructions [50–52]. In particular, we study the hinge modes in an open system and show that they are fractionalized excitations characterized by a central charge $c = 1$ and Luttinger parameter $K = 1/2$, like the FCI edge modes. We then study the linear independence of different interacting wave functions obtained by changing the boundary conditions for the underlying fermions, thus finding a non-trivial topological degeneracy for the numerically accessible system sizes. Finally, we study the TEE of the bulk system, and that of the gapped surfaces. Whereas our computations indicate a vanishing bulk TEE, we show that the gapped surfaces host a non-trivial two-dimensional topological phase with a TEE per surface compatible with half that of a Laughlin 1/2 state.

II. MODEL WAVE FUNCTION

We consider an interacting model wave function obtained by Gutzwiller projection of the ground state of a non-interacting 3D second-order TI with chiral hinge modes. The CHI model is described by a local Hamiltonian for spinless fermions with four sites per unit cell [10] (see Fig. 1 (a) for a sketch of the model). The ground state $|\psi\rangle$ of the CHI model lies at filling $\nu = 1/2$ of the lattice. With open boundary conditions (OBC) in the x and y directions, each of the four hinges of the CHI parallel to the z-axis supports a single chiral mode localized at the hinge. Each hinge mode corresponds to a free bosonic mode with central charge $c = 1$ and Luttinger parameter $K = 1$ akin to the edge modes of a Chern insulator (see App. C). Since the CHI model is non-interacting, it does not have TO or a non-trivial ground state degeneracy with periodic boundary conditions (PBC).

In order to define the interacting model wave function $|\Psi\rangle$, we take two copies $|\psi_s\rangle$ of the ground state of the CHI model at half filling, to which we assign different values $s \in \{\uparrow, \downarrow\}$ of a spin-like degree of freedom. The interacting wave function is obtained as the Gutzwiller projection

$$|\Psi\rangle = P_G \left[|\psi_\uparrow\rangle \otimes |\psi_\downarrow\rangle\right] \tag{1}$$

of the product of the two non-interacting wave functions. With $\hat{n}_{s,i}$ denoting the particle number operator for fermions of spin s on the lattice site i, the Gutzwiller projection operator is expressed as

$$P_G = \prod_i (1 - \hat{n}_{\uparrow,i}\hat{n}_{\downarrow,i}). \tag{2}$$

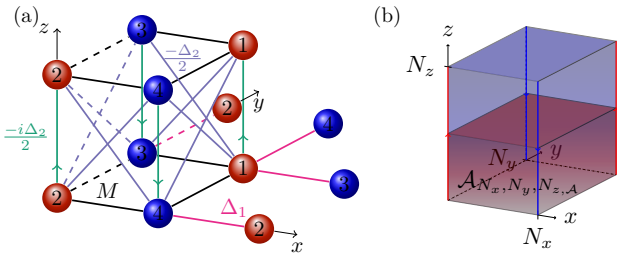

FIG. 1. (a) Local real-space model for a 3D second order TI with chiral hinge states. The Hamiltonian is defined on a cubic lattice with a unit cell of four sites lying in the xy-plane. In this plane, sites in the same unit cell are connected by a nearest-neighbour hopping M marked by black lines ($-M$ for dashed black lines). In the xy-plane, sites in adjacent unit cells are connected by a nearest-neighbour hopping Δ_1 marked by violet lines ($-\Delta_1$ for dashed violet lines). In the z direction, adjacent unit cells are connected by a real next-nearest neighbour hopping $-\Delta_2/2$ marked by light blue lines ($\Delta_2/2$ for dashed light blue lines). In addition, there is a purely imaginary nearest neighbour hopping between adjacent unit cells in the z direction with value $-i\Delta_2/2$ in the direction of the green arrows. We study the model for parameter values $M = \Delta_1 = \Delta_2 = 1$, where the correlation length is close to its minimal value (see App. C). (b) 3D system with OBC and N_x, N_y unit cells in the x, y directions, and periodic boundaries and N_z sites in the z direction. The subsystem $\mathcal{A}_{N_x,N_y,N_{z,\mathcal{A}}}$ consists of N_x, N_y unit cells in the x, y directions and $N_{z,\mathcal{A}}$ unit cells in the z direction.

It forbids simultaneous occupancy of any lattice site i by both a particle with spin $\uparrow$ and spin $\downarrow$. Therefore, it simulates the effect of a very large on-site Hubbard interaction. Since each copy of the ground state of the CHI model has a filling $\nu_{\psi_\uparrow} = \nu_{\psi_\downarrow} = 1/2$, the Gutzwiller projection enforces that the interacting wave function lies at filling $\nu_\Psi = 1/2$ with exactly one particle per lattice site (each lattice site having a spin degree of freedom which can take two values). Hence, charge fluctuations are completely frozen and the only relevant degree of freedom in the interacting wave function is the spin s.

III. CHARACTERIZATION OF HINGE MODES

With OBC in the x and y directions, the interacting model wave function $|\Psi\rangle$ is expected to posses one gapless chiral mode at each of the four hinges parallel to the z-axis, inherited from the hinge modes of the non-interacting CHI. Like the edge modes of chiral topologically ordered phases in two dimensions, we expect the hinge modes of $|\Psi\rangle$ to be described by a chiral conformal field theory (CFT). Moreover, since $|\Psi\rangle$ is interacting, we expect its hinge CFT to be possibly different than the trivial free-boson CFT describing the hinge modes of the non-interacting CHI.

In order to characterize the chiral hinge modes, we adapt the methods that have previously been employed

for 2D chiral phases [46, 47, 53] to the 3D setting: We study the second Renyi entropy $S^{(2)}$ and spin fluctuations of $|\Psi\rangle$, in focusing on the critical contributions stemming from the *physical* hinges. We evaluate these observables for the interacting wave function $|\Psi\rangle$ in large-scale MC simulations using the SWAP-operator technique [54] with sign-problem refinement [55] (see App. A).

We consider the geometry sketched in Fig. 1(b): A total system with $N_x \times N_y \times N_z$ unit cells, OBC in the xy-plane, and PBC in the z direction to ensure that the only gapless excitations are the four hinge states. We consider a series of subsystems $\mathcal{A}_{N_x,N_y,N_{z,\mathcal{A}}}$ with N_x, N_y unit cells in the x, y directions and $N_{z,\mathcal{A}} \in \{1, \ldots, N_z - 1\}$ unit cells in the z direction, marked in red in Fig. 1(b). The $\mathcal{A}_{N_x,N_y,N_{z,\mathcal{A}}}$ bisect each of four physical hinge modes into a part of length $N_{z,\mathcal{A}}$ contained in $\mathcal{A}_{N_x,N_y,N_{z,\mathcal{A}}}$, and the remaining part outside of the subsystem. Hence, we expect that the EE and spin fluctuations *w.r.t.* $\mathcal{A}_{N_x,N_y,N_{z,\mathcal{A}}}$ will contain signatures from the hinges.

Specifically, if the hinge modes are described by a chiral CFT with central charge c, the second Renyi entropy $S^{(2)}$ of $|\Psi\rangle$ *w.r.t.* the $\mathcal{A}_{N_x,N_y,N_{z,\mathcal{A}}}$ for different $N_{z,\mathcal{A}}$ at fixed N_x and N_y is expected to scale as

$$S^{(2)}_{\mathcal{A}_{N_x,N_y,N_{z,\mathcal{A}}}}(N_{z,\mathcal{A}}) = \alpha + 4 \times S^{(2)}_{\text{crit}}(N_{z,\mathcal{A}}; N_z). \quad (3)$$

Here, α is a constant independent of $N_{z,\mathcal{A}}$. It includes the area law contributions from the virtual surfaces at $z = 0, N_{z,\mathcal{A}}$ which scale proportional to $N_x N_y$, and are therefore independent of $N_{z,\mathcal{A}}$ in the thermodynamic limit, and any potential corner contributions. In Eq. (3),

$$S^{(2)}_{\text{crit}}(N_{z,\mathcal{A}}; N_z) = \frac{c}{8} \ln\left[\frac{N_z}{\pi} \sin\left(\frac{\pi N_{z,\mathcal{A}}}{N_z}\right)\right] \quad (4)$$

is the second Renyi entropy of a periodic one-dimensional chiral critical mode with central charge c and total system size N_z restricted to a single interval of length $N_{z,\mathcal{A}}$ [45]. The factor of 4 in Eq. (3) takes into account the four hinge modes, which contribute equally to the EE.

The scaling of the second Renyi entropy of $|\Psi\rangle$ as computed from MC is shown in Fig. 2(a) for two different system sizes $2 \times 2 \times 20$ and $3 \times 2 \times 20$. For computational reasons, we choose N_x and N_y much smaller than N_z (see App. C). Due to the short correlation length of the CHI, equal to one lattice spacing (see App. C), we may expect that the characteristic parameters approach their thermodynamic limit even for small N_x, N_y. The logarithmic scaling from the hinge states is clearly visible, and numerical values for c and α can be extracted by fitting the data to Eq. (3). The numerical value for the central charge is $c = 1.19 \pm 0.07$ for $2 \times 2 \times 20$ and $c = 1.03 \pm 0.14$ for $3 \times 2 \times 20$. This provides strong evidence that the hinge modes of the interacting model wave function $|\Psi\rangle$ are described by a chiral free-boson CFT with central charge $c = 1$.

Free-boson CFTs with $c = 1$ are characterised by their Luttinger parameter K. For such Luttinger liquids, the variance of the U(1) current integrated over a subsystem

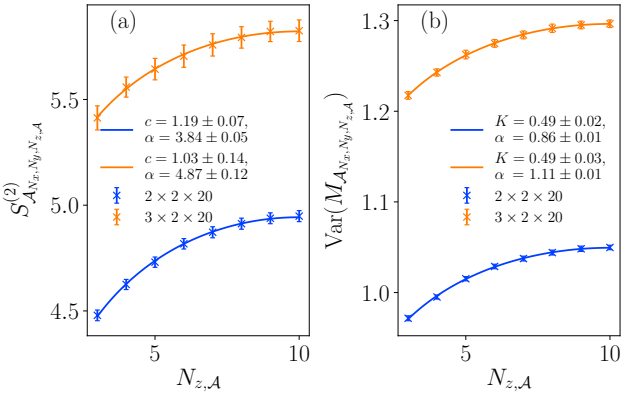

FIG. 2. Second Renyi entropy and spin fluctuations of the interacting model wave function $|\Psi\rangle$ for a series of subsystems $\mathcal{A}_{N_x,N_y,N_{z,\mathcal{A}}}$ (for a sketch see Fig. S1(b)). We plot MC data obtained for two different systems sizes $2 \times 2 \times 20$ (in blue) and $3 \times 2 \times 20$ (in orange). (a) Scaling of the second Renyi entropy, fit to the prediction of Eq. (3). (b) Scaling of the spin fluctuations, fit to the prediction of Eq. (6).

scales proportionally to the EE, where the proportionality constant allows the extraction of K [53]. Since charge fluctuations are completely frozen in the wave function $|\Psi\rangle$, the relevant U(1) symmetry stems from the spin degree of freedom, and we need to consider the fluctuations of the number $M_{\mathcal{A}}$ of particles with spin $\uparrow$ in a subsystem $\mathcal{A}$. Concretely, we consider the variance

$$\mathrm{Var}(M_{\mathcal{A}_{N_x,N_y,N_{z,\mathcal{A}}}}) \equiv \langle M^2_{\mathcal{A}_{N_x,N_y,N_{z,\mathcal{A}}}}\rangle - \langle M_{\mathcal{A}_{N_x,N_y,N_{z,\mathcal{A}}}}\rangle^2. \quad (5)$$

which is expected to scale as [53]

$$\mathrm{Var}(M_{\mathcal{A}_{N_x,N_y,N_{z,\mathcal{A}}}}) = 2 \times \frac{K}{\pi^2} \ln\left[\frac{N_z}{\pi} \sin\left(\frac{\pi N_{z,\mathcal{A}}}{N_z}\right)\right] + \alpha' \quad (6)$$

with the Luttinger parameter K and a constant α' independent of $N_{z,\mathcal{A}}$.

The scaling of the spin fluctuations in the wave function $|\Psi\rangle$ as computed from MC is shown in Fig. 2(b) for two different system sizes $2 \times 2 \times 20$ and $3 \times 2 \times 20$. Remarkably, even for these small sizes, the numerical value for K extracted by fitting the data to Eq. (6) is $K = 0.49 \pm 0.02$ for $2 \times 2 \times 20$ and $K = 0.49 \pm 0.03$ for $3 \times 2 \times 20$. This provides strong evidence that the Luttinger parameter for the chiral hinge modes of the interacting higher order TI is $K = 1/2$, similarly to the edge modes of a FCI.

IV. TOPOLOGICAL DEGENERACY AND TOPOLOGICAL ENTANGLEMENT ENTROPY

In two dimensions, fractionalized excitations such as those of the edge modes of an FCI are an indication for bulk TO. Above, we showed that the FCHI has fractional

hinge modes. It is therefore natural to investigate if it also possesses non-trivial topology in the bulk.

2D topologically ordered systems are characterized by a non-zero TEE and a non-trivial topological degeneracy on surfaces with a genus greater than zero. In three dimensions, TEE and topological degeneracy remain important bulk signatures of non-trivial topology and can display various forms. For example, 3D systems with intrinsic TO have a ground state degeneracy which depends only on the topology of the space, such as the 3D Kitaev model, which has a topological degeneracy of 8 on the 3-torus [56]. On the other hand, fractonic systems possess a ground state degeneracy which might grow exponentially with the system size [2]. They can also exhibit non-trivial corrections to the area law, which are also size-dependent [50–52].

a. Topological degeneracy In order to study the topological degeneracy of the FCHI we closely follow a well-known approach established for 2D projected wave functions such as the FCI. On the 2D torus, one defines four interacting wave functions by choosing PBC or anti-periodic boundary conditions (APBC) for the underlying fermions in each direction of the torus. For the FCI, these four states yield two linearly independent wave functions as expected in the phase of the Laughlin wave function with filling $\nu = 1/2$ (see App. B 4).

For the FCHI, we consider 8 independent ansatz states on the 3D torus obtained by Gutzwiller projection of the non-interacting CHI wave function with PBC or APBC in each direction. The ground state degeneracy is then given by the rank of an 8-dimensional overlap matrix $\mathcal{O}$ containing the normalized overlaps of these ansatz states (see App. D). Note that the topological degeneracy could in principle be larger than 8, in particular for fractonic systems. In such a case, the rank of the overlap matrix considered here would still be at most 8 and our approach would fail to measure the full ground state degeneracy.

We have studied the topological degeneracy of the FCHI on isotropic 3-tori with $N \times N \times N$ unit cells up to $N = 4$ using variational MC simulations (see App. D). The results are shown in Fig. 3(a). For these system sizes, we observe a separation of the eigenvalues of the overlap matrix $\mathcal{O}$ into a group of two larger eigenvalues and a group of 6 smaller eigenvalues. However, there is no clear trend indicating that the former would converge to a finite value and the latter to zero in the thermodynamic limit.

On the other hand, for very anisotropic 3-tori with N_z much larger than $N_x = N_y$ we observe a clear separation of the eigenvalues of $\mathcal{O}$ into a group of four large and a group of four small eigenvalues, which approach the values 2 and 0, respectively, *exponentially* fast as a function of growing N_z for N_x and N_y constant. In the limit $N_z \to \infty$, we thus find four linearly independent wave functions associated with the four different boundary conditions in the horizontal directions, whereas the system becomes insensitive to the boundary conditions in the z direction. This is tightly related to the behavior of

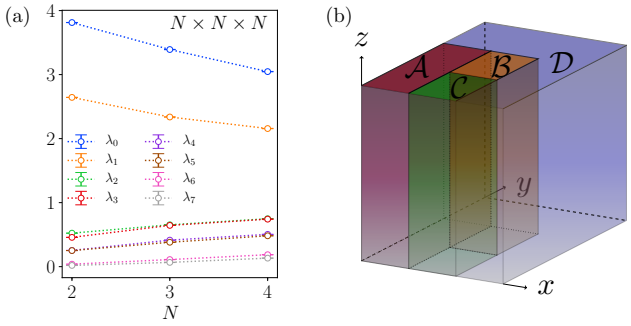

FIG. 3. (a) Scaling of the eigenvalues λ_i with $i = 0, \ldots, 7$ of the overlap matrix $\mathcal{O}$ of the FCHI on the isotropic 3-torus with $N \times N \times N$ unit cells. (b) Subsystems $\mathcal{A}$, $\mathcal{B}$, $\mathcal{C}$ and $\mathcal{D}$ for the extraction of the bulk TEE using a Kitaev-Preskill cut. Note that the subsystems are translation invariant in the z-direction.

the underlying non-interacting wave function, for which the normalised overlap between two many-body wave functions corresponding to different boundary conditions in the z direction also approaches unity as $N_z \to \infty$ for N_x and N_y constant. However, in the non-interacting system this approach is only algebraic as a function of N_z, whereas it is exponential in the interacting system (see App. D).

b. Topological entanglement entropy In order to compute the TEE of the FCHI, we use the Kitaev-Preskill construction [48] extended to 3D systems [50]. As sketched in Fig. 3(b), the system is divided into four regions $\mathcal{A}$, $\mathcal{B}$, $\mathcal{C}$ and $\mathcal{D}$, which are translation invariant in the z direction and whose cross sections with the xy-plane form the pattern required for the usual 2D Kitaev-Preskill cut. The EE of these regions and their unions can be collected into the linear combination

$$-\gamma = S^{(2)}_{\mathcal{ABC}} - S^{(2)}_{\mathcal{AB}} - S^{(2)}_{\mathcal{BC}} - S^{(2)}_{\mathcal{AC}} + S^{(2)}_{\mathcal{A}} + S^{(2)}_{\mathcal{B}} + S^{(2)}_{\mathcal{C}} \quad (7)$$

which cancels all contributions from the virtual surfaces and hinges. The remaining quantity, denoted γ, could contain two contributions $\gamma = \gamma_{3D} + N_z \times \gamma_{2D}$. The constant γ_{3D} is the 3D TEE [50]. $\gamma_{2D} N_z$ would occur for layered constructions of 2D topological orders perpendicular to the z direction with 2D TEE γ_{2D} [50] or in some fractonic systems [1, 2].

We have computed γ for the FCHI on the 3-torus in large-scale variational MC computations. For the geometry sketched in Fig. 3(b), we were able to study the FCHI with $3 \times 3 \times 2$ unit cells, where we found $\gamma = -0.08 \pm 0.04$, and with $3 \times 3 \times 3$ unit cells, where we found $\gamma = -0.06 \pm 0.11$. In both cases, the subsystem $\mathcal{A}$ is of size $1 \times 2 \times N_z$ unit cells, and the subsystems $\mathcal{B}$ and $\mathcal{C}$ are of size $1 \times 1 \times N_z$ unit cells [57]. Because of the intrinsic anisotropy of the FCHI, also considered a second geometry obtained by rotating the subsystems in Fig. 3(b) along the y axis such that they are translation invariant in the x direction, while leaving the insulator

unchanged. Here, we computed γ for a system of $2\times3\times5$ unit cells [58] and found $\gamma = -0.009 \pm 0.102$. All these values are consistent with $\gamma = 0$ (up to small finite-size effects for $3 \times 3 \times 2$) *irrespective* of the orientation of the cut. We stress that γ is several orders of magnitude smaller that any of the EE appearing in Eq. (7), excluding the existence of both a non-vanishing 3D TEE γ_{3D} and a non-zero γ_{2D}.

Since we have not been able to find any clear signature of a true non-trivial bulk topology, we now probe the nature of the gapped surfaces perpendicular to the x direction [59]. Since the vertical hinges host fractionalized one-dimensional modes like those of an FCI, we may speculate that the vertical surfaces host some non-trivial TO [60]. To characterize it, we compute γ according to Eq. (7) for the geometry obtained by rotating the subsystems in Fig. 3(b) as described above, OBC in the x direction and PBC in the y and z directions. We have performed this computation for a system with $2 \times 3 \times 5$ unit cells and found $\gamma = 0.31 \pm 0.20$ [61]. Since the same computation with PBC in x yields a vanishing result for γ as discussed above, this non-zero value is due entirely to the two surfaces at $x = 0$ and $x = N_x - 1$ and confirms that the vertical surfaces host a non-trivial 2D TO. The value for γ is consistent with $\ln\sqrt{2}$, the TEE of a *single* 2D FCI in the Laughlin 1/2 phase, which would imply that each of the surface TOs has a TEE of $(\ln\sqrt{2})/2$.

We mention that we have also studied the degeneracy of the four ansatz states for the FCHI in this geometry, which are generated by changing the boundary conditions for the underlying CHI in the two periodic directions. We have found very similar behavior to the the full-PBC case discussed above, namely two larger eigenvalues but no clear evidence of a reduction of the bulk degeneracy in the thermodynamic limit (see App. D).

V. DISCUSSION AND CONCLUSION

We have studied a model wave function for a 3D chiral hinge insulator with strong interactions at fractional band filling. By studying the EE and spin fluctuations in an open geometry, we showed that the hinges host fractional gapless modes which have the same characterization as the edge modes of an FCI in the Laughlin 1/2 phase. We have also studied the system's topology through the topological degeneracy and the TEE. While the results for the topological degeneracy remain inconclusive due to the small number of numerically accessible system sizes, our results point to the absence of a bulk TEE. However, we found clear signatures of a non-trivial 2D topological order on the vertical surfaces. Interestingly, the TEE contribution per surface is consistent with $(\ln\sqrt{2})/2$, in other words half of the TEE of an FCI, which cannot be described using a quantum dimension [62]. This suggests a non-trivial relation between the surface topology and the hinge modes [60]. In this letter, we have restricted our analysis to the gapped surfaces and their gapless edges. It would be highly interesting but very numerically challenging to consider the top and bottom surfaces, which host single Dirac cones in the non-interacting CHI [63]. Their fate in the interacting system is yet unknown and beyond the scope of the present work, but it should be the focus of further study.

VI. ACKNOWLEDGMENT

We thank Benoit Estienne for enlightening discussions. A.Hackenbroich and N.S. acknowledge support by the European Research Council (ERC) under the European Union's Horizon 2020 research and innovation programme through the ERC Starting Grant WASCOSYS (No. 636201) and the ERC Consolidator Grant SEQUAM (No. 863476), and by the Deutsche Forschungsgemeinschaft (DFG) under Germany's Excellence Strategy (EXC-2111 – 390814868). A.Hackenbroich and N.R. were supported by Grant No. ANR-17-CE30-0013-01. N.R. was partially supported by NSF through the Princeton University's Materials Research Science and Engineering Center DMR-2011750B. A.Hudomal acknowledges funding provided by the Institute of Physics Belgrade, through the grant by the Ministry of Education, Science, and Technological Development of the Republic of Serbia. Part of the numerical simulations were performed on the PARADOX-IV supercomputing facility at the Scientific Computing Laboratory, National Center of Excellence for the Study of Complex Systems, Institute of Physics Belgrade. B.A.B. was supported by the DOE Grant No. DE-SC0016239, the Schmidt Fund for Innovative Research, Simons Investigator Grant No. 404513, the Packard Foundation, the NSF-EAGER No. DMR 1643312, NSF-MRSEC No. DMR-1420541 and DMR-2011750, ONR No. N00014-20-1-2303, Gordon and Betty Moore Foundation through Grant GBMF8685 towards the Princeton theory program, BSF Israel US foundation No. 2018226, and the Princeton Global Network Funds.

[1] R. M. Nandkishore and M. Hermele, Fractons, Annual Review of Condensed Matter Physics **10**, 295 (2019), https://doi.org/10.1146/annurev-conmatphys-031218-013604.

[2] M. Pretko, X. Chen, and Y. You, Fracton phases of matter, International Journal of Modern Physics A **35**, 2030003 (2020), https://doi.org/10.1142/S0217751X20300033.

[3] C. Castelnovo and C. Chamon, Topological order in a three-dimensional toric code at finite temperature, Phys. Rev. B **78**, 155120 (2008).

[4] S. Ryu, Three-dimensional topological phase on the diamond lattice, Phys. Rev. B **79**, 075124 (2009).

[5] I. Mondragon-Shem and T. L. Hughes, Entanglement of a 3d generalization of the kitaev model on the diamond lattice, Journal of Statistical Mechanics: Theory and Experiment **2014**, P10022 (2014).

[6] S. Mandal and N. Surendran, Exactly solvable kitaev model in three dimensions, Phys. Rev. B **79**, 024426 (2009).

[7] N. C. Randeep and N. Surendran, Topological entanglement entropy of the three-dimensional kitaev model, Phys. Rev. B **98**, 125136 (2018).

[8] W. A. Benalcazar, B. A. Bernevig, and T. L. Hughes, Quantized electric multipole insulators, Science **357**, 61 (2017).

[9] W. A. Benalcazar, B. A. Bernevig, and T. L. Hughes, Electric multipole moments, topological multipole moment pumping, and chiral hinge states in crystalline insulators, Physical Review B **96**, 245115 (2017).

[10] F. Schindler, A. M. Cook, M. G. Vergniory, Z. Wang, S. S. Parkin, B. A. Bernevig, and T. Neupert, Higher-order topological insulators, Science advances **4**, eaat0346 (2018).

[11] Z. Song, Z. Fang, and C. Fang, $(d-2)$-dimensional edge states of rotation symmetry protected topological states, Phys. Rev. Lett. **119**, 246402 (2017).

[12] J. Langbehn, Y. Peng, L. Trifunovic, F. von Oppen, and P. W. Brouwer, Reflection-symmetric second-order topological insulators and superconductors, Phys. Rev. Lett. **119**, 246401 (2017).

[13] S. Parameswaran and Y. Wan, Topological insulators turn a corner, Physics **10** (2017).

[14] E. Khalaf, Higher-order topological insulators and superconductors protected by inversion symmetry, Phys. Rev. B **97**, 205136 (2018).

[15] M. Geier, L. Trifunovic, M. Hoskam, and P. W. Brouwer, Second-order topological insulators and superconductors with an order-two crystalline symmetry, Phys. Rev. B **97**, 205135 (2018).

[16] L. Trifunovic and P. W. Brouwer, Higher-order bulk-boundary correspondence for topological crystalline phases, Phys. Rev. X **9**, 011012 (2019).

[17] Y. You, T. Devakul, F. J. Burnell, and T. Neupert, Higher-order symmetry-protected topological states for interacting bosons and fermions, Phys. Rev. B **98**, 235102 (2018).

[18] A. Rasmussen and Y.-M. Lu, Classification and construction of higher-order symmetry-protected topological phases of interacting bosons, Phys. Rev. B **101**, 085137 (2020).

[19] S. A. A. Ghorashi, X. Hu, T. L. Hughes, and E. Rossi, Second-order dirac superconductors and magnetic field induced majorana hinge modes, Phys. Rev. B **100**, 020509 (2019).

[20] O. Dubinkin and T. L. Hughes, Higher-order bosonic topological phases in spin models, Phys. Rev. B **99**, 235132 (2019).

[21] Y. X. Zhao, Y. Lu, and S. A. Yang, Topological second-order spin-3/2 liquids with hinge Fermi arcs, arXiv e-prints , arXiv:2005.14500 (2020), arXiv:2005.14500 [cond-mat.str-el].

[22] Y. You, J. Bibo, and F. Pollmann, Higher-order entanglement and many-body invariants for higher-order topological phases, Physical Review Research **2**, 033192 (2020), arXiv:2001.07724 [cond-mat.str-el].

[23] B. Kang, W. Lee, and G. Y. Cho, Many-Body Invariants for Chern and Chiral Hinge Insulators, arXiv e-prints , arXiv:2003.13706 (2020), arXiv:2003.13706 [cond-mat.str-el].

[24] F. Schindler, Z. Wang, M. G. Vergniory, A. M. Cook, A. Murani, S. Sengupta, A. Y. Kasumov, R. Deblock, S. Jeon, I. Drozdov, H. Bouchiat, S. Guéron, A. Yazdani, B. A. Bernevig, and T. Neupert, Higher-order topology in bismuth, Nature Physics **14**, 918 (2018).

[25] M. Serra-Garcia, V. Peri, R. Süsstrunk, O. R. Bilal, T. Larsen, L. G. Villanueva, and S. D. Huber, Observation of a phononic quadrupole topological insulator, Nature **555**, 342 (2018).

[26] H. Xue, Y. Yang, F. Gao, Y. Chong, and B. Zhang, Acoustic higher-order topological insulator on a kagome lattice, Nature Materials **18**, 108 (2019).

[27] X. Ni, M. Weiner, A. Alù, and A. B. Khanikaev, Observation of higher-order topological acoustic states protected by generalized chiral symmetry, Nature Materials **18**, 113 (2019).

[28] S. Mittal, V. V. Orre, G. Zhu, M. A. Gorlach, A. Poddubny, and M. Hafezi, Photonic quadrupole topological phases, arXiv preprint arXiv:1812.09304 (2018).

[29] A. E. Hassan, F. K. Kunst, A. Moritz, G. Andler, E. J. Bergholtz, and M. Bourennane, Corner states of light in photonic waveguides, arXiv preprint arXiv:1812.08185 (2018).

[30] B.-Y. Xie, G.-X. Su, H.-F. Wang, H. Su, X.-P. Shen, P. Zhan, M.-H. Lu, Z.-L. Wang, and Y.-F. Chen, Visualization of higher-order topological insulating phases in two-dimensional dielectric photonic crystals, arXiv preprint arXiv:1812.06263 (2018).

[31] Y. Yang, Z. Jia, Y. Wu, Z.-H. Hang, H. Jiang, and X. Xie, Gapped topological kink states and topological corner states in graphene, arXiv preprint arXiv:1903.01816 (2019).

[32] C. W. Peterson, W. A. Benalcazar, T. L. Hughes, and G. Bahl, A quantized microwave quadrupole insulator with topologically protected corner states, Nature **555**, 346 (2018).

[33] S. Imhof, C. Berger, F. Bayer, J. Brehm, L. W. Molenkamp, T. Kiessling, F. Schindler, C. H. Lee, M. Greiter, T. Neupert, and R. Thomale, Topolectrical-circuit realization of topological corner modes, Nature Physics **14**, 925 (2018).

[34] M. Serra-Garcia, R. Süsstrunk, and S. D. Huber, Observation of quadrupole transitions and edge mode topology in an lc circuit network, Phys. Rev. B **99**, 020304 (2019).

[35] D. Sheng, Z.-C. Gu, K. Sun, and L. Sheng, Fractional quantum hall effect in the absence of landau levels, Nature communications **2**, 1 (2011).

[36] T. Neupert, L. Santos, C. Chamon, and C. Mudry, Fractional quantum hall states at zero magnetic field, Phys. Rev. Lett. **106**, 236804 (2011).

[37] N. Regnault and B. A. Bernevig, Fractional chern insulator, Phys. Rev. X **1**, 021014 (2011).

[38] Y. You, F. J. Burnell, and T. L. Hughes, Multipolar Topological Field Theories: Bridging Higher Order Topological Insulators and Fractons, arXiv e-prints , arXiv:1909.05868 (2019), arXiv:1909.05868 [cond-mat.str-el].

[39] R. B. Laughlin, Anomalous quantum hall effect: An incompressible quantum fluid with fractionally charged ex-

citations, Phys. Rev. Lett. **50**, 1395 (1983).
[40] G. Moore and N. Read, Nonabelions in the fractional quantum hall effect, Nuclear Physics B **360**, 362 (1991).
[41] Y. Zhang and A. Vishwanath, Establishing non-abelian topological order in gutzwiller-projected chern insulators via entanglement entropy and modular $\mathcal{S}$-matrix, Phys. Rev. B **87**, 161113 (2013).
[42] J. Shao, E.-A. Kim, F. D. M. Haldane, and E. H. Rezayi, Entanglement entropy of the $\nu = 1/2$ composite fermion non-fermi liquid state, Phys. Rev. Lett. **114**, 206402 (2015).
[43] Y. Zhang, T. Grover, and A. Vishwanath, Topological entanglement entropy of F_2 spin liquids and lattice laughlin states, Phys. Rev. B **84**, 075128 (2011).
[44] M. Srednicki, Entropy and area, Phys. Rev. Lett. **71**, 666 (1993).
[45] P. Calabrese and J. Cardy, Entanglement entropy and conformal field theory, Journal of Physics A: Mathematical and Theoretical **42**, 504005 (2009).
[46] V. Crépel, N. Claussen, B. Estienne, and N. Regnault, Model states for a class of chiral topological order interfaces, Nature communications **10**, 1 (2019).
[47] V. Crépel, N. Claussen, N. Regnault, and B. Estienne, Microscopic study of the halperin–laughlin interface through matrix product states, Nature communications **10**, 1 (2019).
[48] A. Kitaev and J. Preskill, Topological entanglement entropy, Phys. Rev. Lett. **96**, 110404 (2006).
[49] M. Levin and X.-G. Wen, Detecting topological order in a ground state wave function, Phys. Rev. Lett. **96**, 110405 (2006).
[50] T. Grover, A. M. Turner, and A. Vishwanath, Entanglement entropy of gapped phases and topological order in three dimensions, Phys. Rev. B **84**, 195120 (2011).
[51] H. Ma, A. T. Schmitz, S. A. Parameswaran, M. Hermele, and R. M. Nandkishore, Topological entanglement entropy of fracton stabilizer codes, Phys. Rev. B **97**, 125101 (2018).
[52] H. He, Y. Zheng, B. A. Bernevig, and N. Regnault, Entanglement entropy from tensor network states for stabilizer codes, Phys. Rev. B **97**, 125102 (2018).
[53] B. Estienne and J.-M. Stéphan, Entanglement spectroscopy of chiral edge modes in the quantum hall effect (2019), arXiv:1911.10125 [cond-mat.str-el].
[54] M. B. Hastings, I. González, A. B. Kallin, and R. G. Melko, Measuring renyi entanglement entropy in quantum monte carlo simulations, Phys. Rev. Lett. **104**, 157201 (2010).
[55] Y. Zhang, T. Grover, and A. Vishwanath, Entanglement entropy of critical spin liquids, Phys. Rev. Lett. **107**, 067202 (2011).
[56] S. Mandal and N. Surendran, Fermions and nontrivial loop-braiding in a three-dimensional toric code, Phys. Rev. B **90**, 104424 (2014).
[57] We recall that the number of physical sites for these subsystems is $2 \times 4 \times N_z$ and $2 \times 2 \times N_z$, respectively.
[58] We recall that the number of physical sites in this case is $4 \times 6 \times 5$. Thus despite $N_x = 2$, the PBC along x are non-trivial. Here, the subsystem $\mathcal{A}$ is of size $2 \times 2 \times 2$ unit cells, and the subsystems $\mathcal{B}$ and $\mathcal{C}$ are of size $2 \times 1 \times 2$ unit cells.
[59] We could alternatively choose those perpendicular to the y direction.
[60] A. Tiwari, M.-H. Li, B. A. Bernevig, T. Neupert, and S. A. Parameswaran, Unhinging the surfaces of higher-order topological insulators and superconductors, Phys. Rev. Lett. **124**, 046801 (2020).
[61] Here, the statistical error bar is a conservative estimate, in particular much larger than the remaining fluctuations in the mean of the MC computations (see App. E). We stress that our conservative error bar confirms a non-trivial TEE smaller than $\log \sqrt{2}$ per surface.
[62] A TEE of $(\ln \sqrt{2})/2$ would correspond to a total quantum dimension $2^{1/4}$, whereas any non-trivial total quantum dimension has to be larger or equal to $\sqrt{2}$.
[63] Manuscript in Preparation.
[64] J. Pei, S. Han, H. Liao, and T. Li, Topological entanglement entropy in gutzwiller projected spin liquids, Phys. Rev. B **88**, 125135 (2013).
[65] J. Wildeboer and N. E. Bonesteel, Spin correlations and topological entanglement entropy in a non-abelian spin-one spin liquid, Phys. Rev. B **94**, 045125 (2016).

Supplemental Material for "Fractional Chiral Hinge Insulator"

CONTENTS

LIST OF FIGURES

INTRODUCTION TO THE APPENDICES

In this work, we have built and studied a model state for a three-dimensional (3D) fractional chiral hinge insulator (FCHI). In the following, we provide additional information on our numerical methods, their benchmark on a two-dimensional (2D) fractional Chern insulator and the non-interacting 3D chiral hinge insulator, and additional results for the topological degeneracy of the 3D model.

We begin in Appendix A by introducing the Monte Carlo (MC) observables that we used for the computations of entanglement entropy and the overlap matrix whose results are discussed in the main text. In Appendix B, we proceed to give a detailed account of the benchmark of our MC algorithm and the entanglement observables from the main text on a 2D fractional Chern insulator. This includes a characterization of the edge modes from variational MC simulations, and the computation of the topological entanglement entropy and topological degeneracy. In Appendix C, we complement the characterization of the fractional hinge modes of the FCHI in the main text by a similar analysis for the underlying non-interacting chiral hinge insulator, confirming that its hinge modes are of the same nature as the edge modes of a non-interacting Chern insulator. In Appendix D, we give additional details about the computation of the topological overlap matrix for the FCHI whose eigenvalue scaling for isotropic system sizes is discussed in the main text. We also provide results for the scaling of the overlap matrix for highly anisotropic systems that are much larger in the z direction than in the x and y directions, and for geometries with open boundary conditions in the x direction and periodic boundary conditions in the y and z directions. Finally, in Appendix E we provide technical data about our MC computations, including the computational cost.

Appendix A: Monte Carlo simulations

In this appendix, we provide a quick overview of the Monte Carlo (MC) procedure that was used to derive the results in the main text. The technical details of the MC simulation will be discussed in Appendix E.

1. Entanglement entropy

For a quantum state $|\psi\rangle$, the Renyi entropy of order n *w.r.t.* a subsystem $\mathcal{A}$ is given by

$$S_{\mathcal{A}}^{(n)} = \frac{1}{1-n} \ln \left(\mathrm{Tr}_{\mathcal{A}} \left[\rho_{\mathcal{A}}^{n} \right] \right). \tag{A1}$$

Here, $\rho_{\mathcal{A}} = \mathrm{Tr}_{\mathcal{B}} \left[|\psi\rangle\langle\psi| \right]$ is the reduced density matrix of the subsystem $\mathcal{A}$ obtained by tracing over the degrees of freedom in its complement $\mathcal{B}$. We use the notation $\mathrm{Tr}_{\mathcal{A}}$ for the trace over the degrees of freedom in region $\mathcal{A}$. In the limit $n \to 1$, $S^{(n)}$ corresponds to the von Neumann entropy $S_{\mathcal{A}} = -\mathrm{Tr}_{\mathcal{A}} \left[\rho_{\mathcal{A}} \ln \left(\rho_{\mathcal{A}} \right) \right]$. Since the von Neumann entropy is hard to evaluate numerically, we focus on the second Renyi entropy $S^{(2)}$, which can be computed using the replica trick with the SWAP operator technique [54].

To that end, we consider two identical copies of the system, which together are in the quantum state $|\psi\rangle \otimes |\psi\rangle$. The SWAP operator acts by exchanging the degrees of freedom within the subsystem $\mathcal{A}$ between the two copies, while leaving the degrees of freedom in $\mathcal{B}$ unchanged. Specifically, let $\{|v\rangle\}$ be an orthonormal basis of (a single copy of) the system, whose elements $|v\rangle = |v_{\mathcal{A}}, v_{\mathcal{B}}\rangle$ factorize as a tensor product of states describing only the subsystem $\mathcal{A}$ and its complement $\mathcal{B}$, respectively. Expressed in this basis, the SWAP operator acts on the two copies as

$$\mathrm{SWAP} \left(|v\rangle \otimes |v'\rangle \right) = \mathrm{SWAP} \left(|v_{\mathcal{A}}, v_{\mathcal{B}}\rangle \otimes |v'_{\mathcal{A}}, v'_{\mathcal{B}}\rangle \right) = |v'_{\mathcal{A}}, v_{\mathcal{B}}\rangle \otimes |v_{\mathcal{A}}, v'_{\mathcal{B}}\rangle. \tag{A2}$$

It can be shown that the second Renyi entropy is related to the expectation value $\langle \mathrm{SWAP} \rangle$ as [54]

$$e^{-S_{\mathcal{A}}^{(2)}} = \mathrm{Tr}_{\mathcal{A}} \left[\rho_{\mathcal{A}}^{2} \right] = \langle \mathrm{SWAP} \rangle = \frac{\langle \psi \otimes \psi | \, \mathrm{SWAP} \, | \psi \otimes \psi \rangle}{\langle \psi \otimes \psi | \psi \otimes \psi \rangle}. \tag{A3}$$

The expectation value $\langle \mathrm{SWAP} \rangle$ can be computed using MC simulations on the double-copy system. Computations of the entanglement entropy with this method have been successfully performed in the context of topological phases for systems such as spin liquids [41, 43], Laughlin states [43] and non-Fermi-liquids [42].

Since the Renyi entropy of a quantum ground state obeys an area law and the expectation value $\langle \mathrm{SWAP} \rangle$ measured in MC simulations is given by $e^{-S_{\mathcal{A}}^{(2)}}$, the value of $\langle \mathrm{SWAP} \rangle$ decays exponentially with $|\partial \mathcal{A}|$. Therefore, for larger subsystems the convergence of $\langle \mathrm{SWAP} \rangle$ quickly becomes extremely slow. This can partially be mitigated by a sign

trick [55] for non-positive wave functions, which allows to separately evaluate the contributions to $\langle \mathrm{SWAP} \rangle$ from the amplitude and the phase of the wave function. To that end, we write

$$\langle \mathrm{SWAP} \rangle = \langle \mathrm{SWAP}_{\mathrm{amp}} \rangle \times \langle \mathrm{SWAP}_{\mathrm{phase}} \rangle \,, \tag{A4}$$

where $\langle \mathrm{SWAP}_{\mathrm{amp}} \rangle$ and $\langle \mathrm{SWAP}_{\mathrm{phase}} \rangle$ can be measured in separate MC simulations with faster convergence. Denoting by $\psi(v) \equiv \psi(v_{\mathcal{A}}, v_{\mathcal{B}}) \equiv \langle v|\psi\rangle$ the coefficient of the quantum state $|\psi\rangle$ *w.r.t.* the basis state $|v\rangle$, the two expectation values are given by [55]

$$\langle \mathrm{SWAP}_{\mathrm{amp}} \rangle = \sum_{v,v'} \rho(v,v')_{\mathrm{amp}} \times f(v,v')_{\mathrm{amp}}, \tag{A5a}$$

$$\langle \mathrm{SWAP}_{\mathrm{phase}} \rangle = \sum_{v,v'} \rho(v,v')_{\mathrm{phase}} \times f(v,v')_{\mathrm{phase}}, \tag{A5b}$$

where

$$\rho(v,v')_{\mathrm{amp}} = \frac{|\psi(v)|^2}{\langle\psi|\psi\rangle} \frac{|\psi(v')|^2}{\langle\psi|\psi\rangle}, \tag{A5c}$$

$$f(v,v')_{\mathrm{amp}} = |f(v,v')| \,, \tag{A5d}$$

$$\rho(v,v')_{\mathrm{phase}} = \frac{|\psi(v'_{\mathcal{A}}, v_{\mathcal{B}})\psi(v_{\mathcal{A}}, v'_{\mathcal{B}})\psi(v_{\mathcal{A}}, v_{\mathcal{B}})\psi(v'_{\mathcal{A}}, v'_{\mathcal{B}})|}{\sum_{v,v'} |\psi(v'_{\mathcal{A}}, v_{\mathcal{B}})\psi(v_{\mathcal{A}}, v'_{\mathcal{B}})\psi(v_{\mathcal{A}}, v_{\mathcal{B}})\psi(v'_{\mathcal{A}}, v'_{\mathcal{B}})|}, \tag{A5e}$$

$$f(v,v')_{\mathrm{phase}} = e^{i \arg[f(v,v')]}, \tag{A5f}$$

and we used the shorthand

$$f(v,v') \equiv \frac{\psi(v'_{\mathcal{A}}, v_{\mathcal{B}})\psi(v_{\mathcal{A}}, v'_{\mathcal{B}})}{\psi(v_{\mathcal{A}}, v_{\mathcal{B}})\psi(v'_{\mathcal{A}}, v'_{\mathcal{B}})} \tag{A6}$$

split into its norm $|f(v,v')|$ and its phase, $\arg[f(v,v')]$. The expectation values $\langle \mathrm{SWAP}_{\mathrm{amp}} \rangle$ and $\langle \mathrm{SWAP}_{\mathrm{phase}} \rangle$ can be evaluated using MC simulations with the probability densities $\rho(v,v')_{\mathrm{amp}}$ and $\rho(v,v')_{\mathrm{phase}}$ and estimators $f(v,v')_{\mathrm{amp}}$ and $f(v,v')_{\mathrm{phase}}$, respectively. We note that for the entropy computations in the FCHI presented in Fig. 2 of the main text, the convergence of the $\langle \mathrm{SWAP}_{\mathrm{phase}} \rangle$ observable is much faster than that of the $\langle \mathrm{SWAP}_{\mathrm{amp}} \rangle$ observable. Similar observations have been made for RVB states, where this was linked to an approximate Marshall sign rule [64].

2. Wave function overlap

In Appendix D, we will compute the overlap matrix of the different ansatz states for the FCHI on the 3D torus in order to check if the system has a topological degeneracy. The overlap matrix element $\mathcal{O}_{\psi_1,\psi_2}$ between two a priori unnormalized ansatz states $|\psi_1\rangle$ and $|\psi_2\rangle$ is given by

$$\mathcal{O}_{\psi_1,\psi_2} = \frac{\langle\psi_1|\psi_2\rangle}{\sqrt{\langle\psi_1|\psi_1\rangle}\sqrt{\langle\psi_2|\psi_2\rangle}}. \tag{A7}$$

In order to compute this overlap with MC, we make use of the identity

$$\mathcal{O}_{\psi_1,\psi_2} = \sum_v \frac{\psi_1(v)^* \, \psi_2(v)}{\sqrt{\langle\psi_1|\psi_1\rangle}\sqrt{\langle\psi_2|\psi_2\rangle}} = \sqrt{\mathcal{O}^{1,abs}_{\psi_1,\psi_2} \times \mathcal{O}^{2,abs}_{\psi_1,\psi_2}} \times \mathcal{O}^{phase}_{\psi_1,\psi_2}, \tag{A8}$$

where

$$\mathcal{O}^{1,abs}_{\psi_1,\psi_2} = \sum_v \rho(v)^{1,abs} \times f(v)^{1,abs}, \tag{A9a}$$

$$\mathcal{O}^{2,abs}_{\psi_1,\psi_2} = \sum_v \rho(v)^{2,abs} \times f(v)^{2,abs}, \tag{A9b}$$

$$\mathcal{O}^{phase}_{\psi_1,\psi_2} = \sum_v \rho(v)^{phase} \times f(v)^{phase}. \tag{A9c}$$

and

$$\rho(v)^{1,abs} = \frac{|\psi_1(v)|^2}{\langle\psi_1|\psi_1\rangle}, \tag{A10a}$$

$$f(v)^{1,abs} = \frac{|\psi_2(v)|}{|\psi_1(v)|}, \tag{A10b}$$

$$\rho(v)^{2,abs} = \frac{|\psi_2(v)|^2}{\langle\psi_2|\psi_2\rangle}, \tag{A10c}$$

$$f(v)^{2,abs} = \frac{|\psi_1(v)|}{|\psi_2(v)|}, \tag{A10d}$$

$$\rho(v)^{phase} = \frac{|\psi_2(v)||\psi_1(v)|}{\sum_v |\psi_2(v)||\psi_1(v)|}, \tag{A10e}$$

$$f(v)^{phase} = e^{i(\arg[\psi_2(v)]-\arg[\psi_1(v)])}. \tag{A10f}$$

In Eq. (A9), the sum is over all configurations v. As before, $\arg[\psi_i(v)]$ refers to the phase of the wave function $\psi_i(v) = \langle v|\psi_i\rangle$ for $i = 1, 2$. The quantities $\mathcal{O}^{1,abs}_{\psi_1,\psi_2}$, $\mathcal{O}^{2,abs}_{\psi_1,\psi_2}$ and $\mathcal{O}^{phase}_{\psi_1,\psi_2}$ can be evaluated in separate MC computations with weights $\rho(v)^{1,abs}$, $\rho(v)^{2,abs}$, $\rho(v)^{phase}$ and measurement estimators $f(v)^{1,abs}$, $f(v)^{2,abs}$ and $f(v)^{phase}$, respectively. It is also possible to express the overlap matrix element as the product of three expectation values that can be sampled in MC computations with the same weight [65].

In order to compare the physical validity of different unnormalized ansatz states, it can be useful to compare their norms. To that end, we note that the ratio of the norms of the ansatz states $|\psi_1\rangle$, $|\psi_2\rangle$ is given by

$$\frac{\langle\psi_1|\psi_1\rangle}{\langle\psi_2|\psi_2\rangle} = \frac{\mathcal{O}^{2,abs}_{\psi_1,\psi_2}}{\mathcal{O}^{1,abs}_{\psi_1,\psi_2}}, \tag{A11}$$

and is therefore a by-product of the MC computations for the overlap matrix.

Appendix B: Fractional Chern insulator

In this section, we test the concepts developed in the main text and benchmark our tools by considering a fractional Chern insulator (FCI) in two dimensions. The latter is obtained as the Gutzwiller projection of two copies of a simple two-band Chern insulator (CI) described in Ref. 43. We begin by briefly presenting the non-interacting CI model in Sec. B 1. In Sec. B 2, we then benchmark the methods used in the main text for the hinge mode characterization on the edge modes of the FCI. Subsequently, we study the stability of the FCI under the addition of a staggered chemical potential in Sec B 3, before concluding with a study of the topological degeneracy in Sec. B 4.

1. Chern insulator

We consider the two-band Chern insulator (CI) of Ref. 43 at half filling whose valence band has a non-zero Chern number $\mathcal{C} = 1$. The corresponding tight-binding Hamiltonian sketched in Fig. S1(a) is defined on a square lattice with N_x unit cells in the horizontal direction and N_y unit cells in the vertical direction, where each unit cell consists of an A and a B site. It is characterized by a real next-nearest neighbour hopping t and a purely imaginary next-to-nearest neighbour hopping $i\Delta$. We will also consider an additional staggered chemical potential with $+\mu$ on A sites and $-\mu$ on B sites. The Bloch Hamiltonian of the CI is given by

$$H(k_x, k_y) = [2\Delta\sin(k_x)(\cos(k_y) - 1) + t(\cos(k_y) + 1)]\,\sigma_x + [(2\Delta\sin(k_x) + t)\sin(k_y)]\,\sigma_y + [\mu + 2t\cos(k_x)]\,\sigma_z, \tag{B1}$$

where σ_x, σ_y and σ_z are the Pauli matrices. The Bloch bands have energy $\pm\epsilon(k_x, k_y)$, with

$$\epsilon(k_x, k_y) = \sqrt{[2\Delta\sin(k_x)(\cos(k_y) - 1) + t(\cos(k_y) + 1)]^2 + [(2\Delta\sin(k_x) + t)\sin(k_y)]^2 + [\mu + 2t\cos(k_x)]^2}. \tag{B2}$$

For $\mu = 0$, the single-particle gap is maximal when the hopping parameters are $t = 1$ and $\Delta = 1/2$. In the following, we therefore always choose $t = 1$ and $\Delta = 1/2$.

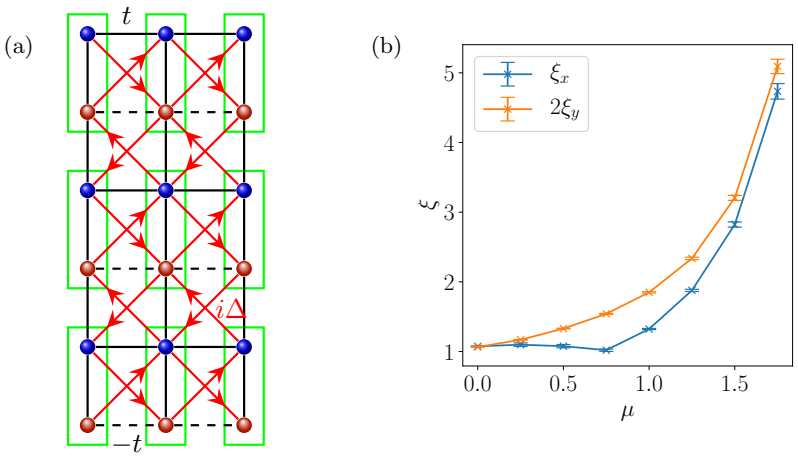

FIG. S1. (a) Microscopic model for the Chern insulator of Ref. 43 defined on a square lattice with two sublattices, A in blue and B in red. The nearest-neighbour hopping t ($-t$ for dashed lines) drawn in black is real, whereas the next-nearest neighbour hopping $i\Delta$ in the direction of the red arrows is purely imaginary. (b) Correlation lengths ξ_x and ξ_y (in units of the unit cell) for the two-point correlator in the ground state of the perturbed CI with staggered chemical potential μ. The correlation lengths diverge at the critical value $\mu_c = 2$. Note that due to the anisotropy of the unit cell, ξ_x and $2\xi_y$ are comparable.

Increasing μ away from 0 leads to a trivialization of the model (i.e., when the two bands have a zero Chern number) for μ larger than a critical value μ_c where the band gap closes. For $t = 1$ and $\Delta = 1/2$, the single-particle gap closes at $\mu_c = 2$. As expected, the correlation length of the CI ground state at half filling diverges as μ approaches μ_c, but stays reasonably small for values $\mu \leq 1$ (see Fig.S1(b)).

a. Twisted boundary conditions

On the torus, we can consider the CI with twisted boundary conditions determined by phases Φ_x and Φ_y that a particle should pick up on a loop parallel to the x and y axes, respectively. Here, we choose to implement the twisted boundary conditions in the tight-binding model in a translation-invariant way by multiplying all hopping terms in the positive x and y directions with phases λ_x and λ_y, respectively, where

$$\lambda_x = e^{i\frac{\Phi_x}{N_x}}, \tag{B3a}$$

$$\lambda_y = e^{i\frac{\Phi_y}{2N_y}}. \tag{B3b}$$

Correspondingly, hopping terms with a component in the negative x and y directions are multiplied with the complex conjugate phases λ_x^* and λ_y^*.

b. Particle-hole symmetry

The unperturbed CI model with zero staggered chemical potential $\mu = 0$ possesses a unitary particle-hole (PH) symmetry, which relates states with different boundary conditions on the torus. The PH conjugation acts on the creation operators as

$$c_{A,(x,y)} \mapsto c^\dagger_{A,(x,y)}, \tag{B4a}$$

$$c_{B,(x,y)} \mapsto -c^\dagger_{B,(x,y)}, \tag{B4b}$$

where $x \in \{0, \ldots, N_x - 1\}$ and $y \in \{0, \ldots, N_y - 1\}$ are the unit cell coordinates. It is straightforward to verify that on the torus, this symmetry maps the CI Hamiltonian with twist phase factors (λ_x, λ_y) to the CI Hamiltonian with modified phase factors (λ'_x, λ'_y), given by

$$(\lambda'_x, \lambda'_y) = (-\lambda_x^*, \lambda_y^*). \tag{B5}$$

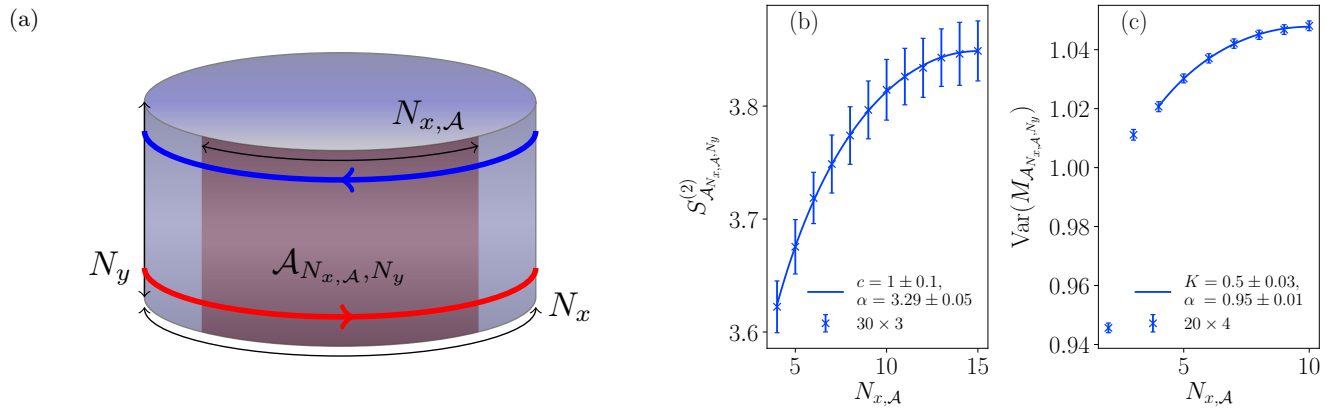

FIG. S2. (a) Geometry used for the extraction of the edge physics: Cylinder with periodic boundary conditions and N_x unit cells in the horizontal direction, and open boundaries and N_y sites in the vertical direction. The rectangular subsystem $\mathcal{A}_{N_{x,\mathcal{A}},N_y}$ consists of $N_{x,\mathcal{A}}$ unit cells in the horizontal direction and N_y sites in the vertical direction. (b), (c) MC results for the EE and spin fluctuations characterizing the edge modes extracted from the geometry in (a).

Using Eq. (B3), this implies that the non-interacting ground state with (Φ_x, Φ_y) is mapped to the ground state with

$$\left(\Phi'_x, \Phi'_y\right) = (-\Phi_x + N_x\pi, -\Phi_y) \tag{B6}$$

Note that for N_x odd, the change in Φ_x is an odd multiple of π, such that the symmetry relates states with periodic and anti-periodic boundary conditions in the horizontal direction.

2. FCI edge modes

The FCI obtained as the Gutzwiller projection of two copies of the CI at half filling lies in the same universality class as the bosonic Laughlin state at filling $\nu = 1/2$. In particular, its chiral gapless edge modes are described by the chiral CFT $\mathfrak{su}(2)_1$. Two key characteristic quantities of this CFT, the central charge $c = 1$ and the Luttinger parameter $K = 1/2$, can be extracted numerically from the scaling of the entanglement entropy (EE) and spin fluctuations in a suitable geometry, respectively [46, 47, 53]. Here, we reproduce these known results with our MC setup using a geometry which can easily be generalized to the 3D setting of the main text. This serves both as a benchmark for our numerical tools, and as a validation of the geometry used here and in the main text.

We consider the FCI in the "ribbon" geometry sketched in Fig. S2(a). The system is defined on a cylinder with periodic boundary conditions and N_x unit cells in the x-direction, and open boundaries and N_y unit cells in the y-direction. We consider the EE and spin fluctuations *w.r.t.* a series of subsystems $\mathcal{A}_{N_{x,\mathcal{A}},N_y}$ which have $N_{x,\mathcal{A}} \in \{1, N_x/2\}$ unit cells in the horizontal direction and span the full height of the cylinder in the vertical direction. The $\mathcal{A}_{N_{x,\mathcal{A}},N_y}$ cuts break the translation invariance in the horizontal direction and introduce virtual boundaries perpendicular to the physical edge states (marked in red and blue). Hence, the EE and spin fluctuations *w.r.t.* $\mathcal{A}_{N_{x,\mathcal{A}},N_y}$ will contain contributions from both chiral edge modes, in addition to the area law and corner contribution which do not depend on $N_{x,\mathcal{A}}$.

Concretely, the second Renyi entropy $S^{(2)}$ is expected to scale with $N_{x,\mathcal{A}}$ as

$$S^{(2)}_{\mathcal{A}_{N_{x,\mathcal{A}},N_y}}(N_{x,\mathcal{A}}) = \alpha_{2D} + 2 \times S^{(2)}_{\mathrm{crit}}(N_{x,\mathcal{A}}; N_x). \tag{B7}$$

Here, α_{2D} contains the area law contributions proportional to N_y from the virtual cuts, as well as the corner contributions or constant corrections. It is therefore a constant independent of $N_{x,\mathcal{A}}$. In Eq. (B7),

$$S^{(2)}_{\mathrm{crit}}(N_{x,\mathcal{A}}; N_x) = \frac{c}{8} \ln\left[\frac{N_x}{\pi} \sin\left(\frac{\pi N_{x,\mathcal{A}}}{N_x}\right)\right] \tag{B8}$$

is the second Renyi entropy of a periodic one-dimensional chiral critical mode with central charge c and total system size N_x restricted to a single interval of length $N_{x,\mathcal{A}}$ [45]. The factor of 2 in Eq. (B7) takes into account the two edge modes, which each contribute equally to the EE.

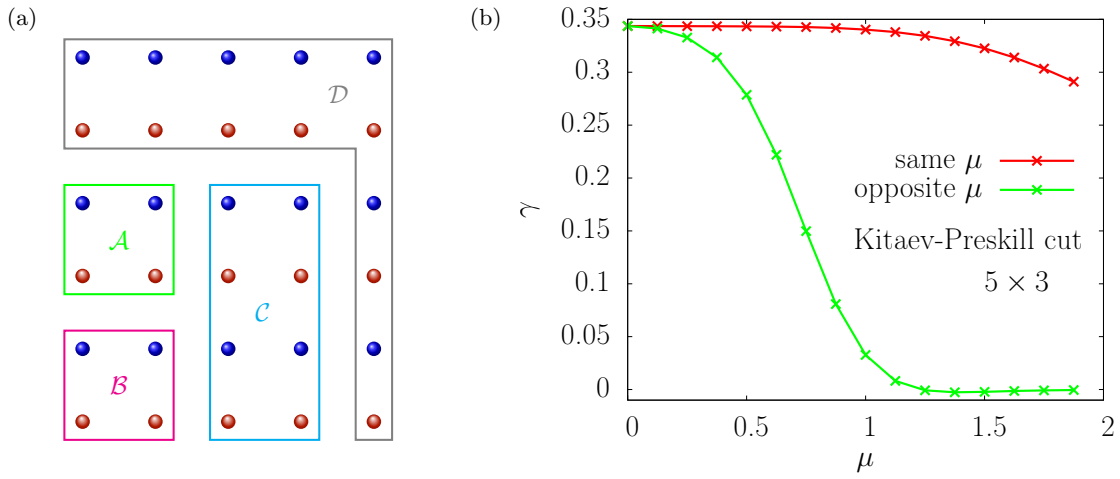

FIG. S3. (a) Sketch of the Kitaev-Preskill cut for a system of 5×3 unit cells. (b) Topological entanglement entropy for the FCI as a function of staggered chemical potential μ. The results were obtained for the system size 5×3 using exact diagonalization and the Kitaev-Preskill scheme shown in (a).

In the main text, we also considered the variance of the number $M_{\mathcal{A}}$ of spin up particles in the region $\mathcal{A}$, given by

$$\mathrm{Var}(M_{\mathcal{A}}) \equiv \langle M_{\mathcal{A}}^2 \rangle - \langle M_{\mathcal{A}} \rangle^2. \tag{B9}$$

For the $\mathcal{A}_{N_x,\mathcal{A},N_y}$ cut used here, the variance is expected to scale as [53]

$$\mathrm{Var}(M_{\mathcal{A}_{N_x,\mathcal{A},N_y}}) = \alpha'_{2D} + \frac{K}{\pi^2} \ln \left[\frac{N_x}{\pi} \sin \frac{\pi N_{x,\mathcal{A}}}{N_x} \right], \tag{B10}$$

where K is the Luttinger parameter of the CFT describing the edge modes, and α'_{2D} is a constant independent of $N_{x,\mathcal{A}}$ subsuming the corner and area law contributions to the spin fluctuations.

The scaling of the EE and spin fluctuations for the FCI as computed from MC, fit to the predictions of Eqs. (B7) and (B10), are shown in Fig. S2(b) and (c). In both cases, the logarithmic contributions from the edge states are clearly visible. The fit values of the central charge $c = 1.0 \pm 0.1$ and the Luttinger parameter $K = 0.50 \pm 0.03$ are very close to the expected values $c = 1$ and $K = 1/2$, respectively.

3. Topological entanglement entropy

We now explore the stability of the FCI under the perturbation by a staggered chemical potential μ as defined in Eq. (B1). To this end, we compute the topological entanglement entropy (TEE) [48] denoted γ. For the FCI obtained as the Gutzwiller projection of two copies of the non-interacting CI, the TEE is expected to be $\gamma = \ln(2)/2 \approx 0.347$.

In order to test our MC calculations, we first extract the TEE using exact diagonalization (ED) and the Kitaev-Preskill scheme [48]. Here by ED we mean that the ground state at half filling of the CI is obtained directly by ED, providing the ground state decomposition onto the real space many-body basis. With such a decomposition, we can easily perform the Gutzwiller projection and exactly compute any EE, while the EE calculation using MC is considerably more complex, as described in Appendix A 1. For the system size we study here, ED is fast enough and provides exact results without any errors. It can therefore be used as a reference for MC calculations.

We study a system of size 3×5 unit cells with periodic boundary conditions in both directions and a cut shown in Fig. S3(a). The system is divided into four regions labeled $\mathcal{A}$, $\mathcal{B}$, $\mathcal{C}$ and $\mathcal{D}$ (see Fig. S3(a)). The linear combination of the entanglement entropies of these regions and their unions

$$S_{\mathcal{ABC}} - S_{\mathcal{AB}} - S_{\mathcal{BC}} - S_{\mathcal{AC}} + S_{\mathcal{A}} + S_{\mathcal{B}} + S_{\mathcal{C}} \tag{B11}$$

suppresses all unwanted contributions (such as the area law or corner contributions) and only the TEE term remains.

The TEE for the FCI as a function of staggered chemical potential μ is presented in Fig. S3(b). We consider two different cases, same μ in both non-interacting CI copies (i.e., before projection) and mixed μ ($+\mu$ in one copy and

$-\mu$ in the other). As can be seen from Fig. S1(b), for $\mu \leq 1$ the correlation length of the CI ground state is shorter than two lattice spacings of the underlying square lattice. We may therefore expect that in this case the subsystem sizes considered here are large enough compared to the correlation length that our computation gives a finite size TEE close to the result in the thermodynamic limit. Indeed, for $\mu = 0$, the numerically obtained value is $\gamma \approx 0.344$, which is close to the predicted value of 0.347. The agreement is expected to be even better in larger systems which are not accessible in our ED calculations. In the case of same μ (red line), the TEE stays approximately constant for $\mu \leq 1$ and then it starts to deviate due to increasing correlation length. In contrast, the TEE for opposite μ (green line) immediately decreases from the expected value and drops to zero shortly after $\mu = 1$. We can conclude that the FCI is only stable to addition of a staggered chemical potential with the same sign in both CI copies, while it is destroyed by a staggered chemical potential with opposite signs.

Finally, we repeat the calculation for system size 5×3 and $\mu = 0$ using MC and the Kitaev-Preskill scheme. The TEE obtained in this way is $\gamma = 0.34 \pm 0.03$, which is in good agreement with the ED result and the theoretical prediction.

4. Topological degeneracy

In Appendix D we will discuss the topological degeneracy of the fractional chiral hinge insulator with periodic boundary conditions in all directions. For sake of comparison, here we compute the topological degeneracy of the FCI on the torus. The topological degeneracy is given by the number of linearly independent states generated by Gutzwiller projection of the non-interacting CI with twisted boundary conditions characterized by the phases Φ_x and Φ_y as introduced in Appendix B 1 a above. Denoting by $|\psi_\sigma^{(\Phi_x,\Phi_y)}\rangle$ the ground state of the CI model with twisted boundary conditions with spin $\sigma \in \{\uparrow,\downarrow\}$, we compute the rank of the overlap matrix

$$\left(P_G\left[\langle\psi_\uparrow^{(\Phi_x,\Phi_y)}| \otimes \langle\psi_\downarrow^{(\Phi_x,\Phi_y)}|\right] P_G\left[|\psi_\uparrow^{(\Phi'_x,\Phi'_y)}\rangle \otimes |\psi_\downarrow^{(\Phi'_x,\Phi'_y)}\rangle\right]\right)_{(\Phi_x,\Phi_y),(\Phi'_x,\Phi'_y)}. \tag{B12}$$

For simplicity, we only consider phases $\Phi_x, \Phi_y, \Phi'_x, \Phi'_y \in \{0, \pi\}$. This choice ensures that the Gutzwiller projected state has periodic boundary conditions, while the underlying electronic system has periodic or anti-periodic boundary conditions.

a. Unperturbed FCI ($\mu = 0$)

We use ED, as discussed in Appendix B 3, in order to obtain the rank of the overlap matrix for the FCI in different system sizes. In contrast to MC where we need to perform an independent calculation for each matrix element of the overlap matrix, as explained in Appendix A 2, in the case of ED it is enough to compute the four Gutzwiller projected states $P_G\left[|\psi_\uparrow^{(\Phi_x,\Phi_y)}\rangle \otimes |\psi_\downarrow^{(\Phi_x,\Phi_y)}\rangle\right]$ for different combinations of phases (Φ_x, Φ_y). The full overlap matrix is then straightforwardly obtained by simply computing the scalar products of these states.

The expected topological degeneracy for the FCI is 2. For system sizes with odd N_x, there are indeed two pairs of linearly dependent states, thus an exact twofold degeneracy. This exact degeneracy is due to the dressed particle-hole symmetry of the CI model which relates states with different boundary conditions (Φ_x, Φ_y) and (Φ'_x, Φ'_y) in accordance with Eq. (B6). However, when N_x is even all states are linearly independent and the overlap matrix rank is equal to 4. In this case, each of the four states is mapped to itself by the PH conjugation. It is important to note that for even N_x there are two eigenvalues approximately equal to 2 and two very small eigenvalues (see Fig. S4(b) and (c) for $\mu = 0$). As will be shown in the next subsection, the two largest eigenvalues are approaching 2 with increasing system size, while the two smallest eigenvalues are decreasing towards zero. This points to the conclusion that the overlap matrix rank will be equal to 2 in the thermodynamic limit, as expected.

We note that we first normalize the states obtained by the Gutzwiller projection of two copies of the CI ground state and then generate the overlap matrix and compute its rank. This may lead to numerical inaccuracy in larger systems where the weight of the Gutzwiller projected state is small, as numerical errors might be significantly amplified by normalization. It is also possible to generate the overlap matrix using unnormalized states. However, the trace of the overlap matrix will no longer be equal to its dimension in that case.

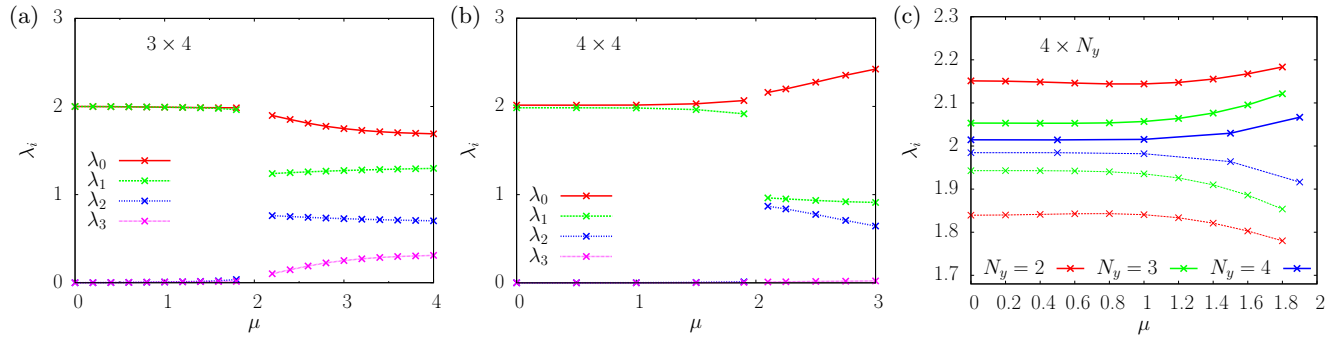

FIG. S4. Eigenvalues of the overlap matrix computed from ED for the FCI as a function of the staggered chemical potential μ for different system sizes. In all cases, the chemical potential is the same in both copies of the CI wave function underlying the FCI. The size of the torus is in (a) 3×4 and in (b) 4×4. In both cases, the overlap matrix for $\mu < \mu_c = 2$ has two very small eigenvalues and two eigenvalues close to 2, indicating a topological degeneracy of 2 as expected for the FCI. The phase transition at $\mu_c = 2$ is clearly visible in the discontinuity of some eigenvalues, with an *a priori* unclear phase for $\mu > \mu_c$ (see text). In (c), comparison of the scaling of the two largest overlap matrix eigenvalues for three different system sizes $4 \times N_y$ with $N_y \in \{2, 3, 4\}$ in the FCI phase with $\mu < \mu_c = 2$. The eigenvalues approach the value 2 with increasing N_y, implying due to the conserved trace of the overlap matrix that the remaining two eigenvalues (not shown) approach the value 0.

b. Staggered chemical potential

We also consider the effect of staggered chemical potential μ on the eigenvalues and the rank of the overlap matrix. The key idea is to move away from the dressed PH symmetry at $\mu = 0$ that enforces exactly two linearly independent states for odd N_x, knowing the nature of the FCI should be unchanged. We again consider the FCI with PBC in both directions and perform ED.

The eigenvalues λ_i of the overlap matrix as a function of μ for two different system sizes can be observed in Fig. S4(a) and (b). In both cases, some of the eigenvalues clearly have a discontinuity at $\mu_c = 2$. As previously discussed in Sec. B 1, a staggered potential larger than the critical value $\mu_c = 2$ trivializes the CI model. The number of nonzero eigenvalues (rank of the overlap matrix) in the region $\mu > 2$ is 4. However, the same is formally true even in the FCI phase, except for odd N_x at $\mu = 0$ where there is an exact degeneracy due to the dressed PH symmetry. As already discussed in the previous subsection for even N_x and $\mu = 0$, the main difference is that in the topological phase there are two very small eigenvalues and two eigenvalues of the overlap matrix close to 2. Fig. S4(c) shows the scaling of the two largest overlap matrix eigenvalues for system sizes with even N_x. The two largest eigenvalues are approaching the value 2 with increasing system size. At the same time, the other two eigenvalues are decreasing towards zero (not shown here), as the sum of all eigenvalues must be exactly 4. These results suggest that the rank of of the overlap matrix in the FCI phase is 2 in the thermodynamic limit.

We note that the Gutzwiller projection for $\mu > 2$ might not be meaningful. In the limit of large μ, all the particles are located at B sites in the CI ground state. The Gutzwiller projection removes double occupancies, meaning that the projected state in the high-μ region will consist only of particle fluctuations. These fluctuations are then squared during the overlap matrix calculation, which may further lead to numerical instability. We therefore cannot infer the nature of the phase beyond $\mu_c = 2$. In contrast, the Gutzwiller projection of two CI ground state copies with opposite μ is well defined, as there are no doubly occupied sites in the $\mu \to \infty$ limit: one copy has the electrons sitting on A sites while the other copy has its electrons sitting on B sites. The Gutzwiller projected state is this a perfect Mott insulator. However, the TEE calculations in Appendix B 3 have shown that the FCI is not stable to the addition of opposite staggered chemical potential in the two CI copies. Although the system is in that case clearly in the trivial phase for $\mu > 2$, the nature of the phase for a Gutzwiller projection of two states with opposite μ is unknown for $\mu < 2$.

Appendix C: Chiral hinge HOTI

In this appendix, we revisit the non-interacting chiral hinge HOTI [10] whose Gutzwiller projection leads to the FCHI wave function studied in the main text. We begin in Sec. C 1 with a quick review of the tight-binding Hamiltonian. In Sec. C 2, we then characterize the non-interacting hinge states via their EE and particle number fluctuations analogously to the analysis of the FCHI hinge modes in the main text. This allows us to test our MC methods on a

similar system where a direct, non-interacting, calculation is available.

1. Tight-binding model

The second-order chiral hinge TI was introduced using a band structure which can be realized both in a tight-binding model for spin-1/2 electrons as well as an optical lattice set-up with spinless fermions [10]. Here, we study a variant of the latter realization with an additional staggered chemical potential of magnitude μ. The model is described by a local Hamiltonian for spinless fermions on the cubic lattice with four sites per unit cell lying in the xy plane, labeled 1 to 4 as sketched in Fig. 1(a) of the main text. In this plane, sites in the same unit cell are connected by a nearest-neighbour hopping M, whereas sites in adjacent unit cells are connected by a nearest-neighbour hopping Δ_1. Additionally, there is a π-flux through each plaquette in the xy-plane. In the z-direction, adjacent unit cells are connected by a real next-nearest neighbour hopping $-\Delta_2/2$, and a purely imaginary nearest neighbour hopping with value $-i\Delta_2/2$. In addition, we consider a staggered chemical potential with $+\mu$ on sites 1 and 2 and $-\mu$ on sites 3 and 4. All in all, the Bloch Hamiltonian of this model is

$$\begin{aligned} H(k_x,k_y,k_z) = &\left[M+\Delta_1\cos(k_x)-\Delta_2\cos(k_z)\right]\tau_x\sigma_0 + \left[M+\Delta_1\cos(k_y)-\Delta_2\cos(k_z)\right](-\tau_y\sigma_y) \\ &+\Delta_1\sin(k_x)\,(-\tau_y\sigma_z)+\Delta_1\sin(k_y)\,(-\tau_y\sigma_x)+\left[\mu-\Delta_2\sin(k_z)\right](\tau_z\sigma_0)\,, \end{aligned} \tag{C1}$$

where $\tau_x,\tau_y,\tau_z,\sigma_x,\sigma_y,\sigma_z$ are the Pauli matrices and σ_0 the identity matrix acting on the sublattice degree of freedom. The valence and conduction bands of the CHI model are doubly degenerate with energies $\pm\epsilon$, where

$$\epsilon^2 = \left[M+\Delta_1\cos(k_x)-\Delta_2\cos(k_z)\right]^2+\left[M+\Delta_1\cos(k_y)-\Delta_2\cos(k_z)\right]^2+\Delta_1^2\left[\sin(k_x)^2+\sin(k_y)^2\right]+(\mu-\Delta_2\sin(k_z))^2. \tag{C2}$$

We consider the model at half filling $\nu=1/2$.

Note that the CHI model in the topological phase can be seen as a trivial-to-topological dipole pumping interpolation of the topological quadrupole model of Refs. [8, 9]. Indeed, for each fixed k_z, the Bloch Hamiltonian of Eq. (C1) for $\mu=0$ defines an instance of the two-dimensional quadrupole model with a staggered chemical potential. With the notation of Eq. (VI.55) of Ref. [9], the Hamiltonian parameters $\delta(k_z)$, $\lambda(k_z)$ and $\gamma(k_z)$ of this two-dimensional model at fixed k_z are related to the parameters M, Δ_1 and Δ_2 of the three-dimensional model as

$$\delta(k_z) = -\Delta_2\sin(k_z), \tag{C3a}$$

$$\lambda = \Delta_1, \tag{C3b}$$

$$\gamma(k_z) = M-\Delta_2\cos(k_z). \tag{C3c}$$

For $M=\Delta_1=\Delta_2=1$ and $\mu=0$, the CHI model is in its topological phase: Indeed, the parameters of the quadrupole model at $k_z=0$ are $(\delta,\lambda,\gamma)=(0,1,0)$, so we get the obstructed atomic limit phase of the quadrupole model. For $k_z=\pi$, the parameters are $(\delta,\lambda,\gamma)=(0,1,2)$, so the model is in the trivial phase of the quadrupole model. Therefore, the CHI model realizes a trivial-to-topological interpolation of the topological quadrupole model, under which the corner states of the quadrupole model map to the hinge states of the CHI model.

At $\mu=0$, the topological phase of the CHI model around the point $M=\Delta_1=\Delta_2=1$ is bordered by phase transitions lines when $\Delta_2/M=\Delta_1/M\pm1$ and $\Delta_2/M=-\Delta_1/M\pm1$. At these parameter values, the minimal direct gap

$$\Delta_E \equiv \min_{k_x,k_y,k_z}\epsilon(k_x,k_y,k_z) \tag{C4}$$

of the CHI Hamiltonian of Eq. (C1) closes. This can be seen in Fig. S5(a), where we show the inverse of the minimal direct gap in units of M. The horizontal and vertical correlation lengths ξ_x (which is equal to ξ_y) and ξ_z shown in Fig. S5(b) and (c), respectively, diverge around the phase transition lines. Note that due to the intrinsic anisotropy of the CHI model, the correlation lengths in the vertical z direction and the horizontal x and y directions do not need to be identical. The minimal direct gap reaches its maximal value $\sqrt{2}$ for parameters $\Delta_2/M=\Delta_1/M\geq2$. However, the smallest value of the larger of the two correlation lengths, $\max(\xi_x,\xi_z)$ shown in Fig. S5(d), is obtained for parameter values close to $\Delta_2/M=\Delta_1/M=1$. Since we want to minimize the finite-size effects, we therefore always choose $M=\Delta_1=\Delta_2=1$.

Increasing μ away from zero at half filling leads to a trivialization of the model for μ larger than a critical value μ_c. For $M=\Delta_1=\Delta_2=1$, the single-particle gap closes at $\mu_c=1$. As expected, the correlation length of the CHI ground state diverges as μ approaches μ_c, but stays reasonably small for values $\mu\leq1/2$ (see Fig.S6).

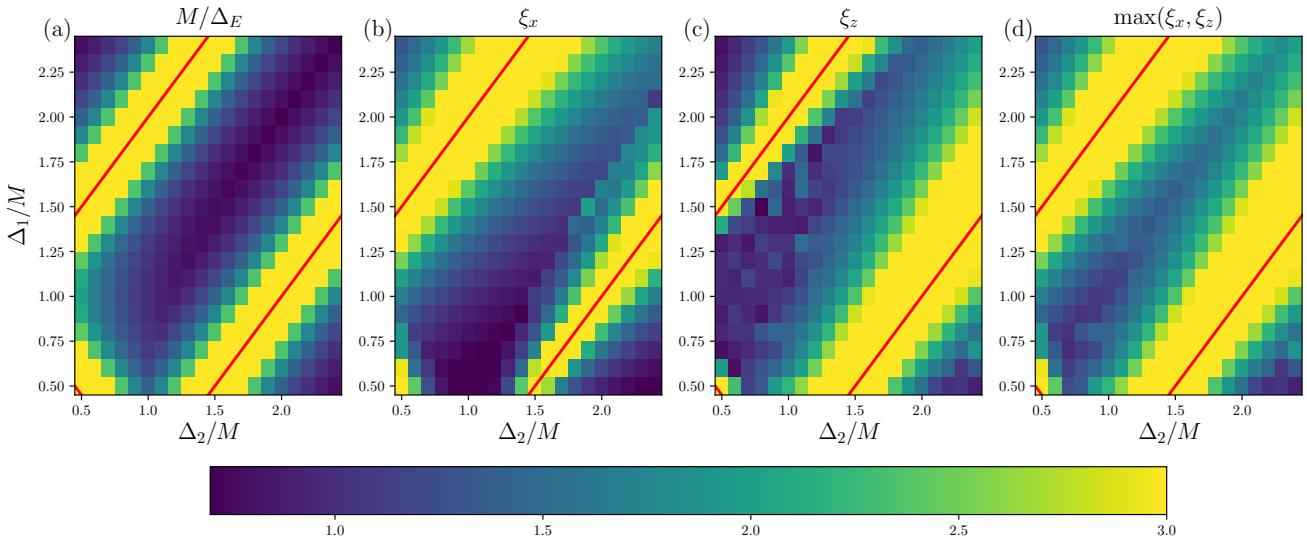

FIG. S5. Inverse gap and correlation lengths of the CHI model of Eq. (C1) for different Hamiltonian couplings Δ_1/M and Δ_2/M when $\mu = 0$. The model in in its topological phase in the region around the point $M = \Delta_1 = \Delta_2 = 1$, bordered by phase transitions when $\Delta_2/M = \Delta_1/M \pm 1$ and $\Delta_2/M = -\Delta_1/M \pm 1$ (marked by red lines). In (a), inverse of the minimal direct gap Δ_E in units of M, *i.e.* M/Δ_E. In (b) and (c), horizontal and vertical correlation lengths $\xi_x (= \xi_y)$ and ξ_z, respectively, in units of unit cells and computed from the two-point correlation function. In (d), the largest correlation length $\max(\xi_x, \xi_z)$, which attains its minimal value close to the point $\Delta_1/M = \Delta_2/M = 1$.

The CHI model is invariant under the product $C_4^z\mathcal{T}$ of the fourfold rotation C_4^z and time reversal $\mathcal{T}$ [10]. This is the symmetry which protects the higher-order topological phase. In addition, the model is invariant under the product $I\mathcal{T}$ with the inversion I [10].

Similarly to the 2D case discussed in Appendix B 1 a, on the 3D torus we can also consider the CHI with twisted boundary conditions set by phases Φ_x, Φ_y and Φ_z that a particle should pick up on a loop in x, y and z direction, respectively. These phases are implemented in the tight-binding model by multiplying all hopping terms in the positive x, y, and z directions with phases λ_x, λ_y, and λ_z, respectively, where

$$\lambda_x = e^{i\frac{\Phi_x}{2N_x}}, \tag{C5a}$$

$$\lambda_y = e^{i\frac{\Phi_y}{2N_y}}, \tag{C5b}$$

$$\lambda_z = e^{i\frac{\Phi_z}{N_z}}. \tag{C5c}$$

Correspondingly, hopping terms with a component in the negative x, y, and z directions are multiplied with the complex conjugate phases λ_x^*, λ_y^*, and λ_z^*.

2. Hinge state characterization

In the CHI ground state with open boundary conditions in the xy-directions, each of the four hinges parallel to the z-axis supports a single chiral mode localized at the hinge [10]. Since the CHI model is non-interacting, each hinge mode is expected to correspond to one free bosonic mode described by a CFT with central charge $c = 1$ and Luttinger parameter $K = 1$, analogous to the edge states of a non-interacting Chern insulator with Chern number $\mathcal{C} = 1$. In order to confirm this expectation, we numerically extract c and K from the EE and particle number fluctuations using the same geometry as in the main text for the FCHI hinge modes, see Fig. 1(b). This geometry is a 3D generalization of the "ribbon" geometry used for similar analyses of 2D edge states [46, 47, 53], see Fig. S2(a) and Appendix B 2. In both cases the cut is perpendicular to the hinge/edge modes, which results in contribution of these modes to the EE and the particle/spin fluctuations.

Since the CHI is a free-fermion model, the EE and particle number fluctuations can be computed efficiently using the correlation matrix (CorrM) method for free fermions. The results are shown in Fig. S7(a) for the second Renyi

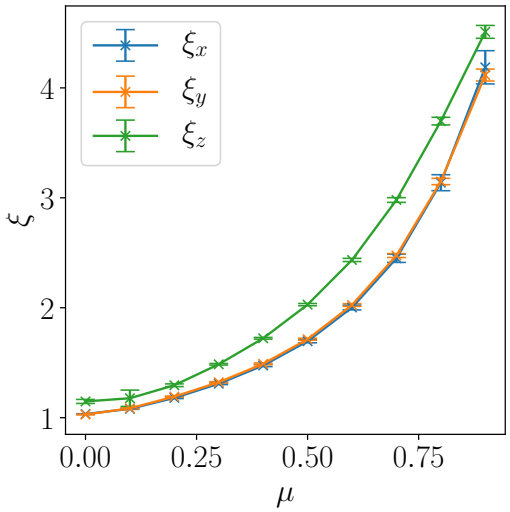

FIG. S6. Correlation lengths ξ_x , ξ_y and ξ_z (in units of the unit cell) for the two-point correlator of the CHI as a function of staggered chemical potential μ for $M = \Delta_1 = \Delta_2 = 1$.

entropy $S^{(2)}$, which is expected to obey the scaling of Eq. (3) with central charge $c = 1$,

$$S^{(2)}_{\mathcal{A}_{N_x,N_y,N_{z,\mathcal{A}}}}(N_{z,\mathcal{A}}) = \alpha + 4 \times S^{(2)}_{\text{crit}}(N_{z,\mathcal{A}}; N_z), \tag{C6}$$

where $S^{(2)}_{\text{crit}}(N_{z,\mathcal{A}}; N_z)$ is given by Eq. (4) and the factor 4 comes from the number of hinge modes. From Fig. S7(a) we see that the data agree very well with this prediction, where the observed value for the central charge is $c = 0.98$. The numerical value for c is in even closer agreement with the expected value $c = 1$ for bigger system sizes.

Analogously to the main text and Appendix B 2 where we considered the variance $\text{Var}(M_{\mathcal{A}})$ (B9) of the number $M_{\mathcal{A}}$ of spin up particles in the region $\mathcal{A}$, we now consider the variance of the number of particles $\tilde{M}_{\mathcal{A}}$ (note that the particles are "spinless" in the non-interacting CHI model and we have a single copy):

$$\text{Var}(\tilde{M}_{\mathcal{A}_{N_x,N_y,N_{z,\mathcal{A}}}}) \equiv \langle \tilde{M}^2_{\mathcal{A}_{N_x,N_y,N_{z,\mathcal{A}}}} \rangle - \langle \tilde{M}_{\mathcal{A}_{N_x,N_y,N_{z,\mathcal{A}}}} \rangle^2. \tag{C7}$$

The Luttinger parameter K for the hinge modes of the CHI can be extracted from the scaling of the particle number fluctuations. Note that for the non-interacting CHI, the particle number fluctuations $\text{Var}(\tilde{M}_{\mathcal{A}_{N_x,N_y,N_{z,\mathcal{A}}}})$ give access to a conserved current analogous to the spin fluctuations $\text{Var}(M_{\mathcal{A}_{N_x,N_y,N_{z,\mathcal{A}}}})$ for the fractional CHI as studied in the main text. Therefore, $\text{Var}(\tilde{M}_{\mathcal{A}_{N_x,N_y,N_{z,\mathcal{A}}}})$ in the CHI is expected to scale according to Eq. (6) with Luttinger parameter $K = 1$:

$$\text{Var}(\tilde{M}_{\mathcal{A}_{N_x,N_y,N_{z,\mathcal{A}}}}) = 2 \times \frac{K}{\pi^2} \ln\left[\frac{N_z}{\pi} \sin\left(\frac{\pi N_{z,\mathcal{A}}}{N_z}\right)\right] + \alpha'. \tag{C8}$$

From Fig. S7(b) we see that the data agree very well with this expectation, where the observed value of the Luttinger parameter $K = 0.99$ is very close to the expected value $K = 1$.

Moreover, we can use this geometry to benchmark our MC algorithm on a 3D system of similar size and nature as the FCHI studied in the main text. To that end, we compare the results for the EE obtained from the CorrM computation to those obtained from the MC algorithm, as sketched in Fig. S7(c) for a system of size $2 \times 2 \times 20$. It is clear that the results obtained from the two techniques are in very good agreement. Furthermore, in Fig. S7(d) we show how the MC result for the entanglement entropy is obtained by addition of the contributions stemming from the amplitude and the phase of the wave function (*cf.* Appendix A). For the CHI, the amplitude contribution is dominant and contributes more significantly to the logarithmic hinge scaling.

Note that the computation of the EE via MC in this geometry is feasible only for systems which have a small cross section in the xy plane. Indeed, for larger cross sections, the area law contribution contained in the constant α quickly grows such that the EE can no longer be computed in MC due to exponentially long convergence times

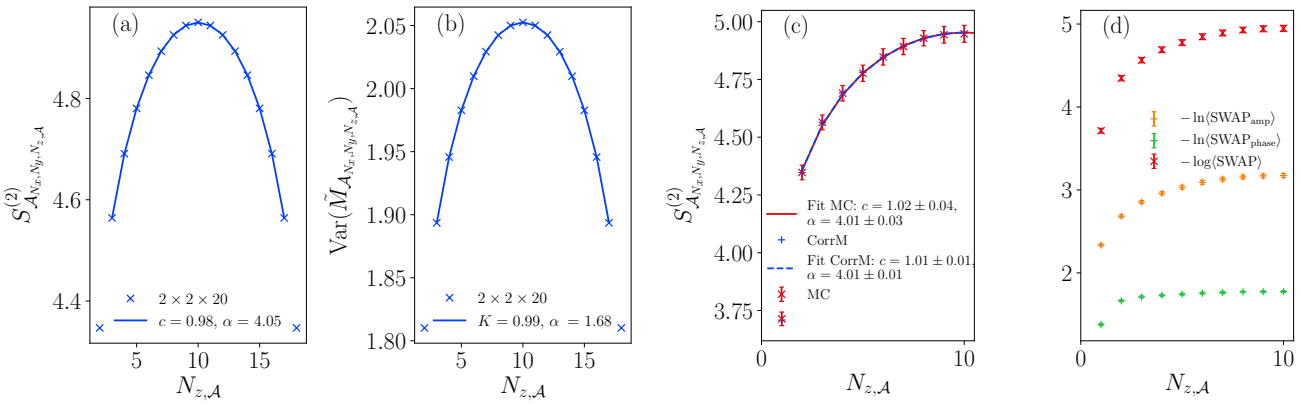

FIG. S7. Numerical extraction of the central charge c and Luttinger parameter K of the CFT describing the chiral hinge modes of the non-interacting CHI. In (a), scaling of the second Renyi entropy as computed from the CorrM technique fit to the prediction of Eq. (C6), and in (b), scaling of the particle number fluctuations as computed from the CorrM technique fit to the prediction of Eq. (C8) *w.r.t.* the series of subsystems $\mathcal{A}_{N_x,N_y,N_{z,\mathcal{A}}}$ as a function of $N_{z,\mathcal{A}}$. In (c), comparison of the MC results for the EE with those from the CorrM technique. In (d), formation of the MC result for the EE by addition of the contributions from the amplitude and phase of the wave function (*cf.* Appendix A). In all cases, the system has open boundary conditions and $N_x = 2$, $N_y = 2$ unit cells in the x, y directions, and periodic boundary conditions and $N_z = 20$ unit cells in the z direction.

(*cf.* Appendix A). The data presented in Fig. S7 show that the correlation length of the CHI model is sufficiently small that a cross section of 2×2 is already big enough to extract the universal properties of the hinge states, despite a finite hinge state hybridization which is estimated around 0.57 in a system of size $2 \times 2 \times N_z$ (assuming an exponential localization of the hinge modes in the x and y directions).

Appendix D: Topological degeneracy of the Fractional Chiral Hinge Insulator

In this appendix, we present our results for the topological degeneracy of the fractional chiral hinge insulator (FCHI). We begin in Appendix D 1 with a description of our approach and a discussion of topological degeneracy for 3D systems. We then proceed to present our results for the topological degeneracy of the FCHI in isotropic geometries in Appendix D 2, and for anisotropic geometries with $N_z > N_x, N_y$ in Appendix D 3. Finally, in Appendix D 4 we discuss the topological degeneracy of the FCHI with open boundary conditions in the x direction and periodic boundary conditions in the y and z directions.

1. Topological degeneracy for 3D systems

In order to characterize the topological degeneracy of the FCHI, we consider a set of ansatz states obtained by Gutzwiller projection of the non-interacting CHI wave function with different boundary conditions for the underlying electronic degrees of freedom, and compute the number of linearly independent states among them. We are following the same procedure described in Appendix B 4 for a FCI. Concretely, to compute the topological degeneracy on the three-torus we consider the non-interacting wave function with periodic boundary conditions (PBC) or anti-periodic boundary conditions (APBC) in each direction. Indeed, both PBC and APBC for fermions lead to PBC for the Gutzwiller projected state. This yields eight ansatz states for the FCHI on the three-torus.

In keeping with the notation from the main text, we denote by $|\psi_s^{(\Phi_x,\Phi_y,\Phi_z)}\rangle$ the ground state of the non-interacting CHI model with twisted boundary conditions $\Phi_x, \Phi_y, \Phi_z \in \{0, \pi\}$ corresponding to PBC and APBC, respectively, and with spin $s \in \{\uparrow, \downarrow\}$. The fractional wave function obtained by Gutzwiller projection of two copies of the non-interacting wave function with the same flux insertions but with opposite spin is denoted

$$|\Psi^{(\Phi_x,\Phi_y,\Phi_z)}\rangle = P_G \left[|\psi_\uparrow^{(\Phi_x,\Phi_y,\Phi_z)}\rangle \otimes |\psi_\downarrow^{(\Phi_x,\Phi_y,\Phi_z)}\rangle \right]. \tag{D1}$$

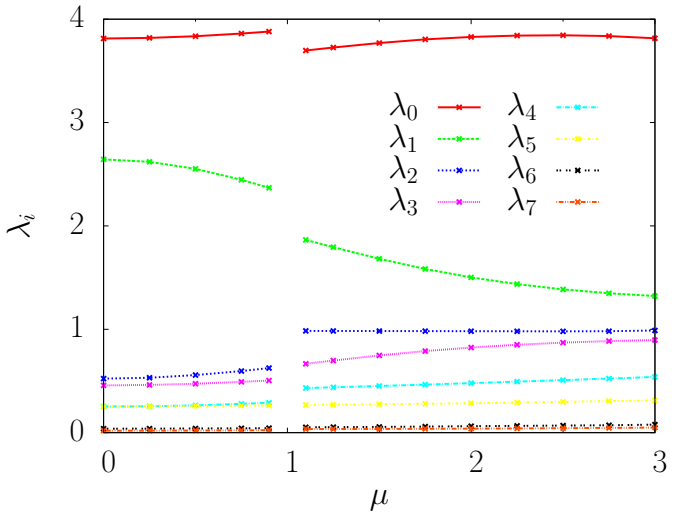

FIG. S8. Overlap matrix eigenvalues (λ_0 to λ_7) as a function of staggered chemical potential μ for the FCHI on a three-torus. The system size is $2 \times 2 \times 2$ unit cells.

In order to determine the topological degeneracy, we need to compute the rank of the overlap matrix $\mathcal{O}$, whose entries

$$\mathcal{O}_{(\Phi_x,\Phi_y,\Phi_z),(\Phi'_x,\Phi'_y,\Phi'_z)} = \frac{\left\langle \Psi^{(\Phi_x,\Phi_y,\Phi_z)} | \Psi^{(\Phi'_x,\Phi'_y,\Phi'_z)} \right\rangle}{\sqrt{\left\langle \Psi^{(\Phi_x,\Phi_y,\Phi_z)} | \Psi^{(\Phi_x,\Phi_y,\Phi_z)} \right\rangle} \sqrt{\left\langle \Psi^{(\Phi'_x,\Phi'_y,\Phi'_z)} | \Psi^{(\Phi'_x,\Phi'_y,\Phi'_z)} \right\rangle}}. \tag{D2}$$

contain the overlap between the normalised ansatz states for the FCHI. Since we start with eight ansatz states, the rank of the overlap matrix can be at most equal to eight. In the following, we study if this maximal rank is saturated or if there are linear dependencies between the ansatz states leading to a reduction of its rank.

2. Isotropic case

a. Stability under staggered chemical potential μ for $2 \times 2 \times 2$

As we already did for the FCI in Appendix B 4 b, we now consider the effect of a staggered chemical potential μ as defined in Eq. (C1) on the eigenvalues of the overlap matrix for the FCHI on a three-torus. Here, the chemical potential μ is the same in both copies of the non-interacting CHI underlying the FCHI wave function. We study a system of size $2 \times 2 \times 2$ unit cells and perform ED. The computation of the overlap matrix elements is simpler using ED compared to MC, as previously discussed in Appendix B 4 a.

The overlap matrix eigenvalues as a function of the staggered chemical potential μ are shown in Fig. S8. Similar to the case of the FCI, most of the eigenvalues are obviously discontinuous at $\mu_c = 1$. This is the critical point where the underlying CHI model becomes trivial, see Appendix C 1. This is a very small system and there are no exact degeneracies, therefore it is expected that the finite size overlap matrix rank is equal to the maximal value 8. However, the separation between sets of eigenvalues is not as clear as for the FCI case, albeit the two largest eigenvalues stand out from the rest. For the FCHI case we cannot explore the scaling of overlap matrix eigenvalues with the system size using ED, as $2 \times 2 \times 2$ is the largest system accessible to this method. Larger systems will be studied in the following sections using MC computations.

We again emphasize that the Gutzwiller projection in the limit of large μ might not be meaningful: all the particles are (mostly) located on the same sites (3 and 4) in both CHI copies and the Gutzwiller projection excludes double occupancies thus leaving only particle fluctuations. This was discussed in more details in Appendix B 4 b. In particular, we have not investigated the opposite staggered chemical potential for FCHI as we have shown this was not physically meaningful in the "topological" regime for the FCI (see Appendix B 3).

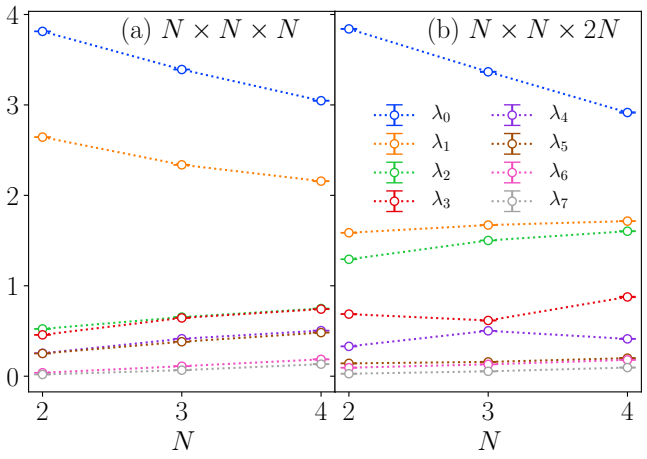

FIG. S9. Scaling of the overlap matrix eigenvalues for the FCHI on a three-torus for isotropic systems of size $N \times N \times N$ in (a) and size $N \times N \times 2N$ in (b).

b. Larger systems at $\mu = 0$

We now move on to bigger systems, which are accessible only via MC computations. Focusing solely on $\mu = 0$, we attempt to study the overlap matrix eigenvalues of the FCHI if we increase the system size in an isotropic fashion. We consider two cases: on one hand, a system of $N \times N \times N$ unit cells, and on the other hand, a system of $N \times N \times 2N$ unit cells (where the number of lattice sites in each direction is equal since the unit cell contains two sites in the horizontal x and y directions, but only a single site in the z direction). The results for the eigenvalues of the overlap matrix as computed from MC are sketched in Fig. S9(a) and (b) for these two cases, respectively. Due to the 3D setting and the large number of observables that we have to compute to obtain the full overlap matrix (*cf.* Appendix A), we are restricted to relatively small systems up to $N = 4$. For the biggest of these systems, the computations already consumed a considerable number of CPU hours (see Appendix E).

From the data presented in Fig. S9 we cannot infer a non-trivial reduction of the number of linearly independent states for the FCHI in the thermodynamic limit for isotropic systems. Indeed, it appears that the largest eigenvalue is decreasing as N increases, whereas the smaller eigenvalues appear to increase. This would indicate that the number of linearly independent states is equal to 8 which is the maximal number given the size of the overlap matrix. However, it is possible that this is a finite size effect and that the result differs for bigger systems which are not accessible in numerical computations.

3. Anisotropic case

In addition to the isotropic case, we also studied the topological degeneracy of the FCHI for anisotropic systems, where $N_x = N_y$ such that the C_4 rotation symmetry in the horizontal plane is preserved, but where N_z is larger than N_x and N_y. Note that this is the aspect ratio which we used in the main text to study the hinge mode physics, albeit with open instead of periodic boundary conditions in the horizontal directions.

In contrast to the isotropic case, for anisotropic systems the ground state degeneracy is reduced if N_z is much larger than N_x and N_y. Indeed, the normalized overlap between the two ansatz states $|\Psi^{(\Phi_x,\Phi_y,0)}\rangle$ and $|\Psi^{(\Phi_x,\Phi_y,\pi)}\rangle$, with the same fluxes (Φ_x, Φ_y) in the horizontal directions but differing flux in the z direction, approaches unity *exponentially* fast as N_z increases. This is shown in Fig. S10(a) and (d) for systems of size $2 \times 2 \times N_z$ and $3 \times 3 \times N_z$, respectively. This implies that the two ansatz states $|\Psi^{(\Phi_x,\Phi_y,0)}\rangle$ and $|\Psi^{(\Phi_x,\Phi_y,\pi)}\rangle$ become linearly dependent in the limit $N_z \to \infty$. Since there are four different flux patterns (Φ_x, Φ_y) in the horizontal directions, in the limit $N_z \to \infty$ the 8 ansatz states split into four pairs, where the two states in each pair have the same (Φ_x, Φ_y) and are linearly dependent.

We note that a similar phenomenon occurs for the non-interacting CHI whose ground states generate the FCHI ansatz states by Gutzwiller projection. Indeed, we have checked for several fixed values of $N_x = N_y$ that the overlap

$$\left| \left\langle \psi_s^{(\Phi_x,\Phi_y,0)} | \psi_s^{(\Phi_x,\Phi_y,\pi)} \right\rangle \right|^2 \tag{D3}$$

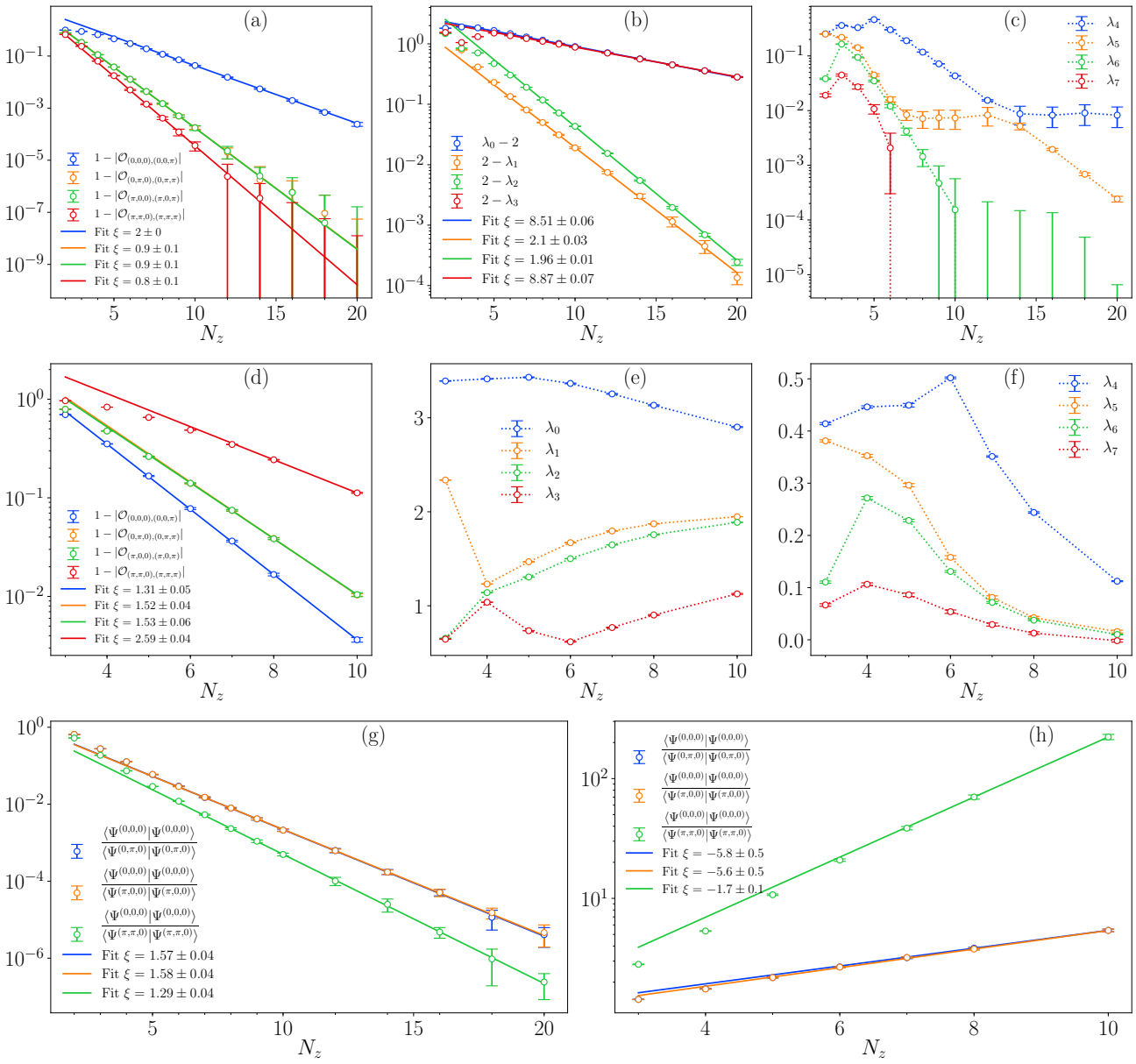

FIG. S10. Characterization of the overlap matrix in the anisotropic limit for systems of size $2 \times 2 \times N_z$ in (a), (b), (c) and (g), and for systems of size $3 \times 3 \times N_z$ in (d), (e), (f) and (h). Where possible, we have fit the data to an exponential decay of the form $ue^{-iN_z/\xi}$ with a "correlation length" ξ in units of unit cells and an amplitude u (not shown). In (a) and (d), we find an exponentially fast approach to the value 1 of the normalised overlap between states differing only by a π-flux in the z direction, showing that the states become identical in the limit $N_z \to \infty$. In (b) and (e), scaling of the four largest eigenvalues of the overlap matrix as a function of N_z. Note that in (b), we show the difference from the value 2 of the eigenvalues on a logarithmic scale to demonstrate the exponential approach to the value 2. In (c) and (f), scaling of the four smallest eigenvalues of the overlap matrix. In (g) and (h), ratio of the norms of the ansatz states with vanishing flux in the z direction after Gutzwiller projection but before normalization. For N_x, N_y even, the norms of the states with zero or only a single π-flux in the horizontal directions are exponentially suppressed compared to the weight of the states with π-fluxes in both horizontal directions. For N_x, N_y odd, the weights of states with at least one π-flux in the horizontal directions are exponentially suppressed compared to the weight of the state without any π-fluxes. Note that the exponential growth in (h) corresponds to negative values of the fitted correlation length ξ.

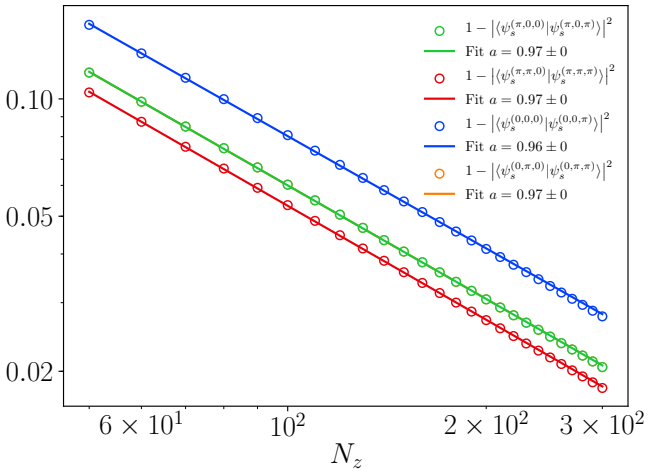

FIG. S11. Difference from unity of the squared overlap $|\langle\psi_s^{(\Phi_x,\Phi_y,0)}|\psi_s^{(\Phi_x,\Phi_y,\pi)}\rangle|^2$ between the normalised many-body non-interacting CHI ground states with the same fluxes (Φ_x, Φ_y) in the horizontal directions but differing flux in the z direction in the anisotropic limit for a system of size $2 \times 2 \times N_z$. The data is fit to an algebraic decay $b \times N_z^{-a}$ with power a.

between the normalised many-body non-interacting ground states with the same fluxes (Φ_x, Φ_y) in the horizontal directions but differing flux in the z direction also approaches unity as N_z increases. One example for systems of size $2 \times 2 \times N_z$ is shown in Fig. S11. (Note that for two non-interacting many-body states $|\psi_s^{(\Phi_x,\Phi_y,0)}\rangle$ and $|\psi_s^{(\Phi_x,\Phi_y,\pi)}\rangle$ their square overlap can easily be computed as the determinant of the sum of their correlation matrices). This implies that the two states $|\psi_s^{(\Phi_x,\Phi_y,0)}\rangle$ and $|\psi_s^{(\Phi_x,\Phi_y,\pi)}\rangle$ become identical in the limit $N_z \to \infty$. However, we have observed that for the non-interacting model this convergence to the value one is *algebraic* and thus much slower than for the FCHI, where the overlap approaches one exponentially. Therefore, we believe that the behavior shown in Fig. S10(a) and (d) is qualitatively new and reserved to the interacting wave function.

As a result of the linear dependencies between the FCHI ansatz states for N_z much larger than N_x and N_y, the ground state degeneracy of the FCHI in this case can be at most four. As shown in Fig. S10(b) and (e), the four larger eigenvalues of the overlap matrix approach a non-zero value as N_z increases, implying that the four different horizontal flux combinations generate four linearly independent ansatz states. On the other hand, the four smaller eigenvalues go to zero exponentially fast with increasing N_z as shown in Fig. S10(c) and (f). It is interesting to note that the four largest eigenvalues all approach the same value $\lambda = 2$ exponentially. This is a similar behavior as for the FCI, where the two non-zero eigenvalues also approach the same value in the thermodynamic limit (*cf.* Appendix B 4). However, we have not found any arguments indicating that the asymptotic degeneracy of all non-zero eigenvalues of the overlap matrix contains information on the topology of a system.

In the discussion above, we have always considered the normalized overlap matrix, which measures the topological degeneracy on the manifold of *normalized* ansatz states. In other words, we have defined different ansatz states for the interacting model by projecting the wave function of the non-interacting model, normalizing each ansatz state separately and only then considering linear dependencies.

However, it may also be valid to follow a different approach where one considers the linear independence of the *unnormalized* ansatz states for the interacting model. In other words, one considers linear combinations of the ansatz states after the Gutzwiller projection but before normalization. In the thermodynamic limit, this may lead to a different result for the rank of the overlap matrix if the different unnormalized ansatz states for the interacting model have very different weights. Indeed, this is the case here as shown in Fig. S10(g) and (h) for systems of size $2 \times 2 \times N_z$ and $3 \times 3 \times N_z$, respectively. In both cases, there is one out of the four horizontal flux combinations, denoted (Φ_x^0, Φ_y^0), for which the corresponding ansatz states $|\Psi^{(\Phi_x^0,\Phi_y^0,\Phi_z)}\rangle$ have a weight which grows exponentially with increasing N_z compared to the weights of the ansatz states obtained for the other three horizontal flux combinations. Note that the weights of $|\Psi^{(\Phi_x^0,\Phi_y^0,0)}\rangle$ and $|\Psi^{(\Phi_x^0,\Phi_y^0,\pi)}\rangle$ are asymptotically identical. This dominant horizontal flux combination (Φ_x^0, Φ_y^0) is staggered in N_x and N_y, where

$$(\Phi_x^0, \Phi_y^0) = \begin{cases} (\pi, \pi) & \text{for } N_x = N_y \text{ even} \\ (0, 0) & \text{for } N_x = N_y \text{ odd} \end{cases} . \tag{D4}$$

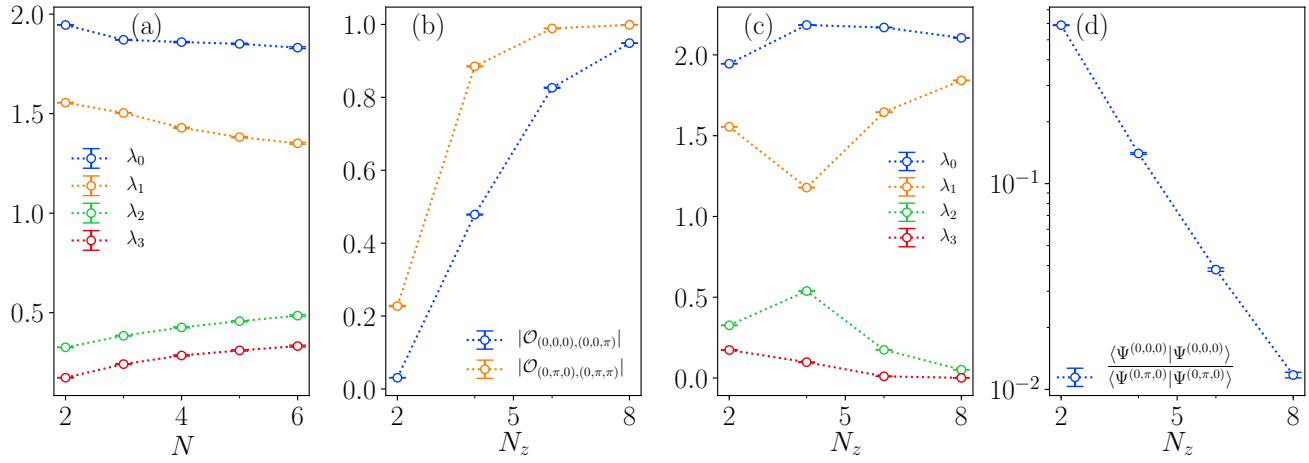

FIG. S12. Ground state degeneracy of the FCHI with OBC in the x direction and PBC in the y and z directions. In (a), overlap matrix eigenvalues for isotopic systems with $N \times N \times N$ unit cells. In (b) to (d), scaling of the overlap matrix for anisotropic systems of size $2 \times 2 \times N_z$ as a function of N_z. In (b), normalized overlap of states differing only by a π-flux in the z direction approaching the value one in the limit $N_z \to \infty$. In (c), overlap matrix eigenvalues. In (d), ratio of the norms of the two states with different fluxes in the the y direction and no flux in the z direction.

Following this approach, the ground state degeneracy is given by the rank of a rescaled overlap matrix $\tilde{\mathcal{O}}$ with entries

$$\tilde{\mathcal{O}}_{(\Phi_x,\Phi_y,\Phi_z),(\Phi'_x,\Phi'_y,\Phi'_z)} = \frac{\left\langle \Psi^{(\Phi_x,\Phi_y,\Phi_z)} \middle| \Psi^{(\Phi'_x,\Phi'_y,\Phi'_z)} \right\rangle}{\left\langle \Psi^{(\Phi^0_x,\Phi^0_y,0)} \middle| \Psi^{(\Phi^0_x,\Phi^0_y,0)} \right\rangle}. \tag{D5}$$

Note that the trace of the overlap matrix of the unnormalized ansatz states is not normalized to eight. Here, we have therefore normalized $\tilde{\mathcal{O}}$ *w.r.t.* the weight of the state with dominant horizontal flux combination, which allows for a meaningful comparison between the eigenvalues of $\tilde{\mathcal{O}}$ for different system sizes. For the anisotropic FCHI, the rescaled overlap matrix $\tilde{\mathcal{O}}$ has one dominant eigenvalue converging to the value $\lambda = 2$, and seven eigenvalues decaying exponentially to zero with different correlation lengths. Therefore, following this approach, the FCHI has only one ground state for N_z much larger than N_x and N_y. Note that for the isotropic case discussed above, the spectrum of the rescaled overlap matrix $\tilde{\mathcal{O}}$ is very similar to that of $\mathcal{O}$ for the system sizes we have studied.

The large difference in the weight of the ansatz states that we observe for the anisotropic FCHI does not appear to be a necessary consequence of the reduction of the rank of the overlap matrix to a value lower than 8 in the thermodynamic limit. For instance, for the FCI on the two-torus with 6×6 and 8×8 unit cells the construction discussed in Appendix B 4 yields four ansatz states with approximately the same weight, even though the rank of the overlap matrix is reduced from four to two. Therefore, for the FCI the normalised and the rescaled overlap matrix give the same result for the topological degeneracy.

4. OBC in x

Finally, let us discuss the topological degeneracy of the FCHI with OBC in the x direction and PBC in the other two directions. This is the configuration which we used in the main text to extract the TEE contributed by the gapped surface states. For these boundary conditions, we consider four ansatz states for the FCHI obtained by Gutzwiller projection of the non-interacting wave function with either PBC and APBC in the y and z directions. In the x direction, all four ansatz states have vanishing flux. Therefore, the overlap matrix $\mathcal{O}$ now has dimension four.

The results for the topological degeneracy of the FCHI with this boundary configuration are very similar to those discussed above for the 3D torus. We first increase the system size in an isotropic fashion. While there is a separation between two larger and two smaller eigenvalues, they seem to converge to a finite value as shown in Fig. S12(a). This indicates that for isotropic systems the maximum rank of the overlap matrix is saturated. However, as before we are restricted to relatively small systems (albeit bigger that the all PBC case discussed in Appendix D 2 due to the smaller number of overlaps to compute; note that the MC algorithm does not benefit from an intrinsic speedup due to PBC

like an exact diagonalization would). Therefore we cannot make any reliable statements about the thermodynamic limit.

On the other hand, for anisotropic systems the normalized overlap between two ansatz states $|\Psi^{(0,\Phi_y,0)}\rangle$ and $|\Psi^{(0,\Phi_y,\pi)}\rangle$, with the same flux Φ_y in the y direction but differing flux in the z direction, approaches unity as N_z increases. This is shown in Fig. S12(b) for systems of size $2 \times 2 \times N_z$. Correspondingly, as shown in Fig. S12(c) the normalised overlap matrix for N_z much larger than N_x and N_y has two finite eigenvalues converging to the value $\lambda = 2$, and two eigenvalues that vanish as N_z increases. Again, the weight of the ansatz states before normalisation is not the same, with the weight of the states with $\Phi_y = 0$ being exponentially suppressed compared to the weight of the states with $\Phi_y = \pi$ for $N_x = N_y = 2$ as shown in Fig. S12(d). This implies that the overlap matrix $\tilde{\mathcal{O}}$ computed from the ansatz states before normalization has one finite and 3 vanishing eigenvalues for N_z much larger than N_x and N_y.

Appendix E: Technical data for MC computations

In this appendix, we provide some technical details on our MC simulations. In Appendix E 1, we discuss the update used in the simulations, and in Appendix E 3 we give the technical parameters and run times for all computations whose results are presented in the main text.

1. Monte Carlo update

As discussed in the main text, charge fluctuations in the FCHI wave function are frozen out and the layer index (which will from now on be dubbed spin) is the only relevant degree of freedom on each site. The same holds for the FCI wave function studied in Appendix B. Therefore, our MC computations are performed in the basis of spin configurations $|v\rangle = |s_0, \ldots, s_{N-1}\rangle$ with $s_i \in \{\uparrow, \downarrow\}$ on each site $i = 0, \ldots, N-1$, where N is the total number of physical lattice sites. We used a single-spin-exchange update to suggest a new many-body configuration after each MC step. In other words, after each MC step, the configuration $|v\rangle$ is updated by exchanging the spin values s_i and s_j on two randomly chosen sites with opposite spin occupations $s_i \neq s_j$.

In order to improve the acceptance rate of the simulations, we limited the range of the spin exchange to an integer value r_{update}. Concretely, we require that the graph distance $d(i, j)$ on the relevant lattice of the two sites i, j should satisfy $d(i, j) \leq r_{\text{update}}$. Here, the relevant lattices are the cubic lattice for the FCHI and the square lattice for the FCI. Therefore, for $r_{\text{update}} = 1$ this permits spin exchange only between nearest-neighbour sites, whereas for $r_{\text{update}} = 2$ spin exchange both between nearest-neighbour and next-nearest-neighbour sites is allowed.

We have observed that the parameter r_{update} has a small systematic influence on the mean value of the MC simulations. For instance, Fig. S13 provides a comparison of the MC results for the spin fluctuations in the FCHI, as discussed in the main text, for different values $r_{\text{update}} = 2, 3, 4, \infty$. The data points for $r_{\text{update}} = 2$ do not agree within the statistical error bar with the data points for the most accurate measurement with $r_{\text{update}} = \infty$. However, for larger values $r_{\text{update}} = 3$ and 4, the data points quickly move much closer to those for $r_{\text{update}} = \infty$ and their statistical error bars overlap. Indeed, the fit values for the parameters K and α' agree within the statistical error bars for all four simulations. For all MC simulations presented in this paper, we chose r_{update} sufficiently big that the systematic deviation is insignificant compared to the statistical uncertainty, while increasing the acceptance rate as much as possible.

2. MC errors

Here, we briefly explain how we obtain the estimates for the errors of our MC measurements. For each MC measurement, we launched N_{seed} instances of the algorithm, with each instance having a distinct seed of the random number generator. Typically, we chose $N_{\text{seed}} = 100$. For each seed, the algorithm was performed until the Metropolis chain had a length of N_{MC} MC steps, after which we evaluated the average of each run separately. Then, we computed the final value and error of the MC measurement as the mean and standard deviation, respectively, of the collection of N_{seed} averages per run. Therefore, the final value is the average after $N_{\text{seed}} \times N_{MC}$ total MC steps.

In practice we have observed that the error estimated in this way is much larger than the fluctuations of the mean value of the measurements as a function of the number of MC steps after the initial convergence phase. For instance, in Fig. S14 we show the evolution of the mean value of the SWAP_{amp} observable of Eq. (A5a) for the four EE measurements required for the computation of the TEE of the FCHI, namely $S^{(2)}_{\mathcal{B}}$, $S^{(2)}_{\mathcal{AB}}$, $S^{(2)}_{\mathcal{AC}}$, $S^{(2)}_{\mathcal{ABC}}$ as defined

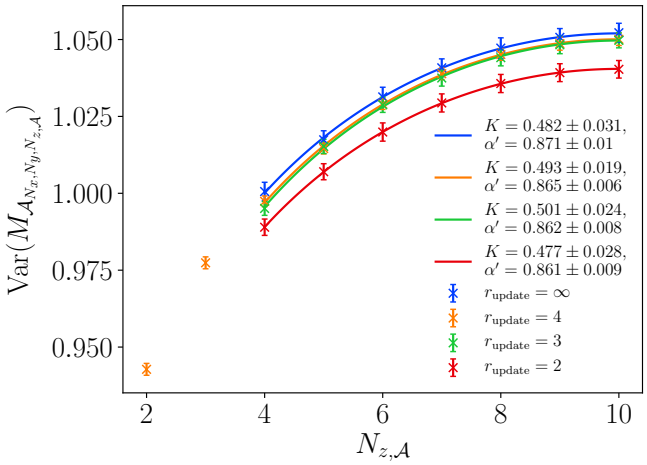

FIG. S13. MC results for computations with different r_{update} for the spin number variance $\mathrm{Var}(M_{\mathcal{A}_{N_x,N_y,N_{z,\mathcal{A}}}})$ in the subsystem $\mathcal{A}_{N_x,N_y,N_{z,\mathcal{A}}}$ of the FCHI as a function of $N_{z,\mathcal{A}}$, fit to the prediction of Eq. (6).

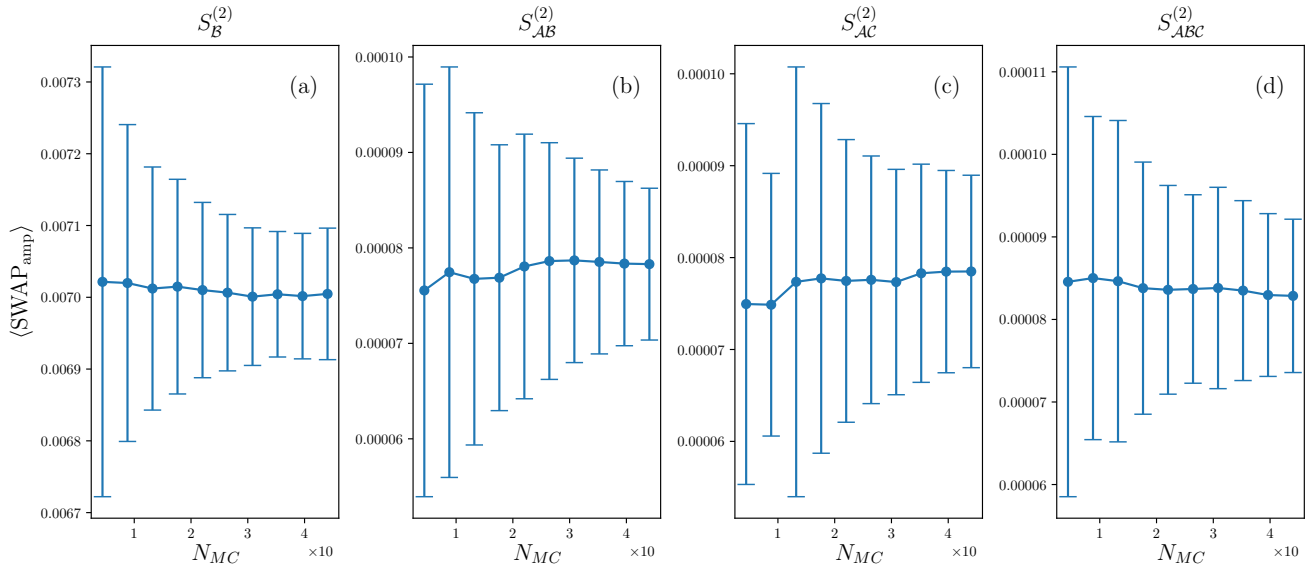

FIG. S14. Evolution of the mean value of the $\mathrm{SWAP}_{\mathrm{amp}}$ observable for the four EE measurements $S^{(2)}_{\mathcal{B}}$ in (a), $S^{(2)}_{\mathcal{AB}}$ in (b), $S^{(2)}_{\mathcal{AC}}$ in (c) and $S^{(2)}_{\mathcal{ABC}}$ in (d) required for the computation of the TEE of the FCHI with OBC in the x direction and PBC in the y and z directions. Here, the system has $2 \times 3 \times 5$ unit cells and the subsystems are rotated compared to Fig. 3(b) along the y axis such that they are translation invariant in the x direction. The fluctuations of the mean as a function of the number N_{MC} of MC steps per run are much smaller than the statistical error.

Physical observable	System size	Boundary conditions	MC observable	r_{update}	Acceptance rate [%]	MC Steps	Total CPU hours
$S^{(2)}_{\mathcal{A}_{N_x,N_y,N_{z,\mathcal{A}}}}$ in Fig. 2(a)	$2\times2\times20$	OBC × OBC × PBC	$\langle\text{SWAP}_{\text{amp}}\rangle$	2	3.6	10^8	115500
	$2\times2\times20$	OBC × OBC × PBC	$\langle\text{SWAP}_{\text{phase}}\rangle$	2	3.7	10^7	25000
	$3\times2\times20$	OBC × OBC × PBC	$\langle\text{SWAP}_{\text{amp}}\rangle$	2	2.1	1.2×10^8	383370
	$3\times2\times20$	OBC × OBC × PBC	$\langle\text{SWAP}_{\text{phase}}\rangle$	2	2.2	10^7	62854
$\text{Var}(\mathcal{A}_{N_x,N_y,N_{z,\mathcal{A}}})$ in Fig. 2(b)	$2\times2\times20$	OBC × OBC × PBC	$\text{Var}(M_{\mathcal{A}})$	3	11	8×10^7	43000
	$3\times2\times20$	OBC × OBC × PBC	$\text{Var}(M_{\mathcal{A}})$	3	11	8×10^7	147300
Overlap matrix $\mathcal{O}$ with eigenvalues shown in Fig. 3(a)	$2\times2\times2$	PBC × PBC × PBC	$\mathcal{O}^{1,abs}_{\psi_1,\psi_2}$, $\mathcal{O}^{2,abs}_{\psi_1,\psi_2}$	∞	18	1×10^7	1385
	$2\times2\times2$	PBC × PBC × PBC	$\mathcal{O}^{phase}_{\psi_1,\psi_2}$	∞	18	1×10^7	900
	$3\times3\times3$	PBC × PBC × PBC	$\mathcal{O}^{1,abs}_{\psi_1,\psi_2}$, $\mathcal{O}^{2,abs}_{\psi_1,\psi_2}$	∞	8	1×10^7	2500
	$3\times3\times3$	PBC × PBC × PBC	$\mathcal{O}^{phase}_{\psi_1,\psi_2}$	∞	8	1×10^7	2500
	$4\times4\times4$	PBC × PBC × PBC	$\mathcal{O}^{1,abs}_{\psi_1,\psi_2}$, $\mathcal{O}^{2,abs}_{\psi_1,\psi_2}$	∞	7	1×10^7	7000
	$4\times4\times4$	PBC × PBC × PBC	$\mathcal{O}^{phase}_{\psi_1,\psi_2}$	∞	7	1×10^7	7000
Topological entanglement entropy γ from Kitaev-Preskill cut in Fig. 3(b)	$3\times3\times2$	PBC × PBC × PBC	$\langle\text{SWAP}_{\text{amp}}\rangle$	∞	1	1.6×10^9	112182
	$3\times3\times2$	PBC × PBC × PBC	$\langle\text{SWAP}_{\text{phase}}\rangle$	∞	1	10^8	14312
	$3\times3\times3$	PBC × PBC × PBC	$\langle\text{SWAP}_{\text{amp}}\rangle$	∞	1	3.6×10^9	331495
	$3\times3\times3$	PBC × PBC × PBC	$\langle\text{SWAP}_{\text{phase}}\rangle$	∞	1	10^8	14312
Topological entanglement entropy γ from rotated Kitaev-Preskill cut	$2\times3\times5$	PBC × PBC × PBC	$\langle\text{SWAP}_{\text{amp}}\rangle$	∞	1.7	1.4×10^9	142341
	$2\times3\times5$	PBC × PBC × PBC	$\langle\text{SWAP}_{\text{phase}}\rangle$	∞	2	2×10^8	56728
	$2\times3\times5$	OBC × PBC × PBC	$\langle\text{SWAP}_{\text{amp}}\rangle$	∞	1	4.4×10^9	438886
	$2\times3\times5$	OBC × PBC × PBC	$\langle\text{SWAP}_{\text{phase}}\rangle$	∞	1.2	2×10^8	37083

TABLE S1. Overview of technical data of all MC runs whose results are discussed in the main text. Here, the MC observables are defined in Appendix A. As introduced in Appendix E 1, the parameter r_{update} controls the maximal range of the spin exchange in the MC update, which can take a finite integer value or the value ∞ (meaning that there is no restriction on the maximal range).

in Eq. (7) of the main text. We focus here on the OBC case, *i.e.* OBC in the x direction and PBC in the y and z directions. Therefore, we think that the statistical fluctuations computed in this way might overestimate the actual error of the final MC measurement.

3. Technical data

For the convenience of anyone wishing to reproduce our results, we have summarized some technical data including the acceptance rate, the number of MC steps and the run time of all computations discussed in the main text in Table S1. The computations were performed for the most part on machines with CPUs of type Intel(R) Xeon(R) E5-2680 v2 @ 2.80GHz (Ivybridge), with between 500 and 1000 cores in use simultaneously.

Chapter 6

Conclusion

Almost 40 years after their discovery, topological phases of matter remain an active research field of both experimental and theoretical Condensed Matter Physics. The search for experimentally relevant systems with intrinsic topological order continues, which may become platforms for topological quantum computing. Novel phenomena can emerge even in non-interacting systems, as evidenced by the recent discovery of higher order topological phases. These phases may also shed new light on the generalization of topological order to three dimensions, where many fundamental open questions remain. To tackle these challenges, efficient numerical methods are required as the exponential growth of the quantum-mechanical Hilbert space renders numerical computations in interacting and higher-dimensional systems extremely difficult. TNS are a class of variational wave functions which offer an efficient encoding of relevant quantum many body states, and are thus a promising candidate for the description of interacting topological phases. This dissertation focuses on the representation of chiral topological phases in two and three dimensions using TNS, and their diagnosis using entanglement observables.

In the first part of this dissertation, we reviewed topological phases of matter and their characterization using quantum entanglement. In Chapter 2, we discussed SPT phases which can be realized in systems of free fermions. Focusing on the examples of the 1D SSH model and the 2D CI, we showed that such systems possess characteristic gapless modes at physical boundaries. We also discussed that the boundary physics is tightly related to non-trivial values of bulk topological invariants, which in the case of the CI lead to a quantization of the Hall conductivity. Finally we reviewed an example of a 2D HOTI with gapless protected corner modes. In Chapter 3, we considered interacting phases with intrinsic topological order, focusing on the Laughlin states for the fractional QHE. We discussed the generalized Pauli principle satisfied by these wave functions and reviewed how this can be used to explain the fractional Hall conductivity as well as the chiral edge spectra. We pointed out that the chiral edges modes can be described using Luttinger liquids characterized by a chiral CFT. We also reviewed the bulk boundary correspondence, according to which this CFT also describes certain bulk properties. Lastly, we considered a lattice model and discussed that it can host an FCI phase with intrinsic chiral topological order. In Chapter 4 we reviewed quantum entanglement and its application to the descrip-

tion of quantum many body states. We began with a discussion of the EEs and their area law scaling for gapped quantum systems, as well as their logarithmic scaling in gapless 1D systems. We then moved to the ES and illustrated its usefulness as a diagnostic numerical tool using the SSH model, the CI and the Laughlin states. In particular, we discussed the bulk boundary correspondence allowing the extraction of edge spectra from the bulk ground state. Finally, we gave a brief overview of TNS, beginning with the construction of MPS and PEPS. We discussed their in-built area law scaling of the EE and their resulting numerical efficiency. We concluded with a review of the applicability of TNS to topological phases with and without time reversal symmetry.

The second part of this dissertation contains a reprint of my publications. In Sec. 5.1 we studied a PEPS for a chiral spin liquid in the same phase as the Laughlin state at filling 1/2. By a careful analysis of its symmetries we were able to explain certain discrepancies between its chiral ES and the expected CFT spectrum. In a parameter region where the PEPS possesses an additional U(1) symmetry we were able to resolve these discrepancies and obtain an ES with the correct state counting and conformal weight of the CFT $\mathfrak{su}(2)_1$. In Sec. 5.2 we constructed exact PEPS with a constant finite bond dimension in hybrid real-momentum space for a CI and a 3D HOTI with chiral hinge modes. After an inverse Fourier transform in the momentum-space direction, the resulting real-space PEPS have a finite constant bond dimension in all but one direction, making them candidates for an efficient numerical description of these phases. The construction of the hybrid TNS is based on a charge pumping argument relating the CI model to the 1D SSH model, and the chiral hinge model to the 2D topological quadruple model. We were thus able to identify gapped next-nearest neighbor Hamiltonians interpolating between the fully dimerized trivial and topological phases of the SSH and quadrupole models. Their ground states are given by an MPS and a PEPS with a constant bond dimension equal to 2, respectively. In Sec. 5.2 we studied a wave function for a strongly interacting 3D fractional chiral hinge insulator constructed by Gutzwiller projection of two copies of the chiral hinge insulator. Using large-scale variational Monte Carlo computations, we showed that the gapless hinge states are of the same nature as the edge states of the Laughlin state at filling 1/2. We also showed that the gapped surfaces host a 2D topological phase with a TEE incompatible with any known topological quantum field theory for purely 2D systems.

All in all, we have thus studied different aspects of both interacting and non-interacting chiral topological phases, focusing in particular on their entanglement structure and their representations using TNS. We have also taken steps towards a better understanding of interacting chiral topological phases in three dimensions, using the route of HOTIs. There are several directions for future research related to our work. Further investigation of the numerical applicability of PEPS to chiral topological phases can definitely be useful. Furthermore, it would be very interesting, yet also extremely numerically challenging, to investigate the fate of the single Dirac cones on the horizontal surfaces of the chiral hinge insulator under the addition of strong interactions. More generally, a characterization of the appropriate topological field theory for the 3D fractional chiral hinge insulator and possible relations to topologically ordered and fractonic systems would be desirable.

Bibliography

[1] Anna Hackenbroich, Antoine Sterdyniak, and Norbert Schuch. "Interplay of SU(2), point group, and translational symmetry for projected entangled pair states: Application to a chiral spin liquid". In: *Phys. Rev. B* 98 (8 Aug. 2018), p. 085151.

[2] Anna Hackenbroich, B. Andrei Bernevig, Norbert Schuch, and Nicolas Regnault. "Fermionic tensor networks for higher-order topological insulators from charge pumping". In: *Phys. Rev. B* 101 (11 Mar. 2020), p. 115134.

[3] Anna Hackenbroich, Ana Hudomal, Norbert Schuch, B. Andrei Bernevig, and Nicolas Regnault. "Fractional Chiral Hinge Insulator". In: *arXiv e-prints* (Oct. 2020). arXiv: 2010.09728 [cond-mat.str-el].

[4] K. v. Klitzing, G. Dorda, and M. Pepper. "New Method for High-Accuracy Determination of the Fine-Structure Constant Based on Quantized Hall Resistance". In: *Phys. Rev. Lett.* 45 (6 Aug. 1980), pp. 494–497.

[5] D. C. Tsui, H. L. Stormer, and A. C. Gossard. "Two-Dimensional Magnetotransport in the Extreme Quantum Limit". In: *Phys. Rev. Lett.* 48 (22 May 1982), pp. 1559–1562.

[6] D. J. Thouless, M. Kohmoto, M. P. Nightingale, and M. den Nijs. "Quantized Hall Conductance in a Two-Dimensional Periodic Potential". In: *Phys. Rev. Lett.* 49 (6 Aug. 1982), pp. 405–408.

[7] C. L. Kane and E. J. Mele. "Quantum Spin Hall Effect in Graphene". In: *Phys. Rev. Lett.* 95 (22 Nov. 2005), p. 226801.

[8] B. Andrei Bernevig, Taylor L. Hughes, and Shou-Cheng Zhang. "Quantum Spin Hall Effect and Topological Phase Transition in HgTe Quantum Wells". In: *Science* 314.5806 (2006), pp. 1757–1761. eprint: https://science.sciencemag.org/content/314/5806/1757.full.pdf.

[9] Liang Fu, C. L. Kane, and E. J. Mele. "Topological Insulators in Three Dimensions". In: *Phys. Rev. Lett.* 98 (10 Mar. 2007), p. 106803.

[10] Markus König et al. "Quantum Spin Hall Insulator State in HgTe Quantum Wells". In: *Science* 318.5851 (2007), pp. 766–770. eprint: https://science.sciencemag.org/content/318/5851/766.full.pdf.

[11] D Hsieh et al. "A topological Dirac insulator in a quantum spin Hall phase". In: *Nature* 452 (May 2008), pp. 970–4.

[12] Yiman Xia et al. "Observation of a large-gap topological-insulator class with a single Dirac cone on the surface". In: *Nature Physics* 5 (May 2009), pp. 398–402.

[13] Xiao-Gang Wen. "Topological orders and edge excitations in fractional quantum Hall states". In: *Advances in Physics* 44.5 (1995), pp. 405–473. eprint: https://doi.org/10.1080/00018739500101566.

[14] A.Yu. Kitaev. "Fault-tolerant quantum computation by anyons". In: *Annals of Physics* 303.1 (2003), pp. 2–30.

[15] R de-Picciotto et al. "Direct observation of a fractional charge". In: *Physica B: Condensed Matter* 249-251 (1998), pp. 395–400.

[16] L. Saminadayar, D. C. Glattli, Y. Jin, and B. Etienne. "Observation of the $e/3$ Fractionally Charged Laughlin Quasiparticle". In: *Phys. Rev. Lett.* 79 (13 Sept. 1997), pp. 2526–2529.

[17] H. Bartolomei et al. "Fractional statistics in anyon collisions". In: *Science* 368.6487 (2020), pp. 173–177. eprint: https://science.sciencemag.org/content/368/6487/173.full.pdf.

[18] James Nakamura, S. Liang, G. Gardner, and M. Manfra. "Direct observation of anyonic braiding statistics". In: *Nature Physics* 16 (Sept. 2020), pp. 1–6.

[19] Michael Pretko, Xie Chen, and Yizhi You. "Fracton phases of matter". In: *International Journal of Modern Physics A* 35.06 (2020), p. 2030003. eprint: https://doi.org/10.1142/S0217751X20300033.

[20] Wladimir A Benalcazar, B Andrei Bernevig, and Taylor L Hughes. "Quantized electric multipole insulators". In: *Science* 357.6346 (2017), pp. 61–66.

[21] Frank Schindler et al. "Higher-order topological insulators". In: *Science advances* 4.6 (2018), eaat0346.

[22] Wladimir A. Benalcazar, B. Andrei Bernevig, and Taylor L. Hughes. "Electric multipole moments, topological multipole moment pumping, and chiral hinge states in crystalline insulators". In: *Physical Review B* 96.24 (Dec. 2017), p. 245115.

[23] Josias Langbehn, Yang Peng, Luka Trifunovic, Felix von Oppen, and Piet W. Brouwer. "Reflection-Symmetric Second-Order Topological Insulators and Superconductors". In: *Phys. Rev. Lett.* 119 (24 Dec. 2017), p. 246401.

[24] Zhida Song, Zhong Fang, and Chen Fang. "$(d-2)$-Dimensional Edge States of Rotation Symmetry Protected Topological States". In: *Phys. Rev. Lett.* 119 (24 Dec. 2017), p. 246402.

[25] Frank Schindler et al. "Higher-order topology in bismuth". In: *Nature Physics* 14.9 (Sept. 2018), pp. 918–924.

[26] R. B. Laughlin. "Anomalous Quantum Hall Effect: An Incompressible Quantum Fluid with Fractionally Charged Excitations". In: *Phys. Rev. Lett.* 50 (18 May 1983), pp. 1395–1398.

[27] Gregory Moore and Nicholas Read. "Nonabelions in the fractional quantum hall effect". In: *Nuclear Physics B* 360.2 (1991), pp. 362–396.

[28] N. Read and E. Rezayi. "Beyond paired quantum Hall states: Parafermions and incompressible states in the first excited Landau level". In: *Phys. Rev. B* 59 (12 Mar. 1999), pp. 8084–8092.

[29] Alexei Kitaev and John Preskill. "Topological Entanglement Entropy". In: *Phys. Rev. Lett.* 96 (11 Mar. 2006), p. 110404.

[30] Michael Levin and Xiao-Gang Wen. "Detecting Topological Order in a Ground State Wave Function". In: *Phys. Rev. Lett.* 96 (11 Mar. 2006), p. 110405.

[31] Hui Li and F. D. M. Haldane. "Entanglement Spectrum as a Generalization of Entanglement Entropy: Identification of Topological Order in Non-Abelian Fractional Quantum Hall Effect States". In: *Phys. Rev. Lett.* 101 (1 July 2008), p. 010504.

[32] Steven R. White. "Density matrix formulation for quantum renormalization groups". In: *Phys. Rev. Lett.* 69 (19 Nov. 1992), pp. 2863–2866.

[33] Ulrich Schollwöck. "The density-matrix renormalization group in the age of matrix product states". In: *Annals of Physics* 326.1 (2011), pp. 96–192.

[34] Philippe Corboz. "Variational optimization with infinite projected entangled-pair states". In: *Phys. Rev. B* 94 (3 July 2016), p. 035133.

[35] V. Zauner-Stauber, L. Vanderstraeten, M. T. Fishman, F. Verstraete, and J. Haegeman. "Variational optimization algorithms for uniform matrix product states". In: *Phys. Rev. B* 97 (4 Jan. 2018), p. 045145.

[36] Norbert Schuch, Ignacio Cirac, and David Perez-Garcia. "PEPS as ground states: Degeneracy and topology". In: *Annals of Physics* 325.10 (2010), pp. 2153–2192.

[37] Norbert Schuch, David Perez-Garcia, and Ignacio Cirac. "Classifying quantum phases using matrix product states and projected entangled pair states". In: *Phys. Rev. B* 84 (16 Oct. 2011), p. 165139.

[38] F. Verstraete, M. M. Wolf, D. Perez-Garcia, and J. I. Cirac. "Criticality, the Area Law, and the Computational Power of Projected Entangled Pair States". In: *Phys. Rev. Lett.* 96 (22 June 2006), p. 220601.

[39] Zheng-Cheng Gu, Michael Levin, Brian Swingle, and Xiao-Gang Wen. "Tensor-product representations for string-net condensed states". In: *Physical Review B* 79.8 (2009), p. 085118.

[40] F. Verstraete and J. I. Cirac. "Renormalization algorithms for quantum-many body systems in two and higher dimensions". In: (2004). arXiv: cond-mat/0407066 [cond-mat].

[41] T. B. Wahl, H.-H. Tu, N. Schuch, and J. I. Cirac. "Projected Entangled-Pair States Can Describe Chiral Topological States". In: *Phys. Rev. Lett.* 111 (23 Dec. 2013), p. 236805.

[42] Thorsten B. Wahl, Stefan T. Haßler, Hong-Hao Tu, J. Ignacio Cirac, and Norbert Schuch. "Symmetries and boundary theories for chiral projected entangled pair states". In: *Phys. Rev. B* 90 (11 Sept. 2014), p. 115133.

[43] J. Dubail and N. Read. "Tensor network trial states for chiral topological phases in two dimensions and a no-go theorem in any dimension". In: *Phys. Rev. B* 92 (20 Nov. 2015), p. 205307.

[44] Shuo Yang, Thorsten B. Wahl, Hong-Hao Tu, Norbert Schuch, and J. Ignacio Cirac. "Chiral Projected Entangled-Pair State with Topological Order". In: *Phys. Rev. Lett.* 114 (10 Mar. 2015), p. 106803.

[45] Didier Poilblanc, J. Ignacio Cirac, and Norbert Schuch. "Chiral topological spin liquids with projected entangled pair states". In: *Phys. Rev. B* 91 (22 June 2015), p. 224431.

[46] Didier Poilblanc, Norbert Schuch, and Ian Affleck. "$SU(2)_1$ chiral edge modes of a critical spin liquid". In: *Phys. Rev. B* 93 (17 May 2016), p. 174414.

[47] Ji-Yao Chen et al. "$SU(3)_1$ Chiral Spin Liquid on the Square Lattice: A View from Symmetric Projected Entangled Pair States". In: *Phys. Rev. Lett.* 125 (1 June 2020), p. 017201.

[48] N. Read. "Compactly supported Wannier functions and algebraic K-theory". In: *Phys. Rev. B* 95 (11 Mar. 2017), p. 115309.

[49] E. Fradkin. *Field Theories of Condensed Matter Physics*. Field Theories of Condensed Matter Physics. Cambridge University Press, 2013.

[50] W. P. Su, J. R. Schrieffer, and A. J. Heeger. "Soliton excitations in polyacetylene". In: *Phys. Rev. B* 22 (4 Aug. 1980), pp. 2099–2111.

[51] F. D. M. Haldane. "Model for a Quantum Hall Effect without Landau Levels: Condensed-Matter Realization of the "Parity Anomaly"". In: *Phys. Rev. Lett.* 61 (18 Oct. 1988), pp. 2015–2018.

[52] Cui-Zu Chang et al. "Experimental Observation of the Quantum Anomalous Hall Effect in a Magnetic Topological Insulator". In: *Science* 340.6129 (2013), pp. 167–170.

[53] M. Aidelsburger et al. "Realization of the Hofstadter Hamiltonian with Ultracold Atoms in Optical Lattices". In: *Phys. Rev. Lett.* 111 (18 Oct. 2013), p. 185301.

[54] Hirokazu Miyake, Georgios A. Siviloglou, Colin J. Kennedy, William Cody Burton, and Wolfgang Ketterle. "Realizing the Harper Hamiltonian with Laser-Assisted Tunneling in Optical Lattices". In: *Phys. Rev. Lett.* 111 (18 Oct. 2013), p. 185302.

[55] Monika Aidelsburger et al. "Measuring the Chern number of Hofstadter bands with ultracold bosonic atoms". In: *Nature Physics* 11 (Dec. 2014).

[56] Gregor Jotzu et al. "Experimental realization of the topological Haldane model with ultracold fermions". In: *Nature* 515 (Nov. 2014), pp. 237–40.

[57] Andreas W. W. Ludwig, Matthew P. A. Fisher, R. Shankar, and G. Grinstein. "Integer quantum Hall transition: An alternative approach and exact results". In: *Phys. Rev. B* 50 (11 Sept. 1994), pp. 7526–7552.

[58] M. Büttiker. "Absence of backscattering in the quantum Hall effect in multiprobe conductors". In: *Phys. Rev. B* 38 (14 Nov. 1988), pp. 9375–9389.

[59] M. Nakahara. *Geometry, Topology and Physics, Second Edition*. Graduate student series in physics. Taylor & Francis, 2003.

[60] Andreas P. Schnyder, Shinsei Ryu, Akira Furusaki, and Andreas W. W. Ludwig. "Classification of topological insulators and superconductors in three spatial dimensions". In: *Phys. Rev. B* 78 (19 Nov. 2008), p. 195125.

[61] Shinsei Ryu, Andreas P Schnyder, Akira Furusaki, and Andreas W W Ludwig. "Topological insulators and superconductors: tenfold way and dimensional hierarchy". In: *New Journal of Physics* 12.6 (June 2010), p. 065010.

[62] Alexei Kitaev. "Periodic table for topological insulators and superconductors". In: *AIP Conference Proceedings* 1134.1 (2009), pp. 22–30. eprint: `https://aip.scitation.org/doi/pdf/10.1063/1.3149495`.

[63] M. Z. Hasan and C. L. Kane. "Colloquium: Topological insulators". In: *Rev. Mod. Phys.* 82 (4 Nov. 2010), pp. 3045–3067.

[64] Xiao-Liang Qi and Shou-Cheng Zhang. "Topological insulators and superconductors". In: *Rev. Mod. Phys.* 83 (4 Oct. 2011), pp. 1057–1110.

[65] Liang Fu. "Topological Crystalline Insulators". In: *Phys. Rev. Lett.* 106 (10 Mar. 2011), p. 106802.

[66] Timothy Hsieh et al. "Topological Crystalline Insulators in the SnTe Material Class". In: *Nature communications* 3 (July 2012), p. 982.

[67] F. D. M. Haldane and S. Raghu. "Possible Realization of Directional Optical Waveguides in Photonic Crystals with Broken Time-Reversal Symmetry". In: *Phys. Rev. Lett.* 100 (1 Jan. 2008), p. 013904.

[68] Zheng Wang, Yidong Chong, John D Joannopoulos, and Marin Soljačić. "Observation of unidirectional backscattering-immune topological electromagnetic states". In: *Nature* 461.7265 (2009), pp. 772–775.

[69] CL Kane and TC Lubensky. "Topological boundary modes in isostatic lattices". In: *Nature Physics* 10.1 (2014), pp. 39–45.

[70] Roman Süsstrunk and Sebastian D. Huber. "Observation of phononic helical edge states in a mechanical topological insulator". In: *Science* 349.6243 (2015), pp. 47–50. eprint: https://science.sciencemag.org/content/349/6243/47.full.pdf.

[71] Zhaoju Yang et al. "Topological Acoustics". In: *Phys. Rev. Lett.* 114 (11 Mar. 2015), p. 114301.

[72] Jia Ningyuan, Clai Owens, Ariel Sommer, David Schuster, and Jonathan Simon. "Time- and Site-Resolved Dynamics in a Topological Circuit". In: *Phys. Rev. X* 5 (2 June 2015), p. 021031.

[73] Victor V. Albert, Leonid I. Glazman, and Liang Jiang. "Topological Properties of Linear Circuit Lattices". In: *Phys. Rev. Lett.* 114 (17 Apr. 2015), p. 173902.

[74] Oleg Dubinkin and Taylor L. Hughes. "Higher-order bosonic topological phases in spin models". In: *Phys. Rev. B* 99 (23 June 2019), p. 235132.

[75] Yizhi You, Trithep Devakul, F. J. Burnell, and Titus Neupert. "Higher-order symmetry-protected topological states for interacting bosons and fermions". In: *Phys. Rev. B* 98 (23 Dec. 2018), p. 235102.

[76] Sunil Mittal et al. "Photonic quadrupole topological phases". In: *Nature Photonics 13, 692-696 (2019)* (Dec. 21, 2018). arXiv: 1812.09304v2 [physics.optics].

[77] Marc Serra-Garcia et al. "Observation of a phononic quadrupole topological insulator". In: *Nature* 555.7696 (2018), p. 342.

[78] Haoran Xue, Yahui Yang, Fei Gao, Yidong Chong, and Baile Zhang. "Acoustic higher-order topological insulator on a kagome lattice". In: *Nature Materials* 18.2 (Feb. 2019), pp. 108–112.

[79] Xiang Ni, Matthew Weiner, Andrea Alù, and Alexander B. Khanikaev. "Observation of higher-order topological acoustic states protected by generalized chiral symmetry". In: *Nature Materials* 18.2 (Feb. 2019), pp. 113–120.

[80] Bi-Ye Xie et al. "Visualization of higher-order topological insulating phases in two-dimensional dielectric photonic crystals". In: *Phys. Rev. Lett. 122, 233903 (2019)* (Dec. 15, 2018). arXiv: 1812.06263v2 [cond-mat.mes-hall].

[81] Yuting Yang et al. "Gapped Topological Kink States and Topological Corner States in Graphene". In: *Science Bulletin, 65, 531 (2020)* (Mar. 5, 2019). arXiv: 1903.01816v1 [cond-mat.mes-hall].

[82] Christopher W Peterson, Wladimir A Benalcazar, Taylor L Hughes, and Gaurav Bahl. "A quantized microwave quadrupole insulator with topologically protected corner states". In: *Nature* 555.7696 (2018), p. 346.

[83] Stefan Imhof et al. "Topolectrical-circuit realization of topological corner modes". In: *Nature Physics* 14.9 (2018), p. 925.

[84] Marc Serra-Garcia, Roman Süsstrunk, and Sebastian D. Huber. "Observation of quadrupole transitions and edge mode topology in an LC circuit network". In: *Phys. Rev. B* 99 (2 Jan. 2019), p. 020304.

[85] Qian Niu, D. J. Thouless, and Yong-Shi Wu. "Quantized Hall conductance as a topological invariant". In: *Phys. Rev. B* 31 (6 Mar. 1985), pp. 3372–3377.

[86] SM Girvin and R Prange. "The quantum Hall effect". In: (1987).

[87] N.R. Cooper. "Rapidly rotating atomic gases". In: *Advances in Physics* 57.6 (2008), pp. 539–616. eprint: https://doi.org/10.1080/00018730802564122.

[88] B. Andrei Bernevig and F. D. M. Haldane. "Model Fractional Quantum Hall States and Jack Polynomials". In: *Phys. Rev. Lett.* 100 (24 June 2008), p. 246802.

[89] Richard P Stanley. "Some combinatorial properties of Jack symmetric functions". In: *Advances in Mathematics* 77.1 (1989), pp. 76–115.

[90] P. Di Francesco, P. Mathieu, and D. Sénéchal. *Conformal Field Theory*. Graduate texts in contemporary physics. Island Press, 1996.

[91] Daniel C Mattis and Elliott H Lieb. "Exact solution of a many-fermion system and its associated boson field". In: *Bosonization*. World Scientific, 1994, pp. 98–106.

[92] X. G. Wen. "Chiral Luttinger liquid and the edge excitations in the fractional quantum Hall states". In: *Phys. Rev. B* 41 (18 June 1990), pp. 12838–12844.

[93] M. Hermanns, A. Chandran, N. Regnault, and B. Andrei Bernevig. "Haldane statistics in the finite-size entanglement spectra of $1/m$ fractional quantum Hall states". In: *Phys. Rev. B* 84 (12 Sept. 2011), p. 121309.

[94] Pasquale Calabrese and John Cardy. "Entanglement entropy and conformal field theory". In: *Journal of Physics A: Mathematical and Theoretical* 42.50 (Dec. 2009), p. 504005.

[95] Benoit Estienne and Jean-Marie Stéphan. *Entanglement spectroscopy of chiral edge modes in the Quantum Hall effect*. 2019. arXiv: 1911.10125 [cond-mat.str-el].

[96] Masaki Oshikawa, Yong Baek Kim, Kirill Shtengel, Chetan Nayak, and Sumanta Tewari. "Topological degeneracy of non-Abelian states for dummies". In: *Annals of Physics* 322.6 (2007), pp. 1477–1498.

[97] X. G. Wen and Q. Niu. "Ground-state degeneracy of the fractional quantum Hall states in the presence of a random potential and on high-genus Riemann surfaces". In: *Phys. Rev. B* 41 (13 May 1990), pp. 9377–9396.

[98] X.G. Wen. *Quantum Field Theory of Many-Body Systems:From the Origin of Sound to an Origin of Light and Electrons: From the Origin of Sound to an Origin of Light and Electrons*. Oxford Graduate Texts. OUP Oxford, 2004.

[99] A. Kol and N. Read. "Fractional quantum Hall effect in a periodic potential". In: *Phys. Rev. B* 48 (12 Sept. 1993), pp. 8890–8898.

[100] V. Kalmeyer and R. B. Laughlin. "Equivalence of the resonating-valence-bond and fractional quantum Hall states". In: *Phys. Rev. Lett.* 59 (18 Nov. 1987), pp. 2095–2098.

[101] Titus Neupert, Luiz Santos, Claudio Chamon, and Christopher Mudry. "Fractional Quantum Hall States at Zero Magnetic Field". In: *Phys. Rev. Lett.* 106 (23 June 2011), p. 236804.

[102] DN Sheng, Zheng-Cheng Gu, Kai Sun, and L Sheng. "Fractional quantum Hall effect in the absence of Landau levels". In: *Nature communications* 2.1 (2011), pp. 1–5.

[103] N. Regnault and B. Andrei Bernevig. "Fractional Chern Insulator". In: *Phys. Rev. X* 1 (2 Dec. 2011), p. 021014.

[104] Siddharth A. Parameswaran, Rahul Roy, and Shivaji L. Sondhi. "Fractional quantum Hall physics in topological flat bands". In: *Comptes Rendus Physique* 14.9 (2013). Topological insulators / Isolants topologiques, pp. 816–839.

[105] Yi Zhang, Tarun Grover, and Ashvin Vishwanath. "Topological entanglement entropy of $\mathbb{Z}_2$ spin liquids and lattice Laughlin states". In: *Phys. Rev. B* 84 (7 Aug. 2011), p. 075128.

[106] Luigi Amico, Rosario Fazio, Andreas Osterloh, and Vlatko Vedral. "Entanglement in many-body systems". In: *Rev. Mod. Phys.* 80 (2 May 2008), pp. 517–576.

[107] Steven T. Flammia, Alioscia Hamma, Taylor L. Hughes, and Xiao-Gang Wen. "Topological Entanglement Rényi Entropy and Reduced Density Matrix Structure". In: *Phys. Rev. Lett.* 103 (26 Dec. 2009), p. 261601.

[108] Mark Srednicki. "Entropy and area". In: *Phys. Rev. Lett.* 71 (5 Aug. 1993), pp. 666–669.

[109] J. Eisert, M. Cramer, and M. B. Plenio. "Colloquium: Area laws for the entanglement entropy". In: *Rev. Mod. Phys.* 82 (1 Feb. 2010), pp. 277–306.

[110] Matthew B Hastings. "An area law for one-dimensional quantum systems". In: *Journal of Statistical Mechanics: Theory and Experiment* 2007.08 (2007), P08024.

[111] Pasquale Calabrese and John Cardy. "Entanglement entropy and quantum field theory". In: *Journal of Statistical Mechanics: Theory and Experiment* 2004.06 (June 2004), P06002.

[112] Nicolas Laflorencie. "Quantum entanglement in condensed matter systems". In: *Physics Reports* 646 (2016). Quantum entanglement in condensed matter systems, pp. 1–59.

[113] A. Sterdyniak, N. Regnault, and B. A. Bernevig. "Extracting Excitations from Model State Entanglement". In: *Phys. Rev. Lett.* 106 (10 Mar. 2011), p. 100405.

[114] Ingo Peschel. "Calculation of reduced density matrices from correlation functions". In: *Journal of Physics A: Mathematical and General* 36.14 (2003), p. L205.

[115] Lukasz Fidkowski. "Entanglement Spectrum of Topological Insulators and Superconductors". In: *Phys. Rev. Lett.* 104 (13 Apr. 2010), p. 130502.

[116] Ignacio Cirac, David Perez-Garcia, Norbert Schuch, and Frank Verstraete. "Matrix Product States and Projected Entangled Pair States: Concepts, Symmetries, and Theorems". In: *arXiv e-prints*, arXiv:2011.12127 (Nov. 2020), arXiv:2011.12127. arXiv: 2011.12127 [quant-ph].

[117] Michael M. Wolf, Frank Verstraete, Matthew B. Hastings, and J. Ignacio Cirac. "Area Laws in Quantum Systems: Mutual Information and Correlations". In: *Phys. Rev. Lett.* 100 (7 Feb. 2008), p. 070502.

[118] Bo-Xiao Zheng et al. "Stripe order in the underdoped region of the two-dimensional Hubbard model". In: *Science* 358.6367 (2017), pp. 1155–1160.

[119] Mark Fannes, Bruno Nachtergaele, and Reinhard F Werner. "Finitely correlated states on quantum spin chains". In: *Communications in mathematical physics* 144.3 (1992), pp. 443–490.

[120] D. Perez-Garcia, F. Verstraete, M. M. Wolf, and J. I. Cirac. "Matrix Product State Representations". In: *Quantum Info. Comput.* 7.5 (July 2007), pp. 401–430.

[121] T. Xiang. "Density-matrix renormalization-group method in momentum space". In: *Phys. Rev. B* 53 (16 Apr. 1996), R10445–R10448.

[122] Michael P. Zaletel and Roger S. K. Mong. "Exact matrix product states for quantum Hall wave functions". In: *Phys. Rev. B* 86 (24 Dec. 2012), p. 245305.

[123] Christina V. Kraus, Norbert Schuch, Frank Verstraete, and J. Ignacio Cirac. "Fermionic projected entangled pair states". In: *Phys. Rev. A* 81 (5 May 2010), p. 052338.

[124] Nick Bultinck, Dominic J Williamson, Jutho Haegeman, and Frank Verstraete. "Fermionic matrix product states and one-dimensional topological phases". In: *Physical Review B* 95.7 (2017), p. 075108.

[125] Norbert Schuch, Michael M. Wolf, Frank Verstraete, and J. Ignacio Cirac. "Computational Complexity of Projected Entangled Pair States". In: *Phys. Rev. Lett.* 98 (14 Apr. 2007), p. 140506.

[126] J. Ignacio Cirac, Didier Poilblanc, Norbert Schuch, and Frank Verstraete. "Entanglement spectrum and boundary theories with projected entangled-pair states". In: *Phys. Rev. B* 83 (24 June 2011), p. 245134.

[127] Ian P McCulloch and Miklós Gulácsi. "The non-Abelian density matrix renormalization group algorithm". In: *EPL (Europhysics Letters)* 57.6 (2002), p. 852.

[128] Michael A. Levin and Xiao-Gang Wen. "String-net condensation: A physical mechanism for topological phases". In: *Phys. Rev. B* 71 (4 Jan. 2005), p. 045110.

[129] Marius Lemm and Evgeny Mozgunov. "Spectral gaps of frustration-free spin systems with boundary". In: *Journal of Mathematical Physics* 60.5 (2019), p. 051901. eprint: https://doi.org/10.1063/1.5089773.